Active Electromagnetics at the Mid–Ocean Ridge

by

Mark E. Everett

Geophysics Division
Department of Physics
University of Toronto

A Thesis submitted in conformity with
the requirements for the degree of
Doctor of Philosophy at the
University of Toronto

Abstract

The 59,000 km long global mid–ocean ridge system is the site of formation of 20 km^3 of oceanic crust yearly. Two–thirds of all heat loss from the interior of our planet is through the ocean floors, 40% of this amount is focused through the ridge. Activity involves complex interactions among a number of processes occurring over wide ranges of depths and lateral distances, including melting of the earth's mantle, delivery of the molten rock to a crustal magma chamber, cooling of the magma intrusion by hydrothermal circulation and volcanic eruption, chemical exchange between hot rock surrounding the magma chamber and the overlying seawater, and even the establishment of exotic biological communities near hydrothermal vents at the ridge axis. These features justify the expanding scientific interest in the study of the ridge.

Transient controlled–source electromagnetics (CSEM) is a geophysical exploration technique capable of determining the electrical conductivity beneath fast–spreading segments of the mid–ocean ridge. Geological structure beneath the mid–ocean ridge that is readily accessible to transient CSEM exploration is located at crustal levels and includes the axial magma chamber and its associated zones of partial melt and hydrothermal activity. Seismic images of the top several kilometers beneath the fast spreading East Pacific Rise (EPR) between 9–13°N have already been obtained. Multi-channel reflection profiles place strong constraints on the geometry of the top of the axial magma chamber but refraction data provide only coarse estimates of the sub–surface temperature, distribution of partial melt and porosity, parameters required to distinguish between proposed petrological models of the ridge. Electrical conductivity is a strong indicator of all these critical parameters and therefore CSEM methods are well–suited to improve the estimates and help characterize the ridge environment.

In this thesis, a pair of forward modeling computer programs have been developed to design ridge–going experiments and assist interpretation of mid–ocean ridge transient CSEM data sets, as they become available. The programs may also be used to evaluate the transient CSEM technique as it might be applied to investigate other tectonically active regions of the seafloor. One program rapidly computes the theoretical response, as

a function of time, of an arbitrary, two dimensional earth to a sudden switch–on of electric current in a line source of electromagnetic energy. The other program is more advanced, requires more computer time, and is referred to as a 2.5–D program because it can handle excitation of the earth by a more realistic, finite source.

The programs solve the forward problem as follows. Electromagnetic boundary value problems based on the governing Maxwell's equations are solved by the finite element method in the Laplace frequency s–domain. The calculated electromagnetic field components are then transformed into the time domain by means of the Gaver–Stehfest algorithm. In the 2.5–D program, Maxwell's equations are additionally Fourier transformed in the direction parallel to the strike of the 2–D conductivity structure, and field components are computed in the along–strike wavenumber q–domain. Following the calculation, inverse transforms are performed to obtain the along–strike spatial variations of the field components. The codes have been validated through comparisons with known analytic solutions in which the earth is modeled as a uniformly conducting half–space. Convergence of the finite element approximation is found to be $O(h)$, where h measures the size of the triangles comprising the finite element mesh. An extrapolation formula is described by which numerical solutions on progressively finer meshes are combined. The formula permits great accuracy to be attained in the computed field components, using relatively coarse meshes.

A numerical study of the performance of an idealized transient CSEM system at the East Pacific Rise has been carried out using the 2–D code. The system consists of an infinite source located 5 km west of the ridge axis, and seafloor magnetic field sensors placed at various distances across the ridge crest. The source is oriented with respect to the strike of the ridge so as to produce only the H–polarization mode of electric current flow. The results indicate that this system can detect the axial magma chamber and the associated zones of hydrothermal activity and partial melt by monitoring two electromagnetic response parameters, the diffusion time τ and the response amplitude $\dot{B}_{\mathbf{max}}$, as a function of transmitter/receiver separation. These response parameters are easily extracted from measured data and are diagnostic of the sub–surface electrical conductivity. The presence of a highly conductive magma chamber slows and attenuates signals diffusing beneath the ridge, increasing τ and decreasing $\dot{B}_{\mathbf{max}}$. Hydrothermal circulation in the highly fractured,

extrusive basalt layer has the same effect on the data for receivers placed within 3 km of the ridge axis, but very little effect elsewhere. Inferences made from the numerical results suggest that a horizontal electric dipole (HED) of moment 10^4 A·m and receivers sampling the seafloor magnetic field at 10–25 Hz with a sensitivity of 1 pT/s over a time window extending to 10 s are sufficient to detect these crustal targets.

Interpretation of transient CSEM data requires forward modeling using a more realistic, finite source. The 2.5–D code is capable of achieving this. Sample field patterns produced in the vicinity of the ridge by a sudden switch–on of electric current in a horizontal electric dipole (HED) are computed. The patterns illustrate diffusion, in three spatial dimensions and time, of various along–strike electromagnetic field components through typical mid–ocean ridge structures. The results demonstrate the utility of the 2.5–D code, *i.e.* its potential for interpreting data from a transient CSEM ridge–going experiment.

Acknowledgements

Many individuals have made contributions to this thesis, in a variety of ways. I would like to take this opportunity to acknowledge them. Firstly, I express sincere gratitude to Professor R.N. Edwards, not only for his excellence as a Ph.D. thesis adviser and an educator of physics, but for his friendly encouragement and his commitment to ensuring my well–being as a graduate student.

I acknowledge and thank Profs I.J. Ferguson, R.C. Bailey, G.F. West, M.C. Sinha and S.D. Scott for their time spent reading the thesis and for providing many valuable suggestions which greatly improved its quality.

I received generous and continuous financial support from the Natural Sciences and Engineering Research Council of Canada. That organization has made this thesis possible. I received ample and valuable computing advice and resources from Jim Stacey, David Blyth and my good friend, the CRAY XMP, who are all affiliated with the Ontario Center for Large Scale Computation.

During my years at the University of Toronto, I enjoyed interactions, discussions and adventures with numerous students, researchers and visiting scientists. These included, in roughly chronological order, Stephen Cheesman, Hisashi Utada, Karl Kwan, Ian Ferguson, Jim Craven, Alan Chave, Martyn Unsworth, Rob Evans, Min Hu, Liming Yu and Peter Michalek. I acknowledge the technical assistance provided by Maria Wong and defer to the squash–playing prowess of Khader Khan.

On a personal level I would like to thank my parents for their everlasting support and kindness. I would like to thank Stephen Mihailov, Dave Anthony and Bill Dykshoorn for cataloging Norman's comments. Most importantly, I would like to thank my wife Elaine for her contagious enthusiasm, her loving support and for abandoning trying to teach me common sense when it became obvious that I wasn't actually learning anything. Finally, thanks to Taylor James, who without knowing it guided me through the last stages of this project.

Active Electromagnetics at the Mid–Ocean Ridge

Chapter 1

Introduction

1.0 Introduction

A great challenge to the marine geophysicist involves the determination of the sub–surface geology of the seafloor to depths of several kilometers. Knowledge of the aforementioned is important not only for the sake of the exploration of a large but relatively unknown part of the earth's crust, but also to investigate the formation of economic geological structures, including mineral deposits, and to constrain certain geo–dynamic models associated with plate tectonics, such as those describing the formation of oceanic crust at mid–ocean ridges (MORs) and its destruction at subduction zones.

At the geophysicist's disposal are seismic, gravity, magnetic and electromagnetic techniques, measurements from which are sensitive to the elastic properties, density, magnetic and the electrical properties of the earth, respectively. Regardless of technique chosen, a response of the earth can be measured and either directly *inverted*, or compared to theoretical responses that have been computed for *models* of the earth. The result, in both cases, is a profile of the critical physical property in one or more dimensions. This profile is often converted into a geological map using the available information about rock properties. Since many rocks have similar values for a given physical property, the geological interpretation is likely to be ambiguous, so that wherever possible it is desirable to apply more than a single geophysical technique.

In broad terms, this thesis is concerned with transient controlled–source electromagnetics (CSEM) as a technique to determine the electrical conductivity structure of the mid–ocean ridge. In particular, a pair of forward modeling computer programs have been developed, ostensibly to assist interpretation of mid–ocean ridge transient CSEM data sets, as they become available, but in actual fact the programs may be used to evaluate transient CSEM techniques at many other places on the deep seafloor. One program rapidly computes the theoretical electromagnetic response of an arbitrary, two dimensional earth to its excitation by a 2–D infinite source. The other program is more advanced, requires more computer time, and is referred to as a 2.5–D program because it is capable of handling finite source excitation.

Active electromagnetic exploration of the mid–ocean ridge is very much in its infancy, and there remains much that can be done. While ridge–going transient CSEM experiments are likely to provide hard constraints on models of oceanic crust formation (Constable 1990), there is no doubt that they will be difficult and costly to perform. A full–scale design using the programs described in this thesis can optimize an experiment, with respect to a wide range of criteria. For example, one can find the resolution of the mid–crustal, axial magma chamber and other MOR geological features, and identify optimal transmitter/receiver configurations and expected signal magnitudes. I have investigated this problem in great detail using the 2–D code,

and the results are presented in later chapters. In addition, once an experiment is completed, the data may be interpreted either with trial and error forward modeling using the 2.5–D code or else by direct inversion where the 2.5–D code is but a single component of a larger inversion package.

In this introductory chapter, in which I will describe the motivation for studying the mid–ocean ridge by controlled–source electromagnetics, I will present a review of the electrical properties of the ocean crust and identify some well–known factors which influence its electrical conductivity, especially in the vicinity of an active ridge. Then, I will give a brief overview of transient CSEM techniques capable of mapping seafloor electrical conductivity. Finally, I will present an outline of what is to be found in the remainder of the thesis.

1.1 Electrical Properties of Oceanic Crust

The major rock units in a cross–section of the top several kilometers of seafloor near an active mid–ocean ridge, as inferred primarily from studies of ophiolites and the results of seismic reflection and refraction experiments, typically include a thin layer of young, unconsolidated sediments, whose thickness depends on crustal age, a 1–2 km thick layer of basalts subdivided into lavas and sheeted dykes directly beneath the sediments, 4–6 km of gabbros at the base of the oceanic crust and, finally, peridotites which comprise the upper mantle. Like all rocks, those of young oceanic crust and upper mantle are assemblages of minerals, with the electrical properties of rocks depending not only on the kinds of minerals present, but also on the way in which the minerals are distributed throughout. At fast spreading ridges, a mid–crustal reservoir containing hot, partially molten material and associated zones of hydrothermal fluid circulation throughout the upper basalt layer may exist. The electrical properties of rocks located directly beneath ridges will depend, in addition to the factors already given, on the amount of fluid or partial melt present, its distribution and temperature.

The electrical properties of a given material include its electrical conductivity σ and electric permittivity ϵ. Electrical conductivity measures the resistance of a material to the establishment of long term current flow through it, and is widely variable throughout the earth, spanning many orders of magnitude. Electric permittivity measures the ability of a material to become polarized by an external electric field $\mathbf{E}$. The dielectric constant $\kappa \equiv \epsilon/\epsilon_0$ of most minerals and rocks is in the range 1–100, and depends on the frequency of the applied field (Keller 1989).

Magnetic permeability μ, although it appears in the governing equations of electromagnetism, is normally considered to be a magnetic property. Magnetic permeability measures the ability of a material to become magnetized by an external magnetic field $\mathbf{H}$. The permeabilities of most ocean crust materials are close to the free space value μ_0, except those of rocks containing a great quantity of iron. For example, the relative permeability $\mu_r \equiv \mu/\mu_0$ of basalts containing 2 vol% magnetite (Fe_3O_4) is μ_r=1.08, and that of basalts containing 5 vol% magnetite is μ_r=1.18 (Carmichael 1989). The relative permeabilities of gabbros and peridotites, and their typical magnetite contents, are similar to those quoted above.

The spatial variations in magnetic permeability μ throughout oceanic crust are not sufficiently large to have an appreciable effect on seafloor electromagnetic measurements, although it should be noted that the magnetic exploration technique produces data whose interpretation is very sensitive to small changes in permeability. In addition, due to the low frequencies $\omega \ll \sigma/\epsilon$ used in seafloor CSEM, measurements do not

depend on spatial variations in electric permittivity (Keller 1987). The large spatial variations in electrical conductivity, on the other hand, strongly influence electromagnetic responses. In view of this, the electrical conductivity of minerals and rocks deserves to be examined in greater detail.

If a sample of conducting material is placed in an external electric field **E**, a current will flow in the material. The current density **J** depends on the electrical conductivity, as summarized by Ohm's Law:

$$\mathbf{J} = \overline{\sigma}(\mathbf{r}, \mathbf{E})\mathbf{E} \tag{1.1}$$

In equation (1.1), $\overline{\sigma}$ is the electrical conductivity tensor, and must be determined empirically. If the material is found to be linear and isotropic, the conductivity tensor reduces to the scalar quantity $\sigma(\mathbf{r})$. The vast majority of minerals and rocks are linear but anisotropic, nonetheless, for large formations in which the constituent rocks may not be systematically aligned, it is common to write Ohm's Law in its simplest form

$$\mathbf{J} = \sigma(\mathbf{r})\mathbf{E}. \tag{1.2}$$

The units of electrical conductivity, derived from the MKS units of **E** and **J**, are siemens per meter (S/m).

Minerals may be divided into metallic conductors, semiconductors and solid electrolytes. The various conduction mechanisms, which are described below, are discussed in far greater detail in Keller (1987). Values for rock conductivities that are given below have also been taken from this reference.

To start with, native metals, which have been found among hydrothermally altered sufides at the mid–ocean ridge (*e.g.* Hannington *et.al.* 1988), are rare but extremely conductive. For instance, the conductivity of native copper is 3.0×10^6–8.0×10^7 S/m. Graphite is a strongly anisotropic metal: the conductivity of graphite is about 2×10^6 S/m if **J** is parallel to the basal cleavage but can be two orders of magnitude less if **J** is perpendicular to the basal cleavage. In semiconductors, a few eV of activation energy is required to move a charge carrier from one atom to the next, effectively reducing the electrical conductivity relative to that of metals. The activation energy may be supplied *e.g.* by heating the mineral. Sulphides and oxides, a group which includes many economic ore minerals, are semiconductors with electrical conductivity in the range $10^{-4}\leq\sigma\leq10^6$ S/m; they can become as conductive as true metals at sufficiently large temperatures.

Most rock forming minerals are solid electrolytes. Electrolytic conduction in solids proceeds via the motion of ions, under the influence of an applied **E** field, through the crystal lattice. It is the result of *defects* in the lattice that ions are provided for conduction. The conductivity of solid electrolytes depends on the ion mobility, which is the apparent velocity under an applied field of strength 1 V/m, the number density of the charge carriers and also temperature, since thermal agitation can displace ions from their normal positions.

The conductivity of solid electrolytes as a function of absolute temperature T has been found from laboratory measurements to be of the following form:

$$\sigma(T) = A_1\exp(-U_1/kT) + A_2\exp(-U_2/kT) \tag{1.3}$$

where A_1 and A_2 are constants, k=1.381×10^{-23} J/deg is Boltzmann's constant, and U_1 and U_2 are identified as activation energies. Basalts, gabbros and peridotites are

all solid electrolytes and values for their parameters A_i and U_i are given in the table below (Keller 1987):

	A_1	A_2	U_1	U_2
gabbro	0.7 S/m	10^7 S/m	0.70 eV	2.2 eV
basalt	0.7	10^7	0.57	2.0
peridotite	4.0	10^7	0.81	2.3.

Seawater is an aqueous electrolyte, *i.e.* under an applied **E** field, its constituent cations and anions are accelerated in different directions. High temperature lowers the viscosity of the seawater, which raises the ion mobility and therefore its electrical conductivity. The conductivity of porous rocks depends primarily on the amount of water present, its distribution and temperature. The amount of water present in a rock is governed by its ***porosity***, which is the volume fraction of void space. The distribution of water in the rock is governed by its *texture*, which is a description of the pore geometry. In order to conduct electricity, the pore spaces must be interconnected and filled with water. An empirical formula relating conductivity to porosity in ***fully*** saturated rocks is given by Archie's Law (Keller 1987):

$$\sigma = a\sigma_w W^m \tag{1.4}$$

where σ_w is the conductivity of the aqueous electrolyte, W is the fraction of the volume of pore space to the total volume of the rock and a and m are empirically determined parameters. There is a large scatter in the (σ, W) data which is due not to experimental uncertainties but to variability in the texture of porous rock. In young oceanic crust, textures may range from the inter–granular space in marine sediments to the large, poorly interconnected structures (vesicles, vugs, drained pillows, etc.) with high (20–40 %) porosity that are commonly found in the extrusive volcanics.

For ***partially*** saturated rocks, Archie's Law is modified to

$$\sigma = a\sigma_w S^n \theta^m \tag{1.5}$$

where $n \approx 2$ is empirically determined, S is the fraction of the pore volume filled with aqueous electrolyte and θ is the volume fraction of void space in the rock. Archie's Law holds provided the rock is minimally saturated: there must be at least a continuous thin film of water over all the grain surfaces in the rock, but the entire pore volume need not be filled with water as in the case of fully saturated rocks.

Pertaining to regions where melt co–exists with solid, such as in the mid–crustal reservoir beneath fast spreading ridges, and using simple geometric models of partially molten rock, Waff (1974) has derived relationships between the effective conductivity σ^* of a two–phase melt/solid system and melt fraction ϕ and connectivity. The best possible ***bounds*** $\sigma_- \leq \sigma^* \leq \sigma_+$ for the effective conductivity are referred to as the Hashin–Shtrikman bounds (Schmeling 1986) and are given by

$$\sigma_- = \sigma_s + \phi \left(\frac{1}{\sigma_m - \sigma_s} + \frac{1-\phi}{3\sigma_s} \right)^{-1} \tag{1.6}$$

$$\sigma_+ = \sigma_m + (1-\phi) \left(\frac{1}{\sigma_s - \sigma_m} + \frac{\phi}{3\sigma_m} \right)^{-1} \tag{1.7}$$

where σ_m is the conductivity of the melt phase and σ_s is that of the solid phase. The lower bound σ_- corresponds to dry rocks or to a completely unconnected melt, such as isolated melt pockets at grain triple junctions, while the upper bound σ_+ applies when the melt is completely connected, such as fluid–filled tubes or films along grain interfaces. The Hashin-Shtrikman bounds are valid for two phase material that is macroscopically homogenous and isotropic.

Although this section of the thesis has been largely descriptive in nature, numerical estimates of the electrical conductivity of various, proposed mid–ocean ridge structures can be found in §2.3.

1.2 Seafloor Transient CSEM Techniques

In order to determine an electromagnetic response of the earth at the seafloor, and thereby enable mapping of the sub–surface conductivity, a source of electromagnetic energy must be available and receivers must be deployed. The seafloor magnetotelluric method (MT) is the oldest and most established technique. It uses fluctuations in the *natural* ionospheric electric currents as the source of electromagnetic energy, and seafloor electric and/or magnetic field sensors as receivers. A typical MT response function $R(\omega)$ that can be extracted from the data consists of a horizontal component of the magnetic field divided by the orthogonal horizontal electric field component *e.g.* $R(\omega)=B_y(\omega)/E_x(\omega)$, measured as a function of frequency. If the conductivity of the earth $\sigma(z)$ is assumed to vary only with depth z, the response function $R(\omega)$ at a given frequency can be inverted to give a value for electrical conductivity that is averaged over a certain, frequency–dependent range of depths Δz (Parker 1970).

Seafloor MT measurements are, however, of limited use for determining the conductivity of oceanic crust, because of the following facts. On the deep seafloor, far from coastlines, the amplitudes of all frequency components of the natural electromagnetic field greater than about 10^{-2} Hz are severely attenuated, with respect to their values at the sea surface, due to the presence of the overlying, conducting ocean. Also, at very low frequencies $f \leq 10^{-4}$ Hz, electromagnetic fields induced in the oceans by internal waves, tides and currents contaminate the field of ionospheric origin. As useful indicators of the sub–surface conductivity structure, MT response functions are therefore band–limited to the two or three intermediate decades of frequency 10^{-2}–10^{-4} Hz (Constable 1990). These frequencies are such that electrical conductivity profiles constructed by direct inversion of seafloor MT data best resolve earth structure at depths of 50–200 kilometers, which is well into the upper mantle (Oldenburg 1981). But the targets of interest to the geophysicist or mineral explorationist are often located in the crust. To explore this regime using electromagnetic techniques, controlled sources activated on the seafloor are suitable since they generate the high frequency ($f \geq 10^{-2}$ Hz) signals that are removed from the natural spectrum by the overlying seawater.

CSEM systems consist of a transmitter, which may or may not be in direct contact with the earth, and remote receivers sensitive to one or more components of the transmitted electromagnetic fields **E** and **B**. On land, CSEM systems have for decades been used throughout the mining industry to locate and assess the extent of buried mineral deposits. However, a CSEM exploration system that is successful on land, where the overlying medium is the non–conducting air, may not necessarily be well–suited to investigate structure beneath the oceans. A good example of the

incompatibility between land–based and marine instrumentation is illustrated by the Slingram system, which consists of co–planar transmitter and receiver loops at fixed separation, and is commonly used for mineral exploration on land. On the seafloor, where the overlying medium is highly conductive seawater, the Slingram system is unlikely to produce data sensitive to the more resistive earth (Cheesman *et.al.* 1987), since it measures the vertical component of the magnetic field, a quantity which vanishes at the surface of a good conductor. The fact that only certain electromagnetic systems, when deployed on the seafloor, are sensitive to seafloor conductivity, plus the fact that equipment must be engineered to withstand high pressures and rough treatment on the sea bottom, clearly indicates that the design of a seafloor system must carefully take into account factors relating to the unique environment in which it is to be deployed.

Most electromagnetic measurements are made in the frequency domain, that is, the transmitter current $I(t)$ is *harmonic* in time, *i.e.* proportional to $\exp(i\omega t)$, and the measurements are expressed in terms of field amplitudes and phase shifts relative to a prescribed "primary" electromagnetic field (*e.g.* Grant and West 1965). Recently, however, it has been recognized that in some instances time domain measurements offer practical advantages over frequency domain measurements (Swift 1987), even though the total information contents of both sets of measurements are, in principle, identical. A single transient waveform is obtained with less effort than it takes to record the frequency responses for many different values of transmitted frequency ω, but the wide–band time domain measurement is more susceptible to noise, which can be filtered out of a frequency domain measurement (Swift 1987).

A simple *transient* CSEM system consists of a transmitter carrying a current $I(t)$ which is stepped on from zero to a steady value at time t=0 and a remote receiver which is sensitive to one or more components of the resultant fields $\mathbf{E}(t)$ and $\mathbf{B}(t)$. The shape of the response curve, *i.e.* the actual quantity that is measured by the receiver, is often indicative of the electrical conductivity along a path between the transmitter and the receiver. For example, Edwards and Chave (1986) have analyzed the theoretical response from a seafloor in–line electric dipole–dipole (ERER) configuration when it is deployed over a uniform earth. They noted that a peak in the ERER response $\partial_t E_x(t)$ due to diffusion of electromagnetic fields through the resistive crust occurs at relatively early times after step–on while a later peak in the response is due to diffusion through the much more conductive ocean. A typical transient CSEM response curve corresponding to a double half–space conductivity model is shown plotted as squares in Figure 1.1. The two characteristic peaks seen in the response curve are well separated in time and are diagnostic of the electrical conductivities of the earth and the sea, respectively. Cheesman *et.al.* (1987) discovered a similar result for a seafloor co–axial horizontal magnetic dipole–dipole (HRHR) configuration, and further commented that the response from an idealized Slingram system consisting of co–planar vertical magnetic dipoles (HZHZ) is insensitive to the least conducting of the half–spaces, which is almost always the seafloor. The conclusion drawn by these authors is that transient ERER and HRHR systems are well–suited to the determination of seafloor conductivity in the most common instance where the seafloor is less conductive than the seawater. Systems of these types have already been designed, built and tested at sea (Cheesman *et.al.* 1990, Everett *et.al.* 1989), and behave as predicted by the theory.

In heterogenous environments, transient CSEM data interpretation is made easier once the robustness of the first peak arrival time as an indicator of seafloor conductivity is recognized. The effect of a non–uniform seafloor electrical conductivity in the

vicinity of the transmitter on the first peak arrival time is of direct relevance to the interpretation of marine CSEM data collected in many places, *e.g.* near a mid–ocean ridge, a coast or even a crack in the seafloor. A theoretical analysis (Everett *et.al.* 1989) of the responses from a pair of simple heterogenous conductivity models serves to illustrate the point, which will be taken up again in much more detail in later chapters of this thesis. The presence of a shore line attenuates the CSEM response $\partial_t E_x(t)$ slightly but does not significantly alter either the crustal or direct seawater arrival times at the receiver, Figure 1.1. If there is a crack in the seafloor between the transmitter and receiver, the early signal arrival is delayed and its magnitude greatly attenuated by the presence of highly conductive seawater in the crack, Figure 1.2. The response curves of Figure 1 are calculated, and may be interpreted, using the theory and numerical methods developed in Chapters 3 and 4 of this thesis. The manner by which transient CSEM responses are altered in the presence of mid–ocean ridge structures such as the magma chamber and associated zones of hydrothermal circulation is the focus of Chapters 5 and 7 of this thesis, and is in fact the principal *raison d'etre* of the thesis.

1.3 Outline of the Thesis

The remainder of the thesis is organized as follows. In the next chapter, I will present a review of mid–ocean ridge geology and electrical conductivity. In Chapter 3, I will review some necessary electromagnetic theory, present solutions to simple electromagnetic boundary value problems of relevance to marine geophysics, and develop some diagnostics for determining the sub–surface electrical conductivity from these solutions. In Chapter 4, I will outline the development of a numerical method based on finite elements to solve 2–D transient electromagnetic boundary value problems. In Chapter 5, I employ the finite element method to solve ridge–related problems, in particular a feasibility study for doing transient CSEM experiments at an active seafloor spreading site is undertaken. In Chapter 6, I outline an extension of the numerical method to handle a finite source, which solves the so–called 2.5–D problem, and in Chapter 7 I will present results from a model study of the mid–ocean ridge to illustrate the utility of this more advanced code. Conclusions drawn from the work are presented in the final chapter.

References

Carmichael, R.S., 1989. The magnetic properties of minerals and rocks, in (ed. Carmichael, R.S.) *C.R.C. Practical Handbook of Physical Properties of Rocks and Minerals*, C.R.C. Press Inc., Boca Raton, FL.

Cheesman, S.J., R.N. Edwards and A.D. Chave, 1987. On the theory of sea–floor conductivity mapping using transient electromagnetic systems, *Geophysics*, **52**, 204–217.

Cheesman, S.J., R.N. Edwards and L.K. Law, 1990. A test of a short–baseline sea–floor transient electromagnetic system, *Geophys. J. Int.*, **103**, in press.

Constable, S.C., 1990. Marine electromagnetic induction studies, *Surv. Geophys.*, **11**, 303–327.

Edwards, R.N. and A.D. Chave, 1986. On the theory of a transient electric dipole–dipole method for mapping the conductivity of the sea floor, *Geophysics*, **51**, 984–987.

Everett, M.E., R.N. Edwards, S.J. Cheesman, H. Utada and I.J. Ferguson, 1989. Interpretation of seafloor electromganetic data in applied geophysics, in (ed. Miya, K.) *Applied electromagnetic in materials*, Pergamon Press, Oxford UK, 143–153.

Grant, F.S. and G.F. West, 1965. *Interpretation theory in applied geophysics*, McGraw–Hill Book Co., New York NY.

Hannington, M.D., G. Thompson, P.A. Rona and S.D. Scott, 1988. Gold and native copper in supergene sulfides from the Mid–Atlantic Ridge, *Nature*, **333**, 64–66.

Keller, G.V., 1987. Rock and mineral properties, in (ed. Nabighian, M.N.) *Electromagnetic Methods in Applied Geophysics*, Society of Exploration Geophysicists, Tulsa OK, 13–51.

Keller, G.V., 1989. Electrical properties, in (ed. Carmichael, R.S.) *C.R.C. Practical Handbook of Physical Properties of Rocks and Minerals*, C.R.C. Press Inc., Boca Raton, FL.

Oldenburg, D.W, 1981. Conductivity structure of oceanic upper mantle beneath the Pacific plate, *Geophys. J. R. Astr. Soc.*, **65**, 359–394.

Parker, R.L., 1970. The inverse problem of electrical conductivity in the mantle, *Geophys. J. R. Astr. Soc.*, **22**, 121–138.

Schmeling, H., 1986. Numerical models on the influence of partial melt on elastic, anelastic and electrical properties of rocks. Part II: electrical conductivity, *Phys. Earth Planet. Int.*, **43**, 123–136.

Swift, C.M. Jr., 1987. Fundamentals of the Electromagnetic Method, in (ed. Nabighian, M.N.) *Electromagnetic Methods in Applied Geophysics*, Society of Exploration Geophysicists, Tulsa, OK, 5–10.

Waff, H.S., 1974. Theoretical considerations of electrical conductivity in a partially molten mantle and its implications for geothermometry, *J. Geophys. Res*, **79**, 4003–4010.

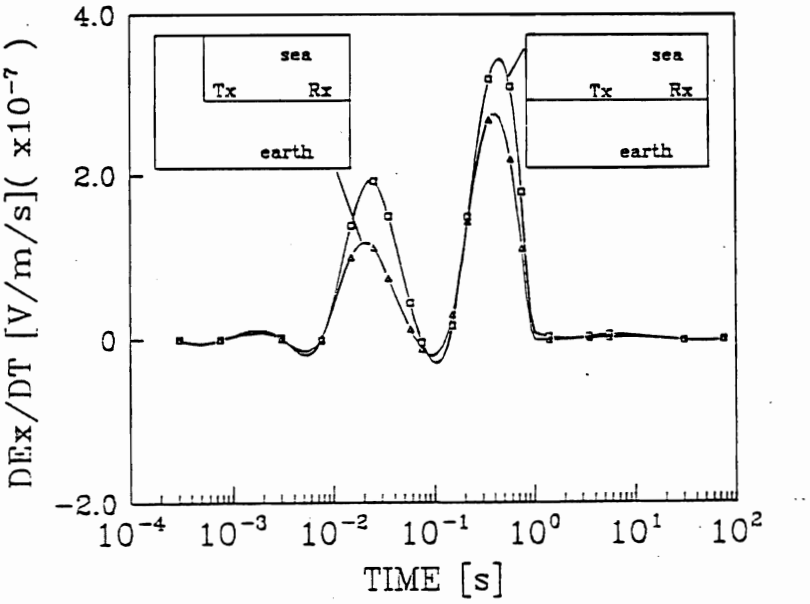

Fig.1.1 A typical transient CSEM response (squares), in this case the time derivative of a horizontal electric field component $\partial_t E_x(t)$, as it might be measured by a seafloor receiver. The first peak is due to electromagnetic energy diffusing from a line source Tx through the earth to a receiver Rx. The second peak is due to energy diffusing through seawater. The shape of the response is not altered greatly if the transmitter is deployed near a shoreline and the receiver is placed further off–shore (triangles).

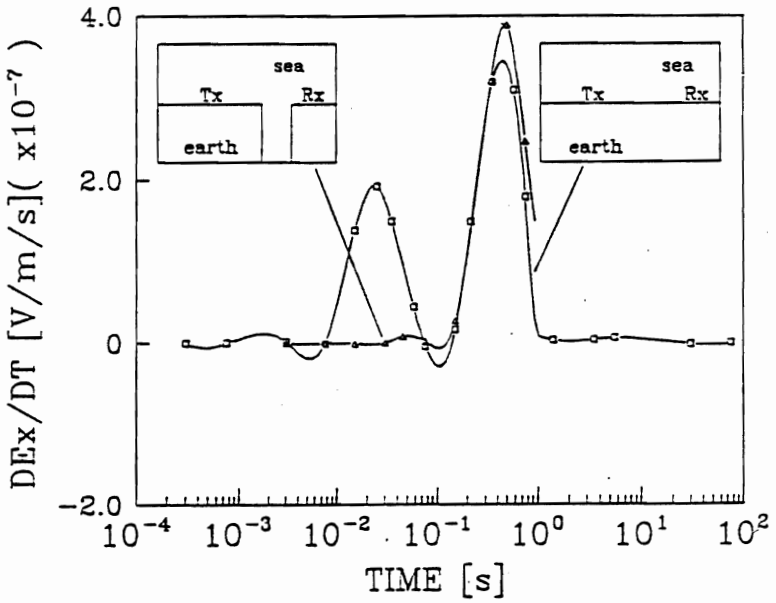

Fig.1.2 The presence of a crack in the seafloor between the transmitter and receiver attenuates the first peak in the response curve $\partial_t E_x(t)$.

Chapter 2

Mid–Ocean Ridge Geology and Electrical Conductivity

2.0 Introduction

New oceanic crust is being formed along active segments of the global mid–ocean ridge (MOR) system. The spreading rates are as high as 18 cm yr^{-1}. The presence of an axial magma chamber and associated zones of partial melt and hydrothermal activity located up to several kilometers beneath the seafloor at these locations is central to almost all recently proposed theories of crustal formation. Seismic images of the top few kilometers beneath the fast spreading East Pacific Rise (EPR) near 9–13°N have already been obtained. Multi–channel reflection profiles place strong constraints on the geometry of the axial magma chamber but refraction data provide only coarse estimates of the sub–surface temperature, distribution of partial melt and porosity, parameters required to distinguish between proposed petrological models of the ridge. Electrical conductivity is a strong indicator of all these critical parameters and therefore controlled–source electromagnetic (CSEM) methods are well–suited to improve the estimates and help characterize the ridge environment.

Before describing in later chapters results from numerical modeling to support this claim, in this chapter I wish to review mid–ocean ridge geology and the electrical conductivity of mid–ocean ridge structures, in part to motivate the study of active electromagnetics at the ridge and in part to provide a framework from which geo–electrical models of the ridge may be constructed. To preface the discussion, a schematic EPR cross–section based on the interpretation of the seismic reflection data

is shown in Figure 2.1*a*. A more recent interpretation which takes into account both the reflection and refraction data is shown in Figure 2.2.

2.1 A Rapid Overview of the Geology

Ocean crust formation along active ridge segments, an essential feature of plate tectonics, begins as ascending partial melt supplied from 30–60 km deep within the mantle enters a crustal reservoir, where it undergoes low–pressure chemical differentiation processes and mixes with resident, more evolved magmas (Langmuir, Klein and Plank 1991). After occupying this reservoir, the axial magma chamber, for a length of time which depends on the supply rate, some of the contents are extruded onto the seafloor within a very narrow 1–2 km wide neo–volcanic zone centered on the ridge axis. At the start of a volcanic cycle, eruptions are in the form of sheet flows but as material accumulates above the magma chamber, direct conduits to the seafloor become increasingly rare. Magmas subsequently extruded from the chamber are forced through networks of cracks and fissures in the growing volcanic edifice and those that reach the seafloor emerge as pillow lavas (MacDonald 1982). The result is a complex of sheeted dykes and overlying pillow lavas which comprises the top 1–2 km basaltic layer of very young oceanic crust; this layer is also referred to as seismic layer 2. Further down, the magma remaining inside the chamber begins to cool. The material in the coldest part of the chamber, usually close to the edges, crystallizes into gabbros. This leads to the formation beneath the upper basalts of a 4–6 km thick base layer of gabbros, seismic layer 3. The newly created layers of crust then migrate away from the ridge axis under the influence of tectonic forces.

Stress caused by the horizontal acceleration of the crust away from the ridge axis produces crustal fissuring aligned along–axis. At fast spreading ridge segments, fissures are typically 1–3 m wide and are most intense in 1–2 km wide bands at the edges of the neo–volcanic zone (MacDonald 1982). Since the fissures are observed on

the seafloor, a fact established during manned submersible observations, cold seawater is able to penetrate the crust. The seawater temperature rises with its depth of penetration due to the presence of the hot, underlying magma chamber. The magmatic heat source is of sufficient size and temperature to drive a vigorous circulation of seawater and dissolved minerals throughout the upper basalts. To complete the circulation, hot hydrothermal fluids are discharged within several hundred meters of the ridge axis through vents. MOR hydrothermal activity transfers heat from the magmatic intrusion across the seafloor into the oceans (Lister 1980).

The global mid–ocean ridge involves complex interactions among a number of processes occurring over wide ranges of depths and spatial scales, including melting of the earth's mantle, delivery of the molten rock to the crustal magma chamber, cooling of the magma intrusion by hydrothermal circulation and volcanic eruption, chemical exchange between the hot rock surrounding the magma chamber and the overlying seawater, and even the establishment of exotic biological communities near the vents (Munk *et.al.* 1988). However, amongst these, the features of the mid–ocean ridge that are readily accessible to transient CSEM exploration, as it is discussed in this thesis, are located at crustal levels and include the axial magma chamber and associated zones of partial melt and hydrothermal activity. After a brief discussion on the deep structure of the ridge, which shapes the geo–dynamics at all other levels, I will examine some of the geophysical evidence that has led to our current understanding of the major crustal features. This is done in order to characterize the ridge in three dimensions on the appropriate 1–10 kilometer length scale.

2.2 Mid–Ocean Ridge Geophysics

How melt gets from its mantle source region into the crustal reservoir, and the time it takes to do so, are open questions and a focus of ongoing research into the fundamental nature of the deep structure of the ridge by marine geologists and geo-

physicists worldwide (Phipps Morgan and Delaney 1991). Obtaining answers is made the more difficult by the fact that the geometry and melt fraction of the mantle melting region beneath the ridge, or indeed beneath any other tectonically active zone, is not well constrained by the sparse seismic and magnetotelluric data available (Shankland *et.al.* 1981). Possible mechanisms by which melt segregates from and rises through a residual mantle matrix to eventually concentrate into the narrow (2–6 km wide) crustal accretion zone at the base of the lithosphere have been explored through the use of numerical models of two–phase porous flow in a deformable matrix (Scott and Stevenson 1989, Buck and Su 1989, Spiegelman and MacKenzie 1987, Phipps Morgan 1987), geo–chemical analyses of dredged mid–ocean ridge basalt (MORB) samples (Langmuir *et.al.* 1991), studies of mantle flow patterns fossilized in the Samail ophiolite of Oman, a volcanic outcrop believed to be the remnant of an ancient oceanic spreading center (Rabinowicz *et.al.* 1987), and laboratory experiments on two–phase silicate liquid/olivine mixtures (Riley *et.al.* 1991). Debates concerning the deep structure will almost certainly not be settled without the input of additional seismic and MT data.

For many years, the existence of a mid–crustal magma chamber beneath fast spreading ridges has been inferred from the study of ophiolite analogues and MORB geo–chemical systematics. More recently, geophysical evidence for a magma chamber has come from seismic studies. Multi–channel seismic reflection profiles from between 8°50′N—13°30′N across and along the EPR axis have revealed in many places, most notably at 9°30′N, the presence of a strong reflector 4–6 km wide at depths of 1.2–2.4 km beneath the seafloor. The reflector has been interpreted as the top of a crustal magma chamber (Detrick *et.al.* 1987). The width of the reflector may however be as little as 0.8–1.2 km wide, according to forward ray–tracing models of the diffraction hyperbolae that appear around the reflector's edges in the common–mid–point stacked sections (Kent *et.al.* 1990). The floor of the chamber could not be imaged by the reflection data but the top could be traced in along–axis profiles as a continuous

reflector for tens of kilometers between ridge axis discontinuities. When added to the reflection data just described, expanding spread profiles (ESPs) from 13°N (Harding *et.al.* 1989) are consisent with a small, transient axial magma lens of high melt fraction ponding atop a much larger permanent region of hot rock containing only isolated pockets of melt. This latter region, centered on the axis, might extend to 20 km wide at the base of the crust.

The along–strike variability of the magma chamber can not be neglected in an accurate view of the mid–ocean ridge at the 1–10 kilometer length scale. A recent seismic tomography experiment (Toomey *et.al.* 1990) centered on the EPR at latitude 9°30′N has produced data indicating that the 3–D seismic velocity structure of the crust shows along–axis heterogeneity over distances of a few kilometers. The inferred structure is consistent with injection of mantle–derived melt midway along the linear segment of the ridge between the Clipperton Fracture Zone and the 9°03′N overlapping spreading center. The viewpoint emerging from the EPR tomographic results, which provide the first 3–D seismic images of the crust beneath the ridge but are limited to 1 km resolution, is that ridge *segments* define discrete magmatic units. The same conclusion may also be inferred from gravity data collected over the Mid–Atlantic Ridge (MAR). On this slow spreading ridge, mantle Bouguer anomalies show gravity lows centered on all six of the segments surveyed by Lin *et.al.* (1990). On the basis of high resolution bathymetric data from the EPR, MacDonald *et.al.* (1988) have also proposed that ridge segmentation is defined by sources of partial melt: segments with an axial magma chamber, broad cross–section and a summit graben are shallow and swollen with magma; those without a magma chamber or graben and possessing a narrow cross–section are deeper and starved of magma.

Mid–ocean ridge axial topography is strongly influenced by spreading rate (Phipps Morgan *et.al.* 1987). Extensional stresses caused by the horizontal acceleration of the strong, brittle lithosphere that thickens with distance from the ridge axis can generate both the kilometer–scale relief observed on slow (5–25 mm/yr) spreading ridges and

the lack of appreciable relief that is observed on fast (>45 mm/yr) spreading ridges. Relief at ridge hot spots (*e.g* the Reykjanes Ridge) and at ridge discontinuities is probably more dependent on the distribution of partial melt beneath the ridge than on spreading rate. The width of the axial valley, 30 km wide at slow spreading ridges and zero at fast spreading ridges, is controlled by plate thickness (Phipps Morgan *et.al.* 1987). Surveys of the EPR near 12°50′N by a submersible (Choukroune *et.al.* 1984) and near 3°25′S by a deeply–towed instrument package (Lonsdale 1977), and others, have identified an active tectonic zone comprising the central volcano and extending up to about 2 km from either side of the ridge axis. Beyond this is a tectonically inactive horst and graben zone that is formed by tensional faulting and evolves by progressive shearing on inclined fault planes. Pelagic sedimentation, which occurs on the 3°25′S site at a maximum rate of 22 m/10^6 yr (Lonsdale 1977), gradually infills open fissures and smooths the roughness of the fault blocks.

Hydrothermal circulation in the ocean crust can be divided into two zones: active circulation is restricted to the spreading axis and passive circulation occurs off–axis. In the active zone, convecting seawater penetrates the crust and cools the crystallizing magma chamber. In the passive zone, heat is transferred to the seawater principally by conduction from below and the circulation is less vigorous. Alt *et.al.* (1986) have reconstructed in detail the mineralogy and chemistry of the hydrothermally altered basalts as a function of distance from the spreading axis based on analyses of samples from the upper 1 km section of oceanic crust at the Deep Sea Drilling Project (DSDP) Hole 504B site, and have verified the above classification scheme. A general feature associated with hydrothermal circulation is that the seawater temperature rises with the depth of penetration (Bowers and Taylor 1985) due to the presence of the underlying magma chamber. Hot ($\approx$ 350°C) hydrothermal fluids may be discharged within several hundred meters of the ridge axis through vent fissures (Ballard *et.al.* 1984). At these high–temperature vent openings, the dissoved minerals come into contact with cold seawater and some of them precipitate out of the hydrothermal

solution, forming polymetallic sulfide deposits on the seafloor.

Although little is known about the spatial distribution of the sub–seafloor portions of ridge hydrothermal systems, ESP data from the East Pacific Rise between 9–10°N suggest that the maximum penetration depth of the active, axial hydrothermal circulation occurs probably a few hundred meters above the dike–gabbro (seismic layer 2–layer 3) transition (Vera *et.al.* 1990). Two–dimensional numerical models of the fluid flow in MOR hydrothermal systems have examined the influence of magma chamber geometry on the spatial extent and vigour of hydrothermal circulation (Brikowski and Norton 1989). If the geometry of the magma chamber is like that inferred from the seismic multi–channel reflection data (Detrick *et.al.* 1987), the numerical results suggest that active hydrothermal upflow and hot springs are concentrated within 1.5 km of the ridge axis. Based on $\delta^{18}O$ isotopic analyses of samples from the Samail ophiolite, off–axis, passive hydrothermal circulation may penetrate to the base of the crust (Gregory and Taylor 1981). However, marine geologists treat this observation with caution since structure inferred from ophiolitic crustal sections may not necessarily correspond to structure found in present–day oceanic crust. The Samail ophiolite, located in Oman, is believed to be a fossilized, outcropping fragment of an ancient seafloor spreading center that has been thrust to the earth's surface.

2.3 Electrical Conductivity

In any setting, the formulation of an electrical model of the earth requires a synthesis of the geological information and the results of conductivity measurements made either in the laboratory or *in situ* on the prevalent rock types. In this section of the thesis, I will examine some of the published electrical conductivity data that in §2.4 will be applied towards the development of an electrical model of the ridge.

Many factors that control the electrical conductivity of the materials in active MOR environments have been identified. The electrical conductivity of seawater de-

pends on temperature, pressure and salinity. Although there is a slight increase near the seafloor due to pressure, the electrical conductivity at 42.5°N in the Pacific Ocean is approximately constant and equal to 3.2 S/m below the main thermocline (Chave and Luther 1990). In the uppermost few hundred meters of the crust, the amount of fracturing, the presence of seawater in these fractures and the size and connectedness of the fluid passages determines the electrical conductivity. From a large–scale resistivity experiment at the DSDP Hole 504B site, the *in situ* electrical conductivity of the pillow lavas is about 0.1 S/m (Becker *et.al.* 1989). The conductivity at this site falls off by a factor of 100 in the sheeted dikes near the base of seismic layer 2. The decrease in conductivity with depth is expected since fractures do not form or close under increasing pressure. Since Hole 504B was drilled into 5.9 Ma crust and hence may have experienced crack sealing by precipitates from a cooling hydrothermal system, the electrical conductivity of younger and hotter basalts closer to a spreading axis may exhibit a much less dramatic decrease in electrical conductivity at the base of layer 2. In regions where hydrothermal circulation is most pronounced, the electrical conductivity will be enhanced with respect to that of drier, less fractured basalt, although by how much will depend on the water/rock ratios. Based on seafloor electrical measurements made from the submersible *Cyana* on a seamount close to the EPR axis (Francis 1985), the electrical conductivity of sulphide deposits has been found to be generally one to two orders of magnitude greater than that of the surrounding pillow basalts and at one site it even exceeded the electrical conductivity of the overlying seawater.

The electrical conductivity of dry gabbros ranges from 10^{-5} S/m at 500°C to nearly 0.01 S/m at 1000°C (Kariya and Shankland 1983). The electrical conductivity of magmatic liquids is 3–4 orders of magnitude greater than their refractory residues (Waff and Weill 1975), and a relatively small amount of partial melt can dominate the bulk conductivity. The effect on the melt conductivity due to changes in the oxygen fugacity f_{O2} can be neglected. As oxygen fugacity increases, the oxidation state of Fe

changes from predominantly Fe^{2+} to Fe^{3+}. The electrical conductivity of magmatic melt ranges from about 2.5–6.0 S/m as temperature increases from 1200°C to 1500°C (Waff and Weill 1975), with compositional variations of the melt accounting for much less than an order of magnitude variation in the electrical conductivity.

Large conductivity anomalies from magnetotelluric measurements in tectonically active areas (*e.g.* the mid–ocean ridge) cannot be explained by the laboratory electrical conductivity data on solid crystalline olivine (Shankland and Waff 1977), therefore the need to invoke the presence of partial melting in the upper mantle is strong. Laboratory measurements of the electrical conductivity of molten basalts at mantle pressures of 25 kbar and temperatures 1200°C$\leq$T$\leq$1400°C seem to require partial melting of the order $\phi \geq 5$–10% in order to explain the MT conductivity anomalies in terms of the partial melt hypothesis (Tyburczy and Waff 1983). However, a given field measurement of conductivity σ in a tectonic zone may be due to either rock at high temperature T and small melt fraction ϕ or at low T large ϕ. The electrical conductivity of a dunite, a rock composed primarily of the. mineral olivine, under controlled oxygen fugacity is 10^{-6} S/m at 800°C and 10^{-3} S/m at 1400°C (Constable and Duba 1990). An upper mantle conductivity of 10^{-5} S/m has been inferred (Cox *et.al.* 1986) based on controlled-source electromagnetic data. This value, inferred from data collected over 25 Ma tectonically inactive oceanic lithosphere, might increase closer to the ridge.

According to the above information, there probably exist large contrasts in electrical conductivity beneath an active ridge segment. This gives rise to expectations that electromagnetic methods, which exploit such contrasts, can provide an electrical image of the sub–surface.

2.4 Ridge Geo–Electrical Models

Major structures found beneath a fast spreading center, as inferred from geophysical

and geological information, are illustrated in Figures 2.1*a* and 2.2. Simplified 2–D electrical conductivity models based on mid–ocean ridge geology are shown in Figures 2.1*b* and 2.3*a–d*. The electrical models consist of polygonal representations of the geological structures, with the electrical conductivity σ of each polygon assumed to be uniform and its value selected on the basis of the available data, which is summarized in §2.3. Although the models are only approximate representations of the true electrical conductivity structure beneath a fast spreading mid–ocean ridge, they are useful as preliminary models by which to attack forward modeling problems. As electromagnetic and other geophysical data becomes available from sea–going experiments, the models without doubt will stand in need of refinement.

Figure 2.1*a*, in particular, shows a simplified geo–electric cross–section of the East Pacific Rise near 9°N. This latitude corresponds to a site of recent multi–channel seismic reflection surveys and is the location where the axial magma chamber is seismically best resolved. The geometry shown is adapted from Figure 6 of Detrick *et.al.* (1987). Figure 2.1*b* shows a conductivity model based on the geologic cross–section. If a controlled–source experiment were to be done at this location, electromagnetic signals could, for example, be generated at some source location (Tx) and the associated electric and/or magnetic field recorded at various seafloor locations (A–D) across the ridge. The magma chamber depicted in Figure 2.1*b* has an electrical conductivity of σ=1.0 S/m and represents a region of about 60% basaltic melt at 1200°C (Shankland and Waff 1977).

In Figure 2.2, the geometry from 9°N has been modified to take into account new seismic data from expanding spread profiles (ESPs) (Harding *et.al.* 1989). The region of high melt fraction is restricted to a thin lens at the top of a much larger, broader region of hot rock containing only isolated pockets of melt. Figure 2.3*a* shows a quasi–layered oceanic crust, the region of hot rock is added as a broad zone of conductivity σ=0.05 S/m in Figure 2.3*b*. This conductivity value represents 1–2% partial melt at 1200°C. The thin lens of completely molten material, assigned σ=4.0

S/m, is represented in Figure 2.3*c*. In Figure 2.3*d* three bands of conductivity σ=0.3 S/m are added to account for axial hydrothermal circulation throughout the upper basaltic sequence, reflecting the fact that the conductivity in the hydrothermal regime will be enhanced with respect to that of dry layer 2 basalts. The bands may not reflect any true structure beneath the ridge, but are simply representative of regions where the spatially averaged electrical conductivity is larger than surrounding regions due to an increased fluid/rock ratio.

In Chapter 5, I will find transient electromagnetic responses of the mid–ocean ridge geo–electric models shown here. The responses are calculated using a finite element numerical procedure, described in the next two chapters of this thesis, which solves the governing electromagnetic diffusion equations.

References

Alt, J.C., J. Honnorez, C. Laverne and R. Emmermann, 1986. Hydrothermal alteration of a 1 km section through the upper oceanic crust, Deep Sea Drilling Project Hole 504B: mineralogy, chemistry, and evolution of seawater–basalt interactions, *J. Geophys. Res.*, **91**, 10 309–10 335.

Ballard, R.D., R. Hekinian and J. Francheteau, 1984. Geological setting of hydrothermal activity at 12°50′N on the East Pacific Rise: a submersible study, Earth Planet. Sci. Lett., **69**, 176–186.

Becker, K., H. Sakai, A.C. Adamson, J. Alexandrovich, J.C. Alt, R.N. Anderson, D. Bideau, R. Gable, P.M. Herzig, S. Houghton, H. Ishizuka, H. Kawahata, H. Kinoshita, M.G. Langseth, M.A. Lovell, J. Malpas, H. Masuda, R.B. Merrill, R.H. Morin, M.J. Mottl, J.E. Pariso, P. Pezard, J. Phillips, J. Sparks and S. Uhlig, 1989. Drilling deep into young oceanic crust, hole 504B, Costa Rica Rift, *Rev. Geophys.*, **27**, 79–102.

Bowers, T.S. and H.P. Taylor, Jr., 1985. An integrated chemical and stable–isotope model of the origin of midocean ridge hot spring systems, *J. Geophys. Res.*, **90**, 12 583–12 606.

Brikowski, T. and D. Norton, 1989. Influence of magma chamber geometry on hydrothermal activity at mid–ocean ridges, *Earth Planet. Sci. Lett.*, **93**, 241–255.

Buck, W.R. and W. Su, 1989. Focused mantle upwelling below mid–ocean ridges due to feedback between viscosity and melting, *Geophy. Res. Lett.*, **16**, 641–644.

Chave, A.D. and D.S. Luther, 1990. Low–frequency, motionally induced electromagentic fields in the ocean 1. Theory, *J. Geophys. Res.*, **95**, 7185–7200.

Choukroune, P., J. Francheteau and R. Hekinian, 1984. Tectonics of the East Pacific Rise near 12°50′N: a submersible study, *Earth Planet. Sci. Lett.*, **68**, 115–127.

Constable, S.C. and A. Duba, 1990. Electrical conductivity of olivine, a dunite, and the mantle, *J. Geophys. Res.*, **95**, 6967–6978.

Cox, C.S., S.C. Constable, A.D. Chave and S.C. Webb, 1986. Controlled–source electromagnetic sounding of the oceanic lithosphere, *Nature*, **320**, 52–54.

Detrick, R.S., P. Buhl, E. Vera, J. Mutter, J. Orcutt, J. Madsen and T. Brocher, 1987. Multi–channel seismic imaging of a crustal magma chamber along the East Pacific Rise, *Nature*, **326**, 35–41.

Francis, T.J.G., 1985. Resistivity measurements of an ocean floor sulphide mineral deposit from the submersible *Cyana*, *Mar. Geophys. Res.*, **7**, 419–438.

Gregory, R.T. and H.P Taylor, Jr., 1981. An oxygen isotope profile in a section of Cretaceous oceanic crust, Samail ophiolite, Oman: evidence for $\delta^{18}O$ buffering of the oceans by deep (>5 km) seawater–hydrothermal circulation at mid–ocean ridges, *J. Geophys. Res.*, **86**, 2737–2755.

Harding, A.J., J.A. Orcutt, M.E. Kappus, E.E. Vera, J.C. Mutter, P. Buhl, R.S. Detrick and T.M. Brocher, 1989. Structure of young oceanic crust at 13°N on the East Pacific Rise from expanding spread profiles, *J. Geophys. Res.*, **94**, 12 163–12 196.

Kariya, K.A. and T.J. Shankland, 1983. Electrical conductivity of dry lower crustal rocks, *Geophysics*, **48**, 52-61.

Kent, G.M., A.J. Harding and J.A. Orcutt, 1990. Evidence for a smaller magma chamber beneath the East Pacific Rise at 9°30′N, *Nature*, **344**, 650–653.

Langmuir, C.H., 1989. Geochemical consequences of *in situ* crystallization, *Nature*, **340**, 199–205.

Langmuir, C.H., E.M. Klein and T. Plank, 1991. Geochemical constraints on melt formation and segregation, in J.P. Morgan and J.R. Delaney (eds), Proceedings of the First Annual RIDGE Summer Institute, July 25–August 12, 1990, Boulder CO, in press.

Lin, J., G.M. Purdy, H. Schouten, J.–C. Sempere and C. Zervas, 1990. Evidence from gravity data for focused magmatic accretion along the Mid–Atlantic Ridge, *Nature*, **344**, 627–632.

Lister, C.R.B., 1980. Heat flow and hydrothermal circulation, *Ann. Rev. Earth Planet. Sci.*, **8**, 95–117.

Lonsdale, P., 1977. Structural geomorphology of a fast–spreading rise crest: the East Pacific Rise near 3°25′S, Mar. Geophys. Res., **3**, 251–293.

MacDonald, K.C., P.J. Fox, L.J. Perram, M.F. Eisen, R.M. Haymon, S.P. Miller, S.M.

Carbotte, M.–H. Cormier and A.N. Shor, 1988. A new view of the mid–ocean ridge from the behaviour of ridge–axis discontinuities, *Nature*, **335**, 217–225.

MacDonald, K.C., 1982. Mid–ocean ridges: fine scale tectonic, volcanic and hydrothermal processes within the plate boundary zone, *Ann. Rev. Earth Planet. Sci.*, **10**, 155–190.

Munk, W.H. (Chairman) and the Ocean Studies Board, Commission on Physical Sciences, Mathematics and Resources, National Research Council, 1988. *The mid–ocean ridge — a dynamic global system*, National Academy Press, Washington DC, 352pp.

Phipps Morgan, J., and J.R. Delaney, 1991. Mantle flow, melt generation and lithospheric deformation at mid–ocean ridges, *Proceedings of the RIDGE Summer Institute*, July 25–August 12, 1990, Boulder CO, in press.

Phipps Morgan, J., 1987. Melt migration beneath mid–ocean ridges centers, *Geophys. Res. Lett.*, **14**, 1238–1241.

Phipps Morgan, J., E.M. Parmentier and J. Lin, 1987. Mechanisms for the origin of mid–ocean ridge axial topography: implications for the thermal and mechanical structure of accreting plate boundaries, *J. Geophys. Res.*, **92**, 12 823–12 836.

Rabinowicz, M., G. Ceuleneer and A. Nicolas, 1987. Melt segregation and flow in mantle diapirs below spreading centers: evidence from the Oman ophiolite, *J. Geophys. Res.*, **92**, 3475–3486.

Riley, G.N. Jr., D.L. Kohlstedt and F.M. Richter, 1991. Melt migration in a silicate liquid–olivine system: an experimental test of compaction theory, in J.P. Morgan and J.R. Delaney (eds), *Proceedings of the RIDGE Summer Institute*, July 25–August 12, 1990, Boulder CO, in press.

Scott, D.R. and D.J. Stevenson, 1989. A self–consistent model of melting, magma migration and buoyancy–driven circulation beneath mid–ocean ridges, *J. Geophys. Res*, **94**, 2973–2988.

Shankland, T.J., R.J. O'Connell, H.S. Waff, 1981. Geopysical constraints on partial melt in the upper mantle, *Rev. Geophys. Space Phys.*, **19**, 394–406.

Shankland, T.J. and H.S. Waff, 1977. Partial melting and electrical conductivity anomalies in the upper mantle, *J. Geophys. Res.*, **82**, 5409–5417.

Spiegelman, M. and D. MacKenzie, 1987. Simple 2–d models for melt extraction at mid–ocean ridges and island arcs, *Earth Planet. Sci. Lett.*, **83**, 137–152.

Toomey, D.R., G.M. Purdy, S.C. Solomon and W.S.D. Wilcock, 1990. The three–dimensional seismic velocity structure of the East Pacific Rise near latitude 9°30′N, *Nature*, **347**, 639–645.

Tyburczy, J.A. and H.S. Waff, 1983. Electrical conductivity of molten basalt and andesite to 25 kilobars pressure: geophysical significance and implications for charge transport and melt structure, *J. Geophys. Res.*, **88**, 2413–2430.

Vera, E.E., J.C. Mutter, P. Buhl, J.A. Orcutt, A.J. Harding, M.E. Kappus, R.S. Detrick and T.M. Brocher, 1990. The structure of 0– to 0.2–m.y.–old oceanic crust at 9°N on the East Pacific Rise from expanding spread profiles, *J. Geophys. Res.*, in press.

Waff, H.S. and D.F. Weill, 1975. Electrical conductivity of magmatic liquids: effects of temperature, oxygen fugacity and composition, *Earth Planet. Sci. Lett.*, **28**, 254–260.

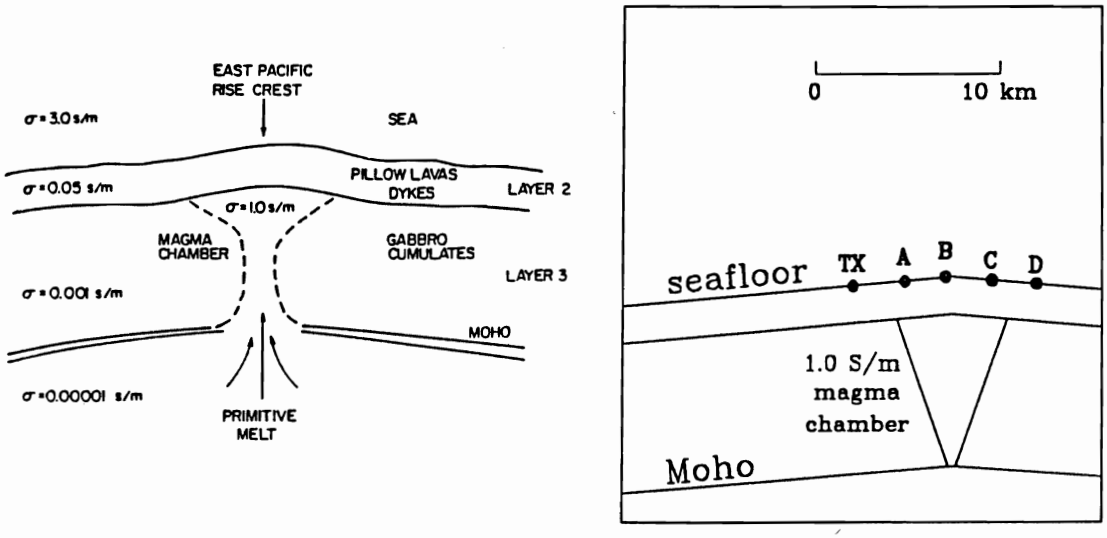

Fig.2.1 (a) A schematic cross–section showing the major geological structures found in the top several kilometers beneath the East Pacific Rise near 9°N (left). The section is based on the interpretation of seismic reflection data from Detrick *et.al.* (1987). The length scale is the same in both plots. There is no vertical exaggeration. (b) A simplified 2–D electrical conductivity model based on the geological section (right). If a transient CSEM experiment were to be done at the East Pacific Rise, a transmitter Tx might be placed a few kilometers off–axis, as shown, and electromagnetic fields recorded at receivers A–D located across the axis of the ridge.

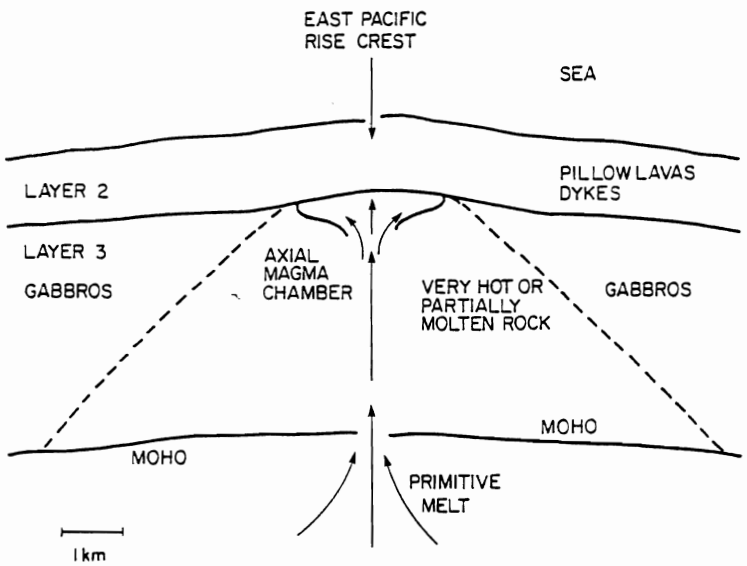

Fig.2.2 Geological cross–section showing the major features found beneath the East Pacific Rise near 9°N, based on the interpretation of seismic reflection (Detrick *et.al.* 1987) and refraction (Harding *et.al.* 1989) data sets. The region of pure melt is a thin lens at the top of a much larger, broad region of very hot or partially molten rock.

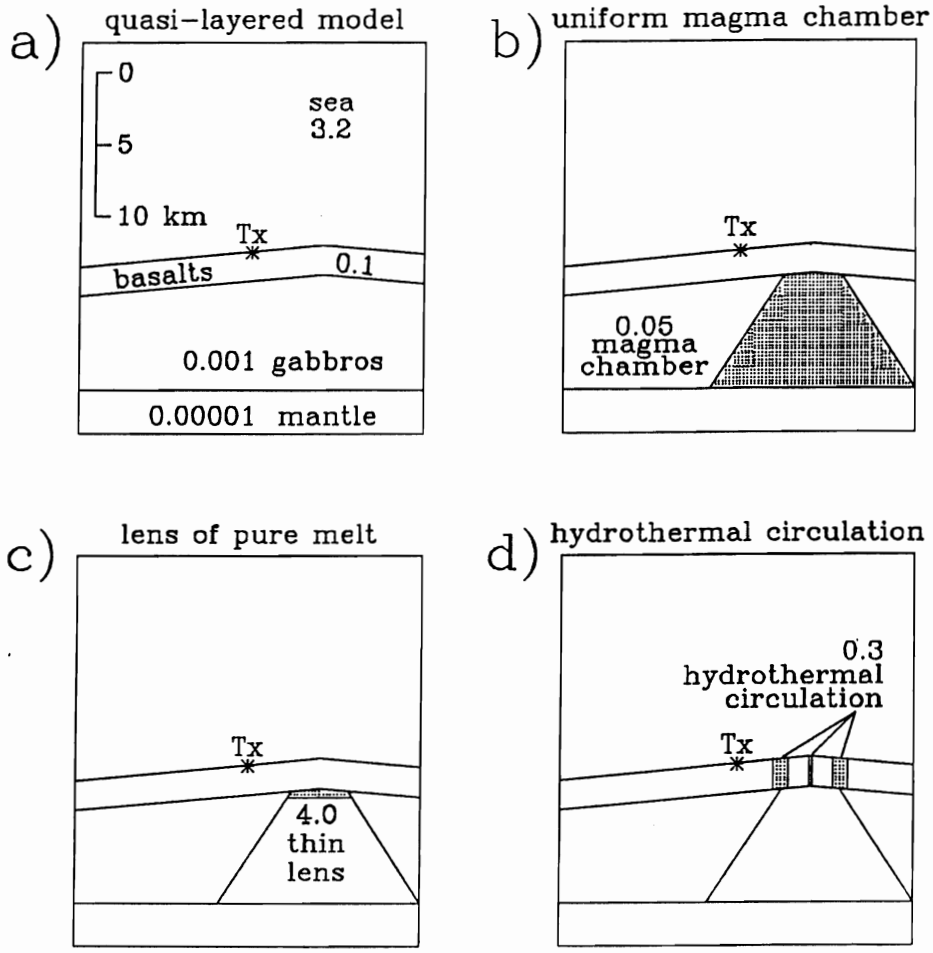

Fig.2.3 Two dimensional electrical models of an active mid–ocean ridge segment, depicting various proposed models of the geology. Layered, "normal" oceanic crust without a magma chamber present (a). A broad region of very hot rock centered on the ridge axis (b). A thin melt lens ponding atop the hot rock (c). Hydrothermal circulation of fluids in the upper, fractured layer of basalts directly above the hot rock (d). Numbers refer to the electrical conductivity in [S/m] of the various geological units. A suitable location for placement of a CSEM transmitter (Tx) is also shown.

Chapter 3

2D Analytical Modeling

3.0 Electromagnetic Source Equations

In the presence of matter or *in vacuo*, the laws of macroscopic electromagnetism are quite often and conveniently expressed in terms of the divergence and curl of the electric field $\mathbf{E}$ [V·m^{-1}] and the magnetic induction $\mathbf{B}$ [T] vectors. According to the Helmholtz theorem of vector calculus, knowledge of the divergence and curl of these vectors gives a complete description of the electromagnetic field throughout space. The theorem provides that if $\nabla\cdot\mathbf{F}$ and $\nabla\times\mathbf{F}$ are known throughout a finite region and vanish elsewhere they suffice to uniquely determine an arbitrary vector field $\mathbf{F}$. For this reason, $\nabla\cdot\mathbf{F}$ and $\nabla\times\mathbf{F}$ are called the *sources* of $\mathbf{F}$. Maxwell's equations, which have been abstracted from the results of fundamental experiments including those performed by Ampère during the period 1821–25 and Faraday in about 1831, are expressions for the sources of the electromagnetic fields $(\mathbf{E}, \mathbf{B})$:

$$\nabla \cdot \mathbf{E} = \frac{\rho_{\mathrm{ch}}}{\epsilon} \tag{3.1}$$

$$\nabla \cdot \mathbf{B} = 0 \tag{3.2}$$

$$\nabla \times \mathbf{E} = -\frac{\partial \mathbf{B}}{\partial t} \tag{3.3}$$

$$\nabla \times \mathbf{B} = \mu\sigma(\mathbf{r})\mathbf{E} + \mu\mathbf{J}_{\mathrm{S}} + \mu\epsilon\frac{\partial \mathbf{E}}{\partial t} \tag{3.4}$$

where ρ_{ch} [C·m^{-3}] is the volume electric charge density and $\mathbf{J}_{\mathrm{S}}$ [A·m^{-2}] is the applied current density, which is that arising from the flow of charges other than by conduction. Often, the experimenter has direct control of the applied current density, *i.e.*

by sending currents through wires with the use of batteries (Wangsness 1979). The above equations are valid *only* in media which are linear, isotropic and homogenous (l.i.h.) with respect to electric permittivity ϵ [F·m^{-1}] and magnetic permeability μ [H·m^{-1}] and linear and isotropic with respect to electrical conductivity $\sigma(\mathbf{r})$ [S·m^{-1}]. That is, the quantities ϵ and μ are scalar constants, characteristic of the material, while the quantity $\sigma(\mathbf{r})$ may vary with position. Hereafter, I will restrict attention to media which have the above properties plus $\sigma(\mathbf{r})\neq 0$ everywhere, at the cost that I will be unable to model electromagnetic fields as they might occur within air or many classes of important and common earth materials, *e.g.* anisotropic conductors such as graphite or non–linear magnetic materials such as iron.

3.1 Controlled–Sources in the Presence of Earth Conductors

Recall that I have restricted discussion to media whose electrical conductivity is everywhere non–vanishing. One consequence of this restriction is that, in the absence of applied currents, $\rho_{\text{ch}}(\mathbf{r},t)=0$ for $t\gg\tau_r$, where $\tau_r=\epsilon/\sigma$ is the *relaxation time*. Since the volume charge density ρ_{ch} decreases with time as $\rho_{\text{ch}}=\rho^0_{\text{ch}}e^{-t/\tau_r}$ following emplacement of free charge on or within a conductor (*e.g.* Wangsness 1979), the relaxation time gives an estimate of the length of time required for the attainment of static equilibrium due to the dissipation of free charge. The relaxation time is but one time scale, a *diffusion time* proportional to $\mu\sigma x^2$ where x is a penetration depth into a conductor will be encountered in §3.6. The diffusion time provides an estimate of the time scale required for current flow in a conductive medium to reach steady state.

Immediately following a variation in source current, localized, induced conduction currents are produced near the source such that the electromagnetic fields *everywhere* within the conductive medium are maintained at the values which existed immediately before the source current change. This statement is in accordance with Lenz' Law, which is an example of Le Chatelier's principle.

I also assume that the electric permittivity and magnetic permeability are every-

where constant and equal to their free space values:

$$\epsilon = \epsilon_0 = 8.85 \times 10^{-12} \text{ F/m}$$
$$\mu = \mu_0 = 4\pi \times 10^{-7} \text{ H/m}$$

so that the electrical conductivity $\sigma(\mathbf{r})$ is the only electrical property that can vary from one conductor to another.

In addition, I assume that there are no applied currents either outside the solution domain Ω or on its bounding surface $\partial\Omega$, *i.e.*:

$$\mathbf{J}_S(\mathbf{r}, t) = 0 \qquad \mathbf{r} \notin \Omega, \ \mathbf{r} = \mathbf{r}_0 \in \partial\Omega \tag{3.5}$$

and that $\partial\Omega$ is sufficiently far from applied currents so that to a specified degree of precision the following holds:

$$\mathbf{E}(\mathbf{r}_0, t) = \mathbf{B}(\mathbf{r}_0, t) = 0 \qquad \mathbf{r}_0 \in \partial\Omega, \ t \gg \tau_r. \tag{3.6}$$

I define a *controlled–source* as a conductor carrying an applied current whose density is a precisely known function of position and time. In addition, a controlled–source must possess a physical analog, *i.e.* a practical device with an equivalent current density can be constructed.

The final assumption that I make is that of the quasi–static approximation. Everywhere within a conductor the following inequality is assumed to be true:

$$\sigma(\mathbf{r})\mathbf{E} \gg \epsilon_0 \frac{\partial \mathbf{E}}{\partial t}. \tag{3.7}$$

The above relationship, which can be conveniently recast as

$$\frac{\partial \mathbf{E}}{\partial t} \ll \frac{\mathbf{E}}{\tau_r} \tag{3.8}$$

implies that the electric field inside a conductor is slowly time–varying, such that it appears to be constant at the time scale defined by the relaxation time τ_r. The inequality (3.8) is valid for most earth conductors (Oristaglio and Hohmann 1984). The

quantity $\mathbf{J}_D = \epsilon \partial \mathbf{E}/\partial t$, appearing in equation (3.4), is often called the displacement current density. When it is set to zero, the quasi–static approximation is said to have been made.

3.2 Electromagnetic Diffusion

After incorporation of the assumptions of §3.1, the two Maxwell's equations that change are, respectively:

$$\nabla \cdot \mathbf{E} = \frac{\rho_{ch}}{\epsilon_0} \tag{3.9}$$

$$\nabla \times \mathbf{B} = \mu_0 \sigma(\mathbf{r}) \mathbf{E} + \mu_0 \mathbf{J}_S. \tag{3.10}$$

From equations (3.9) and (3.3) it is evident that the sources of $\mathbf{E}$ are the volume charge density and time variations of the magnetic induction. From equations (3.10) and (3.2), the sources of the induction $\mathbf{B}$ include applied currents and conduction currents, the latter depending on the electric field. Since $\mathbf{E}$ and $\mathbf{B}$ are *coupled* in the sense that the sources of one field depend on either the value or the time variations of the other field, equations (3.3) and (3.10) must be solved simultaneously in order to determine either field. Eliminating $\mathbf{E}$, for example, gives the *vector diffusion* equation

$$\nabla \times \frac{1}{\sigma(\mathbf{r})} \nabla \times \mathbf{B} + \mu_0 \frac{\partial \mathbf{B}}{\partial t} = \mu_0 \nabla \times \left[\frac{1}{\sigma(\mathbf{r})} \mathbf{J}_S(t) \right]. \tag{3.11}$$

The above equation describes the manner by which time–varying applied currents produce in conductors a magnetic induction $\mathbf{B}(t)$. Similarly, eliminating $\mathbf{B}$ from equations (3.3) and (3.10) gives a second diffusion equation:

$$\nabla^2 \mathbf{E} - \mu_0 \sigma(\mathbf{r}) \frac{\partial \mathbf{E}}{\partial t} = -\mu_0 \frac{\partial \mathbf{J}_S}{\partial t}. \tag{3.12}$$

As described above, the vector diffusion equations (3.11, 3.12) are only valid within conductors. If two different conductors abut, the diffusion equations hold separately within each. However, at the interface between conductors there must

exist a discontinuity in one or more of the electrical properties $\epsilon, \mu, \sigma(\mathbf{r})$. On this interface, the electromagnetic fields satisfy the following conditions:

$$E_{2n} - E_{1n} = \frac{\sigma_{ch}}{\epsilon_0} \tag{3.13}$$

$$B_{2n} = B_{1n} \tag{3.14}$$

$$\mathbf{E}_{2t} = \mathbf{E}_{1t} \tag{3.15}$$

$$\mathbf{B}_{2t} - \mathbf{B}_{1t} = \mu_0 \mathbf{K}_S \times \hat{\mathbf{n}} \tag{3.16}$$

where $\hat{\mathbf{n}}$ is the unit normal vector pointing from medium 1 into medium 2. In the equations (3.13–3.16), I have used the notation B_n to represent the scalar product $\hat{\mathbf{n}}\cdot\mathbf{B}$ and $\mathbf{B}_t, \mathbf{E}_t$ to represent the vectors $\hat{\mathbf{n}}\times\mathbf{B}, \hat{\mathbf{n}}\times\mathbf{E}$ which are tangential to the surface of the discontinuity. Also, σ_{ch} [C·m^{-2}] is the electric charge density on this surface and $\mathbf{K}_S$ [A·m^{-1}] is its applied current density. In static equilibrium, the surface electric charge density σ_{ch} at the interface between two conductors may be different from zero despite the fact that the volume charge density ρ_{ch} vanishes everywhere within the conductors.

The electromagnetic *response* of a system of conductors to controlled–source excitation is described in terms of the solutions to the vector diffusion equations (3.11) and (3.12). A correctly defined response is one which has a physical analog, enabling comparisons to be made between theory and experiment. Before a response can be computed, however, the applied current density $\mathbf{J}_S(\mathbf{r}, t)$ appearing in the RHS of the vector diffusion equations must be specified. Only electric and magnetic dipoles need to be considered since, by the *superposition principle*, they are the building blocks of controlled–sources. I shall now examine the two types of dipole in greater detail.

3.3 Grounded and Insulated Controlled–Sources

Magnetic and electric dipoles are mainly distinguished by the way in which the current they carry interacts with surrounding conductors. The electric dipole is a straight

conducting filament of length Δ carrying a current $I(t)$. The dipole is grounded at both ends to the surrounding conductors. The current density of a point electric dipole (one which has the property that $\Delta \to 0$, $I \to \infty$ such that the product $I\Delta$ is finite) located at the co–ordinate origin is

$$\mathbf{J}_{\mathrm{S}}^{\mathrm{e.d.}}(\mathbf{r},t) = P(t)\delta(\mathbf{r})\hat{x} \tag{3.17}$$

where $P(t)=I(t)\Delta$ [A·m] is the *electric dipole moment.* The unit vector $\hat{x}$ appearing in equation (3.17) signifies that the applied current $I(t)$ flows in the x–direction.

A physical analog of the electric dipole in free space is an open circuit consisting of insulated wire supplied by power from a battery. In a conducting medium the circuit is grounded in the sense that the wire is bared at the free ends in order to make direct electrical contact with its surroundings. The rest of the wire is closely twisted together and connected to a remote battery. In this analog, currents flow along the wire from the (+) terminal of the battery to the free end denoted as the current *source*, through the surrounding conductors, then into the other free end denoted as the current *sink* and along the wire again to the (—) battery terminal thus completing the circuit. At large distances from the free ends in comparison to their separation the electromagnetic fields of this arrangement are identical to those of a point electric dipole.

The magnetic dipole is a circular filament of radius a carrying a current $I(t)$ and is insulated from surrounding conductors, *i.e.* there are no sources or sinks of current. When located at the origin of a cylindrical co–ordinate system the current density of a point magnetic dipole (one which has the property that $a \to 0$, $I \to \infty$ such that the product $I\pi a^2$ is finite) is

$$\mathbf{J}_{\mathrm{S}}^{\mathrm{m.d.}}(\mathbf{r},t) = \frac{M(t)}{\pi a^2}\delta(\rho)\delta(z)\hat{\phi} \tag{3.18}$$

where $\rho=\sqrt{x^2+y^2}$ and $M(t)=I(t)\pi a^2$ [A·m^2] is the *magnetic dipole moment.* The physical analog is a current–carrying loop of radius A with a remote battery supplying

power to the loop. The battery is connected to the loop via closely twisted conducting leads. At large distances from the loop compared to A the electromagnetic fields of the loop are identical to those of a point magnetic dipole.

3.4 H–polarization Boundary Value Problem

The magnetic induction $\mathbf{B}(t)$ in a medium of conductivity $\sigma(\mathbf{r})$ due to its excitation by a point electric or a point magnetic dipole is a solution to the vector diffusion equation (3.11). The dipole current density functions are given by equations (3.17) and (3.18) and are inserted into the equation prior to solving. Unfortunately, finding solutions to this equation for all but the most simple systems of conductors in the presence of either dipole field has proven difficult: analytic examples relevant to geophysics are few (Ward and Hohmann 1987) and specialized numerical techniques are required (Barton and Cendes 1987, Emson and Simkin 1983) in addition to unreasonably large amounts of CPU time (Pridmore *et.al.* 1981) even on vector supercomputers (Adhidjaja and Hohmann 1989). To ease the computational load, whether the solution technique is analytical (Edwards 1988, Inan *et.al.* 1986) or numerical (Oristaglio and Hohmann 1984, Goldman *et.al.* 1986), it is convenient to address a two dimensional analog problem obtained by setting to zero one of the spatial partial derivative operators, for example $\partial_y \equiv 0$. In the 2–D problem created, the vector diffusion equation reduces to a scalar diffusion equation, the latter possessing a greater catalog of analytical solutions and being amenable to standard numerical methods of solution. I assume initially in §3.4 that excitation is by an $\hat{x}$–directed point electric dipole; then in a later section §3.8 I shall consider the case of magnetic excitation.

In the 2–D analog defined as above, the conductivity becomes at most a function of two variables $\sigma(x,z)$. The invariant direction is $\hat{y}$, this direction is sometimes referred to as *along–strike* in analogy to a term used in structural geology. The point electric dipole current density $\mathbf{J}_S^{e.d.}(\mathbf{r},t)$ given by equation (3.17) reduces to that of

an *extended* electric dipole of moment $P'(t)$:

$$\mathbf{J}_S'^{\text{e.d.}}(x,z,t) = P'(t)\delta(x)\delta(z)\hat{x}. \tag{3.19}$$

In equation (3.19), the dipole moment is $P'(t)=\lambda(t)\Delta$ [A] where $\lambda(t)$ is a current per unit length. The extended dipole is non–physical but it is sometimes helpful to visualize it as a conducting strip which is infinitely long along–strike, infinitesimally thin in the $\hat{z}$–direction and of width Δ in the $\hat{x}$–direction. It carries a current/unit length $\lambda(t)$ which flows *across* the strip in the $\hat{x}$–direction, thus there is a line sink of current at $x=\Delta/2$ and a line source of current at $x=-\Delta/2$. The extended dipole also has the property that $\Delta\rightarrow 0$, $\lambda\rightarrow\infty$ such that the product $\lambda\Delta$ is finite. From its symmetry, it is evident that the extended dipole produces only one non–vanishing component of the magnetic induction in the 2–D conductivity structure, namely the along–strike component $\mathbf{B}=B_y(x,z)\hat{y}$. There are two components of the electric field, they are orthogonal to $\mathbf{B}$, *i.e.* $E_x(x,z)\hat{x}$ and $E_z(x,z)\hat{z}$. Since the extended dipole produces only one component of $\mathbf{B}$ it is said to excite the *H–polarization* mode of Maxwell's equations. There exists an orthogonal mode. An infinite insulated line source oriented along–strike can be thought of as an extended magnetic dipole. It generates only one component of $\mathbf{E}$ and thereby excites the *E–polarization* mode.

Since there is only one component of $\mathbf{B}$, the vector diffusion equation (3.11) must reduce to a *scalar* diffusion equation. Inserting $\mathbf{B}(\mathbf{r},t)=B_y(x,z,t)\hat{y}$ into equation (3.11) and simplifying gives the required form:

$$\frac{\partial}{\partial x}\left[\frac{1}{\sigma}\frac{\partial B_y}{\partial x}\right] + \frac{\partial}{\partial z}\left[\frac{1}{\sigma}\frac{\partial B_y}{\partial z}\right] - \mu_0\frac{\partial B_y}{\partial t} = \frac{\mu_0}{\sigma}\frac{\partial J_S'^{\text{e.d.}}}{\partial z} \tag{3.20}$$

where $J_S'^{\text{e.d.}}$ is equal to the dot product $\mathbf{J}_S'^{\text{e.d.}}(\mathbf{r},t)\cdot\hat{x}$.

As a solution to equation (3.20), B_y is a function of time t, but equivalently, it can be described as a function of frequency ω if the current/unit length carried by the dipole oscillates with time according to $\lambda(t)=\lambda_0\exp(i\omega t)$. For many practical cases, however, it is desirable to obtain the solution to (3.20) for a dipole current/unit length

$\lambda(t)$ that is a ***discontinuous*** function of time. When this is the case, B_y is conveniently expressed as a function of the Laplace frequency s [Hz]. In §3.5 for example, I shall describe the transient magnetic field $B_y(t)$ that is generated by a step–on dipole with a current/unit length of the form $\lambda(t)=\lambda_0 u(t)$ where $u(t)$ is the Heaviside function defined by:

$$u(t) = \begin{cases} 0, & \text{if } t \leq 0; \\ 1, & \text{if } t > 0. \end{cases} \tag{3.21}$$

A Laplace transform of an arbitrary function of time $F(t)$ is defined by

$$\overline{F}(s) \equiv \int_0^\infty \exp(-st) F(t)\ dt. \tag{3.22}$$

Application of the transformation (3.22) to the time–dependent equation (3.20) turns it into the time–***independent*** scalar diffusion equation:

$$\frac{\partial}{\partial x}\left[\frac{1}{\sigma}\frac{\partial \overline{B}_y}{\partial x}\right] + \frac{\partial}{\partial z}\left[\frac{1}{\sigma}\frac{\partial \overline{B}_y}{\partial z}\right] - \mu_0 s \overline{B}_y = \frac{\mu_0}{\sigma}\frac{\partial \overline{J}_S^{\text{e.d.}}}{\partial z}. \tag{3.23}$$

The solution to the above equation $\overline{B}_y(x,z,s)$ is said to be in the ***Laplace domain.*** It can be transformed back into the *time domain* by means of an inverse Laplace transformation which, for the arbitrary function $F(t)$ is given by:

$$F(t) \equiv \frac{1}{2\pi i}\int_{\gamma-i\infty}^{\gamma+i\infty} \exp(st)\overline{F}(s)\ dt. \tag{3.24}$$

The analytic representations of the Laplace transformation and its inverse, given by equations (3.22) and (3.24) respectively, are of little practical use for my purposes. Instead, in circumstances where analytic functions are to be transformed from one domain into the other I refer to tables of Laplace transforms (*e.g.* Abramowitz and Stegun 1972) and when a numerical Laplace inversion is required I use the Gaver–Stehfest algorithm (Gaver 1966, Stehfest 1970*a*,*b*) which is introduced in §3.7 and described in detail in Appendix A.

To complete the specification of the H–polarization boundary value problem, the partial differential equation equation (3.23) is supplemented by the condition that

is obeyed by $\overline{B}_y(x,z,s)$ on the bounding curve $\partial\Omega$ of the two dimensional solution domain Ω. The boundary condition for $\overline{B}_y$ is

$$\overline{B}_y(x_0,z_0,s) = 0 \qquad (x_0,z_0) \in \partial\Omega, \;\; s > 0. \tag{3.25}$$

The above equation, which is valid for the 2–D analog problem as formulated in the Laplace domain, is otherwise equivalent to equation (3.6).

What are the effects of addressing the 2–D analog problem as opposed to solving the fully three dimensional vector diffusion problem? Since the effects vary according to the nature of the problem under study, I will restrict discussion to effects that are relevant to geophysical exploration. For example, a major shortcoming of the 2–D approximation as applied to geo–electrical problems is due to the fact that in most regions and over a large range of length scales, the earth's electrical conductivity varies in all three spatial dimensions. Therefore, conductivity functions of the form $\sigma(x,z)$ required by the 2–D formulation are likely to be poor representations of the actual electrical structure of the earth. This limitation of the 2–D approximation may not necessarily apply however if a well–defined strike direction has been established from *a priori* knowledge of the geology. In this case the geological structure, and oftentimes the conductivity, varies systematically or not at all along the strike direction.

Another limitation of the 2–D approximation is that the solution $B_y(x,z,t)$ to the scalar diffusion equation (3.20) is different from the $\hat{y}$–component of the solution $\mathbf{B}(\mathbf{r},t)$ to the vector diffusion equation (3.11). Therefore, aspects of the electromagnetic response including the *pattern* of induced currents in the earth (which is described by $\mathbf{J}=\nabla\times\mathbf{B}/\mu_0$) and the signal *magnitude* $|\mathbf{B}|$ will be unrealistic if the 2–D approximation is employed. Only for very simple earth conductivity structures can exact *conversion factors* be formulated. These factors enable certain 2–D response parameters, defined in §3.6, to be converted into corresponding physical response parameters, *i.e.* those that would be calculated from solutions to the vector diffusion equation. (For further details, see Chapter 5 and Everett and Edwards 1990). For complicated structures such conversion factors are neither exact nor readily available.

To make matters worse, the closest physical analog of the 2–D $\hat{x}$–directed extended dipole, which is a *row* of evenly spaced and similarly directed finite dipoles, will likely never be constructed and deployed. This is because the difficulty of doing so outweighs the main practical benefit of the 2–D extended dipole, which is that of simplifying the electromagnetic field modeling and the *a posteriori* interpretation of data. In other words, it is easier to solve the vector diffusion equation than to build and deploy a 2–D extended dipole. The field of the extended dipole is therefore of interest not with the hope that its physical analog will ever be constructed but rather in the mathematical sense that the extended dipole is the source which excites the fundamental H–polarization mode.

Provided the geological structure has a well–defined strike, there are advantages to performing two–dimensional geo–electrical modeling based on the scalar diffusion equation (3.23). Qualitatively, 2–D modeling identifies which features of a complicated system of earth conductors respond most strongly to 2–D source excitation. Often these features are the same ones which respond strongly to finite source excitation. The 2–D responses can also point to the range of *times* that best illuminate the interesting features of the earth conductors under study. Also, the separation of the two fundamental modes that arises naturally from the 2–D formulation of the problem helps to make the physics of electromagnetic diffusion into conducting bodies understandable. The mode separation is not possible in the fully three dimensional formulation.

3.5 H–polarization Closed–Form and Analytical Solutions

In §4.2–4.4 I shall describe the development and implementation of a finite element technique which finds *approximate* solutions to a class of elliptic boundary value problems (BVPs) based on the diffusion equation in two spatial dimensions. This class includes the H–polarization problem as defined by the partial differential equation (3.23) and boundary condition (3.25). In this section I will develop some closed–form

and analytical solutions to the H–polarization problem; they will be used in §4.5 to estimate the convergence properties of the finite element implementation and here in §3.5 to expedite illustration of the current patterns as induced in a uniformly conducting earth. Since the finite element code was written to enable modeling of *marine* electromagnetic fields, I shall restrict attention at this point to systems of conductors whose geometry and conductivities are appropriate to this environment.

Consider an $\hat{x}$–directed 2–D extended dipole, described by the current density function (3.19) with the spatial co–ordinates oriented such that x is horizontal, y is along–strike and z is vertical, positive upwards. In this section, the conductors excited by this dipole must be kept geometrically simple in order to facilitate the analytical approach. Specifically, the following *double half–space* problem is considered (Edwards 1988). The dipole is located on the interface beneath a semi–infinite uniform conductor $\sigma=\sigma_0$ occupying $z>0$ which represents an infinitely deep ocean and above a similar semi–infinite uniform conductor $\sigma=\sigma_1$ which naïvely represents the earth. The dipole moment $P'(t)$ is assumed to have the Heaviside step–on form $\lambda_0 u(t)\Delta$ where $u(t)$ is given by equation (3.21). In the Laplace domain the Heaviside function is $\overline{u}(s)=1/s$, so that $\overline{P}'(s)\equiv P'=\lambda_0\Delta/s$. The closed–form solution to the double–halfspace problem as described above is given in the Laplace domain by

$$\overline{B}_y^{\text{ocean}}(s) = \frac{\mu_0 P'}{\pi s}\int_0^\infty \left[\frac{\sigma_0\theta_1}{\sigma_1\theta_0+\sigma_0\theta_1}\right]\exp(-\theta_0 z)\cos(\lambda x)\,d\lambda \quad z\geq 0 \tag{3.26}$$

$$\overline{B}_y^{\text{earth}}(s) = \frac{-\mu_0 P'}{\pi s}\int_0^\infty \left[\frac{\sigma_1\theta_0}{\sigma_1\theta_0+\sigma_0\theta_1}\right]\exp(\theta_1 z)\cos(\lambda x)\,d\lambda \quad z\leq 0 \tag{3.27}$$

where $\theta_i=\sqrt{\lambda^2+\mu_0\sigma_i s}$, and $i=0,1$. The above equations may be derived according to the method of Sommerfeld (1926) which is now considered to be standard (Wait 1961).

For any real antenna, let alone the extended dipole which is infinite in extent, the instantaneous switch–on in current as implied by the presence of the Heaviside step–on term in the dipole moment is admittedly an idealization. However, with fast

electronics the current rise time in a finite dipole can be tens of microseconds. In this case, the rise time may be safely neglected when modeling electromagnetic fields within earth conductors since this time scale is small in comparison to typical diffusion times (see §3.6), which are between O(ms) and O(s). Just as the electromagnetic fields at large distances produced by a finite electric dipole are identical to those produced by a point electric dipole (see §3.3), the electromagnetic fields at typical diffusion times produced by a dipole with a microsecond rise time are identical to those produced by an idealized Heaviside dipole.

Returning to the double half–space problem, if the conductivity of the naïve earth model is made the same as that of the ocean $\sigma_0=\sigma_1=\sigma$, *i.e.* the extended dipole is located in a uniformly conducting whole–space, then equations (3.26) and (3.27) simplify to:

$$\overline{B}_y^{\mathrm{ws}}(s) = \pm\frac{\mu_0 P'}{2\pi s}\int_0^\infty \exp(-\theta|z|)\cos(\lambda x)\, d\lambda \tag{3.28}$$

where $\theta=\sqrt{\lambda^2+\mu_0\sigma s}$. The positive sign in equation (3.28) is valid in the upper half–space $z>0$ and the negative sign is valid for $z<0$. Although the integral is divergent at $z=0$ the limit

$$\lim_{|z|\to 0}\overline{B}_y^{\mathrm{ws}}(s) = 0 \tag{3.29}$$

does exist. For $|z|\neq 0$, the integral in equation (3.28) is analytic; an integral of the same form is tabulated *e.g.* in Gradshteyn and Ryzhik (1965):

$$\int_0^\infty \exp(-|z|\sqrt{\lambda^2+\alpha^2})\cos(\lambda x)\, d\lambda = \frac{\alpha|z|}{\sqrt{x^2+z^2}}K_1(\alpha\sqrt{x^2+z^2}) \quad \mathcal{R}(\alpha)>0 \tag{3.30}$$

where $\mathcal{R}(\cdot)$ denotes the real part of an arbitrary complex argument, K_1 is the modified Bessel function of unit order and $\alpha=\sqrt{\mu_0\sigma s}$. Since the electrical parameters μ_0 and σ are everywhere real and positive, the condition $\mathcal{R}(\alpha)>0$ is upheld provided $\mathcal{R}(\sqrt{s})>0$. This latter condition on the Laplace frequency s is consistent with those imposed by the Gaver–Stehfest inversion technique, the significance of which will be discussed in

§3.7. Inserting the above expression into equation (3.28) yields the desired analytic form:

$$\overline{B}_y^{ws}(s) = \frac{\mu_0 P'}{2\pi}\cos\phi\sqrt{\frac{\mu_0\sigma}{s}}K_1(\sqrt{\mu_0\sigma s\rho^2}) \tag{3.31}$$

where $\rho=\sqrt{x^2+z^2}$ and $\cos\phi=z/\rho$.

The ***skin depth*** of a conductor is the distance that an electromagnetic field component is able to penetrate before being attenuated by some prescribed amount. Although the concept of a skin depth is usually formulated in the frequency domain, the appearance of the Bessel function K_1 in equation (3.31) suggests an analogous definition for a skin depth in the Laplace domain. Since the function K_1 decays at large values of its argument β (Abramowitz and Stegun 1972) according to:

$$K_1(\beta) \approx \sqrt{\frac{\pi}{2\beta}}\exp(-\beta)\left[1+O(\frac{1}{\beta})\right], \tag{3.32}$$

the quantity $K_1(\sqrt{\mu_0\sigma s\rho^2})$ appearing in the equation (3.31) may be regarded as a ***damping factor*** which attenuates $\overline{B}_y$ with increasing penetration distance ρ from the source into the conducting whole–space. Denoted by δ^s, the Laplace domain skin depth is ***chosen*** somewhat arbitrarily as the distance ρ at which the damping factor in equation (3.31) becomes equal to $K_1(\sqrt{2})$, *i.e.*:

$$\delta^s \equiv \sqrt{\frac{2}{\mu_0\sigma s}}. \tag{3.33}$$

The skin depth δ^s, being proportional to $1/\sqrt{\sigma}$, increases as the electrical conductivity decreases. Thus, electromagnetic field components are able to readily penetrate resistors but suffer rapid attenuation with range inside good conductors. This phenomenon is in accordance with Lenz' law.

The Laplace domain double half–space solutions, given by equations (3.26) and (3.27), are shown plotted in Figure 3.1 for four different conductivity contrasts σ_0:σ_1 ranging from 3:3 to 3:0.1. The dipole moment is P'=1 A and the conductivity of the upper medium is σ_0=3.0 S/m. The whole–space solution shown in the first plot

of Figure 3.1 is computed from equation (3.31), the three others are computed from the closed–form expressions (3.26) and (3.27), using special software (Chave 1983) to evaluate the oscillatory cosine integrals. The solutions are displayed inside a rectangle described by $-5\delta_1^s<x,z<5\delta_1^s$ where the quantity δ_i^s, given by $\sqrt{2/\mu_0\sigma_i s}$, $i=0,1$ is *defined* as the skin depth of the i–th medium. The extended dipole source, which occupies the line ($x=0,-\infty\leq y\leq\infty,z=0$), is located at the center of each plot. The plot contours, which are logarithmically spaced at intervals of two per decade, are lines of constant $\overline{B}_y$. The solid contours correspond to $\overline{B}_y>0$ and the dashed contours to $\overline{B}_y<0$. Due to the unique symmetry of the H–polarization formulation, the contours also coincide with current streamlines. The currents circulate along the contours from the current source to the current sink. The sense of circulation is therefore clockwise in the lower half–space and counter–clockwise in the upper half–space. The current streamlines are more closely packed in the relatively conducting upper–halfspace medium, this is particularly evident when the four plots of Figure 3.1 are compared. The patterns of currents shown depend only on the conductivity contrast, not on the dipole moment P' nor the Laplace frequency s. However, the numerical values of the contours do depend on these latter two quantities.

3.6 Electromagnetic Response Parameters

In §3.3 I mentioned that the electromagnetic response of a system of conductors to controlled–source excitation is described in terms of the solutions to the vector diffusion equations (3.11) and (3.12). In this section I shall describe some 2–D analogs of response parameters. The analogs, which are defined in terms of the solutions $B_y(t)$ to the more easily solved scalar diffusion equation (3.20), characterize the 2–D transient response of an arbitrary system of conductors but are analytic only for the whole–space geometry described in §3.5. In Chapter 5 exact conversion factors will be determined which relate the analytic 2–D analogs to their 3–D counterparts, from the latter comparison to electrical measurements made at sea can be performed.

Consider the Laplace domain whole–space solution (3.31) to the H–polarization BVP. The equivalent time domain solution can be obtained formally through the Laplace inversion integral (3.24). From tables (Abramowitz and Stegun 1972), however, I find the transform:

$$\mathcal{L}^{-1}\left[\frac{1}{\sqrt{s}}K_1(A\sqrt{s})\right] = \frac{1}{A}\exp(\frac{-A^2}{4t}) \quad A > 0. \tag{3.34}$$

The notation $\mathcal{L}^{-1}[\cdot]$ refers to the inverse Laplace operation. Comparing the above transform with equation (3.31), the assignment $A=\sqrt{\mu_0\sigma\rho^2}$ is appropriate. In addition, the quantity $\sqrt{\mu_0\sigma\rho^2}$ is positive definite, as required by the transform. Thus, the whole–space transient solution to the H–polarization BVP is given by:

$$B_y(t) = \frac{\mu_0 P' z}{2\pi\rho^2}\exp(\frac{-\mu_0\sigma\rho^2}{4t}). \tag{3.35}$$

This is called the *step response* because the source moment $P'(t)$ is proportional to the Heaviside step–on function. Other idealized forms of the source moment $P'(t)$ can lead to responses that are of interest to practitioners. For example, the *impulse response* is simply the time derivative of equation (3.35)

$$\dot{B}_y(t) = \frac{\mu_0^2\sigma P' z}{8\pi t^2}\exp(\frac{-\mu_0\sigma\rho^2}{4t}) \tag{3.36}$$

and describes time variations in the magnetic induction B_y that would be produced in a uniform earth by a impulsive source of moment $P'(t)=\lambda_0\delta(t)\Delta$ [A·s^{-1}] where $\delta(t)$ is the Dirac delta function, sometimes called the impulse function. The impulse response $\dot{B}_y$ is of interest since fluctuations with time in the magnetic induction components are measured by practical receivers such as induction coils.

Following a step–on in the dipole current, the magnetic induction component $B_y(t)$ diffuses into a uniform conductor in the manner described by the step response, equation (3.35). If the dipole current is an impulse function of time, the diffusion is described by the impulse response, equation (3.36). A *diffusion time* (Edwards and Chave 1986), characteristic of the electrical conductivity σ, can be defined as

the time taken for the impulse response to attain its maximum magnitude. A more precise definition of the diffusion time τ is given in the following implicit form:

$$\dot{B}_y(t)|_{t=\tau} = \max \dot{B}_y(t). \tag{3.37}$$

The diffusion time τ is identified as the ***arrival time*** of the magnetic induction B_y at a given point in the conductor. To provide a useful estimate of conductivity, the diffusion time need only be accurate to a quarter of a decade on a logarithmic scale since conductivity varies over many orders of magnitude within the earth. From equations (3.36) and (3.37) I derive the important result valid for a uniform medium that

$$\tau = \frac{\mu_0 \sigma \rho^2}{8} \qquad \text{(2D extended dipole source).} \tag{3.38}$$

For comparison, the finite electric dipole (3–D) diffusion time is $\tau = \mu_0 \sigma r^2/10$ (see Cheesman 1989, also Chapter 5).

Another response parameter of practical importance is the maximum value of the impulse response. The maximum, which governs the ***peak*** voltage that would be recorded in an induction coil, occurs at the diffusion time and is given by

$$\max \dot{B}_y(t) = \dot{B}_y(\tau) = \frac{8P'z}{\pi \sigma e^2 \rho^4}. \tag{3.39}$$

The concept of a skin depth may be formulated in the time domain. Just as there appeared a damping factor in the Laplace domain expression (3.31) for $\overline{B}_y(s)$, so there is one in the corresponding time domain expression (3.35) for $B_y(t)$. The Laplace domain damping factor is a modified Bessel function K_1 but in the time domain the factor is $\exp(-\mu_0 \sigma \rho^2/4t)$, see equation (3.35). For convenience, I ***choose*** the time domain skin depth, denoted by δ^t, to be the distance at which the exponential damping factor becomes equal to 1/e, *i.e.*:

$$\delta^t = \sqrt{\frac{2t}{\mu_0 \sigma}}. \tag{3.40}$$

Defined as above, the time domain skin depth quantifies the concept of late time. Following a transient event in an antenna, electromagnetic field components at positions within the conductor satisfying $\rho \ll \delta^t$ are said to have reached their steady state values and hence at these positions equilibrium has been re–attained.

The late time values of the magnetic induction component can also be useful response parameters. For the step and impulse response respectively, the DC–limits are given by:

$$B_y^{\mathrm{DC}} = \frac{\mu_0 P' z}{2\pi\rho^2}, \quad \dot{B}_y^{\mathrm{DC}} = 0. \tag{3.41}$$

The step response has a non–zero DC–limit as a consequence of the fact that steady applied currents, whether or not they are grounded to conductors, are sources of a magnetostatic field, see §3.0. The late time step response can not be measured by an induction coil, since coils respond only to *changes* in the magnetic induction. Appropriate is a fluxgate, or other high sensitivity, high speed magnetometer providing direct magnetic induction measurements. The impulse response is zero at late time since an impulsive applied current is non–zero only at the time t=0. Since no further current is applied to the conductor, by the DC–limit all currents produced by the initial impulse have dissipated and conditions of static equilibrium throughout the conductor are re–attained.

The step response $B_y(t)$ given by equation (3.35) is shown in Figure 3.2 plotted for a range of times t_0=0.1 s$\leq t \leq t_1$=5.0 s following step–on of the source current. The contours, as in the previous figure, are both current streamlines and lines of constant B_y; the contour interval is again two per decade. The boundary of the plots is the rectangle described by $-5\delta_0^t < x, z < 5\delta_0^t$ where $\delta_0^t = \sqrt{2t_0/\mu_0\sigma}$. The dipole moment is P'=1 A and the conductivity of the medium is σ=3 S/m. The $\pm$1 nT contours, which are the ones nearest the source (*i.e.* at positions $\rho \ll \delta_t$), do not move outwards as time progresses from t_0 to t_1. Thus, the currents near the source have already reached their late time limit by t_0=0.1 s. The currents elsewhere have not yet reached their late time limit. For example, in the t_0=0.1 s snapshot the $\pm$0.1 nT contours have

diffused out to about $1\delta_0^t$ but at the latest time t_1=5 s they have progressed out to somewhere between 4–6δ_0^t. If desired, the rate of outwards progression of currents from the source, which is diagnostic of the conductivity, can be determined.

The time derivative of the step response of Figure 3.2 is the impulse response, it is shown in Figure 3.3. The dipole moment is P'=1 A/s and the conductivity of the medium is σ=3 S/m. The impulse response, which is sharply peaked near the source at t=t_0 with a maximum >0.3 nT/s spreads outwards from the source with time until at the later time t_1=5.0 s it is everywhere less than 0.01 nT/s. At DC, the impulse response vanishes altogether. The $\dot{B}_y$ contour values, again spaced half a decade apart, indicate the rate of change of magnetic field that would be recorded by an induction coil.

As mentioned previously, there are two non–vanishing components of the electric field that are associated with the H–polarization problem, they can be obtained by direct application of Maxwell's equation (3.4). Incorporating the H–polarization symmetry $\mathbf{B}$=$B_y(x,z)\hat{y}$ these electric field components are

$$E_x = -\frac{1}{\mu_0\sigma}\frac{\partial B_y}{\partial z}, \quad E_z = \frac{1}{\mu_0\sigma}\frac{\partial B_y}{\partial x}. \tag{3.42}$$

Of this pair, the $\hat{x}$–component is particularly interesting since the in–line electric dipole–dipole configuration, which features an $\hat{x}$–directed electric dipole and pairs of electrodes oriented such that they measure directly the horizontal field component $E_x(t)$, shows promise both in theory (Edwards and Chave 1987) and in preliminary field tests (Everett *et.al.* 1989). The 2–D analog to the measured field component is computed using the first equation of the pair (3.42) and equation (3.35), it is:

$$E_x(t) = -\frac{P'}{2\pi\sigma}\left[\left(-\frac{\mu_0\sigma z^2}{2t\rho^2}\right)\exp(-\frac{\mu_0\sigma\rho^2}{4t})\right] \tag{3.43}$$

and its corresponding late time value is:

$$E_x^{\mathrm{DC}} = -\frac{P'(x^2-z^2)}{2\pi\sigma\rho^4}. \tag{3.44}$$

Both electric field components E_x,E_z are non–zero at DC by virtue of the fact that the 2–D extended electric dipole is grounded to the conductor, see §3.0. The impulse response electric field is of little interest because practical electric receivers, which are often pairs of electrodes, rarely measure $\dot{\mathbf{E}}(t)$ directly.

3.7 Transient Double Half–Space Solutions

In this section I will employ the Gaver–Stehfest (Gaver 1966, Stehfest 1970*a*,*b*) algorithm to transform the double half–space solutions of the H–polarization from the Laplace domain into the time domain. A detailed derivation of the Gaver–Stehfest algorithm, which will be defined immediately below, appears in Appendix A. For arbitrary geometry, the transformation is accomplished by inserting the Laplace domain function $\overline{B}_y(s)$ into the approximate formula

$$B_y(t) \approx \frac{\ln 2}{t} \sum_{j=1}^{n} V_j(n) \overline{B}_y \left(\frac{j \ln 2}{t} \right) \quad n, \text{even} \tag{3.45}$$

where the Gaver–Stehfest coefficients $\{V_j, j=1,2,...,n\}$ are given by

$$V_j(n) = (-1)^{n/2+j} \sum_{k=[\frac{i+1}{2}]}^{\min[j,\frac{n}{2}]} \frac{k^{n/2}(2k)!}{(n/2-k)!k!(k-1)!(j-k)!(2k-j)!}. \tag{3.46}$$

As an approximation, the linear combination of terms appearing in equation (3.45) gives results accurate to 8–bit precision for the choice n=8 provided the unknown function $B_y(t)$ has no discontinuities, sharp peaks or rapid oscillations. Since the unknown function in this case is the solution to a diffusion equation, it will satisfy all of these requirements. Note that, according to equation (3.45), the Laplace domain function need be known only at the n *real* values of s given by $\{s_j=j\ln 2/t,\ j=1,2,...,n\}$. Rounding errors worsen the result as n becomes too large, because V_j with greater and greater absolute values occur (Stehfest, 1970*a*). The Gaver–Stehfest algorithm was first used to solve electromagnetic induction problems in geophysics by Knight and Raiche (1982) and then later by Edwards and Cheesman (1987).

In the time domain, the double half–space solutions given in the Laplace domain by equations (3.26) and (3.27), when inserted into equation (3.45), become approximately

$$B_y^{\text{ocean}}(t) \approx \frac{\mu_0 P'}{\pi} \int_0^\infty \left[\sum_{j=1}^{n} \frac{V_j(n)}{j} \frac{\sigma_0 \Theta_{1j}(t) \exp[-\Theta_{0j}(t) z]}{\sigma_1 \Theta_{0j}(t) + \sigma_0 \Theta_{1j}(t)} \right] \cos(\lambda x)\, d\lambda \quad z \geq 0 \tag{3.47}$$

$$B_y^{\text{earth}}(t) \approx -\frac{\mu_0 P'}{\pi} \int_0^\infty \left[\sum_{j=1}^{n} \frac{V_j(n)}{j} \frac{\sigma_1 \Theta_{0j}(t) \exp[\Theta_{1j}(t) z]}{\sigma_1 \Theta_{0j}(t) + \sigma_0 \Theta_{1j}(t)} \right] \cos(\lambda x)\, d\lambda \quad z \leq 0 \tag{3.48}$$

with n, even and $\Theta_{ij}(t) = \sqrt{\lambda^2 + j \ln 2 \mu_0 \sigma_i / t}$, i=0,1.

This "semi–analytic" function is shown plotted for the range of times t_0=0.5 s$\leq t \leq t_1$=50 s and for a variety of conductivity contrasts from 3:1 to 3:0.03 in Figures 3.4*a–d*. Apart from the different conductivity contrasts, the geometry is otherwise identical to that of Figure 3.2, for its description see §3.6. The plots of Figure 3.4 all show vortices of currents diffusing outwards from the source at rates which are inversely proportional to the half–space conductivities. For example, the magnetic field component at the early time t_0 diffuses much more rapidly into the relatively resistive earth than into the seawater. Also at early times, in particular, the plots reveal the presence of an outwardly moving diffusive *front* leaking energy across the seafloor. It is this energy that constitutes an earth signal measured by seafloor magnetic field sensors. At the late time t_1 the seawater signal begins to dominate, its effect is to obscure information about the conductivity of the solid earth.

3.8 E–Polarization Analytical Modeling

I have already examined in detail the two dimensional H–polarization mode of Maxwell's equations as excited by an extended electric dipole and have mentioned the existence of an orthogonal mode. This other mode, called the E–polarization mode, is excited by a infinitely long insulated line source oriented along the strike of a two dimensional conductivity structure $\sigma(x, z)$. The line source, carrying a time–varying current $I(t)$ produces only one component of **E**, namely $\mathbf{E}=E_y(x, z)\hat{y}$. There

are two components of **B** in this mode, they are the orthogonal components, *i.e.* $\mathbf{B}=B_x(x,z)\hat{x}+B_z(x,z)\hat{z}$. In this section, I will look at some closed–form and analytic E–polarization mode solutions.

The current density of the infinite line source is

$$\mathbf{J}_{\mathrm{S}}^{\prime\mathrm{m.d.}}(x,z,t) = I(t)\delta(x)\delta(z)\hat{y} \tag{3.49}$$

and its closest physical analog is a segment of an insulated loop of very large radius or alternatively an insulated cable grounded at distant ends (Wait 1952). The infinite cable is an extended magnetic dipole in the sense that the currents in the cable are not in direct electrical contact with the surrounding conductors, *i.e.* the earth is inductively excited. For simple geometries, this mode has been investigated in great detail by Inan *et.al.* (1986). Like the physical analog of the 2–D extended dipole, the infinite cable will likely not be deployed since the practical difficulty of doing so outweighs the the resultant simplification of the modeling and data interpretation.

Since there is only one non–vanishing component of **E**, it is convenient to solve for it since it decouples from the two components of the magnetic induction. The relevant vector diffusion equation (3.12) becomes, when the E–polarization symmetry is incorporated, the scalar diffusion equation

$$\frac{\partial^2 E_y}{\partial x^2} + \frac{\partial^2 E_y}{\partial z^2} - \mu_0\sigma\frac{\partial E_y}{\partial t} = -\mu_0\frac{\partial J_{\mathrm{S}}^{\prime\mathrm{m.d.}}}{\partial t}. \tag{3.50}$$

If the current in the cable is of the step–on form $I(t)=Iu(t)$ then the corresponding time–independent scalar diffusion equation is

$$\frac{\partial^2 \overline{E}_y}{\partial x^2} + \frac{\partial^2 \overline{E}_y}{\partial z^2} - \mu_0\sigma s\overline{E_y} = -\mu_0 s\overline{J}_{\mathrm{S}}^{\prime\mathrm{m.d.}} \tag{3.51}$$

where $\overline{E}_y(x,z,s)$ is the Laplace transform of $E_y(x,z,t)$. To completely specify the E–polarization BVP, equation (3.51) is augmented by the condition on the boundary $\partial\Omega$ that

$$\overline{E}_y(x_0,z_0,s) = 0 \qquad (x_0,z_0)\in\partial\Omega, \quad s>0. \tag{3.52}$$

There exists a closed–form solution to the E–polarization BVP if the double half–space geometry described in §3.5 is employed. Assume that the cable is located on the seafloor interface at the co–ordinate origin. The solution is given by

$$\overline{E}_y^{\text{ocean}}(s) = -\frac{\mu_0 I}{\pi} \int_0^\infty \left[\frac{\exp(-\theta_0 z)}{\theta_0 + \theta_1} \right] \cos(\lambda x)\, d\lambda \quad z \geq 0 \tag{3.53}$$

$$\overline{E}_y^{\text{earth}}(s) = -\frac{\mu_0 I}{\pi} \int_0^\infty \left[\frac{\exp(\theta_1 z)}{\theta_0 + \theta_1} \right] \cos(\lambda x)\, d\lambda \quad z \leq 0. \tag{3.54}$$

This function, which is sensitive to the conductivity contrast σ_0/σ_1, is shown plotted for a range of contrasts in Figure 3.5. The contours are lines of constant $\overline{E}_y$ and, due to the unique symmetry of this mode, are also equipotentials. Like the H–polarization current streamlines (Figure 3.1), the equipotentials are more closely packed in the relatively conducting upper half–space.

The Laplace domain electric field component $\overline{E}_y^{\text{ws}}(s)$ produced by an infinite cable exciting a uniformly conducting whole–space may be obtained from the pair of double half–space equations (3.53) and (3.54) by making the replacements $\sigma_0{=}\sigma_1{=}\sigma$. The result is the closed–form expression:

$$\overline{E}_y^{\text{ws}}(s) = -\frac{\mu_0 I}{2\pi} \int_0^\infty \left[\frac{\exp(-\theta|z|)}{\theta} \right] \cos(\lambda x)\, d\lambda \tag{3.55}$$

which may be simplified further as follows. Taking the z–derivative of both sides of the integral (3.30) and using the relationship that exists between the zero and unit order modified Bessel functions, namely $K_0'(z){=}K_1(z)$ it follows that

$$\int_0^\infty \frac{\exp(-\sqrt{\lambda^2+\alpha^2}|z|)}{\sqrt{\lambda^2+\alpha^2}} \cos(\lambda x)\, d\lambda = K_0(\alpha\rho) \quad \mathcal{R}(\alpha) > 0 \tag{3.56}$$

and when the above expression is inserted into equation (3.55) the whole–space electric field is analytic:

$$\overline{E}_y^{\text{ws}}(s) = -\frac{\mu_0 I}{2\pi} K_0(\sqrt{\mu_0 \sigma s \rho^2}). \tag{3.57}$$

The corresponding expression in the frequency domain $\overline{E}_y^{\text{ws}}(\omega)$ can be found *e.g.* in Wait (1952).

Using the tabulated Laplace transform (Abramowitz and Stegun 1972)

$$\mathcal{L}^{-1}\left[K_0(A\sqrt{s})\right] = \frac{1}{2t}\exp(\frac{-A^2}{4t}) \quad A > 0, \tag{3.58}$$

and associating A once again with $\sqrt{\mu_0\sigma\rho^2}$, the transient whole–space electric field is analytic, namely:

$$E_y(t) = -\frac{\mu_0 I}{4\pi t}\exp(\frac{-\mu_0\sigma\rho^2}{4t}). \tag{3.59}$$

The above function, shown plotted in Figure 3.6, is sharply peaked near the source at time t_0=0.1 s but spreads out as time progresses. As suggested by the plot at the latest time shown (t_1=5.0 s), the DC value of this function is zero, *i.e.* E_y^{DC}=0. This late time behaviour is in accordance with the fact that steady currents, when insulated from conductors, produce only a magnetostatic field.

The two components of induction that are associated with the E–polarization mode may be computed from Maxwell's equation (3.3). After applying the symmetry of this mode, *i.e.* $\mathbf{E}$=$E_y(x,z)\hat{y}$, equation (3.3) reduces to a pair of equations which can be written into integral form as follows:

$$B_x(t) = \int \frac{\partial E_y}{\partial z}\, dt, \qquad B_z(t) = \int \frac{\partial E_y}{\partial x}\, dt. \tag{3.60}$$

For example, the $\hat{x}$–component of the magnetic induction $B_x(t)$, which is obtained by integrating the z–derivative of the expression (3.59), is given by:

$$B_x(t) = \frac{\mu_0 I z}{2\pi\rho^2}\exp(\frac{-\mu_0\sigma\rho^2}{4t}). \tag{3.61}$$

The above component, which does not vanish at late time, has a form which is identical to that of the H–polarization magnetic induction component (3.35). The similarity occurs because both are horizontal induction components orthogonal to the direction of flow of the applied current.

The time domain double half–space solutions may be found approximately by inserting the Laplace domain expressions given by equations (3.53) and (3.54) into

the Gaver–Stehfest equation (3.45), *i.e.*

$$E_y(t) \approx \sum_{j=1}^{n} V_j(n) \overline{E}_y \left(\frac{j \ln 2}{t} \right). \tag{3.62}$$

Upon doing so, there results

$$E_y^{\text{ocean}}(t) \approx -\frac{\mu_0 I \ln 2}{\pi t} \int_0^{\infty} \left[\sum_{j=1}^{n} \frac{V_j(n)}{j} \frac{\exp[-\Theta_{0j}(t) z]}{\Theta_{0j}(t) + \Theta_{1j}(t)} \right] \cos(\lambda x)\, d\lambda \tag{3.63}$$

$$E_y^{\text{earth}}(t) \approx -\frac{\mu_0 I \ln 2}{\pi t} \int_0^{\infty} \left[\sum_{j=1}^{n} \frac{V_j(n)}{j} \frac{\exp[\Theta_{1j}(t) z]}{\Theta_{0j}(t) + \Theta_{1j}(t)} \right] \cos(\lambda x)\, d\lambda, \tag{3.64}$$

plots of which are shown in Figures 3.7*a*,*b* for conductivity contrasts of 3:1 and 3:0.03 and the range of times t_0=0.5 s<t<t_1=50 s. The plots show the patterns of equipotentials diffusing outwards from the line source after step–on at time t=0. The equipotentials, like the current streamlines for the H–polarization mode, initially diffuse outwards at a rate inversely proportional to the half–space conductivity. However at late times, *e.g.* $t > t_1$, the electric field becomes increasingly independent of the conductivity contrast. Finally, at its late time limit, the electric field $E_y(t)$ vanishes by virtue of the fact that steady currents, when insulated from conductors, produce only a magnetostatic field.

References

Abramowitz, M. and I.A. Stegun (ed.), 1972, *Handbook of Mathematical Functions*, Dover Publications, Inc., New York, NY.

Adhidjaja, J.I. and G.W. Hohmann, 1989. A finite difference algorithm for the transient electromagnetic response of three–dimensional bodies, *Geophys. J. Int.*, **98**, 233–242.

Barton, M.L. and Z.J. Cendes, 1987. New vector finite elements for three–dimensional magnetic field computation, *J. Appl. Phys.*, **61**, 3919–3921.

Chave, A.D., 1983. Numerical integration of related Hankel transforms by quadrature and continued fraction expansion, *Geophysics*, **48**, 1671–1686.

Cheesman, S.J., 1989. A short baseline transient electromagnetic method for use on the seafloor, *Research in Applied Geophysics*, **46**, Geophysics Laboratory, University of Toronto.

Edwards, R.N., 1988. Two–dimensional modeling of a towed in–line electric dipole–dipole sea–floor electromagnetic system: The optimum time delay or frequency for target resolution, *Geophysics*, **53**, 846–853.

Edwards, R.N. and A.D. Chave, 1986. A transient electric dipole–dipole method for mapping the conductivity of the seafloor, *Geophysics*, **51**, 984–987.

Edwards, R.N. and S.J. Cheesman, 1987. Two–dimensional modelling of a towed transient magnetic dipole–dipole seafloor EM system, *J. Geophysics*, **61**, 110–121.

Emson, C.R.I. and J. Simkin, 1983. An optimal method for 3–D eddy currents, *I.E.E.E. Trans. Magnetics*, **19**, 2450–2452.

Everett, M.E., R.N. Edwards, S.J. Cheesman, H. Utada and I.J. Ferguson, 1989. Interpretation of seafloor electromagnetic data in applied geophysics, in *Applied Electromagnetics in Materials*, ed. Miya, K., Pergamon Press, Oxford, UK, 143–153.

Everett, M.E. and R.N. Edwards, 1990. Theoretical controlled–source electromagnetic responses of active mid–ocean ridge models, *Geophys. J. Int.*, in press.

Gaver, D.P., 1966. Observing stochastic processes, and approximate transform inversion, *Operations Research* ,**14**, 444–459.

Goldman, Y., C. Hubans, S. Nicoletis and S. Spitz, 1986. A finite–element solution for the transient electromagnetic response of an arbitrary two–dimensional resistivity distribution, *Geophysics*, **51**, 1450–1461.

Gradshteyn, I.S. and I.M. Ryzhik, 1965. *Table of integrals, series and products*, Academic Press, Inc., New York, NY.

Knight, J.H. and A.P. Raiche, 1982. Transient electromagnetic calculations using the Gaver–Stehfest inverse Laplace transform method, *Geophysics*, **47**, 47–50.

Inan, A.S., A.C. Fraser–Smith and O.G. Villard, 1986. ULF/ELF electromagnetic fields generated along the seafloor interface by a straight line current source of infinite length, *Radio Sci.*, **21**, 409–420.

Oristaglio, M.L. and G.W. Hohmann, 1984. Diffusion of electromagnetic fields into a two–dimensional earth: a finite–difference approach, *Geophysics*, *49*, 870–894.

Pridmore, D.F., G.W. Hohmann, S.H. Ward and W.R. Sill, 1981. An investigation of finite–element modeling for electrical and electromagnetic data in three dimensions, *Geophysics*, **46**, 1009–1024.

Stehfest, H., 1970*a*. Algorithm 368. Numerical inversion of Laplace transforms, *Comm. A.C.M.*, **13**, 47–49.

Stehfest, H., 1970*b*. Remark on Algorithm 368. Numerical inversion of Laplace transforms, *Comm. A.C.M.*, **13**, 624.

Sommerfeld, A., 1926. Über die Ausbreitung der Wellen in der drahtlosen Telegraphie

(The propagation of waves in the wireless telegraphy), *Ann. Physik*, **81**, 1135–1153.

Wangsness, R.K., 1979. *Electromagnetic Fields*, John Wiley & Sons, New York, NY.

Wait, J.R., 1952. The cylindrical ore body in the presence of a cable carrying an oscillating current, *Geophysics*, **17**, 378–386.

Wait, J.R., 1961. The electromagnetic fields of a horizontal dipole in the presence of a conducting half–space, *Can. J. Phys.*, **39**, 1017–1028.

Ward, S.H. and G.W. Hohmann, 1987. Electromagnetic theory for geophysical applications, in *Electromagnetic Methods in Applied Geophysics Vol. 1, Theory*, ed. Nabighian, M.N., Society of Exploration Geophysicists, Tulsa, OK., 131–311.

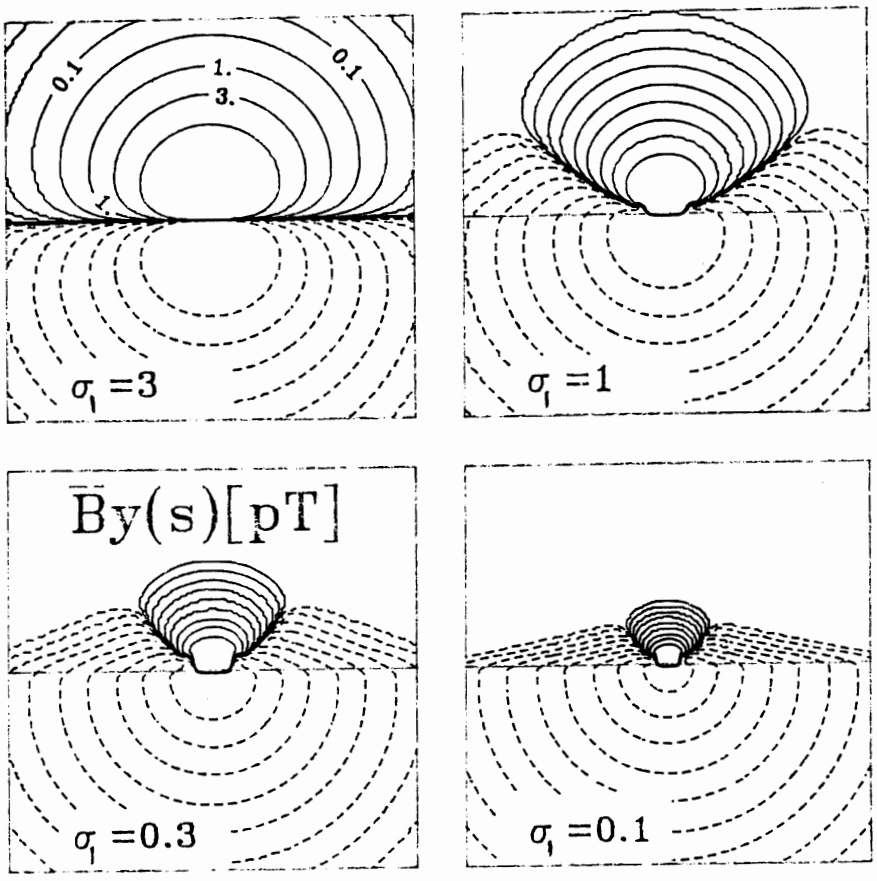

Fig.3.1 Laplace s–domain solution $\overline{B}_y(x,z,s)$ to the H–polarization mode of Maxwell's equations, for a fixed value of s=1 Hz. The regions shown are squares whose sides are $10\delta_1^s$ where $\delta_1^s=\sqrt{2/\mu_0\sigma_1 s}$ is the skin depth of the lower conductor. Contours of magnetic induction B_y are shown for various electrical conductivity contrasts between upper (fixed at σ_0=3 S/m) and lower conducting half–spaces. The field is produced by a 2–D extended dipole of unit moment. The contour lines in these plots are also current streamlines. Contours are logarithmically spaced, two per decade and their values range from ±10 pT near the source outwards to ±0.001 pT remote from the source. The dashed contours correspond to negative values.

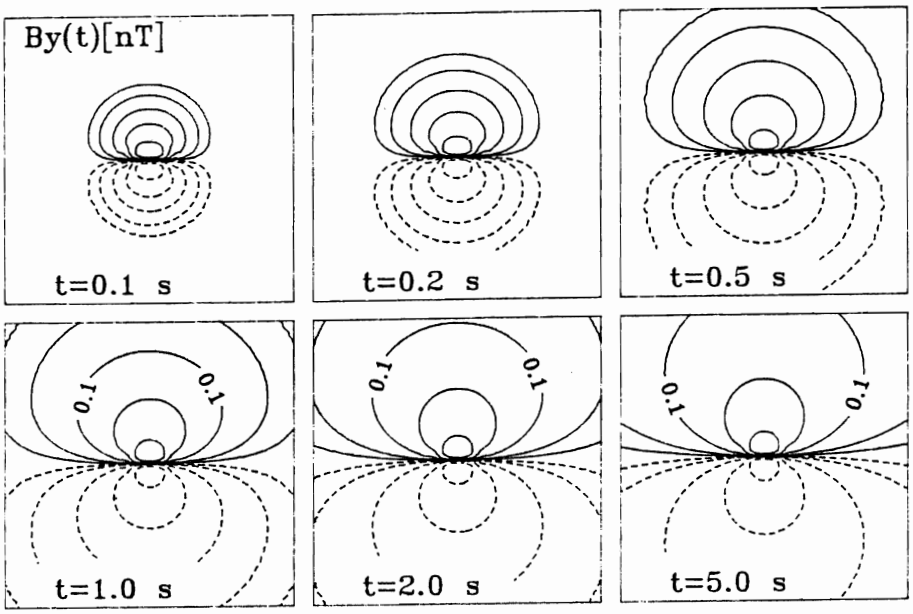

Fig.3.2 Contours of the H–polarization mode step response $B_y(t)$ show electromagnetic diffusion into the first 5 skin depths of a uniform conductor following a rapid switch–on of electric current in a unit moment, extended dipole at time t=0. The contours are logarithmically spaced, two contours per decade. By t=5 s, the step response has reached a final, steady value.

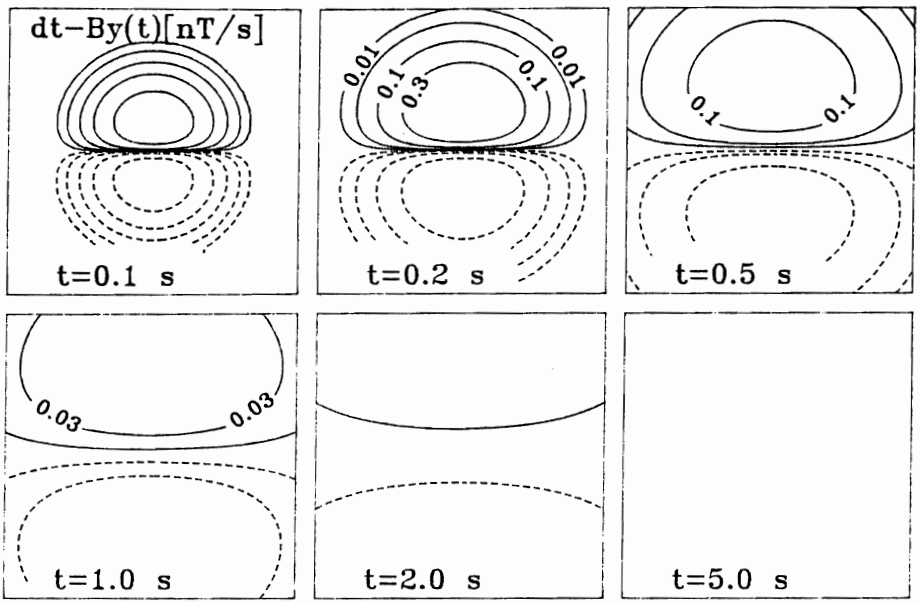

Fig.3.3 Logarithmically spaced contours of the impulse response $\partial_t B_y(t)$ show electromagnetic diffusion into the first 5 skin depths of a uniform conductor following an impulse of electric current in a unit moment, extended dipole at time t=0. In contrast to the step response of the previous figure, the impulse response vanishes at late time.

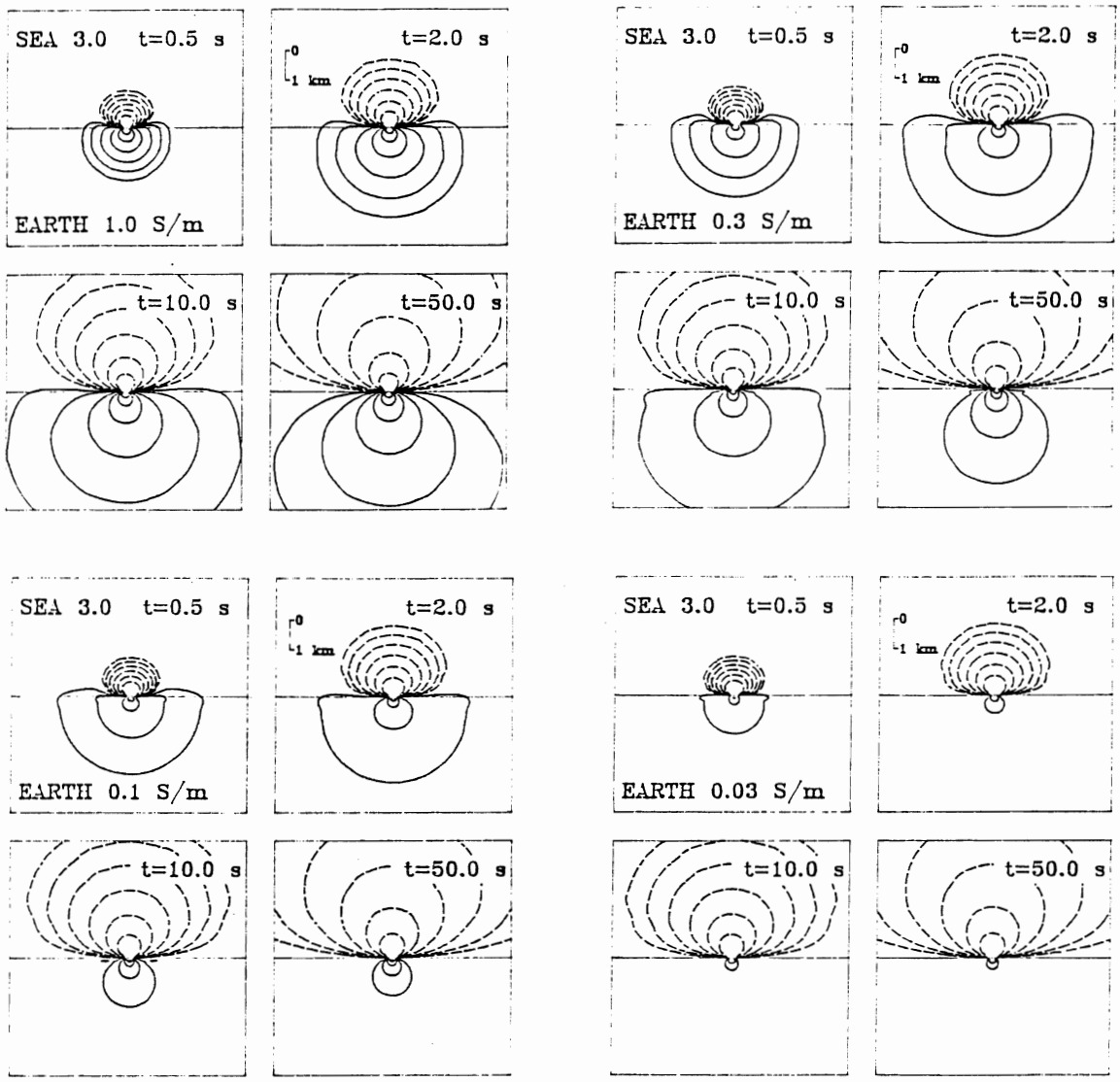

Fig.3.4 Transient double half–space solutions $B_y(x, z, t)$ to the H–polarization mode of Maxwell's equations for a range of electrical conductivity contrasts (a–d, clockwise from upper left, *i.e.* Fig.3.4*a* is the 2×2 block of contour plots in the upper left corner). Logarithmically spaced contours of the magnetic field, which is produced by a rapid switch–on of electric current in an extended dipole at time t=0, are plotted for each of the contrasts as a time sequence from 0.5–50 s to show the different rates of electromagnetic diffusion into the various conducting half–spaces.

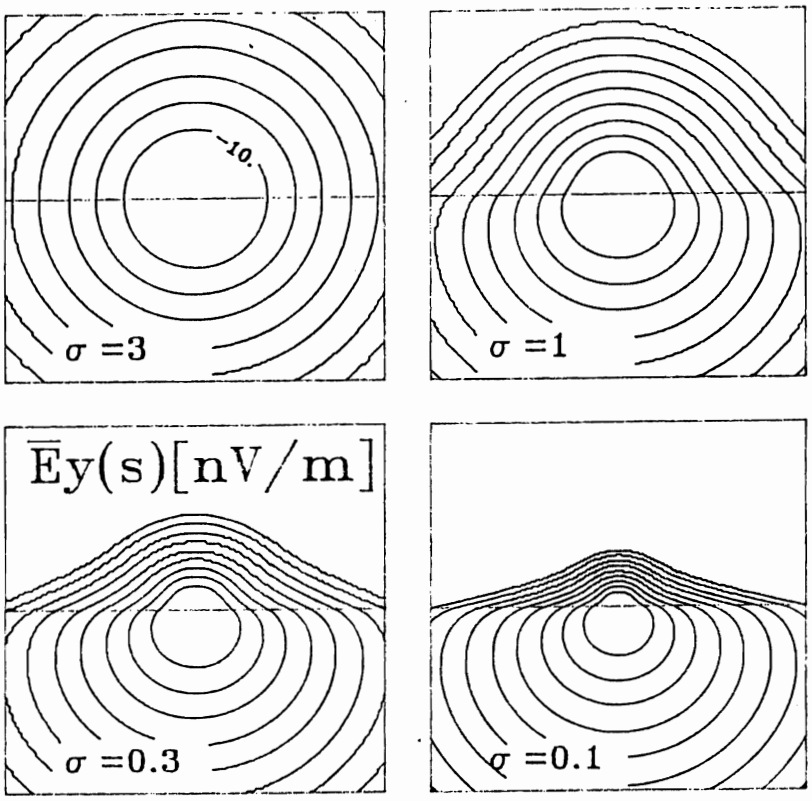

Fig.3.5 Laplace s–domain solution $\overline{E}_y(x, z, s)$ to the E–polarization mode of Maxwell's equations, for a fixed value of s=1 Hz. Logarithmically spaced contours, two per decade, of electric field are shown for various electrical conductivity contrasts between upper (σ=3.0 S/m) and lower conducting half–spaces. The field is produced by electric current flow in an infinite, insulated cable oriented perpendicular to the page, and is displayed to depths of 5 skin depths in the lower conductor. The contour lines in these plots are also equipotentials.

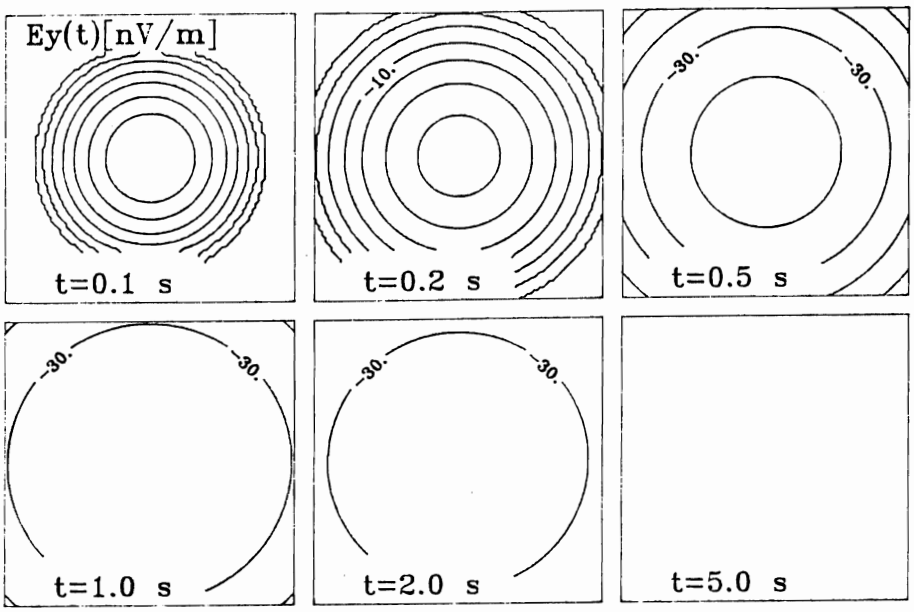

Fig.3.6 Contours of the E–polarization mode step response $E_y(t)$ show electromagnetic diffusion into the first 5 skin depths of a uniform conductor following a rapid switch–on of electric current at time t=0 in a unit moment, infinite insulated cable oriented perpendicular to the page. The contours are logarithmically spaced, two per decade. The electric field step response $E_y(t)$ vanishes at late time, since steady source currents produce only a magnetostatic field in conductors.

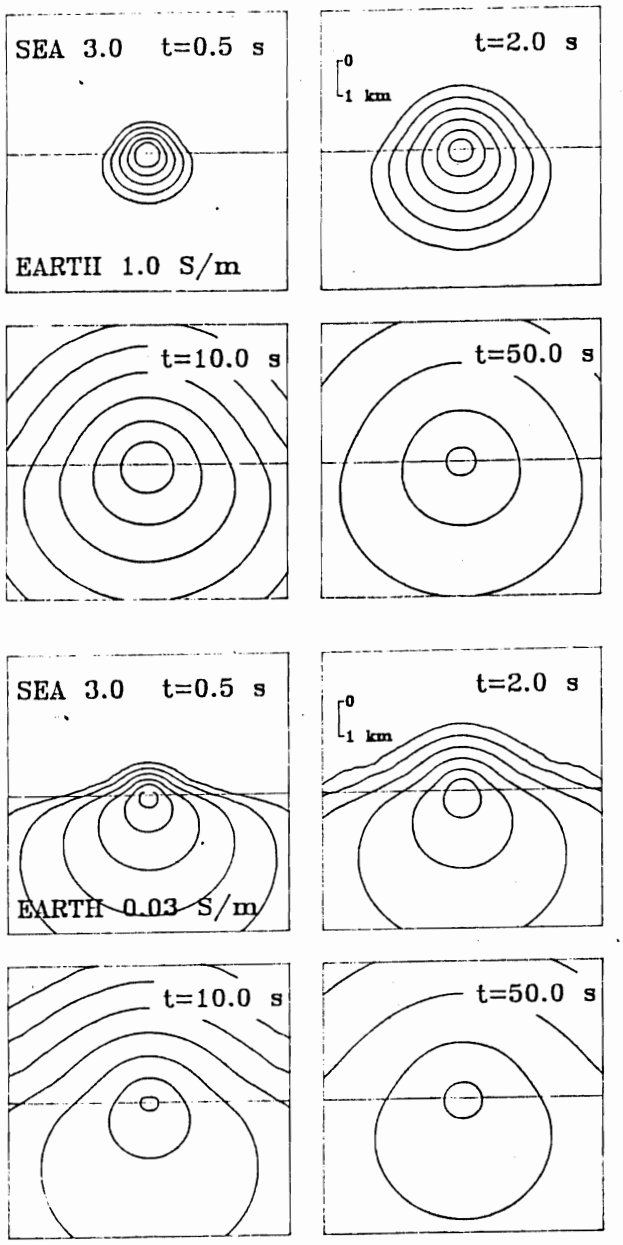

Fig.3.7 Transient double half–space solutions $E_y(x,z,t)$ to the E–polarization mode of Maxwell's equations for a pair of electrical conductivity contrasts (a–b, top to bottom, *i.e.* Fig.3.7*a* is the uppermost 2×2 block of contour plots). Logarithmically spaced contours of the electric field, which is produced by a rapid switch–on of electric current at time t=0 in an infinite, insulated cable oriented perpendicular to the page, are plotted for each contrast as a time sequence from 0.5–50 s to show the different rates of electromagetic diffusion into the various conducting half–spaces. At late times $E_y(x,z,t)$ becomes increasingly independent of the conductivity structure, and eventually vanishes.

Chapter 4

2D Numerical Modeling

4.0 Introduction

In the previous chapter I have shown that if the geo–electromagnetic model, which includes descriptions of the source and the earth geometry that it excites, is granted certain two dimensional symmetries, then the possibility arises for Maxwell's equations to break into one of two orthogonal modes. Specifically, a separation occurs if the applied current density $\mathbf{J}_S$ and the electrical conductivity $\sigma(\mathbf{r})$ are invariant along a common strike ($\hat{y}$) direction. For example, recall that the $\hat{x}$–directed extended electric dipole, as described in §3.4, energizing a 2–D structure $\sigma(x,z)$ excites the H–polarization mode of Maxwell's equations. Similarly, the infinite line source oriented along–strike, refer to §3.8, excites the E–polarization mode. Although these symmetries are entirely artificial and enforced on the model solely to lessen the computational burden, solutions to the governing scalar diffusion equations of either mode are in many cases useful as an aid to interpretation of field data, refer to Chapter 3 for more details. In this chapter, I will outline the development and implementation of a numerical method which solves, within a context of marine electromagnetics, boundary value problems based on the governing equations of the H–polarization and E–polarization modes. Using the resulting set of computer programs, I can evaluate the transient electromagnetic response of two–dimensional earth conductivity models $\sigma(x,z)$, especially ones which represent geological structures such as the mid–ocean ridge, that are of interest to the marine geophysics community. The newly accessible models can have much more complicated geometry than the double half–space and

they virtually never possess analytical solutions.

In the geophysical exploration literature, there have been several successful attempts to model numerically the E–polarization mode of Maxwell's equations. All of the attempts have been motivated by the need for software to interpret data from land–based controlled–source electromagnetic surveys. The earliest paper is due to Coggon (1971) who considered a line source with an oscillating current $I=I_0\exp(i\omega t)$. In the frequency domain, the E–polarization BVP that he solved is

$$\frac{\partial^2 \overline{E}_y(\omega)}{\partial x^2} + \frac{\partial^2 \overline{E}_y(\omega)}{\partial z^2} - \alpha^2 \overline{E}_y(\omega) = i\mu\omega \overline{J}_S^{\text{m.d.}}, \quad (x,z) \in \Omega \tag{4.1a}$$

$$\overline{E}_y(x_0, z_0, \omega) = 0, \quad (x_0, z_0) \in \partial\Omega, \ \omega > 0 \tag{4.1b}$$

where $\alpha=\sqrt{i\mu\sigma\omega + \mu\epsilon\omega^2}$. In this domain, the solution $\overline{E}_y(\omega)$ is complex and is related to the transient solution simply by the Fourier transform:

$$E_y(t) = \int_{-\infty}^{\infty} \overline{E}_y(\omega)\exp(i\omega t)\, d\omega. \tag{4.2}$$

Of more interest are the papers which solve the E–polarization problem directly in the time domain. The boundary value problem in this domain, when displacement currents are *not* neglected, is based on the damped wave equation:

$$\frac{\partial^2 E_y(t)}{\partial x^2} + \frac{\partial^2 E_y(t)}{\partial z^2} - \mu\sigma\frac{\partial E_y(t)}{\partial t} - \mu\epsilon\frac{\partial^2 E_y}{\partial t^2} = \mu\frac{\partial J_S^{\text{m.d.}}}{\partial t}, \quad (x,z) \in \Omega \tag{4.3a}$$

$$E_y(x_0, z_0, t) = 0, \quad (x_0, z_0) \in \partial\Omega, \ t > 0. \tag{4.3b}$$

The above problem was solved by Kuo and Cho (1980) using the finite element method. Later, Oristaglio and Hohmann (1984) used a finite difference method with a DuFort–Frankel explicit time–stepping scheme to solve the electromagnetic time–dependent diffusion equation, which is obtained from equation (4.3*a*) by setting the last term on the left hand side to zero, *i.e.* by invoking the quasi–static approximation described in §3.1. Goldman *et.al.* (1986) have used a finite element method with a Crank–Nicholson implicit scheme to solve the same problem. By incorporating an exact boundary condition on the air/earth interface these latter two authors

were able to avoid discretization of the upper non–conducting half–space, which was an improvement over the earlier efforts of Kuo and Cho. Included in the Oristaglio and Hohmann paper are color snapshots of the patterns of electromagnetic diffusion into simple two–dimensional conductivity models of the earth. Table 4.1 provides a summary of the previous work described above. There has to date been little interest in developing code specifically for interpretation of marine data in part because of the lack of commercial interest in seafloor mining. However, as indicated in Chapters 1 and 2, there is ample scientific motivation to develop such a code.

Table 4.1

Author(s)	Year	Mode		Domain		Method	
		H–pol.	E–pol.	time	frequency	FE	FD
Coggon	1971		√		√	√	
Kuo & Cho	1980		√	√		√	
Oristaglio & Hohmann	1984		√	√			√
Goldman *et.al.*	1986		√	√		√	

Instead of working directly in the time domain, I have chosen to model both the E–polarization and H–polarization modes in the Laplace domain, using the finite element method, and then transform the calculated field component into the time domain by means an inverse Laplace transform. The H–polarization BVP as formulated in the Laplace domain is:

$$\frac{\partial}{\partial x}\left[\frac{1}{\sigma}\frac{\partial \overline{B}_y(s)}{\partial x}\right] + \frac{\partial}{\partial z}\left[\frac{1}{\sigma}\frac{\partial \overline{B}_y(s)}{\partial z}\right] - \mu s \overline{B}_y(s) = \frac{\mu}{\sigma}\frac{\partial \overline{J}_S'^{\text{e.d.}}}{\partial z}, \quad (x,z) \in \Omega \tag{4.4a}$$

$$\overline{B}_y(x_0, z_0, s) = 0, \quad (x_0, z_0) \in \partial\Omega, \; s > 0 \tag{4.4b}$$

and the E–polarization BVP in the Laplace domain is:

$$\frac{\partial^2 \overline{E}_y(s)}{\partial x^2} + \frac{\partial^2 \overline{E}_y(s)}{\partial z^2} - \mu s \overline{E}_y(s) = \mu s \overline{J}_S'^{\text{m.d.}}, \quad (x,z) \in \Omega \tag{4.5a}$$

$$\overline{E}_y(x_0, z_0, s) = 0, \quad (x_0, z_0) \in \partial\Omega, \; s > 0. \tag{4.5b}$$

An advantage of formulating the boundary value problems in the Laplace domain becomes evident when a transient electromagnetic field component $B_y(t)$ or $E_y(t)$ is required to be known at only one or more prescribed "critical" times. In such cases, the Laplace formulation leads to a more efficient use of computer resources than does the direct time domain formulation since the former avoids the potential waste of effort associated with carefully time–stepping the field components from t=0. Using the Gaver–Stehfest inversion algorithm, which was introduced in §3.7, the transient field components evaluated at some prescribed time t_0 are simply linear combinations of several Laplace domain solutions, in accordance with equation (3.45).

4.1 Perturbed Boundary Value Problems

If the two–dimensional geometry is sufficiently simple, the representation of the applied current density J_S in terms of the Dirac delta function, as indicated in equations (3.19) and (3.49), permits analytic solutions of electromagnetic boundary value problems to be found everywhere in the solution domain Ω, despite the presence of singularities in the field components (B_y, E_y) at the points at which currents are applied. However, the same boundary value problem, when attacked numerically, is ill–posed. In order to make the numerical problem well–posed, the singularities must be avoided. This can be achieved if the BVP is represented in the computer in a slightly altered, or perturbed, form. In this section, I will discuss *perturbed* BVPs in general terms and in §4.2 describe a technique based on the finite element method which solves them. In §4.3 I will apply the theory to solve a perturbed version of the H–polarization BVP.

Consider the linear differential equation:

$$Lu(\mathbf{r}) = 0, \qquad \mathbf{r} \in \Omega \tag{4.6}$$

where L is an arbitrary linear partial differential operator. The function u which satisfies the PDE (4.6) is said to be its *classical* solution and is distinguished from a

weak solution that satisfies only

$$(Lu, v)_{\Omega} = 0 \tag{4.7}$$

for all admissible test functions $v(\mathbf{r})$ (Wait and Mitchell 1985). The notation $(\cdot, \cdot)$ refers to the Euclidean, or $\mathcal{L}_2$, inner product

$$(u, v)_{\Omega} = \int_{\Omega} uv \; d\mathbf{r}. \tag{4.8}$$

If it is known *a priori* that there are singularities in the solution u at a point or points within the solution domain Ω, it is advantageous to re–define the BVP by establishing a new solution domain Ω_{h} which is essentially the original domain Ω with a hole or holes cut into it to avoid the singularities. The resultant perturbed boundary value problem is based on the modified equation:

$$(Lu^{\mathrm{h}}, v)_{\Omega \mathrm{h}} = 0 \tag{4.9}$$

with $\Omega_{\mathrm{h}} \subset \Omega$. It is important to note that u and u^{h} are both *exact* solutions but to different problems. Suppose there is known to be only one singularity in the solution u, then the boundary of the new solution domain may be denoted by $\partial\Omega_{\mathrm{h}} = \partial\Omega_{\mathrm{h0}} + \partial\Omega_{\mathrm{h1}}$ where the outer boundary $\partial\Omega_{\mathrm{h0}} = \partial\Omega$ has not changed but $\partial\Omega_{\mathrm{h1}}$ is a new inner boundary which defines the hole in Ω_{h}. An example of a perturbed domain, showing typical locations of the inner and outer boundaries, is depicted in Figure 4.1*a*. Often, the boundary conditions are known precisely on $\partial\Omega$ but only approximately on $\partial\Omega_{\mathrm{h}}$.

Specializing for a moment to 2–D marine electromagnetic problems, the operator L in equation (4.9) is a scalar time–independent diffusion operator and u^{h} represents an electromagnetic field component. The solution u to equation (4.7) may contain singularities caused by applied currents but u^{h}, by construction, does not contain any singularities. The inner boundary $\partial\Omega_{\mathrm{h1}}$ immediately surrounds the point at which current is applied. Throughout the thesis, I assume that currents are applied at only one point and that the inner boundary can be placed sufficiently close to the applied

currents such that $u^{\mathbf{h}}(\mathbf{r}_1)$, $\mathbf{r}_1 \in \partial\Omega_{\mathbf{h}1}$ may be approximated by an analytic whole–space or double half–space expression depending on the conductivity adjacent to the source and is not affected by details of the over–all structure $\sigma(\mathbf{r} \gg \mathbf{r}_1)$.

4.2 Finite Element Solution of Perturbed BVPs

I now proceed to describing a finite element technique which solves a class of perturbed BVPs in two spatial dimensions. In §4.3 I will describe how the technique can be applied to solve numerically the H–polarization BVP. The first step is to partition the domain $\Omega_{\mathbf{h}}$, which is assumed to be polygonal, into a mesh of N_T triangles. Nodes, or discrete points within the domain at which the solution $u^{\mathbf{h}}$ is to be approximated, are to coincide with the vertices of the triangles. A solution $\tilde{u}$, which will be the finite element approximant of the exact solution $u^{\mathbf{h}}$, is sought with the form

$$\tilde{u} = \sum_{i=1}^{N} a_i \alpha_i(x, z). \tag{4.10}$$

In equation (4.10), α_i may be conveniently referred to as a basis function, and is associated with the i–th of N nodes, while a_i is an unknown coefficient.

Every basis function is represented, in turn, by a set of piecewise, two dimensional interpolating polynomials:

$$\alpha_i(x, z) = \sum_{\tau=1}^{N_T} \alpha_i^{\tau}(x, z), \quad i = 1, 2, ..., N. \tag{4.11}$$

In general, the polynomials $\{\alpha_i^{\tau}(x, z), i{=}1, ..., N, \tau{=}1, ..., N_T\}$ are of order m. Setting $m{=}1$ specifies a first order finite element method, setting $m{\geq}2$ yields higher order approximants but at the cost of increasing programming complexity. The interpolating polynomial $\alpha_i^{\tau}(x, z)$ is associated with both the i–th node and the τ–th triangle. With the choice $m{=}1$, the interpolation over each triangle is linear and is performed

over the τ–th triangle by a polynomial that is given by:

$$\alpha_i^\tau(x,z) = \begin{cases} \dfrac{\det\begin{pmatrix} 1 & x & z \\ 1 & x_j & z_j \\ 1 & x_k & z_k \end{pmatrix}}{\det\begin{pmatrix} 1 & x_i & z_i \\ 1 & x_j & z_j \\ 1 & x_k & z_k \end{pmatrix}}, & \text{if } (x,z) \in \Delta_\tau; \\ 0, & \text{otherwise,} \end{cases} \tag{4.12}$$

where Δ_τ denotes the interior of the τ–th triangle. The three vertices of this triangle are located at co–ordinates labelled (x_i, z_i), (x_j, z_j), (x_k, z_k) where consecutive indexing of the vertex co–ordinates is performed in a clockwise sense around the triangle as illustrated in Figure 4.1*b*. From equation (4.12) note that the interpolating polynomials possess the property that

$$\alpha_p^\tau(x_q, z_q) = \delta_{pq}, \qquad \forall\ p \in (i,j,k),\ q \in (i,j,k) \tag{4.13}$$

where δ_{pq} is the Kronecker delta function defined by

$$\delta_{pq} = \begin{cases} 1, & \text{if } p{=}q; \\ 0, & \text{otherwise.} \end{cases} \tag{4.14}$$

Equation (4.13) is the mathematical statement that an interpolating polynomial is zero at all of the nodes except at the node to which it is associated, in which case it is unity. From equation (4.11), which gives the relationship between the interpolating polynomials and the basis functions, it is found that the basis function α_i is zero at all nodes except at node i, in which case the basis function is equal to $\alpha_i{=}N_{i,T}{<}N_T$ where $N_{i,T}$ is the total number of triangles which have node i as a vertex. These triangles define the ***support*** of the i–th basis function.

I shall now describe how the finite element approximant $\tilde{u}$ is computed. Suppose that of the N nodes in the mesh there are $M{=}M_0{+}M_1$ boundary nodes. Let the

interior nodes be numbered by the sequence $\{1,2,...,N-M\}$, the M_0 nodes on the outer boundary by $\{N-M+1, N-M+2, ..., N-M_1\}$ and the M_1 nodes on the inner boundary by $\{N-M_1+1, N-M_1+2, ..., N\}$. This numbering scheme allows boundary nodes to be distinguished from interior nodes, which is important because boundary conditions can be used to determine certain coefficients of the FE approximant (4.10), even before equation (4.9) is solved. For example, since u^{h} vanishes on the outer boundary by virtue of equations similar to (4.4*b*) or (4.5*b*), it follows that the coefficients $a_i=0$, $i=N-M+1, ..., N-M_1$. Also, since u^{h} on the inner boundary is to be evaluated analytically, the coefficients associated with inner boundary nodes are known in advance. For convenience, these latter coefficients can be renamed to $a_j=b_j$, $j=N-M_1+1, ..., N$. When the boundary conditions are incorporated in the manner just described, the FE approximant (4.10) becomes

$$\tilde{u} = \sum_{i=1}^{N-M} a_i \alpha_i(x,z) + \sum_{j=N-M_1+1}^{N} b_j \alpha_j(x,z). \tag{4.15}$$

The finite element technique then consists of solving for $\tilde{u}$ the following set of equations:

$$(L\tilde{u}, \alpha_l)_{\Omega^{\mathrm{h}}} = 0 \quad l = 1, ..., N-M \tag{4.16}$$

where the test function $v(x,z)$ has been *chosen* to be a vector of length $N-M$, with each element of v being a basis function of the form (4.11), specifically

$$v_l = \alpha_l, \quad l = 1, 2, ..., N-M. \tag{4.17}$$

Although this choice for the test function does lead to a unique approximation of u^{h}, it is certainly not the only such choice.

4.3 Numerical Solution of the H–Polarization BVP

The H–polarization BVP, whose geophysical interpretation has been established in §3.5, is defined by the pair of equations:

$$\frac{\partial}{\partial x}\left[\frac{1}{\sigma}\frac{\partial \overline{B}_y(s)}{\partial x}\right] + \frac{\partial}{\partial z}\left[\frac{1}{\sigma}\frac{\partial \overline{B}_y(s)}{\partial z}\right] - \mu_0 s \overline{B}_y(s) = \frac{\mu_0}{\sigma}\frac{\partial \overline{J}_{\mathrm{S}}^{\mathrm{e.d.}}}{\partial z}, \quad (x,z) \in \Omega \tag{4.18}$$

$$\overline{B}_y(x_0, z_0, s) = 0, \qquad (x_0, z_0) \in \partial\Omega \tag{4.19}$$

where $\sigma(x, z)$ is arbitrary. In this section, I will apply the theory as developed in the previous two sections of this chapter towards solving a perturbed version of the boundary value problem given above.

Since it is assumed that the applied current described by the density $\overline{J}_S^{\text{e.d.}}$ occupies the origin, the field component $\overline{B}_y(s)$ is singular there. Therefore, in order to have a well–posed numerical problem I shall avoid this singularity by defining a perturbed solution domain over which the partial differential equation (4.18) is to be solved; a suitable choice for Ω_h is shown in Figure 4.1*c*. The perturbed BVP that results is defined by the following three equations:

$$\frac{\partial}{\partial x}\left[\frac{1}{\sigma}\frac{\partial \overline{B}_y^h(s)}{\partial x}\right] + \frac{\partial}{\partial z}\left[\frac{1}{\sigma}\frac{\partial \overline{B}_y^h(s)}{\partial z}\right] - \mu_0 s \overline{B}_y^h(s) = 0, \quad (x, z) \in \Omega_h \tag{4.20}$$

$$\overline{B}_y^h(x_0, z_0, s) = 0, \qquad (x_0, z_0) \in \partial\Omega_{h0} \tag{4.21}$$

$$\overline{B}_y^h(x_1, z_1, s) = \begin{cases} \overline{B}_y^{\text{ocean}}(x_1, z_1, s) \\ \overline{B}_y^{\text{earth}}(x_k, z_k, s) \end{cases} \qquad (x_1, z_1) \in \partial\Omega_{h1} \tag{4.22}$$

where $\overline{B}_y^{\text{ocean}}$ and $\overline{B}_y^{\text{earth}}$ are analytic solutions to the H–polarization double half–space problem and are given by equations (3.26) and (3.27) respectively. Note that in equation (4.20) there is no longer a source term involving $\overline{J}_S^{\text{e.d.}}$. In the finite element formulation, the point source is replaced by exact boundary data but only on the M_1 nodes of $\partial\Omega_{h1}$, as specified by equation (4.22). Elsewhere on $\partial\Omega_{h1}$, the function $\overline{B}_y^h$ is approximated by interpolating from the exact boundary data.

According to the expansion (4.15), the finite element approximant denoted by $\tilde{B}_y^h$ can be written as

$$\tilde{B}_y^h = \sum_{j=1}^{N-M} a_j \alpha_j(x, z) + \sum_{k=N-M_1+1}^{N} b_k \alpha_k(x, z) \tag{4.23}$$

where the set of coefficients $\{a_j,\ j{=}1,...,N-M\}$ are the unknowns of the problem and must be solved for. The coefficients that are known in advance are $\{b_k,\ k{=}N{-}M{+}1,...,N{-}M_1{+}1,...,N\}$ and they correspond to the boundary nodes:

$$b_k = 0, \quad (x_k, z_k) \in \partial\Omega_{\mathrm{h}0} \tag{4.24}$$

$$b_k = \overline{B}_y^{\mathrm{h}}(x_k, z_k), \quad (x_k, z_k) \in \partial\Omega_{\mathrm{h}1}. \tag{4.25}$$

In equation (4.25), $\overline{B}_y^{\mathrm{h}}$ is given by equation (4.22). Substituting the finite element approximant $\tilde{B}_y^{\mathrm{h}}$ given by equation (4.23) into the set of equations (4.16) gives

$$(L\tilde{B}_y^{\mathrm{h}}, \alpha_l)_{\Omega\mathrm{h}} = 0, \quad l = 1,..,N-M \tag{4.26}$$

where the scalar time–independent diffusion operator L is:

$$L = \frac{\partial}{\partial x}\left(\frac{1}{\sigma}\frac{\partial}{\partial x}\right) + \frac{\partial}{\partial z}\left(\frac{1}{\sigma}\frac{\partial}{\partial z}\right) - \mu_0 s. \tag{4.27}$$

Equation (4.26) represents a set of $N{-}M$ equations, the l–th equation of which is:

$$\sum_{j=1}^{N-M} a_j (L\alpha_j, \alpha_l)_{\Omega\mathrm{h}} = -\sum_{k=N-M_1+1}^{N} \overline{B}_y^{\mathrm{h}}(x_k, z_k)(L\alpha_k, \alpha_l)_{\Omega\mathrm{h}}. \tag{4.28}$$

To simplify notation let the element Γ_{jl} of a matrix $\mathbf{\Gamma}$ be:

$$\Gamma_{jl} = (L\alpha_j, \alpha_l)_{\Omega\mathrm{h}} \tag{4.29}$$

and the element g_l of a vector $\mathbf{g}$ be:

$$g_l = -\sum_{k=N-M_1+1}^{N} \overline{B}_y^{\mathrm{h}} \Gamma_{kl} \tag{4.30}$$

so that equation (4.26) can be re–written in the following matrix form:

$$\mathbf{\Gamma a} = \mathbf{g}. \tag{4.31}$$

The above matrix equation is to be solved for the vector **a** which by virtue of the Kronecker delta relationship (4.13) has elements

$$a_i = \tilde{B}_y^{\mathrm{h}}(x_i, z_i), \quad (x_i, z_i) \in \Omega_{\mathrm{h}} \tag{4.32}$$

i.e. the desired solution at node i. Hence the coefficients $\{a_i\}$ are identical to values of the finite element approximant $\tilde{B}_y^{\mathrm{h}}$ as interpolated at the nodes.

The inner product that appears in matrix element Γ_{jl}, equation (4.29), can written in simple form using Green's Theorem, which in two dimensions is:

$$\int\int_{\Omega} u\frac{\partial v}{\partial x}\,dx\,dz = \oint_{\partial\Omega} uv\,dz - \int\int_{\Omega} \frac{\partial u}{\partial x} v\,dx\,dz \tag{4.33}$$

The first term of the inner product in equation (4.29), with the operator L given by equation (4.27), is re–cast as

$$\left(\frac{\partial}{\partial x}\left[\frac{1}{\sigma}\frac{\partial \alpha_j}{\partial x}\right], \alpha_l\right)_{\Omega \mathrm{h}} = \oint_{\partial\Omega \mathrm{h}} \frac{1}{\sigma}\alpha_l \frac{\partial \alpha_j}{\partial x}\,dz - \left(\frac{1}{\sigma}\frac{\partial \alpha_j}{\partial x}, \frac{\partial \alpha_l}{\partial x}\right)_{\Omega \mathrm{h}}. \tag{4.34}$$

The first term in the RHS of equation (4.34) vanishes since node l is an interior node and its associated basis function α_l is being evaluated only at the boundary nodes along $\partial\Omega_{\mathrm{h}}$. To verify the above assertion, recall the statement made following equation (4.14). With the first term of the RHS of equation (4.34) removed, the inner product that is left contains only first order spatial derivatives of the basis functions. Therefore, the matrix element Γ_{jl} of equation (4.29) becomes, after Green's Theorem has been applied to the first and second terms of the inner product in equation (4.29):

$$\Gamma_{jl} = -\left(\frac{1}{\sigma}\frac{\partial \alpha_j}{\partial x}, \frac{\partial \alpha_l}{\partial x}\right)_{\Omega \mathrm{h}} - \left(\frac{1}{\sigma}\frac{\partial \alpha_j}{\partial z}, \frac{\partial \alpha_l}{\partial z}\right)_{\Omega \mathrm{h}} - \mu_0 s(\alpha_j, \alpha_l)_{\Omega \mathrm{h}}. \tag{4.35}$$

The applicability of Green's Theorem to the evaluation of the inner products, besides simplifying the expression for Γ_{jl}, also is the reason why the basis functions are allowed to be linear in x and z in the first place even though the operator L contains second order spatial derivatives. Thus, the quantity $L\alpha_j$, which is a second order derivative

of a linear function, need not exist everywhere in Ω in order to evaluate the inner product $(L\alpha_j, \alpha_l)_\Omega$.

To summarize this section, the idea is to solve the linear system $\mathbf{\Gamma a}=\mathbf{g}$ where the elements of the matrix $\mathbf{\Gamma}$ are given by equation (4.35) and the elements of the RHS vector $\mathbf{g}$ are given by equation (4.30) with the set of coefficients $\{b_k,\ k=N-M_1+1, ..., N\}$ known *a priori*, see equations (4.24) and (4.25). The solution vector is $\mathbf{a}$ and its elements are identically the finite element approximant $\tilde{B}_y^{\mathrm{h}}(s)$ at the interior nodes, according to equation (4.32). If the finite element approximant is computed at the n values of the Laplace frequency s given by $\{s_j=j\ln 2/t,\ j=1,2, ..., n\approx 8\}$ in accordance with the Gaver–Stehfest requirements, see equation (3.45), than an approximation for $B_y(t)$ in the time domain may be evaluated using

$$B_y(t) \approx \frac{\ln 2}{t} \sum_{j=1}^{n} V_j(n) \tilde{B}_y^{\mathrm{h}} \left(\frac{j \ln 2}{t} \right). \tag{4.36}$$

The above is referred to as a FE–Gaver–Stehfest formula.

4.4 Computational Aspects

The matrix elements $\{\Gamma_{jl},\ j, l=1, ..., N-M\}$ are given in equation (4.35) in terms of inner products over the perturbed solution domain Ω_{h}. I will show in §4.4 that these inner products are analytic when linear interpolating polynomials of the form (4.12) are used over a triangular partition of Ω_{h}. For example, the inner product of two interpolating polynomials appears in the expression for Γ_{jl}. It can be re–written as:

$$(\alpha_j, \alpha_l)_{\Omega \mathrm{h}} = \int_{\Omega \mathrm{h}} \alpha_j \alpha_l \, dx \, dz = \sum_{\tau} \int_{\Delta_\tau} \alpha_j^\tau \alpha_l^\tau \, dx \, dz, \tag{4.37}$$

where use has been made of equation (4.11). Using the following quadrature formula which is *exact* for integration of arbitrary linear functions $f(x, z)$ over a triangular region Δ_τ:

$$\int_{\Delta_\tau} f(x,z) \, dxdz = \frac{A_\tau}{3} \left[f(x_i, z_i) + f(x_j, z_j) + f(x_k, z_k) \right], \tag{4.38}$$

I obtain a desired analytic result:

$$(\alpha_j, \alpha_l)_{\Omega h} = \sum_{\tau} \frac{A_\tau}{3} \delta_{jl}. \tag{4.39}$$

In the above equations, A_τ is the area of the τ–th triangle and the vertices of this triangle are at the co–ordinates (x_i, z_i), (x_j, z_j), (x_k, z_k).

Similarly, analytic expressions are available for the other inner products comprising Γ_{jl}, but only provided the electrical conductivity of each triangle in the mesh is kept constant with respect to x and z. If the discretization of Ω_h is sufficiently fine, keeping the electrical conductivity constant over each element does not preclude modeling complex geological structures. The starting point is

$$\left(\frac{1}{\sigma}\frac{\partial \alpha_j}{\partial x}\frac{\partial \alpha_l}{\partial x}\right)_{\Omega h} = \sum_{\tau} \frac{1}{\sigma_\tau} \int_{\Delta_\tau} \frac{\partial \alpha_j^\tau}{\partial x}\frac{\partial \alpha_l^\tau}{\partial x}\, dx\, dz \tag{4.40}$$

where σ_τ is the electrical conductivity assigned to the τ–th triangle and again use has been made of equation (4.11). Since the interpolating polynomials are linear, the terms under the integral in equation (4.40) are both independent of x and z, therefore they may be brought outside the integration. There results:

$$\left(\frac{1}{\sigma}\frac{\partial \alpha_j}{\partial x}, \frac{\partial \alpha_l}{\partial x}\right)_{\Omega h} = \sum_{\tau} \frac{A_\tau}{\sigma_\tau}\frac{\partial \alpha_j^\tau}{\partial x}\frac{\partial \alpha_l^\tau}{\partial x} \tag{4.41}$$

which is analytic.

Since all the inner products in equation (4.35) may be evaluated analytically, none of the elements of the matrix $\mathbf{\Gamma}$ or the vector $\mathbf{g}$ in the finite element linear system $\mathbf{\Gamma a}=\mathbf{g}$ need to be evaluated with the aid of *numerical* quadrature. Inserting the analytic expressions (4.39) and (4.41) for the inner products of Γ_{jl} back into the original equation (4.35) gives the result:

$$\Gamma_{jl} = -\sum_{\tau} \frac{A_\tau}{\sigma_\tau}\left[\frac{\partial \alpha_j^\tau}{\partial x}\frac{\partial \alpha_l^\tau}{\partial x} + \frac{\partial \alpha_j^\tau}{\partial z}\frac{\partial \alpha_l^\tau}{\partial z} + \frac{\mu_0 \sigma_\tau s}{3}\delta_{jl}\right]. \tag{4.42}$$

From equations (4.42) and (4.12) it is apparent that Γ_{jl} is non–zero only if $j=l$ or if the nodes j and l share common triangles, *i.e.* the basis functions α_j and α_l

have overlapping support. By ordering the nodes in such a way that nodes sharing common triangles are ordered as close as possible to one another, the bandwidth β of the matrix $\mathbf{\Gamma}$ is kept to a minimum. This is important when it is considered that the solution time of the linear system $\mathbf{\Gamma a}=\mathbf{g}$ using band Gaussian elimination is $O[\beta^2(N-M)]$. In addition, the amount of storage required for this algorithm is $O[\beta(N-M)]$. The implementation of the finite element technique described in this chapter uses a band Gaussian elimination routine from the NAG (1983) mathematics software library. The implementation also includes a slightly modified version of the mesh generator TRIMESH written by Travis (1987). This software, once the piecewise constant electrical conductivity $\sigma(x,z)$ and the domain Ω_{h} are specified, automatically partitions Ω_{h} into triangular elements and orders the nodes so as to minimize the bandwidth of $\mathbf{\Gamma}$.

4.5 Convergence of Approximation

When applying a numerical method towards solving a perturbed BVP, two distinct types of errors are encountered. The *approximation error* is $||u-\tilde{u}||$ and the *perturbation error* is $||u-u^{\mathrm{h}}||$ where the notation $||\cdot||$ refers to an arbitrary vector norm. A finite element solution is optimal if the perturbation error is of greater order in h than the approximation error. The perturbation error is caused by any combination of numerical quadrature of the inner products, interpolated boundary conditions and boundary approximation. Since the inner products associated with the finite element formulation of the H–polarization problem may all be evaluated exactly, see §4.4, only "boundary perturbations" contribute to its perturbation error. Although there have been few if any theoretical bounds placed on the perturbation errors for solutions of open boundary problems which contain one or more singularities, *e.g.* controlled–source electromagnetic boundary value problems, the following related error estimate

(Wait and Mitchell 1985) is of interest. Consider the model elliptic problem

$$\frac{\partial^2 u}{\partial x^2} + \frac{\partial^2 u}{\partial z^2} + f(x,z) = 0, \quad (x,z) \in \Omega \tag{4.43a}$$

$$u = 0, \quad (x,z) \in \partial\Omega. \tag{4.43b}$$

The perturbation error for this problem is $||u - u^{\mathrm{h}}||{=}O(h^{3/2})$ if Ω_{h} is a polygon inscribed within Ω. The corresponding approximation error on Ω_{h} is $||u - \tilde{u}||{=}O(h)$ for linear interpolating polynomials on a triangular partition. The parameter h, which is a measure of triangle size, may be interpreted as follows. Consider a mesh composed of triangles of size h. If the mesh is made finer by sub–division of every triangle into four via the creation of new nodes at the mid–points of the element edges, then the triangles of the new mesh are of size $h/2$ (see Figure 4.1*d*). For the model problem, which does not suffer from boundary perturbations due to interpolated boundary conditions, it is also assumed that

$$\lim_{h \to 0} \Omega_{\mathrm{h}} = \Omega. \tag{4.44}$$

The perturbed H–polarization problem, which is defined by equations (4.20–4.22), on the other hand suffers from both types of boundary perturbations, *i.e.* interpolated boundary conditions and boundary approximation. In addition, the limit (4.44) does not hold. Therefore, the error bounds described above for the model problem suggest that the perturbation error for the H–polarization problem is *at best*

$$||\overline{B}_y - \overline{B}_y^{\mathrm{h}}|| = O(h^{3/2}) \tag{4.45}$$

and that with a triangular partition and linear interpolating polynomials the approximation error is at best

$$||\overline{B}_y - \tilde{B}_y^{\mathrm{h}}|| = O(h). \tag{4.46}$$

Recall once again that $\overline{B}_y$ is the exact solution on Ω, $\overline{B}_y^{\mathrm{h}}$ is the exact solution on the perturbed domain Ω_{h} and $\tilde{B}_y^{\mathrm{h}}$ is the FE approximant on Ω_{h}. To study convergence

as a function of triangle size h, the perturbed BVP (4.20–4.22) has been solved on a sequence of progressively finer meshes. A fine mesh, characterized by triangles of size $h/2$, is generated from a coarser one of size h, by dividing every triangle into four smaller ones, joining the mid–points of its edges, as in Figure 4.1*d*.

Define the percent relative error on each node of a mesh of size h containing N nodes as

$$\varepsilon^{\mathrm{h}}(x_i, z_i) = 100 \frac{|\overline{B}_y(x_i, z_i) - \tilde{B}_y^{\mathrm{h}}(x_i, z_i)|}{|\overline{B}_y(x_i, z_i)|}, \quad i = 1, 2, ..., N. \tag{4.47}$$

Figure 4.2*a* shows contours of the percent relative error ε^{h} on a mesh of N=736 nodes as a function of position in the lower half–space of a double half–space conductivity model with a 3:1 conductivity contrast. The seafloor z=0 lies along the top of the figure, the 2–D extended dipole source occupies the upper left corner, and the boundary of the figure is a square whose sides are of length one Laplace domain skin depth, *i.e.* the boundary is $1\delta_1^s \times 1\delta_1^s$ in the x/z–plane. The errors are evaluated based on comparing the output from the finite element program with the analytic solution to the unperturbed problem, equation (3.27). The percent relative error on the mesh of size $h/2$, which contains $2880 \approx 4N$ nodes, decreases everywhere by a factor of two, see Figure 4.2*b*. On the finest mesh, which is of size $h/4$ and contains $11392 \approx 16N$ nodes, the decrease in the error is an additional factor of two, see Figure 4.2*c*. Thus:

$$\varepsilon_i^{\mathrm{h}/4}(x_i, z_i) = \frac{1}{2}\varepsilon_i^{\mathrm{h}/2}(x_i, z_i) = \frac{1}{4}\varepsilon_i^{\mathrm{h}}(x_i, z_i) \tag{4.48}$$

for almost all i=1, 2, ..., N with exception near the corners of $\partial\Omega_{\mathrm{h}}$. At these locations, the full rate of convergence is not achieved due to the presence of singularities that occur in solutions to elliptic equations near the corners of non–smooth domains (*e.g.* Johnson 1987). The results elsewhere, *i.e.* equation (4.48), imply that $\varepsilon^{\mathrm{h}} = O(h)$, in accordance with equation (4.45), and that the relative error on the mesh of size $h/4$ obeys $\varepsilon \approx 2.5\%$. The $O(h)$ empirical relationship as illustrated by Figures 4.2*a–c* is a strong indicator that the implementation of the finite element technique as described in this chapter is optimal.

4.6 Towards Mesh Optimization

The errors associated with the finite element solution of the H–polarization problem, like those of any boundary value problem, depend on the mesh structure, especially some aspects of it which are under the programmer's control. I have developed, after much trial and error, a set of four mesh parameters which, when input to the mesh generator TRIMESH (Travis 1987), completely specify the mesh structure. The set includes *a*) the geometric spacing g of the nodes, *b*) the total number of nodes N in the mesh, *c*) the distance d_1 of the inner boundary $\partial\Omega_{h1}$ from the point where $\overline{B}_y$ is singular and *d*) the position d_0 of the outer boundary $\partial\Omega_{h0}$ with respect to the singularity. Clearly, only three of these parameters are free. In §4.6 I will determine a set of values for the mesh parameters (g, d_0), keeping N fixed, that minimizes a prescribed error criterion on solutions to the H–polarization double half–space problem. While no attempt is made to find universal values for the mesh parameters, which is highly problem dependent, the results from this section may be viewed as a step towards mesh optimization for the double half–space problem. Before proceeding, note that logarithmic spacing of the nodes is desirable since the field component $\overline{B}_y$ decays exponentially with range from its source.

Some examples of meshes generated with different values of the node spacing factor g satisfying $1.1<g<2.4$ are shown in Figures 4.3*a–d*. To show clearly the differences in the mesh structure when g is changed, the position d_0 of the outer boundary and the number of nodes N are kept the same for each mesh. This, in turn, forces the position d_1 to depend on g. The sample mesh with g=1.5 shown in Figure 4.3*b* contains far fewer nodes but is otherwise identical in structure to the mesh of size h which was described in §4.5 and employed to estimate the convergence of the finite element approximation.

Consider the following "seafloor" error indicator:

$$||\varepsilon|| = \sum_{i=1}^{N} \begin{cases} \varepsilon^{\mathrm{h}}(x_i, z_i), & \text{if } z_i{=}0; \\ 0, & \text{otherwise,} \end{cases} \tag{4.49}$$

where the quantity $\varepsilon^{\mathrm{h}}(x_i, z_i)$ is given by equation (4.47). This indicator provides a measure of how accurate the approximation $\tilde{B}_y^{\mathrm{h}}$ is at nodes that are on the interface $z{=}0$ between the upper and lower half–spaces. Minimization of the indicator $||\varepsilon||$ given by equation (4.49) seems a reasonable criterion by which to optimize the mesh in view of the fact that magnetic field measurements are normally made by instruments deployed on the seafloor. Figure 4.4 shows the dependence of the indicator (4.49) on the position d_1 of $\partial\Omega_{\mathrm{h}1}$ and the geometric spacing factor g. The minimum of each curve correponds to the optimal position of the inner boundary, at least as far as minimizing the seafloor error indicator is concerned. Plotting d_1 in units of skin depths removes from $||\varepsilon||$ its dependence on the Laplace frequency s. The best results are obtained when the set of input parameters ($g{=}1.5$, $d_1{=}\ 0.1\delta_1^s$) is chosen. As a final word on mesh optimization, it is up to the programmer to determine the criteria by which he wishes to optimize his mesh. The decision could be based, for example, on the minimization of error at locations where actual measurements are likely to be made.

4.7 Numerical Solution of the E–Polarization BVP

To complete Chapter 4, I will briefly describe how the numerical method described earlier in this chapter is modified to solve a boundary value problem based on the E–polarization mode of Maxwell's equations as it is excited by an infinite line source oriented along–strike of a two–dimensional structure $\sigma(x, z)$. The governing equations, as formulated in §3.8, are

$$\frac{\partial^2 \overline{E}_y(s)}{\partial x^2} + \frac{\partial^2 \overline{E}_y(s)}{\partial z^2} - \mu s \overline{E}_y(s) = \mu s \overline{J}_{\mathrm{S}}^{\mathrm{im.d.}}, \quad (x, z) \in \Omega \tag{4.50}$$

$$\overline{E}_y(x_0, z_0, s) = 0, \quad (x_0, z_0) \in \partial\Omega, \ s > 0. \tag{4.51}$$

As was the case with the H–polarization governing partial differential equation, the applied current density $\overline{J}'$ in equation (4.50) causes a singularity in the along–strike field component $\overline{E}_y(s)$ at the co–ordinate origin. Therefore, to have a well–posed numerical problem, the domain Ω_h illustrated in Figure 4.1*c* is again chosen. The perturbed version of the E–polarization problem is defined on Ω_h as follows:

$$\frac{\partial^2 \overline{E}_y^h(s)}{\partial x^2} + \frac{\partial^2 \overline{E}_y^h(s)}{\partial z^2} - \mu\sigma s \overline{E}_y^h = 0, \quad (x,z) \in \Omega_h \tag{4.52}$$

$$\overline{E}_y^h(x_0, z_0, s), \quad (x_0, z_0) \in \partial\Omega_{h0} \tag{4.53}$$

$$\overline{E}_y^h(x_1, z_1, s) = \begin{cases} \overline{E}_y^{ocean}(x_1, z_1 \geq 0, s) \\ \overline{E}_y^{earth}(x_1, z_1 \leq 0, s) \end{cases} \quad (x_1, z_1) \in \partial\Omega_{h1} \tag{4.54}$$

where $\overline{E}_y^{ocean}(s)$ and $\overline{E}_y^{earth}(s)$ are analytic solutions to the E–polarization double half–space problem and are given by equation (3.53) and (3.54) respectively.

The domain Ω_h is partitioned into a mesh of triangles upon which basis functions of the form (4.11) and linear interpolating polynomials are defined. Writing the finite element approximant $\tilde{E}_y^h$ to the exact solution $\overline{E}_y^h$ in the form (4.23), the terms in the finite element linear system $\mathbf{\Gamma a = g}$ that corresponds to the perturbed E–polarization problem (4.52–4.54) have the elements:

$$\Gamma_{jl} = -\sum_\tau A_\tau \left[\frac{\partial \alpha_j^\tau}{\partial x}\frac{\partial \alpha_l^\tau}{\partial x} + \frac{\partial \alpha_j^\tau}{\partial z}\frac{\partial \alpha_l^\tau}{\partial z} + \frac{\mu\sigma_\tau s \delta_{jl}}{3} \right], \quad j,l = 1,2,...,N-M \tag{4.55}$$

$$a_i = \tilde{E}_y^h(x_i, z_i), \quad i = 1,2,...,N-M \tag{4.56}$$

$$g_l = -\sum_{k=N-M_1+1}^{N} \overline{E}_y^h(x_k, z_k)\Gamma_{kl}, \quad l = 1,2,...,N-M. \tag{4.57}$$

This linear system may then be solved by making the small necessary modifications to the finite element code that solved the H–polarization problem.

The convergence as a function of triangle size h of the approximation error $||\overline{E}_y - \tilde{E}_y^h||$ is $O(h)$. This was established by comparing output from the finite element program run on the sequence of progressively finer meshes described in §4.5 with the

appropriate analytic solution to the unperturbed problem, equation (3.54). Figure 4.5 shows contours of the percent relative error $\varepsilon^{h/4}$ when the numerical problem is solved on the finest mesh of 11392 nodes. The 2–D line source occupies the top left corner of the plot, which is one square skin depth δ_1^s in the x/z plane of the lower half–space of a double half–space conductivity model with 3:1 contrast. The quantity $\varepsilon^{h/4}$ is defined on the i–th node by:

$$\varepsilon^{h/4}(x_i, z_i) = 100 \frac{|\overline{E}_y(x_i, z_i) - \tilde{E}_y^h(x_i, z_i)|}{|\overline{E}_y(x_i, z_i)|}, \quad i = 1, 2, ..., \approx 16N. \tag{4.58}$$

The percent relative error obeys $\varepsilon^{h/4} \approx 1.3\%$ almost everywhere on the mesh with exception once again near the corners of $\partial\Omega_{h1}$.

References

Coggon, J.H., 1971. Electromagnetic and electrical modeling by the finite element method, *Geophysics*, **36**, 132–155.

Goldman, Y., C. Hubans, S. Nicoletis and S. Spitz, 1986. A finite–element solution for the transient electromagnetic response of an arbitrary two–dimensional resistivity distribution, *Geophysics*, **51**, 1450–1461.

Johnson, C., 1987. *Numerical Solution of Partial Differential Equations by the Finite Element Method*, Cambridge University Press, Cambridge, U.K.

Kuo, J.T. and D.H. Cho, 1980. Transient time–domain electromagnetics, *Geophysics*, **45**, 271–291.

NAG, 1983. The band LU factorization F01LBF and band triangular solver F04LDF subroutines are described in: *FORTRAN Library Manual, Mark 10*, Numerical Algorithms Group, Oxford, UK.

Oristaglio, M.L. and G.W. Hohmann, 1984. Diffusion of electromagnetic fields into a two–dimensional earth: a finite–difference approach, *Geophysics*, **49**, 870–894.

Travis, B.J., 1987. TRIMESH: an automatic mesh generator for finite element programs, unpublished sofware.

Wait, R. and A.R. Mitchell, 1985., *Finite Element Analysis and Applications*, John Wiley & Sons Ltd., Chichester, UK.

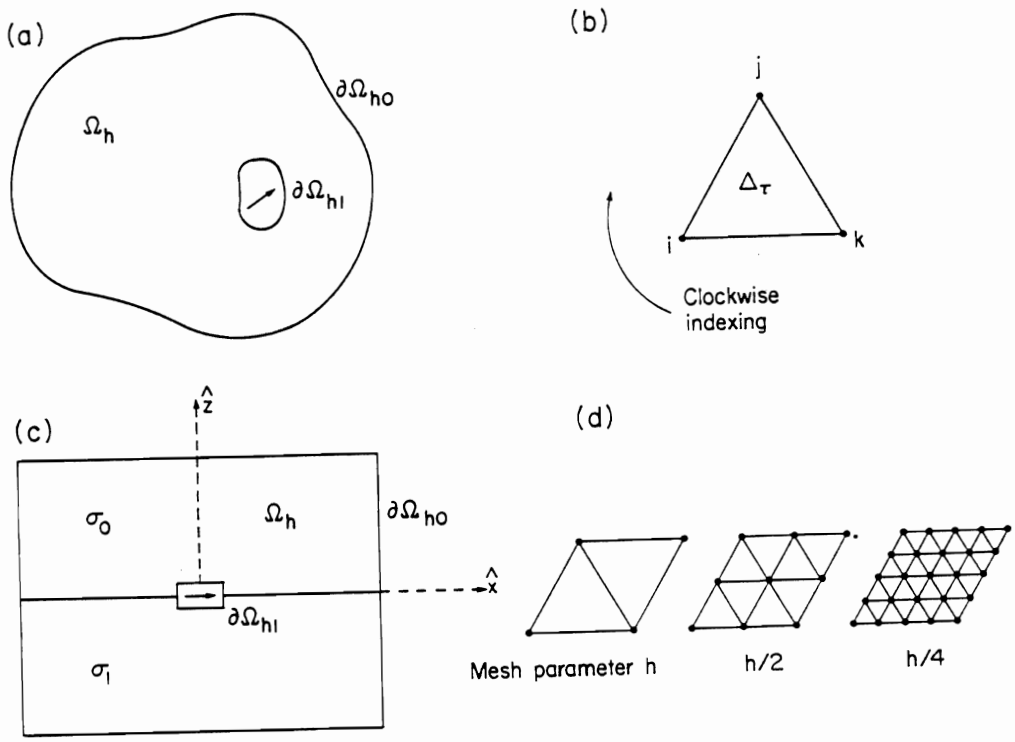

Fig.4.1 Schematic diagram of a perturbed domain Ω_h over which the electromagnetic diffusion equations may be solved numerically (a). Locations of the outer boundary $\partial\Omega_{h0}$ and inner boundary $\partial\Omega_{h1}$, which encloses the source, are shown. The domain Ω_h is divided into triangles, or finite elements. A polynomial associated with the i–th node, or vertex, performs linear interpolation over the τ–th triangle. A consistent scheme to keep track of the vertex co–ordinates is required, *e.g.* clockwise indexing (b). A solution domain appropriate for the H–polarization boundary value problem, in this case a double half–space electrical conductivity structure is being modeled, is shown in (c). Numerical solutions become progressively more accurate as the discretization of the mesh becomes finer. A fine mesh, characterized by triangles of size $h/2$, is generated from a coarser one of size h, by dividing every triangle into four smaller ones, as illustrated for a single triangle in (d). An mesh of size $h/4$ is also shown.

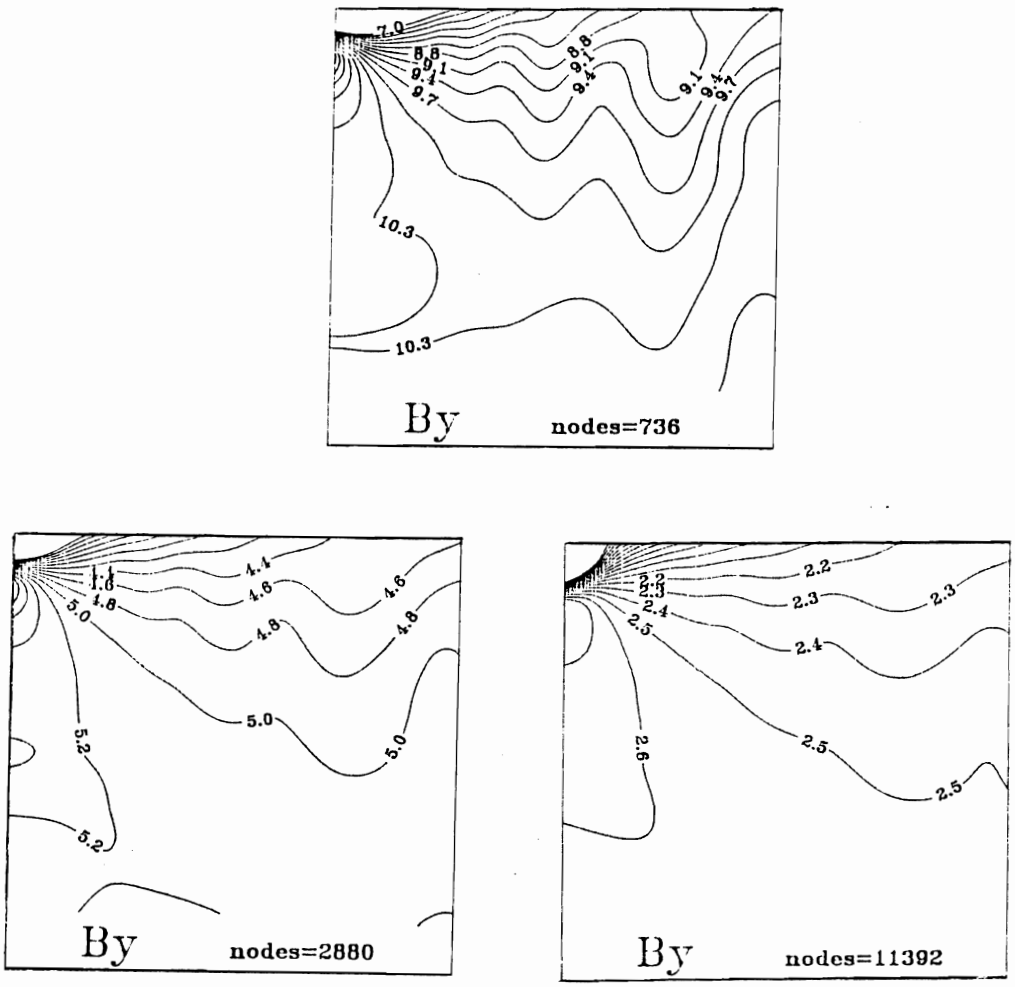

Fig.4.2 Contours of the percent relative error $\epsilon(x, z)$ on finite element meshes with triangles characterized by size h (a, top), $h/2$ (b, bottom left) and $h/4$ (c, bottom right) in the numerical solution to the H–polarization double half–space problem described in §3.5. The conductivity contrast is 3:1 and s=1 Hz. The errors are computed by comparing the output from the 2–D finite element forward modeling code against the analytical solution. The decrease in errors with mesh size h is consistent with an $O(h)$ convergence. The 2–D extended dipole transmitter occupies the top left corner of each plot, while the seafloor is along the top.

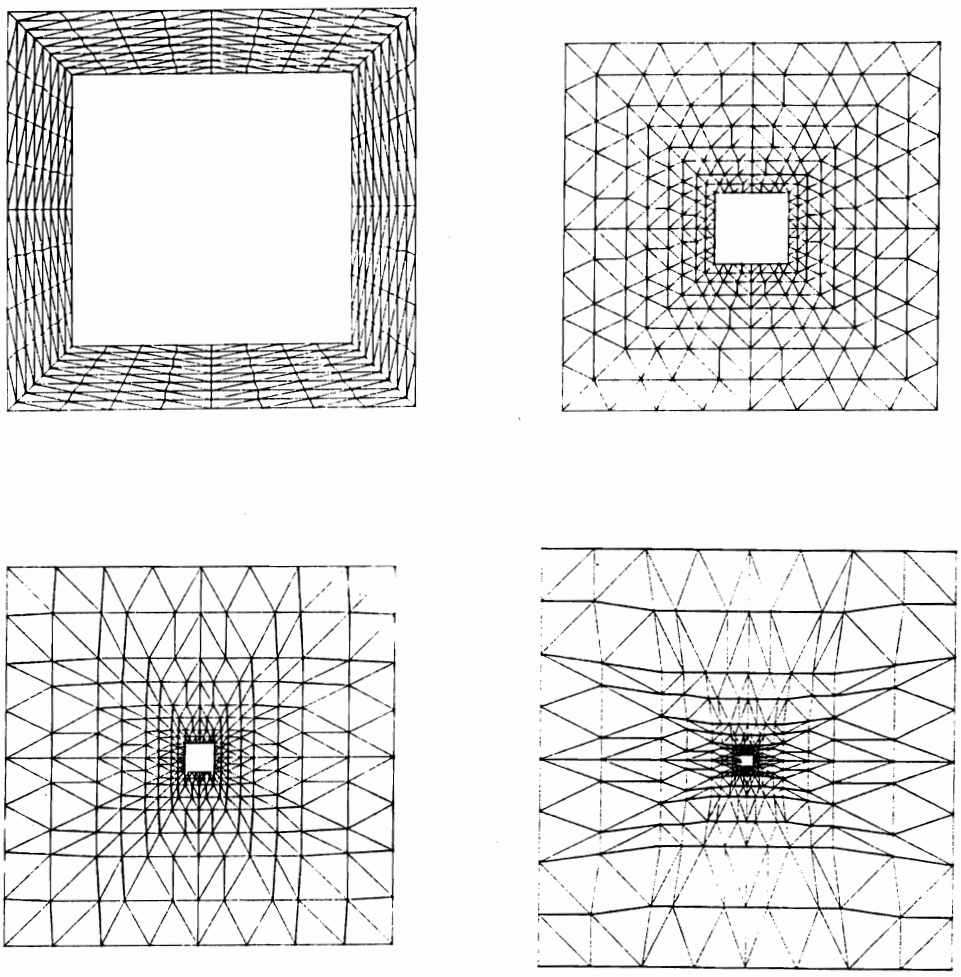

Fig.4.3 Sample finite element meshes generated with a fixed number of nodes but different values of a geometric spacing factor g ranging from 1.1 (a, top left) to 2.4 (d, bottom right). The factor g measures the increasing distance between nodes with increasing distance from the source, which is located in the central cut–out of the mesh. The accuracy of a finite element approximation depends greatly on the mesh structure.

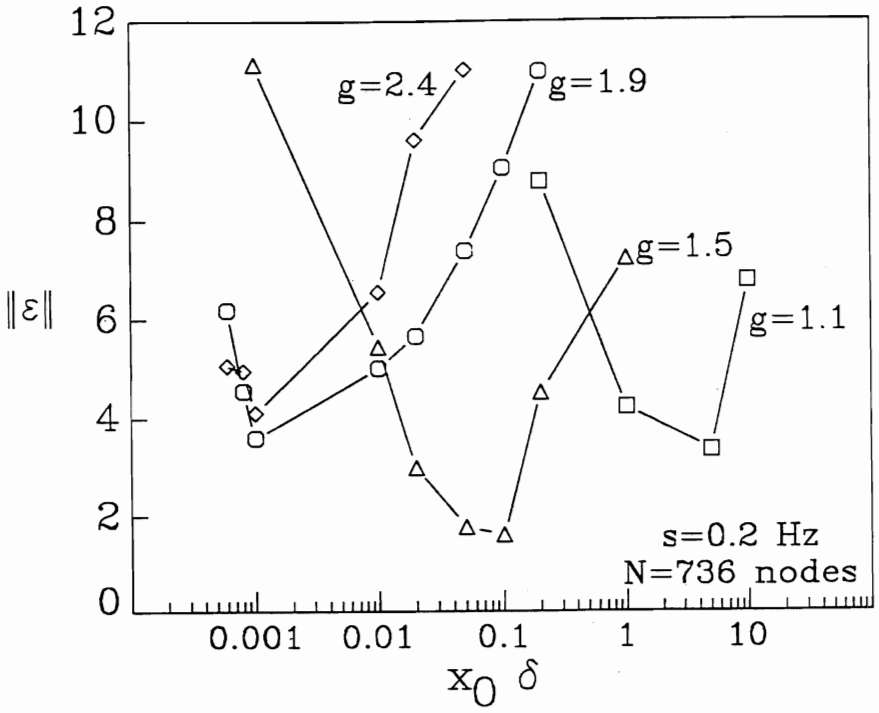

Fig.4.4 An error indicator $||\epsilon||$ as a function of the size x_0, measured in skin depths δ, of the central cut–out of the finite element meshes shown in Fig.4.3. The error indicator measures the accuracy, at nodes along the seafloor, of the finite element approximation to the solution of the H–polarization double half–space problem with a 3:1 electrical conductivity contrast and s=0.2 Hz. Best results are attained when the geometric spacing factor g=1.5 (Fig4.3*b*) and x_0=0.1δ.

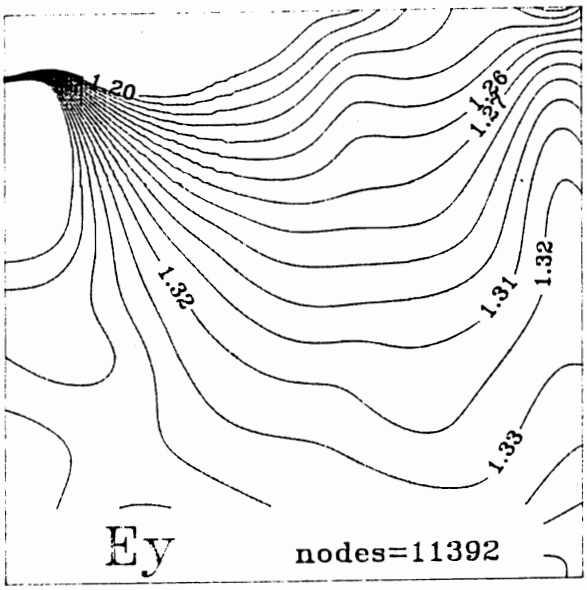

Fig.4.5 Contours of the percent relative error $\epsilon(x, z)$ on a finite element mesh with triangles characterized by size $h/4$ (compare with Fig.4.2*c*) in the numerical solution to the E–polarization double half–space problem described in §3.8, with 3:1 conductivity contrast and s=1 Hz. The errors are computed by comparing the output from the 2–D finite element forward modeling code against the analytical solution.

Chapter 5

2–D Electromagnetic Responses of Active Mid–Ocean Ridge Models

5.0 Introduction

In this chapter I wish to establish, through the use of two dimensional numerical modeling, how transient controlled–source electromagnetic (CSEM) data can help to characterize the geology beneath fast spreading mid–ocean ridge segments. To do this, the data, which consists of seafloor recordings of the various electric and magnetic field components, requires *interpretation* in terms of the sub–surface electrical conductivity, for various source/receiver configurations and positions with respect to the ridge axis. A method of intepreting transient CSEM data is developed in this chapter, initially using elementary layered earth models, and then in the later sections of this chapter the method is applied to some synthetic, noise–free mid–ocean ridge data generated by the finite element program described in the previous chapter. Before proceeding, I might remind the reader that many aspects of mid–ocean ridge geology and the electrical conductivity of the earth beneath active ridge segments such as those along the East Pacific Rise (EPR) are discussed in Chapter 2, please refer there for background information.

In general terms, the problem of geophysical data intepretation may be attacked by identifying diagnostic features from the earth's response that are sensitive to the critical physical property of the sub–surface. Such diagnostics are sometimes referred to as response parameters, and in our case they are chosen to characterize the earth's electromagnetic response in terms of its electrical conductivity. Forward modeling

techniques are used to assist the process. For a given electrical model of the earth and a given CSEM system configuration, for example, electromagnetic response parameters can be *computed* via a forward algorithm. The *sensitivity* of the response parameters to variations in the sub–surface electrical conductivity may be assessed by perturbing the structure of the electrical model and noting the corresponding amount by which the response parameters change. If the response parameters are sensitive to the perturbation, and large enough to be measured in a practical experiment, the structure being perturbed may be said to be well–resolved.

Specifically, using the transient finite element forward modeling algorithm described in Chapter 4, I will compute a set of electromagnetic responses for the electrical models of an active mid–ocean ridge segment described in the last section of Chapter 2. The response parameters I have chosen are the diffusion time τ and $\dot{B}_{\mathbf{max}} \equiv \max \partial_t B_y$, the maximum of the impulse response. These parameters have already been defined and were calculated for simple double half–space electrical conductivity models in Chapter 3. The variation of $(\tau, \dot{B}_{\mathbf{max}})$ in the presence and absence of a conductive magma chamber and zones of hydrothermal circulation is monitored in order to indicate whether transient CSEM systems, when arrayed in a certain configuration, can discriminate between the different structures. The results of this work are presented in this chapter of the thesis.

The forward algorithm is valuable as a means to find the resolution of mid–ocean ridge structures to controlled–source excitation *i.e.* as an experimental design tool, since ridge–going experiments are difficult and costly to perform. In fact, CSEM data from ridge–going experiments is only just becoming available. An experiment which recorded the 0.25–8.0 Hz *frequency* components of the horizontal electric field generated by an electric dipole transmitter at the East Pacific Rise crest near 13°N was performed in June 1989 (Evans *et.al.* 1990), but the data has not yet been completely interpreted nor released. There has also not yet been a *transient* CSEM system, of sufficient strength to image the magma chamber, deployed over an active

mid–ocean ridge segment.

5.1 HED Response Parameters

A pair of electromagnetic response parameters, namely the diffusion time τ and the maximum impulse repsonse $\dot{B}_{\mathbf{max}} \equiv \max \partial_t B_y(t)$, were defined in §3.6. Values for the response parameters were calculated for the case of an infinite line source exciting a uniform conductor, see equations (3.38) and (3.39). In this section, I will compute and plot the magnetic field due to horizontal electric dipole (HED) excitation of a uniform conductor, and then calculate its corresponding diffusion time. This quantity will be used later in the chapter when I compare infinite line source and HED response parameters.

Consider a grounded HED with a time dependent moment $M(t)$ located at the origin and oriented in the x–direction. Define the co–ordinate z as the vertical measure, positive upward. The HED source, situated in a medium possessing an electrical conductivity $\sigma = \sigma(x, y, z)$, generates all six components of the electromagnetic field $(\mathbf{E}, \mathbf{B})$. In a marine environment, the magnetic effects of displacement currents may be neglected, in which case the governing Maxwell's equations reduce to a pair of uncoupled *vector* diffusion equations, one for each of $\mathbf{E}$ and $\mathbf{B}$. As derived in §3.2, the diffusion equation satisfied by the magnetic field $\mathbf{B}$ is

$$\nabla \times \frac{1}{\sigma} \nabla \times \mathbf{B} + \mu \partial_t \mathbf{B} = \mu \nabla \times \frac{\mathbf{J_S}}{\sigma} \tag{5.1}$$

where $\mu = 4\pi \times 10^{-7}$ H/m is the magnetic permeability of free space. The HED source current density $\mathbf{J}_{\mathrm{S}}^{\mathrm{HED}}$ is given by

$$\mathbf{J}_{\mathrm{S}}^{\mathrm{HED}}(t) = P(t) \delta(\mathbf{r}) \hat{x}. \tag{5.2}$$

In equation (5.2), $P(t) = I(t)\Delta$ is the HED dipole moment, a product of the source current $I(t)$ and its length Δ. The HED may therefore be regarded as a point dipole of strength $P(t)$ and oriented in the x–direction. We assume that the current in the

HED is stepped on to a steady value at time t=0 such that $I(t) = Iu_0(t)$ where $u_0(t)$ is the Heaviside unit step function. In this case, the analytic solution (*e.g.* Cheesman *et.al.* 1987) to the differential equation (5.1), subject to the boundary condition that **B** vanishes at infinity and valid for a uniformly conducting medium is

$$\mathbf{B}(t) = \frac{-\mu P(z\hat{y} + y\hat{z})}{4\pi r^3}\left[\mathrm{erfc}(\frac{\sqrt{\mu\sigma}r}{2\sqrt{t}}) + \sqrt{\frac{\mu\sigma r^2}{\pi t}}\exp(\frac{-\mu\sigma r^2}{4t})\right]. \qquad (5.3)$$

Contour plots of $B_y(t)$, with B_y=$\mathbf{B}\cdot\hat{y}$ calculated from equation (5.3), are shown in Figure 5.1 for y=0 and Figure 5.2 for y=1.2 km. The plots illustrate the diffusion of B_y as a function of time into a uniform conductor. At late time, $t\approx$10 s, the magnetic field is steady, *i.e.* $\dot{B}_y(t)$=0. Note that for y>0, local maxima appear above and below the line z=0, and recede vertically from the dipole as time advances.

Define the electromagnetic response of the conductor, at any given location, as the curve $\partial_t B(t)$, and assume that practical receivers capable of measuring it are available. Recall that the diffusion time τ, characteristic of the electrical conductivity σ, is the time taken for the response to attain its maximum magnitude, *i.e.*, τ is the solution to the following equation:

$$\partial_t B(\tau) = \max \partial_t B(t). \qquad (5.4)$$

From equations (5.3) and (5.4) it may be shown that

$$\tau = \frac{\mu\sigma r^2}{10}. \qquad \text{(HED source)} \qquad (5.5)$$

I will show that the diffusion time τ depends largely on the distribution of electrical conductivity along the most resistive path from the source to the receiver. Therefore, given the source/receiver configuration and the electrical conductivity structure, it is straightforward to *predict* τ approximately, without actually solving a governing diffusion equation.

We shall examine variations in the response parameters τ and $\dot{B}_{\mathbf{max}}\equiv\max \partial_t B(t)$ with respect to changes in the source/receiver separation, for different conductivity

models. This analysis will prove sufficient to distinguish between the models. Other parameters from the response curve $\partial_t B(t)$ might well be selected, but since the diffusion time τ and the response amplitude $\dot{B}_{\max}$ are easily obtainable from the experimental record and the dependence of τ on the sub–surface conductivity is known approximately, these two parameters represent a particularly convenient data set.

5.2. Elementary 1–D Earth Models

Let us look at the response curves $\partial_t B_y(t)$ resulting from an infinite line source excitation of some simple layered earth models before proceeding to those from the detailed ridge models described in Chapter 2. Analysis of the response parameters $(\tau, \dot{B}_{\max})$ extracted from the layered earth responses will assist interpretation of the later, more complicated responses. I shall be solving the H–polarization mode of Maxwell's equations in this section of the thesis, *i.e.* the extended dipole source is described by the current density function (3.19).

Consider step–on extended dipole excitation of a *uniform* earth with electrical conductivity σ=0.1 S/m. The response $\partial_t B_y(t)$ that would be measured by a seafloor receiver is calculated by inserting either equation (3.26) or (3.27) into the Gaver–Stehfest derivative formula,

$$\partial_t B_y = \left[\frac{\ln 2}{t}\right] \sum_{n=1}^{N_c} c_n(N_c) s_n \overline{B}_y(s_n) \qquad N_c, \text{even} \tag{5.6}$$

and then setting z=0. The result is shown plotted as squares in Figure 5.3*b*. The dipole is of moment P'=100 A and lies on the seafloor beneath a uniform ocean with σ=3.2 S/m. The source/receiver separation L is 5 km. From the curve, the response parameters are found to be (τ=0.42 s, $\dot{B}_{\max}$=0.57 nT/s).

Now consider a very simple electrical model of young oceanic crust. The model, shown in Figure 5.3*a*, consists of the uniform ocean overlying a layer of conductivity σ_1=0.1 S/m representing the upper basaltic sequence and a σ_2=0.001 S/m half–space representing the gabbros. This model differs from the double half–space model

because of the presence of the resistive gabbroic basement. An expression for the magnetic field resulting from step–on extended dipole excitation of the three–layer model may be derived by extending the double half–space theory found in Edwards (1988). The result, after setting z=0, is

$$\overline{B}_y^{\text{sea}}(s) = \frac{-\mu P'}{\pi s} \int_0^\infty \left[\frac{\sigma_0\theta_1(R_{12} - e^{2\theta_1 h})}{\sigma_0\theta_1(R_{12} - e^{2\theta_1 h}) - \sigma_1\theta_0(R_{12} + e^{2\theta_1 h})} \right] \cos(\lambda x)\, d\lambda, \quad (5.7)$$

where

$$R_{12} = \frac{\sigma_2\theta_1 - \sigma_1\theta_2}{\sigma_2\theta_1 + \sigma_1\theta_2} \quad (5.8)$$

may be regarded as a reflection co–efficient and h is the thickness of the upper layer. Application of the Gaver–Stehfest derivative formula (5.6) gives the response curve $\partial_t B_y(t)$ for this model, which is shown plotted as triangles in Figure 5.3*b*. The response parameters, as extracted from the curve, are (τ=0.25 s, $\dot{B}_{\text{max}}$=0.34 nT/s).

Diffusion Time

The peaks in the layered earth response curves are due to electromagnetic energy diffusing from the source along the most electrically resistive path to the receiver. For the double half–space model, this means directly through the earth. Edwards and Chave (1986) have shown that τ can be inverted using equation (3.38) to give an estimate of the seafloor conductivity and they indicated that this estimate is robust with respect to the conductivity contrast σ_0/σ_1 between the upper and the lower half–spaces. A signal diffusing through the seawater is much smaller and arrives later at approximately τ=12 s (not clearly shown in Figure 5.3*b*).

The diffusion time for the three–layer model is τ=0.25 s which represents a decrease with respect to the double half–space diffusion time of τ=0.42 s. The decrease is clearly due to a change in the most electrically resistive path. The path through the three–layer model is down through the thin layer, across the resistive half–space and then up again through the thin layer to the receiver. Since $\sigma_2 L^2 << \sigma_1(2h)^2$, the diffusion time across the resistive half–space can be neglected with respect to the

diffusion time up and down through the thin layer. A shortening of diffusion time in the presence of a resistive basement is also noted by Cheesman *et.al.* (1987) who modeled in two dimensions magnetic dipole excitation of a three–layered earth. Likewise, the diffusion time τ through a 2–D conductivity structure of arbitrary complexity is determined by the electrical conductivity along the most resistive path from source to receiver.

Diffusion times from the three–layer earth model are plotted, again as triangles, in Figure 5.3*c* as a function of source/receiver separation. For sufficiently large L, τ is constant, reflecting the fact that the first arrivals of electromagnetic energy at those receivers have taken a fast path beneath the upper layer. A marked similarity exists between this curve and a plot of first arrivals as a function of range from a seismic refraction experiment, where in that case the earth would consist of a fast velocity basement underlying a slower velocity layer. The variation with range of the double–halfspace diffusion times is also displayed (squares).

Response Amplitude

The layered earth response amplitudes are $\dot{B}_{\max}$=0.57 nT/s for the double half–space model and $\dot{B}_{\max}$=0.34 nT/s for the three–layer model; these values are taken from the curves plotted in Figure 5.3*b*. The difference in these results is due to the dependence of $\dot{B}_{\max}$ on $\sigma^{-1}l^{-3}$, where l has dimensions of length, see equation (3.39). Thus, as far as the interpretation of the response amplitude is concerned, there is a trade–off between conductivity and signal path length. Consider the three–layer model. Although the basement conductivity of σ=0.001 S/m is less than the thin layer conductivity σ=0.1 S/m, the path length through the three–layered model is longer than the path through the double half–space model. The longer path length results in a *smaller* response amplitude. However, as L increases, the difference in the two path lengths becomes insignificant. At sufficient range, the two path lengths are approximately equal, and the response amplitude is dominated by the difference

in path resistivity σ^{-1}, eventually causing the response amplitude of the three–layer earth to become *greater* than that of the double half–space.

Response amplitudes of the three–layer, plotted as triangles, and double half-space earth models (squares) are shown in Figure 5.3*c* as a function of L. The cross–over in response amplitude as described above occurs at approximately L=12 km. The response amplitude $\dot{B}_{\mathbf{max}}$ is more difficult to predict *a priori* than the diffusion time τ, since $\dot{B}_{\mathbf{max}}$ does not depend on the geometry in an obvious way.

Conversion Factors

In this section, we derive conversion factors to relate experimental determinations of τ and $\dot{B}_{\mathbf{max}}$, as they might be extracted from the response curves of seafloor receivers, to the theoretical values of these parameters that are calculated under the 2–D approximation. From equations (5.5) and (3.38), the effect of the approximation $\partial_y \equiv 0$ is to increase τ by a constant factor

$$\tau^{2\mathrm{D}} = \left[\frac{5}{4}\right] \tau^{\mathrm{HED}}|_{y=0}. \tag{5.9}$$

The above equation, due to its simplicity, has broad implications for reducing the computational load if it can be shown to remain even approximately true for complicated structures, since to obtain $\tau^{2\mathrm{D}}$ only a scalar diffusion equation need be solved. For comparison, a simple analytic form for the diffusion time also exists in the one dimensional ($\partial_x = \partial_y \equiv 0$) magnetotelluric problem. Ferguson and Edwards (1990) show that an infinite current sheet, of density $\mathbf{J}_S \propto \delta(z)$ and aligned parallel to the surface of a uniformly conducting half-space, induces fields which diffuse into it with a characteristic diffusion time of

$$\tau = \frac{\mu\sigma z^2}{6}. \qquad \text{(MT source)}. \tag{5.10}$$

Comparing the 1-D MT, 2-D extended dipole and 3-D HED results, we have

$$\tau^{\mathrm{MT}} = \left[\frac{4}{3}\right] \tau^{2\mathrm{D}}|_{x=0} = \left[\frac{5}{3}\right] \tau^{\mathrm{HED}}|_{x=0,y=0}. \tag{5.11}$$

The 2–D response amplitudes can also be converted into realistic signal amplitudes quite easily. If the earth is uniformly conducting, the effect of the 2–D approximation $\partial_y \equiv 0$ on $\dot{B}_{\max}$ can be assessed as follows. In the Laplace domain, there exists a closed–form solution (Wait 1961) to the vector diffusion equation (5.1) when the current density $\mathbf{J}_S$ corresponds to that of a stepped–on, seafloor HED source and the conductivity $\sigma(z)$ is that of a uniform ocean σ_0 overlying a uniform earth σ_1. The $\hat{y}$–component of the solution, which is expressed as a Hankel transform, is

$$\overline{B}_y^{\mathrm{HED}}(s) = \frac{-\mu P}{2\pi s} \int_0^\infty \left[\theta_0 + \frac{(\sigma_1 - \sigma_0)}{\sigma_0 \theta_1 + \sigma_1 \theta_0} \partial_{xz} \right] \frac{\exp(-\theta_0 z)}{\theta_0 + \theta_1} J_0(\lambda \sqrt{x^2 + y^2})\, \mathrm{d}\lambda \quad (5.12)$$

where J_0 is a Bessel function. The 3-D response $\partial_t B_y^{\mathrm{HED}}(t)$, calculated from equations (5.6) and (5.12), is shown plotted as diamonds in Figure 5.4*a*. The HED moment is P=100 A·m, the double half–space model shown in Figure 5.3*a* is chosen, and L=5 km. Figure 5.4*a* also illustrates the comparison between the 3–D response and its equivalent 2–D response, which I have already calculated and plotted as squares in Figure 5.3*a*. The two response curves are initially of similar shape, but the HED response takes about an order of magnitude longer to decay.

The response amplitudes, extracted from the curves, are $\dot{B}_{\max}^{\mathrm{2D}}$=0.57 nT/s and $\dot{B}_{\max}^{\mathrm{HED}}$=0.11 pT/s, note that there are two vertical scales in this plot. The HED response is much smaller than the extended dipole response due to the fact that the HED is a point source and the extended dipole is a line source. The ratio of the two responses, as a function of the source/receiver separation L, is shown in Figure 5.4*b*. The relationship is a very simple one:

$$\dot{B}_{\max}^{\mathrm{2D}} = L \dot{B}_{\max}^{\mathrm{HED}}. \quad (5.13)$$

Equations (5.9) and (5.13) define *conversion factors* which relate physical measurements of the response parameters $(\tau, \dot{B}_{\max})$ to their values as computed under the two–dimensional approximation, and are valid for the double half–space model.

5.3 A Uniform σ=1.0 S/m Magma Chamber Model

I shall now calculate electromagnetic field components as they might be recorded on the crest of the East Pacific Rise, assuming it has the conductivity structure shown in the model of Figure 2.1*b*. This model is based on the analysis of seismic reflection profiles, see Chapter 2 for further details. An infinite source, or transmitter, lies on the seafloor 5 km west of the axis, as shown by the position marked Tx in Figure 2.1*b*. The seafloor is assumed to slope away from the crest at an angle of 5° with the horizontal. Following a step–on in transmitter current which occurs at time t=0, electromagnetic fields begin to diffuse through the conductivity structure. The finite element—Gaver–Stehfest procedure, outlined in §3.7, is used to compute the diffusing field $B_y(x, z, t)$ at all points throughout the model but only the field at the pre–selected sites on the seafloor labelled A–D will be used for further analysis. The sites are a set of four evenly spaced points along the seafloor across the ridge crest and have been selected as possible receiver sites. These points lie 2.5 km west of the axis, on the axis itself, and 2.5 km and 5.0 km east of the axis.

The patterns of magnetic field $B_y(t)$ diffusing into normal quasi–layered oceanic crust following 2–D extended dipole excitation is shown in Figure 5.5*a*. The patterns represent solutions to the H–polarization mode of Maxwell's equations. At the instant the source is activated, two current vortices form, one above and one below the source. The strength of this initial current flow is precisely that required to maintain the field everywhere at the zero value which existed before step–on. As time progresses the lower, larger–scale vortex circulates in the crust and in a narrow band of seawater near the seafloor. The streamlines at large range near the seafloor and near the interface between layers 2 and 3 of the oceanic crust resemble strikingly the wavefronts of seismic head waves (see also Edwards 1988, de Hoop and Oristaglio 1988). The leaking of energy into the seawater from below at early times is observed on the seafloor as an "earth signal". Both vortices expand with time at a rate inversely proportional to the conductivity and finally, at the late time limit, the current is confined to the seawater. The addition to the model of the magma chamber retards the progress of the crustal

vortex, Figure 5.5*b*. I shall show that this additional body of high conductivity causes a delay in the arrival of the earth signal. At late times, for both models this is t>10 s, a "sea signal" dominates and information about the solid earth is lost.

The time derivative of the magnetic component $\partial_t B_y(t)$ at locations A–D near the crest is shown in Figure 5.6*a*, which permits a qualitative assessment of the response parameters $(\tau, \dot{B}_{\mathbf{max}})$. Recall that the diffusion time τ is the time at which the impulse response reaches its maximum amplitude. At the seafloor positions labelled C and D in Figure 2.1*b* the diffusion time τ is much greater when a magma chamber is included in the model. As expected, the presence of the magma chamber will delay the peak voltage measured in a coil placed on the far side of the rise axis. The response parameters will be examined quantitatively in the next section of the thesis. Here, the objective is simply to illustrate the patterns of fields diffusing into typical mid–ocean ridge structures.

Although we have not defined response parameters in terms of solutions to the E–polarization mode of Maxwell's equations, it is instructive to compute the response from excitation of an earth represented by the model in Figure 2.1*b* by the infinite wire oriented along–strike. Contours of the electric component $E_y(t)$ resulting from such an excitation are shown in Figures 5.5*c*,*d*. The contours represent solutions to the E–polarization mode of Maxwell's equations. The presence of the highly conductive magma chamber is detected by a disruption of the normal progress of the diffusing signal. The electric component at ridge floor locations on the far side of the rise axis at early times (*i.e.* t=1.0 s) appears to be reduced in magnitude when the magma chamber is included in the model. The computed electric component is shown for positions A–D in Figure 5.6*b*. At early times for positions C–D the electric component is indeed attenuated when the magma chamber is present. Figure 5.6*b* also shows that at late time for all the receiver positions the magnitude of the electric component does not depend on the presence of the magma chamber. Indeed, at late times, the inductively generated TM component becomes increasingly independent of the

conductivity structure and eventually vanishes. Once again, it is only the early time measurements of the signal that provide clues to the existence of a magma chamber.

5.4 A Melt Lens Model, and Hydrothermal Circulation

Simplified 2–D models of the geo–electric section at a fast spreading center are shown in Figures 2.3*a–d*. The model geometries consist of block representations of actual structures found beneath an active ridge segment (MacDonald 1989), taking both seismic reflection and refraction data from the East Pacific Rise into account (see Chapter 2). The electrical conductivity σ of each geological structure is once again assumed to be uniform and its value is selected on the basis of the available data summarized in that chapter. To find the electromagnetic response of a particular model to excitation by the extended dipole, the finite element—Gaver–Stehfest method is used. From the transient magnetic field $B_y(t)$ computed by this method, response parameters $(\tau, \dot{B}_{\mathbf{max}})$ are extracted. All of the finite element calculations were performed on the CRAY–XMP/24 at the Ontario Center for Large Scale Computation. The computer code used to solve the governing diffusion equation (3.23) executed at an average speed of 12 Mflops using CRAY single precision arithmetic. A set of six evenly spaced points on the seafloor across the ridge crest have been selected as typical receiver sites. These points lie 1.5 km west of the axis, on the axis itself, and 1.5 km, 3.0 km, 4.5 km and 6.0 km east of the axis. To generate a single snapshot of the magnetic field, about one minute of CRAY CPU–time and 24 MB of memory are required.

Uniform Magma Chamber

The electromagnetic response curves $\partial_t B_y(t)$ of the models shown in Figures 2.3*a* and 2.3*b* are plotted, respectively, as squares and triangles in Figure 5.7. The effect of adding the magma chamber is to delay the diffusion time and to alter the response amplitude. These effects are not noticeable at the receiver located west of the axis

but become increasingly pronounced with range. In particular, at 6 km east of the axis, $\dot{B}_{\mathbf{max}}$ is reduced by about 50% and the τ increases from 0.3 s to 0.7 s.

The observed behaviour of the diffusion time may be understood by analogy with the elementary three–layer model, Figure 5.3*a*. The most resistive path through the quasi–layered model in Figure 2.3*a* is very similar to the most resistive path through the three–layer model. It goes down through the upper basalt layer, across the resistive base layer of gabbros and up again through the basalts to the receiver. By virtue of its high electrical conductivity relative to the surrounding gabbros, the presence of the magma chamber, Figure 2.3*b*, slows down the magnetic field diffusing through it. Since the magma chamber conductivity is less than that of the upper layer basalts, its presence does not, however, perturb the diffusion path.

It is apparent from Figure 5.7 that the response amplitude $\dot{B}_{\mathbf{max}}$ is enhanced at the sites on–axis and up to 3 km east of the axis when the magma chamber is included in the model, but reduced at the sites 4.5 and 6 km east of the axis. This observation may be interpreted as follows. Induced currents in the magma chamber, which are set up when it is excited by the "primary" field $B_y^{\mathrm{p}}(x,z,t)$ diffusing through the quasi–layered structure, act as a secondary source of electromagnetic fields. The "secondary" magnetic field $B_y^{\mathrm{sec}}(x,z,t)$ produced by the induced currents in the magma chamber has a spatial distribution which resembles that of the primary field, *i.e.* a horizontal dipole pattern. The total magnetic field $B_y \equiv B_y^{\mathrm{p}} + B_y^{\mathrm{sec}}$ is then the sum of this field and the primary field. At seafloor sites between the two sources, the primary and secondary fields reinforce one another, while at seafloor sites east of the magma chamber they tend to cancel.

Thin Melt Lens

The response of the model containing the uniform magma chamber, shown again plotted as triangles in Figure 5.8, is now compared to that of a model containing an identical chamber with a thin lens of pure melt at the top (the latter model is shown

in Figure 2.3*c* and its response is plotted as squares in Figure 5.8). The diffusion times for the four closest receiver sites are the same for both models but there is an enhancement in the diffusion time evident at the other two receiver sites, the enhancement is about 0.1 s at the farthest site. Response amplitudes at the receiver locations 0–3 km east of the ridge axis increase by as much as 17% following the addition to the model of the thin lens but are much less elsewhere. The effect on the response parameters ($\tau, \dot{B}_{\mathbf{max}}$) of the melt lens is measureable because the primary diffusion path to the receiver has been diverted slightly by the presence of the lens of enhanced conductivity. The most resistive path goes under the lens.

Hydrothermal Circulation

Finally, the effect of adding hydrothermal circulation to the upper 2 km of the crust (see Figure 2.3*d* for the geometry) is shown in Figure 5.9. In this figure, the response of the uniform magma chamber is plotted as triangles, the response including hydrothermal circulation is plotted as squares. The enhanced electrical conductivity due to the circulating fluids delays the arrival of the signal at all receiver sites. For example, the delay in diffusion time at 6 km east is 0.1 s. The effect of hydrothermal circulation on the diffusion time is much greater at 0–3 km east of the axis, which is directly above the regions of enhanced conductivity. A second effect of adding hydrothermal circulation to the model is to reduce the response amplitude at all receiver sites. This effect is strongest at the receivers 0–3 km east of the axis.

The response amplitude is difficult to predict and interpret since it depends on the conductivity model in a complicated way. For example, the response amplitude increases at certain sites when the magma chamber is added to the quasi–layered model but decreases at those sites when the hydrothermal circulation zones are added, even though both structures are relatively conductive with respect to their hosts.

5.5 On the Resolution of Mid–Ocean Ridge Structures

The response amplitude from the uniform magma chamber model, as predicted from the two dimensional numerical modeling and extracted from the curve plotted as triangles in Figure 5.7, is of the order 1.5 nT/s at 3.5 km source/receiver separation and 50 pT/s at 8 km separation. The above amplitudes are valid for a 2–D extended dipole possessing a moment of P'=100 A. Assuming that the linear relationship between the HED and the 2–D response amplitudes, equation (5.13), is approximately true even for the non–uniform conductivity structure that exists beneath the ridge, putative HED response amplitudes can be computed from the 2–D results. These are, corresponding to an HED with a moment of P=100 A·m, $\dot{B}^{\mathrm{HED}}_{\mathrm{max}}$=0.4 pT/s and $\dot{B}^{\mathrm{HED}}_{\mathrm{max}}$=0.006 pT/s for the 3.5 km and 8 km separations respectively. The small magnitude of the HED response means that practical receivers must be sensitive to sub–pT/s fluctuations in order to detect the signals originating several kilometers away. If the sensitivity of the receivers is only 1 pT/s, the HED dipole moment must be increased to 10^4–10^5 A·m in order to detect a response across the ridge. The University of Toronto fluxgates, for example, are sensitive to 1 pT, although the noise levels are still uncertain.

Asymptotic Behaviour of τ

The dependence of the diffusion time on the source/receiver separation is summarized in Figure 5.10*a*, for the various conductivity models studied. In all cases, the explanation for the asymptotic behaviour of τ at large values of L can be given in terms of the availability of a fast diffusion path through the resistive gabbros, and is analogous to the interpretation of seismic refraction first arrival time. For example, the diffusion time for the quasi–layered model, plotted as squares, is a constant 0.3 s for receiver sites more than 1.5 km east of the axis. This observation is in accordance with the asymptotic behaviour of τ through the three–layer model containing the resistive basement, c.f. the curve plotted as triangles in Figure 5.3c. Let us now examine, in order, the behaviour of τ as a function of L for each of the other MOR conductivity models whose response we have computed.

Consider the uniform σ=0.05 S/m magma chamber model, shown in Figure 2.3*b*. The diffusion times for the various receiver sites are shown plotted as triangles in Figure 5.10*a*. The diffusion time at the most distant site is 0.7 s and there is an indication from the shape of the curve that τ will asymptote to a constant value at larger L, in accordance with the hypothesis of the preceding paragraph. The diffusion time at receiver sites on or east of the ridge axis is greater when the magma chamber is added to the quasi–layered model because, although the magma chamber has not diverted the diffusion path, its presence has enhanced the conductivity along a segment of the path. This gives rise to an increase in the overall diffusion time.

When a thin lens of pure melt at the top of the magma chamber is modeled, the corresponding diffusion times are plotted as circles in Figure 5.10*a*. At the site 6 km east of the ridge axis, the presence of the melt lens delays the diffusion time by 0.1 s. Since the top of the magma chamber is located on the fastest diffusion path, the effect of adding the highly conductive lens to the magma chamber is to perturb slightly the geometry of the diffusion path. At the two farthest receiver sites the new path is most likely one that proceeds beneath the lens.

Now consider the hydrothermal circulation of fluids in the zones of most intense fissuring directly above a uniform magma chamber. The diffusion times are plotted as diamonds in Figure 5.10*a*. At sites 0–3 km east of the axis, they show a marked increase of about 0.3 s with respect to those of the uniform magma chamber model (triangles) because the signals necessarily pass through the regions of enhanced conductivity, see Figure 2.3*d*. At more distant sites, there is a direct path to the receivers beneath the hydrothermal fluids, thus the diffusion time becomes, with range, *independent* of the presence of the hydrothermal circulation.

To differentiate between the ridge conductivity models, the curves shown in Figure 5.10*a* indicate that the response $\partial_t B(t)$ must be known accurately over the window $0.3 \leq t \leq 0.8$ s following source activation. If a receiver returning accurate samples of the magnetic field at about 10–25 Hz is employed, arrival times can be picked out of

the time series to within 3—40 ms.

Behaviour of $\dot{B}_{\max}$

The response parameter $\dot{B}_{\max}$ is shown plotted as a function of increasing transmitter/receiver separation in Figure 5.10*b*. At the most distant receiver site, 6 km east of the axis, the various conductivity models are most easily distinguished. The response amplitude is small, 5 pT/s, when hydrothermal fluids and a uniform magma chamber are present (diamonds) and much larger, 25 pT/s, when they are both absent (squares). If just the magma chamber is present (triangles), the response amplitude is an intermediate value, 12 pT/s, regardless of whether the thin lens of pure melt (circles) is included. At sites 0–3 km east of the axis, however, the difference between the response amplitudes of these latter two models is more pronounced.

REFERENCES

Cheesman, S.J., R.N. Edwards and A.D. Chave, 1987. On the theory of seafloor conductivity mapping using transient electromagnetic systems, *Geophysics*, **52**, 204–217.

Constable, S.C., 1990. Marine Electromagnetic Induction Studies, *Surv. Geophy.*, **11**, 303–327.

Cox, C.S., S.C. Constable, A.D. Chave and S.C. Webb, 1986. Controlled–source electromagnetic sounding of the oceanic lithosphere, *Nature*, **320**, 52–54.

Detrick, R.S., P. Buhl, E. Vera, J. Mutter, J. Orcutt, J. Madsen and T. Brocher, 1987. Multi–channel seismic imaging of a crustal magma chamber along the East Pacific Rise, *Nature*, **326**, 35–41.

Edwards, R.N., 1988. Two–dimensional modeling of a towed in–line electric dipole–dipole sea–floor electromagnetic system: the optimum time delay or frequency for target resolution, *Geophysics*, **53**, 846–853.

Edwards, R.N. and A.D. Chave, 1986. A transient electric dipole–dipole method for mapping the conductivity of the seafloor, *Geophysics*, **51**, 984–987.

Edwards, R.N. and S.J. Cheesman, 1987. Two–dimensional modelling of a towed transient magnetic dipole–dipole seafloor EM system, *J. Geophysics*, **61**, 110–121.

Evans, R., S. Constable, M. Sinha and C. Cox, 1990. Controlled–source em sounding of the East Pacific Rise (abstract 6.6), *10th Workshop on Elecromagnetic Induction in the Earth*, August 22–29, 1990, Ensenada, Mexico, I.A.G.A. Working Group I–2.

Everett, M.E. and R.N. Edwards, 1989. Electromagnetic expression of axial magma chambers, *Geophys. Res. Lett.*, **16**, 1003–1006.

Ferguson, I.J. and R.N. Edwards, 1990. Electromagnetic mode conversion by surface conductivity anomalies: applications for conductivity soundings, *submitted to Geophys. J. Int.*

Gaver, D.P., 1966. Observing stochastic processes, and approximate transform inversion, *Oper. Res.*, **14**, 444–459.

Harding, A.J., J.A. Orcutt, M.E. Kappus, E.E. Vera, J.C. Mutter, P. Buhl, R.S. Detrick and T.M. Brocher, 1989. Structure of young oceanic crust at 13°N on the East Pacific Rise from expanding spread profiles, *J. Geophys. Res.*, **94**, 12163–12196.

Knight J.H. and A.P. Raiche, 1982. Transient electromagnetic calculations using the Gaver–Stehfest inverse Laplace transform method, *Geophysics*, **47**, 47–50.

Stehfest, H., 1970*a*. Numerical inversion of Laplace transforms, *Comm. A.C.M.*, **13**, 47–49.

Stehfest, H., 1970*b*. Remark on Algorithm 368. Numerical inversion of Laplace transforms, *Comm. A.C.M.*, **13**, 624.

Wait, J.R., 1961. The electromagnetic fields of a horizontal dipole in the presence of a conducting half–space, *Can. J. Phys.*, **39**, 1017–1028.

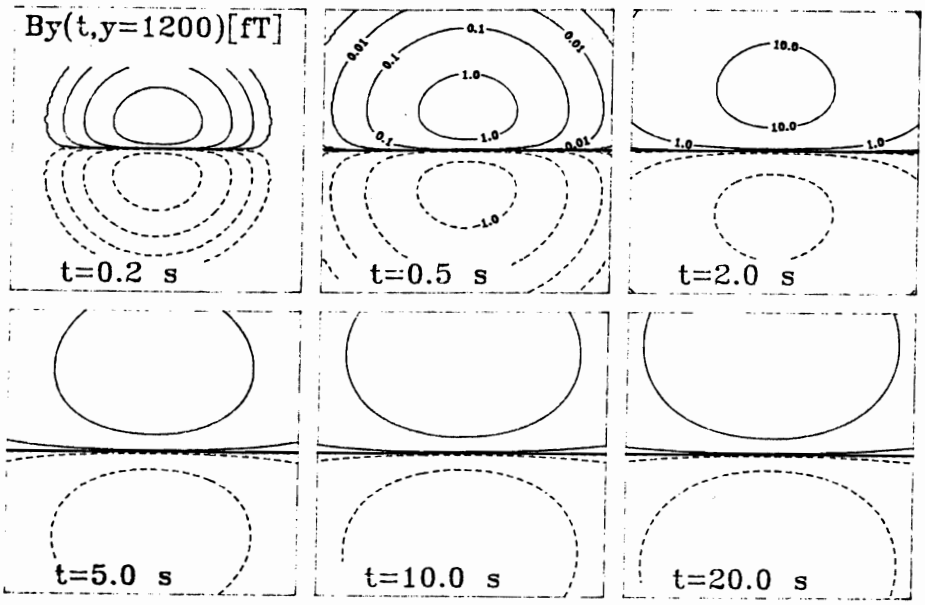

Fig.5.2 Contours of the HED step response at a distance of y=1.2 km along–strike. Maxima in the magnetic field, known as Maxwell's images, appear above and below the dipole whenever $y>0$ and recede vertically as time advances.

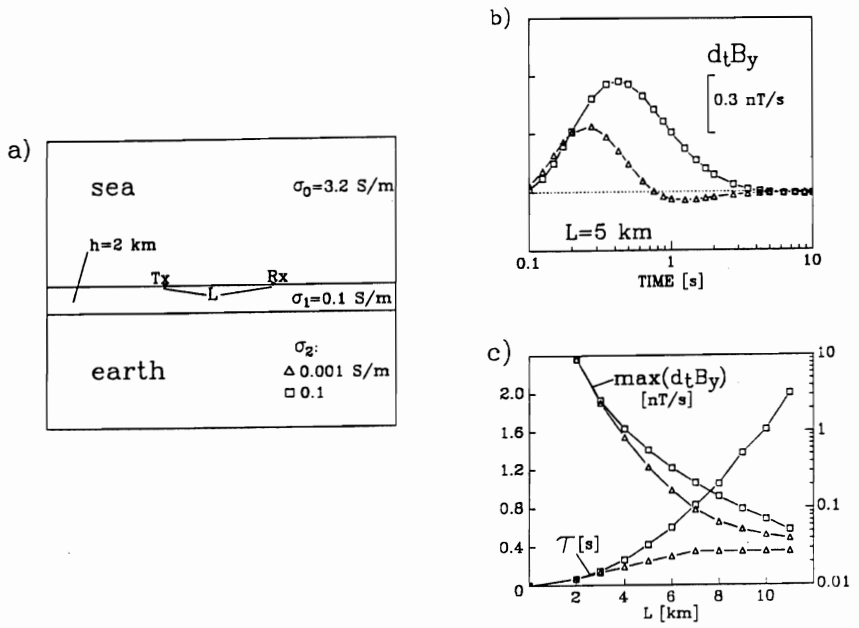

Fig.5.3 A pair of elementary, layered earth electrical models of young oceanic crust (a). Electric $\mathbf{E}(t)$ and magnetic $\mathbf{B}(t)$ are created by a sudden change in electric current in a seafloor transmitter (Tx). The fields diffuse outwards from the source, and may be recorded at a distance L by a seafloor receiver (Rx). The rate of diffusion is governed by the electrical conductivity σ. Response curves $\partial_t B_y(t)$ for the layered models (b). The maximum of each curve is the response amplitude $\dot{B}_{\max} \equiv \max(\partial_t B_y)$ while its position in time is the diffusion time τ. The response amplitude and diffusion time as a function of Tx–Rx separation L, for the layered models (c).

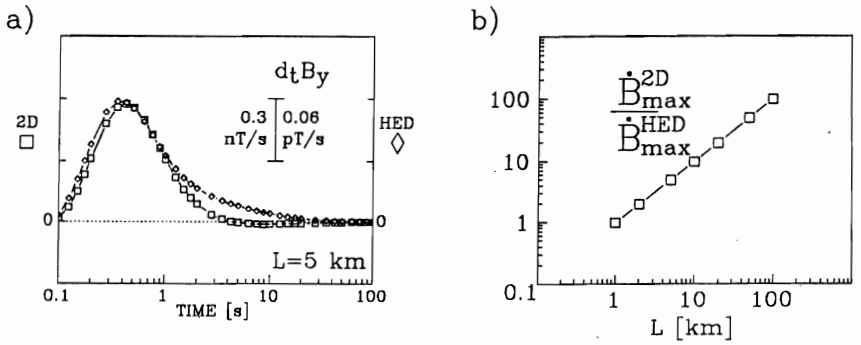

Fig.5.4 Response curves $\partial_t B_y(t)$ corresponding to extended dipole (2–D) and horizontal electric dipole (HED) excitation of a uniform earth, as would be measured by a seafloor receiver located L=5 km away (a). The ratio of response amplitudes $\dot{B}_{\mathbf{max}}$ for the extended dipole and HED transmitters, as a function of the Tx–Rx separation (b).

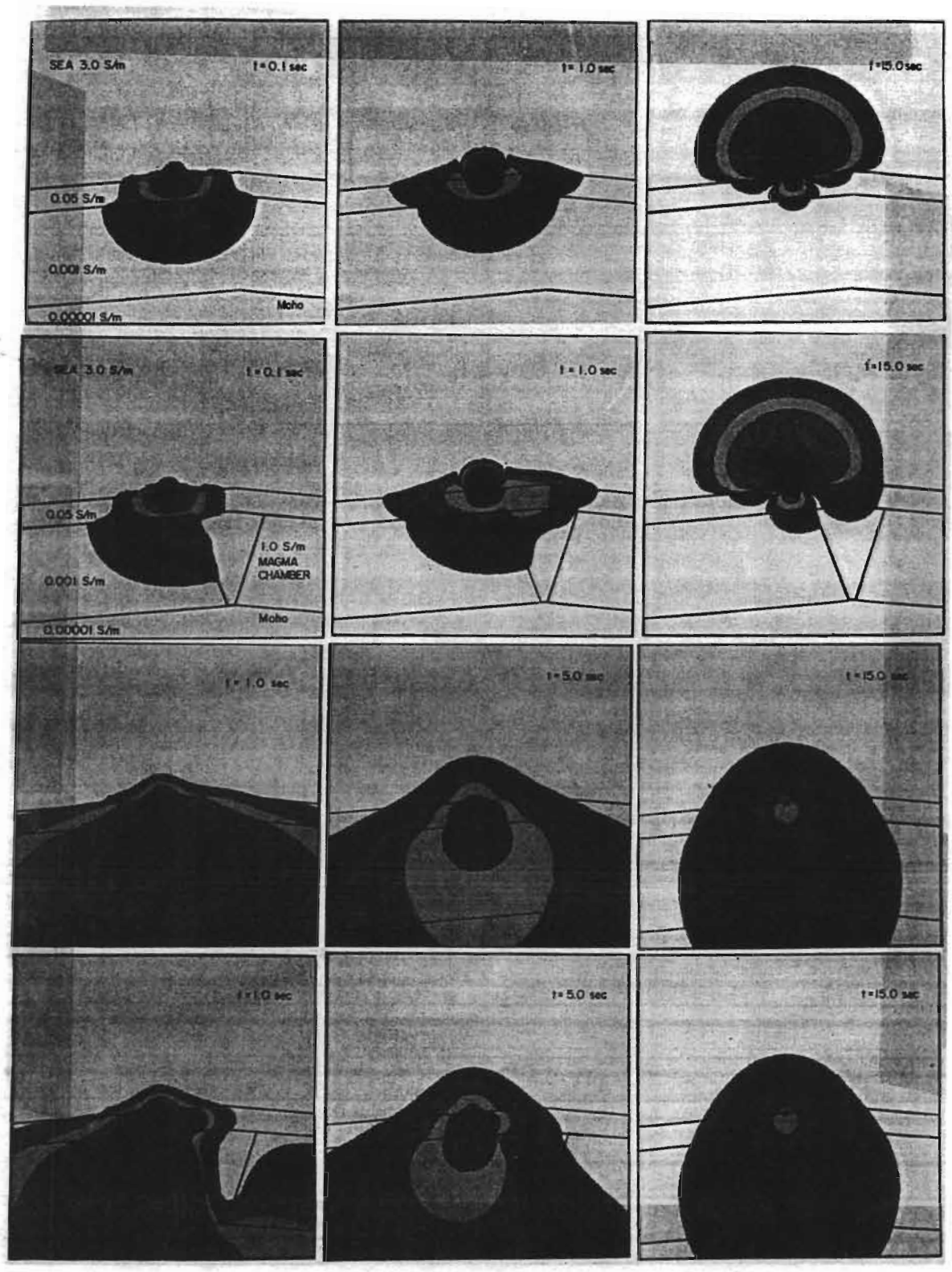
SEA 3.0 S/m
t = 0.1 sec
0.05 S/m
0.001 S/m
Moho
0.00001 S/m
t = 1.0 sec
t = 15.0 sec
SEA 3.0 S/m
t = 0.1 sec
0.05 S/m
1.0 S/m
MAGMA
CHAMBER
0.001 S/m
Moho
0.00001 S/m
t = 1.0 sec
t = 5.0 sec
t = 15.0 sec
t = 1.0 sec
t = 5.0 sec
t = 15.0 sec

Fig.5.5 Electromagnetic field components as they might be recorded on the crest of the East Pacific Rise, assuming it has the conductivity structure shown. Magnetic field $B_y(x,z,t)$ diffusing into "normal", quasi–layered oceanic crust following a step–on of electric current in a 2–D extended dipole located 5 km off–axis (a). The patterns shown represent solutions to the H–polarization mode of Maxwell's equations. The addition to the model of a magma chamber of conductivity σ=1.0 S/m retards the progress of the lower vortex of currents (b), causing a lengthening of the electromagnetic diffusion times to receivers located across the ridge.

Fig.5.5 (cont'd) Electric field $E_y(x,z,t)$ diffusing into layered crust following a step–on of electric current in an infinite, insulated cable oriented parallel to the strike of the ridge (c). The patterns shown represent solutions to the E–polarization mode of Maxwell's equations. The presence of the highly conductive magma chamber disrupts the normal progress of the diffusing field at early times (d), during which time the chamber can be detected by an attenuation in the electric field measured by receivers placed across the ridge.

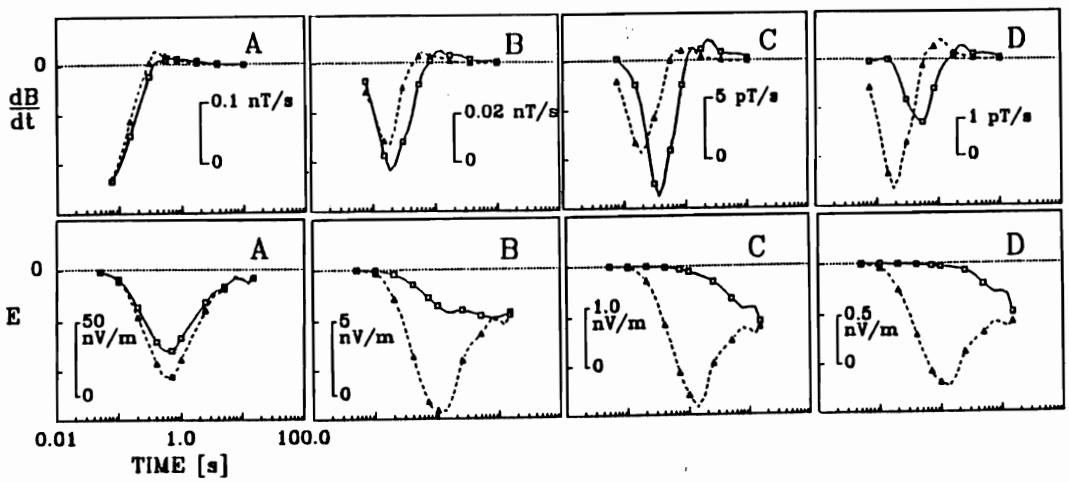

Fig.5.6 Response curves $\partial_t B_y(t)$ at the four seafloor locations A–D shown in Fig.2.1*b*, representing receiver sites across the East Pacific Rise (*a*, top row). The response is extracted from the numerical solution (see Fig.5.5*a*–*b* for snapshots of the solution at times t=0.1,1.0 and 15.0 s following excitation), of the governing, transient H–polarization boundary value problem. Responses shown are for conductivity models that include (solid line) and omit (dashed line) a magma chamber of conductivity σ=1.0 S/m. The electric field component $E_y(t)$, as extracted from E–polarization solutions, see Fig.5.5*c*–*d*, at the same locations A–D, and for models with and without the magma chamber (*b*, bottom row).

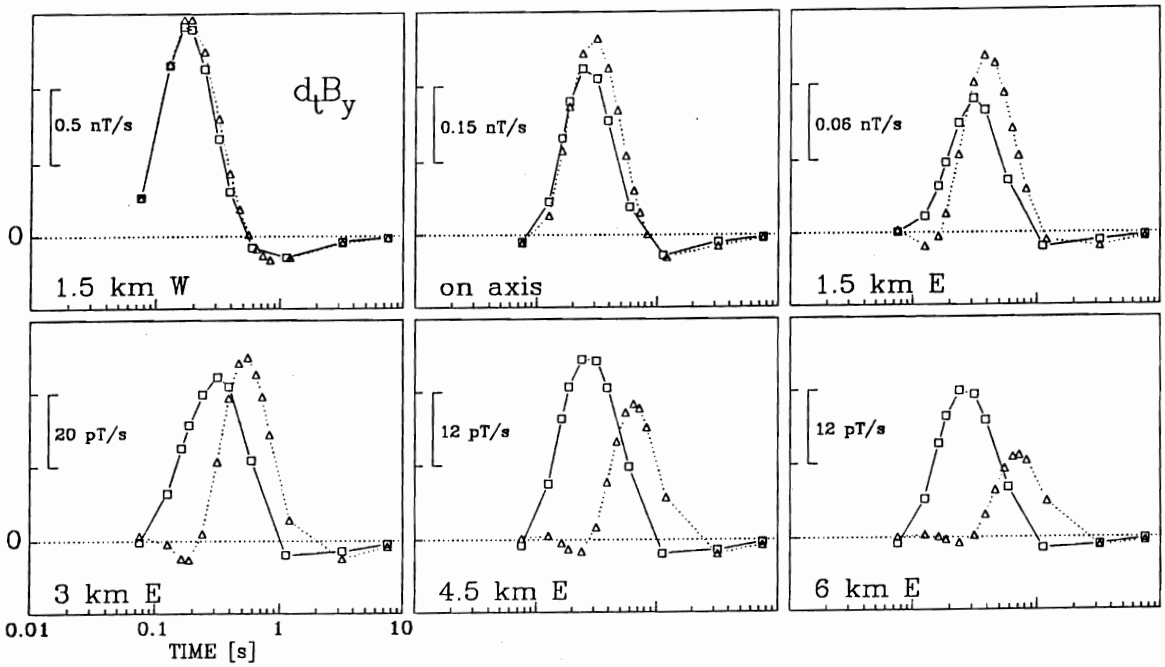

Fig.5.7 Response curves $\partial_t B_y(t)$ at various "seafloor" locations in the quasi–layered mid–ocean ridge conductivity model shown in Fig.2.3*a* (squares) and the model shown in Fig.2.3*b* which includes a uniform magma chamber of conductivity σ=0.05 S/m (triangles). A 2–D extended dipole transmitter is located 5 km west of the ridge axis. The effect of adding the magma chamber is to increase the diffusion time at all locations, increase the response amplitude at locations up to 3 km east of the axis and reduce the response amplitude elsewhere.

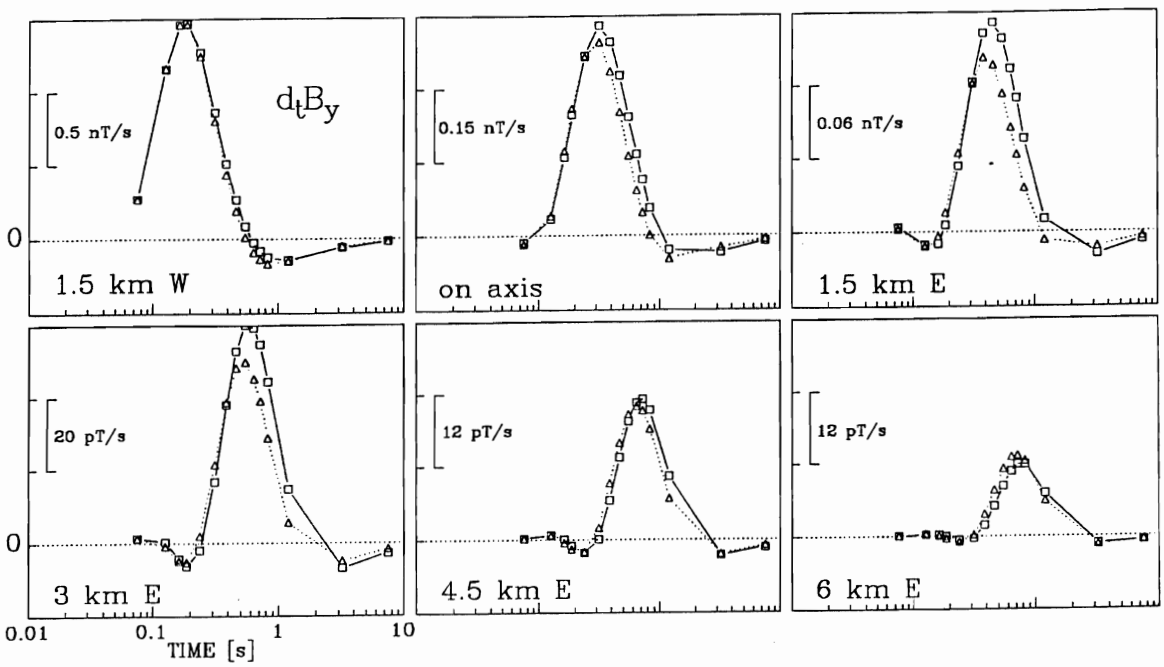

Fig.5.8 Response curves $\partial_t B_y(t)$ for models that omit (triangles) and include (squares) a thin melt lens atop the uniform magma chamber shown in Fig.2.3*b*. The melt lens geometry is shown in Fig2.3*c*. The responses are similar because primary diffusion paths from the transmitter to the various receivers are diverted only slightly by the presence of the thin lens of enhanced electrical conductivity.

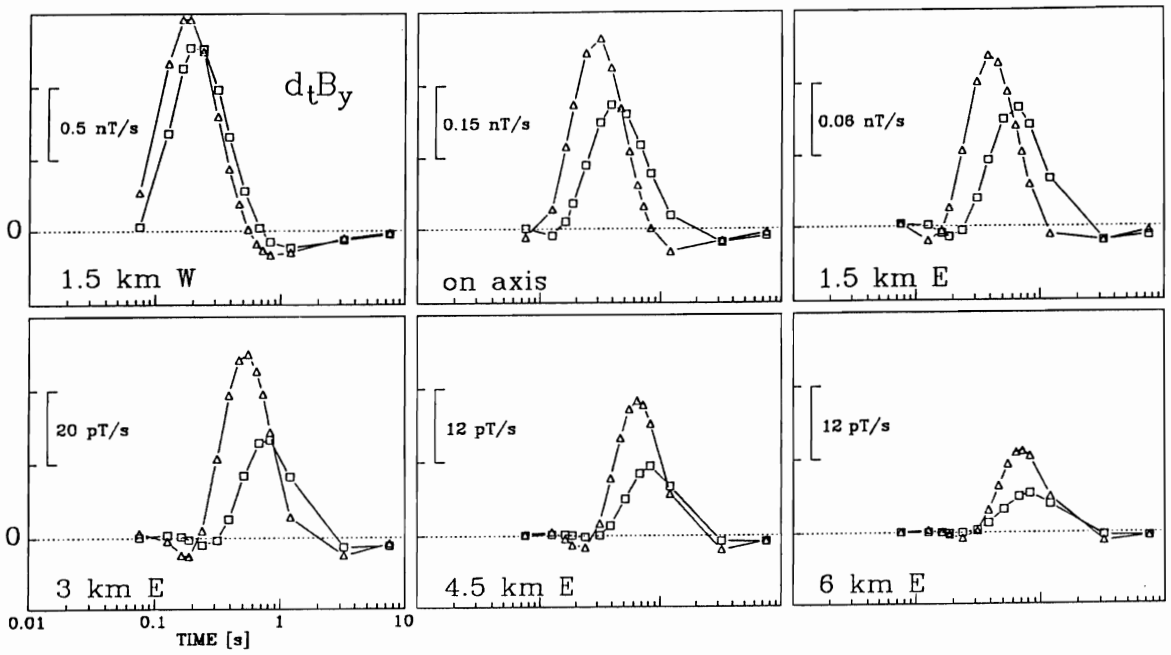

Fig.5.9 Response curves $\partial_t B_y(t)$ for magma chamber models that omit (triangles) and include (squares) a region of enhanced electrical conductivity representing hydrothermal fluid circulation in the upper layer of basalts shown in Fig.2.3*b*. The effect of adding enhanced conductivity due to hydrothermal circulation is to delay the diffusion time and decrease the response amplitude, especially at sites directly above the hydrothermal zone (*e.g.* 0–3 km east of the axis).

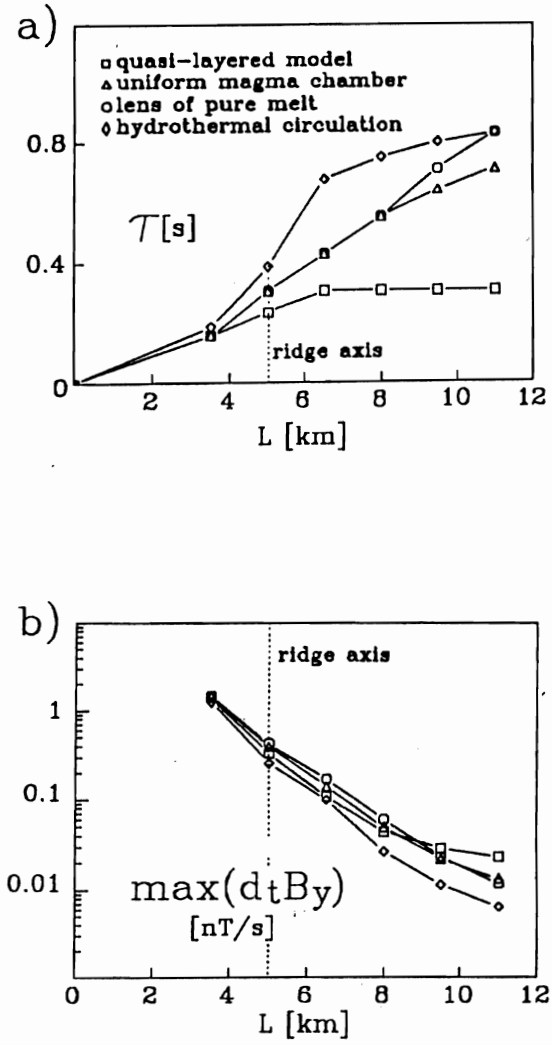

Fig.5.10 The relationship between diffusion time τ and Tx–Rx separation L for the various conductivity models shown in Fig.2.3*a–d* (*a*). The asymptotic behaviour of τ at large L is due to the availability of a fast diffusion path through resistive gabbros. Interpretation of the (τ,L) curves is similar to that of seismic refraction first arrival times. The relationship between response amplitude and Tx–Rx separation (*b*), for the various conductivity models.

Chapter 6

2.5–D Analytical & Numerical Modeling

6.0 Introduction

With very few exceptions, all of the modeling described so far in this thesis has involved transient electromagnetic excitation of 1–D or 2–D earth conductivity structures by means of infinite line sources. These two dimensional numerical models are relatively low–cost and may be used to assist seafloor controlled–source data interpretation (Chapter 4) and experimental design (Chapter 5). Major limitations of the models discussed so far are that infinite sources can never be actualized, and conversion factors which relate electromagnetic responses from an infinite source to those from compact ones are available only for special and simple earth geometries. A more advanced numerical model employing a finite source description can overcome these deficiencies, at the cost of generating a greater computational load. In this chapter I describe a finite source, 2.5–D (*i.e.* 3–D source, 2–D earth) forward modeling algorithm, its finite element implementation and some numerical analysis in terms of its convergence properties. The program models time–dependent electromagnetic fields that are generated in the earth after activation of a seafloor horizontal electric dipole (HED). The earth can be described by an arbitrary two dimensional conductivity function $\sigma(x, z)$; the $\hat{y}$–direction is once again along–strike. Before going into details about the solution technique, I wish to put this model into perspective by indicating through examples from the literature the current state of 2.5–D and 3–D controlled–source electromagnetic modeling.

An early, successful attempt at solving the 2.5–D electromagnetic problem in the

frequency domain on land using finite difference methods was published by Stoyer and Greenfield (1976), who solved for the along–strike field components $E_y(\mathbf{r}, w)$ and $B_y(\mathbf{r}, w)$ that would arise from excitation of a 2–D earth by a point magnetic dipole. The authors found agreement between their numerical results and analytic solutions for a homogenous half–space as well as three dimensional analog model data. Later, Stodt (1978) formulated the same problem in terms of secondary along–strike field components using a finite element method but did not present numerical results. As computers became more powerful through the past decade, a consensus emerged that the fully three dimensional electromagnetic forward problem is at least *as tractable* as the 2.5–D problem, causing interest in the latter to ebb. As a result, very few researchers after Stoyer and Greenfield seriously attacked the 2.5–D problem. But despite the significant advances in computing power, the 3–D controlled–source electromagnetic problem has still not been solved by either finite difference (Adhidjaja and Hohmann 1989) or finite element (Pridmore *et.al.* 1981) methods, although numerous integral equation formulations (*e.g.* Hohmann 1975), even in the time domain (San Filipo and Hohmann 1985, Newman *et.al.* 1986), have met with great success. The integral equation technique, however, is limited to modeling electromagnetic responses from confined bodies in an otherwise homogenous or layered earth.

In the past year or two, interest in finite element solutions to the 2.5–D problem in the frequency domain, particularly with regard to buried dipole sources, has resurged. Flossadottir and Cox (1989) and Unsworth *et.al.* (1990) have presented solutions for seafloor dipole sources, the latter authors reporting very fast execution times for an iterative computation of secondary E_y and B_y field components. Smith *et.al.* (1990) describe a solution, again in the frequency domain, designed for use in interpreting data from coal seams exploration. Their solution for the along–strike total field components employs a nested dissection of the finite element matrix which reduces the amount of computer storage required.

There is no appearance in the literature, at least in a geophysical context, of

a solution to the transient 2.5–D problem. I have attacked the problem following somewhat the philosophy of Stoyer and Greenfield. Finite element approximations to the along–strike magnetic $\overline{b}_y(x,q,z,s)$ and electric $\overline{e}_y(x,q,z,s)$ field components are obtained in the spatial wavenumber q and Laplace frequency s domains, and then sine and cosine transforms are performed to transform the components into the spatial domain, *i.e.* to obtain $\overline{B}_y(\mathbf{r},s)$ and $\overline{E}_y(\mathbf{r},s)$. Finally, the Gaver–Stehfest inverse Laplace transform (see Appendix A for its derivation and Chapter 4 for applications), is used to get the desired transient solutions $B_y(\mathbf{r},t)$ and $E_y(\mathbf{r},t)$. In §6.1–6.4 of the thesis, I shall describe in detail the algorithm and finite element implementation and then in §6.5 discuss errors, convergence and extrapolation properties of the code. In Chapter 7, I shall describe results from a model study to illustrate the utility of the 2.5–D program.

6.1 The Hertz Vector and Double Half–Space Solutions

To find exact solutions to electromagnetic boundary value problems (BVPs) involving compact sources such as the HED, it has often proven convenient although not necessary to employ the Hertz vector, denoted by Π, in terms of which the entire electromagnetic field $\mathbf{E}$ and $\mathbf{B}$ in conductors may be written (*e.g.* Wangsness 1979). In this section of the thesis, as there are no exact solutions available for a 3–D source and 2–D earth problem, I will calculate the Hertz vector $\overline{\Pi}(\mathbf{r},s)$ in the Laplace domain for the following simple 3–D source, 1–D earth problem. The source current density is that of the HED, given by equation (3.17), and the earth is modeled by a conductivity profile $\sigma(z)$ which corresponds to the double half–space geometry, *i.e.*

$$\sigma(z) = \begin{cases} \sigma_0 & z>0 \\ \sigma_1 & z<0. \end{cases} \tag{6.1}$$

Following the calculation, the along–strike components $\overline{E}_y(\mathbf{r},s)$ and $\overline{B}_y(\mathbf{r},s)$ of the electromagnetic field may be obtained from the components of the Hertz vector. An exact solution to a 3–D source, 1–D earth problem such as the one just described is

useful because it provides a standard by which to estimate errors and analyze the convergence properties of a 2.5–D code.

In accordance with the quasi–static approximation and the other simplifications described in §3.1, the governing partial differential equations for marine electromagnetic problems are Maxwell's equations, in the form given by (3.3) and (3.10). In the Laplace domain, this pair of equations becomes

$$\nabla \times \overline{\mathbf{E}}(\mathbf{r}, s) = -s\overline{\mathbf{B}}(\mathbf{r}, s) \tag{6.2}$$

$$\nabla \times \overline{\mathbf{B}}(\mathbf{r}, s) = \mu_0 \sigma(\mathbf{r})\overline{\mathbf{E}}(\mathbf{r}, s) + \mu_0 \overline{\mathbf{J}}_S(\mathbf{r}, s). \tag{6.3}$$

Following Sommerfeld (1926), the Hertz vector $\overline{\mathbf{\Pi}}(\mathbf{r}, s)$ when written in the Laplace domain is *defined* in terms of the electromagnetic field $\overline{\mathbf{E}}(\mathbf{r}, s)$ and $\overline{\mathbf{B}}(\mathbf{r}, s)$ by:

$$\overline{\mathbf{B}}(\mathbf{r}, s) = \mu_0 \sigma(\mathbf{r}) \nabla \times \overline{\mathbf{\Pi}}(\mathbf{r}, s) \tag{6.4}$$

$$\overline{\mathbf{E}}(\mathbf{r}, s) = -\mu_0 \sigma(\mathbf{r}) s\overline{\mathbf{\Pi}}(\mathbf{r}, s) + \nabla \left[\nabla \cdot \overline{\mathbf{\Pi}}(\mathbf{r}, s)\right]. \tag{6.5}$$

Combining equations (6.1–6.5) leads to the diffusion equations obeyed by the Hertz vector

$$\nabla^2 \overline{\mathbf{\Pi}}(\mathbf{r}, s) - \mu_0 \sigma_i s \overline{\mathbf{\Pi}}(\mathbf{r}, s) = \frac{\overline{\mathbf{J}}_S(\mathbf{r}, s)}{\sigma_i}, \quad i = 0, 1 \tag{6.6}$$

which are valid respectively in the upper (i=0, sea) and lower (i=1, earth) uniformly conducting half–spaces. Consider $\mathbf{J}_S$ to be generated by an $\hat{x}$–directed HED lying on the seafloor at the origin of the co–ordinates and stepped–on at time t=0. It follows from symmetry considerations that $\overline{\Pi}_y(\mathbf{r}, s)$ vanishes (Wait 1961), and the exact solutions to equations (6.6) in the two media (see Appendix B for a derivation) for this source can be separated into the following components:

$$\overline{\Pi}_x^{\text{sea}}(\mathbf{r}, s) = \frac{P}{2\pi\sigma_0 s} \int_0^\infty \frac{\exp(-u_0 z)}{u_0 + u_1} \lambda J_0(\lambda\rho)\, d\lambda \quad z > 0 \tag{6.7a}$$

$$\overline{\Pi}_x^{\text{earth}}(\mathbf{r}, s) = \frac{P}{2\pi\sigma_1 s} \int_0^\infty \frac{\exp(u_1 z)}{u_0 + u_1} \lambda J_0(\lambda\rho)\, d\lambda \quad z < 0 \tag{6.7b}$$

$$\overline{\Pi}_y^{\text{sea}} = \overline{\Pi}_y^{\text{earth}} = 0 \tag{6.8}$$

and finally,

$$\overline{\Pi}_z^{\text{sea}}(\mathbf{r},s) = \frac{-P}{2\pi\sigma_0\mu_0 s^2}\frac{\partial}{\partial x}\int_0^\infty \frac{(u_0-u_1)\exp(-u_0 z)}{\sigma_1 u_0+\sigma_0 u_1}\lambda J_0(\lambda\rho)\,d\lambda \quad z>0 \tag{6.9a}$$

$$\overline{\Pi}_z^{\text{earth}}(\mathbf{r},s) = \frac{-P}{2\pi\sigma_1\mu_0 s^2}\frac{\partial}{\partial x}\int_0^\infty \frac{(u_0-u_1)\exp(u_1 z)}{\sigma_1 u_0+\sigma_0 u_1}\lambda J_0(\lambda\rho)\,d\lambda \quad z<0. \tag{6.9b}$$

In equations (6.7) and (6.9), $J_0(\lambda\rho)$ is a Bessel function of zero order, $\rho=\sqrt{x^2+y^2}$ and $u_i=\sqrt{\lambda^2+\mu_0\sigma_i s}$ with i=0,1. The along–strike electromagnetic components can be written in terms of the above Hertz vector components by separating out the $\hat{y}$ component of equations (6.4) and (6.5), *i.e.:*

$$\overline{B}_y(\mathbf{r},s) = \mu_0\sigma\left(\frac{\partial\overline{\Pi}_x(\mathbf{r},s)}{\partial z} - \frac{\partial\overline{\Pi}_z(\mathbf{r},s)}{\partial x}\right) \tag{6.10}$$

$$\overline{E}_y(\mathbf{r},s) = \frac{\partial^2\overline{\Pi}_x(\mathbf{r},s)}{\partial x\partial y} + \frac{\partial^2\overline{\Pi}_z(\mathbf{r},s)}{\partial y\partial z}. \tag{6.11}$$

The above expressions may be evaluated and plotted as a contour map in order to illustrate typical patterns induced in the sea and the earth by the along–strike components of the electromagnetic fields after activation of an HED source. For example, contours of constant along–strike magnetic field component $\overline{B}_y(\mathbf{r},s)$, which is given in the sea and the earth by

$$\overline{B}_y^{\text{sea}}(\mathbf{r},s) = \frac{-\mu_0 P}{2\pi s}\int_0^\infty \left[\frac{u_0+R\partial_{xx}}{u_0+u_1}\right]\exp(-u_0 z)\lambda J_0(\lambda\rho)\,d\lambda \tag{6.12a}$$

$$\overline{B}_y^{\text{earth}}(\mathbf{r},s) = \frac{\mu_0 P}{2\pi s}\int_0^\infty \left[\frac{u_1-R\partial_{xx}}{u_0+u_1}\right]\exp(u_1 z)\lambda J_0(\lambda\rho)\,d\lambda \tag{6.12b}$$

where

$$R \equiv \frac{\sigma_1-\sigma_0}{\sigma_1 u_0+\sigma_0 u_1} \tag{6.13}$$

are shown in Figure 6.1 for the range $0\leq y\leq 3$ km along–strike and s=1 Hz. The geometry is the double half–space, with the conductivity of the sea σ=3.0 S/m and that of the earth σ=1.0 S/m. The HED, situated at the origin at the center of the

12 km × 12 km plots and oriented horizontally, is of strength P=1.0 A·m. The figure shows the decay with distance along–strike in the magnitude of $\overline{B}_y$, and that an "image" of the dipole becomes buried into the more resistive earth as y increases. In the vertical plane of the dipole, y=0, the pattern of the contours resemble current streamlines for the H–polarization mode, see the upper right plot in Figure 3.1. The along–strike magnetic field component $\overline{B}_y(\mathbf{r}, s)$ is symmetric under the interchange $y \rightarrow -y$, as may be seen from equation (6.12).

The along–strike electric field component $\overline{E}_y(\mathbf{r}, s)$, given by

$$\overline{E}_y^{\text{sea}} = \frac{P}{2\pi\sigma_0 s} \int_0^\infty \left[\frac{1 - u_0 R}{u_0 + u_1}\right] \exp(-u_0 z)\lambda \frac{\partial^2 J_0(\lambda\rho)}{\partial x \partial y}\, d\lambda \qquad (6.14a)$$

$$\overline{E}_y^{\text{earth}} = \frac{P}{2\pi\sigma_1 s} \int_0^\infty \left[\frac{1 + u_1 R}{u_0 + u_1}\right] \exp(u_1 z)\lambda \frac{\partial^2 J_0(\lambda\rho)}{\partial x \partial y}\, d\lambda, \qquad (6.14b)$$

is shown contoured in the sea and the earth conducting half–spaces in Figure 6.2. The along–strike electric field vanishes in the vertical plane of the dipole, reflecting the anti–symmetric nature of $\overline{E}_y$ with respect to the interchange $y \rightarrow -y$. As y increases, the contours of constant along–strike electric component extend increasingly more distant from the HED until a maximum spatial extent is reached (for the parameters chosen, this occurs at y=1–2 km), and then the field magnitude decays back to zero for larger along–strike offsets. It is also of interest to note that the positions of the maxima in the magnitude of $\overline{E}_y$ move out horizontally along the seafloor with increasing distance along–strike.

6.2 Double Half–Space Analytical Solutions in the (q, s) Domain

Since the finite element algorithm, which will be outlined in detail in the next section of the thesis, solves for the along–strike field components in the spatial wavenumber domain, double half–space analytic solutions for these components in this domain are desired in order to fix a local boundary condition near the source. A local condition is imposed due to the fact that there exists a singularity in the analytic solution at

the location of the source. As indicated in §4.1, this singularity must be avoided numerically to keep the problem well–posed. The analytic solutions also provide a standard from which to evaluate finite element approximation errors.

In the derivation of the along–strike components $\overline{b}_y(q,s)$ and $\overline{e}_y(q,s)$, several types of integral transforms will be used, so for convenience I will list them here. To begin with, consider an arbitrary function $\overline{F}(y,s)$ of the spatial co–ordinate y and the Laplace frequency s. The function is related to its transform $\overline{f}(q,s)$ in the wavenumber domain by means of the Fourier transform pair

$$\overline{f}(q,s) = \int_{-\infty}^{\infty} \overline{F}(y,s) \mathrm{e}^{iqy}\, dy \tag{6.15}$$

$$\overline{F}(y,s) = \frac{1}{2\pi} \int_{-\infty}^{\infty} \overline{f}(q,s) \mathrm{e}^{-iqy}\, dq. \tag{6.16}$$

For arbitrary functions $\overline{F}(x,y,s)$ of two spatial co–ordinates, the double Fourier transform pair is

$$\overline{f}(p,q,s) = \int_{-\infty}^{\infty}\int_{-\infty}^{\infty} \overline{F}(x,y,s) \mathrm{e}^{ipx+iqy}\, dx\, dy \tag{6.17}$$

$$\overline{F}(x,y,s) = \frac{1}{4\pi^2} \int_{-\infty}^{\infty}\int_{-\infty}^{\infty} \overline{f}(p,q,s) \mathrm{e}^{-ipx-iqy}\, dp\, dq. \tag{6.18}$$

For those functions in which the two spatial variables x and y occur only in the combination $\rho=\sqrt{x^2+y^2}$, *i.e.* $\overline{F}(x,y,s)= \overline{F}(\sqrt{x^2+y^2},s)$ the double Fourier inverse transform (6.18) is related to the Hankel (Fourier–Bessel) transform

$$\overline{F}(\rho,s) = \int_0^{\infty} \overline{f}(\lambda,s)\lambda J_0(\lambda\rho)\, d\lambda \tag{6.19}$$

by means of the formula:

$$\int_0^{\infty} \overline{f}(\lambda,s)\lambda J_0(\lambda\rho)\, d\lambda = \frac{1}{2\pi} \int_{-\infty}^{\infty}\int_{-\infty}^{\infty} \overline{f}(\sqrt{p^2+q^2},s) \mathrm{e}^{-ipx-iqy}\, dp\, dq. \tag{6.20}$$

Now, as the first step towards deriving $\overline{b}_y(q,s)$ and $\overline{e}_y(q,s)$, the Fourier transform pair (6.15,6.16) can be used to transform equations (6.10) and (6.11) into the wavenumber q domain. The resulting equations, which involve spatial derivatives

of the Hertz vector components, are easily solved if equation (6.20) is first used to translate the Hertz vector components from Hankel transforms into double Fourier transforms. As an example, the Hertz vector $\hat{x}$–component is in the required form $\overline{\Pi}(\rho, z, s)$ for (6.20) to be applicable. It is found that

$$\overline{\Pi}_x^{\text{sea}}(x, y, z, s) = \frac{P}{4\pi^2 \sigma_0 s} \int_{-\infty}^{\infty} \int_{-\infty}^{\infty} \frac{\exp(-\overline{u}_0 z)}{\overline{u}_0 + \overline{u}_1} \mathrm{e}^{-ipx - iqy} \, dp \, dq \tag{6.21}$$

where $\overline{u}_i = \sqrt{p^2 + q^2 + \mu_0 \sigma_i s}$ with i=0,1. There is a similar expression in terms of the double Fourier integral (6.20) for $\overline{\Pi}_x^{\text{earth}}(x, y, z, s)$. The Hertz vector $\hat{z}$–components (6.9), on the other hand, are not quite in the form $\overline{\Pi}_z(\rho, z, s)$ since they possess the partial derivative with respect to x, and $\partial_x \sqrt{x^2 + z^2} \neq f(\rho)$. The $\hat{z}$–components can, however, be written in a convenient form $\overline{\Pi}_z(\mathbf{r}, s) = \partial_x \overline{F}(\rho, z, s)$, *i.e.* as a spatial derivative of a Hankel transform of ρ. To translate this form into a double Fourier transform, it is helpful to consider the x derivative of the double Fourier integral (6.20), namely

$$\partial_x \overline{F}(\rho, s) = \frac{-i}{2\pi} \int_{-\infty}^{\infty} \int_{-\infty}^{\infty} p \overline{f}(\sqrt{p^2 + q^2}, s) \mathrm{e}^{-ipx - iqy} \, dp \, dq. \tag{6.22}$$

Applying (6.22) to the Hertz component (6.9a), gives the desired result

$$\overline{\Pi}_z^{\text{sea}}(x, y, z, s) = \frac{iP}{4\pi^2 \mu_0 \sigma_0 s^2} \int_{-\infty}^{\infty} \int_{-\infty}^{\infty} \left[\frac{p(\overline{u}_0 - \overline{u}_1)}{\sigma_1 \overline{u}_0 + \sigma_0 \overline{u}_1} \right] \exp(-\overline{u}_0 z) \mathrm{e}^{-ipx - iqy} \, dp \, dq \tag{6.23}$$

with a similar expression for the Hertz component $\overline{\Pi}_z^{\text{earth}}(x, y, z, s)$ following almost immediately.

Now that both $\hat{x}$ and $\hat{z}$ Hertz vector components have been translated from Hankel transforms into double Fourier transforms, it is a simple matter to find expressions for $\overline{b}_y(x, q, z, s)$ and $\overline{e}_y(x, q, z, s)$, which is the desired result of this section. First, consider the magnetic component. From equations (6.10), (6.20) and (6.22) it follows that

$$\overline{B}_y^{\text{sea}} = \frac{-\mu_0 P}{4\pi^2 s^2} \int_{-\infty}^{\infty} \int_{-\infty}^{\infty} \left[\frac{s \overline{u}_0}{\overline{u}_0 + \overline{u}_1} + \frac{p^2(\overline{u}_0 - \overline{u}_1)}{\mu_0(\sigma_1 \overline{u}_0 + \sigma_0 \overline{u}_1)} \right] \exp(-\overline{u}_0 z) \mathrm{e}^{-ipx - iqy} \, dp \, dq. \tag{6.24}$$

Upon comparison of the above expression with equation (6.16), which defines the 1–D Fourier inverse transform, the kernel $\overline{b}_y^{\text{sea}}(q,s)$ can be identified as:

$$\overline{b}_y^{\text{sea}}(x,q,z,s) = \frac{-\mu_0 P}{2\pi s^2}\int_{-\infty}^{\infty}\left[\frac{s\overline{u}_0}{\overline{u}_0+\overline{u}_1}+\frac{p^2(\overline{u}_0-\overline{u}_1)}{\mu_0(\sigma_1\overline{u}_0+\sigma_0\overline{u}_1)}\right]\exp(-\overline{u}_0 z)\mathrm{e}^{-ipx}\,dp. \tag{6.25}$$

This above expression may be simplified. The pair of terms in the above square brackets are *even* functions of p, thus the formula

$$\int_{-\infty}^{\infty}\overline{f}(p)\mathrm{e}^{-ipx}\,dp = \begin{cases} 2\int_0^{\infty}\overline{f}(p)\cos(px)\,dp & f(p),\ \text{even} \\ -2i\int_0^{\infty}\overline{f}(p)\sin(px)\,dp & f(p),\ \text{odd} \end{cases} \tag{6.26}$$

is used to write $\overline{b}_y^{\text{sea}}(q,s)$ in its final form as a cosine transform:

$$\overline{b}_y^{\text{sea}}(q,s) = \frac{-\mu_0 P}{\pi s^2}\int_0^{\infty}\left[\frac{s\overline{u}_0}{\overline{u}_0+\overline{u}_1}+\frac{p^2(\overline{u}_0-\overline{u}_1)}{\mu_0(\sigma_1\overline{u}_0+\sigma_0\overline{u}_1)}\right]\exp(-\overline{u}_0 z)\cos(px)\,dp \tag{6.27}$$

and similarly in the lower half–space there exists another cosine transform

$$\overline{b}_y^{\text{earth}}(q,s) = \frac{\mu_0 P}{\pi s^2}\int_0^{\infty}\left[\frac{s\overline{u}_1}{\overline{u}_0+\overline{u}_1}+\frac{p^2(\overline{u}_0-\overline{u}_1)}{\mu_0(\sigma_1\overline{u}_0+\sigma_0\overline{u}_1)}\right]\exp(\overline{u}_1 z)\cos(px)\,dp. \tag{6.28}$$

Contours of the above function are shown in Figure 6.3 as a function of position in the x/z–plane for a set of wavenumbers in the range $0 \le q \le 0.003$ m^{-1} and s=1 Hz. The same HED source and earth geometry as in Figures 6.1–2 is used. The contours of $\overline{b}_y(q,s)$ have the same shape as those for y=0 in Figure 6.1, but the magnitude of $\overline{b}_y(q,s)$ tends to zero as q increases. In Figure 6.4, plotted for various distances x (in units of skin depths) from the source, appears the seafloor quantity $\overline{b}_y(x,q,z{=}0)/\overline{b}_y^{\max}$, where $\overline{b}_y^{\max}$ has been evaluated at the value of $q = q_{\max}$ which maximizes $\overline{b}_y(q)$ for a given x. This normalization is done simply to ensure that the ordinate range is from –1 to 1 regardless of the distance from the source, and then all curves can be shown clearly on the same axes. The curves in Figure 6.4 will be used later in this chapter to check the finite element program and aid measurements of its convergence properties.

The along–strike electric component $\overline{e}_y(q,s)$ can be evaluated in a procedure almost identical to that which enabled the expressions (6.27) and (6.28) to be found

for the magnetic component. The main difference between the two calculations is that $\overline{E}_y(\mathbf{r}, s)$ contains a pair of terms which are *odd* functions of p, so from equation (6.26) it is clear that $\overline{e}_y(q, s)$ is imaginary and can be written as sine transforms. The quantity $i\overline{e}_y(q, s)$ is real, however, and given by

$$i\overline{e}_y^{\text{sea}}(q, s) = \frac{-qP}{\pi\sigma_0 s^2} \int_0^\infty \left[\frac{ps}{\overline{u}_0 + \overline{u}_1} + \frac{p\overline{u}_0(\overline{u}_0 - \overline{u}_1)}{\mu_0(\sigma_1\overline{u}_0 + \sigma_0\overline{u}_1)} \right] \exp(-\overline{u}_0 z)\sin(px)\, dp, \quad (6.29)$$

$$i\overline{e}_y^{\text{earth}}(q, s) = \frac{-qP}{\pi\sigma_1 s^2} \int_0^\infty \left[\frac{ps}{\overline{u}_0 + \overline{u}_1} - \frac{p\overline{u}_1(\overline{u}_0 - \overline{u}_1)}{\mu_0(\sigma_1\overline{u}_0 + \sigma_0\overline{u}_1)} \right] \exp(\overline{u}_1 z)\sin(px)\, dp, \quad (6.30)$$

The above function, which vanishes at both $q \to 0$ and $q \to \infty$, is shown contoured as a function of position in Figure 6.5 and, after normalization as described above, for various values of x along the seafloor in Figure 6.6. The curves in the latter plot will also be used to evaluate errors in the finite element approximation.

6.3 The 2.5-D PDE System

Having established some analytical solutions that may be used to check later numerical results, in this section I will derive the set of governing PDEs for the 2.5–D problem. The relevant Maxwell's equations from which to attack the 2.5–D problem numerically are given by equations (6.2) and (6.3) but with $\mathbf{J}_S(\mathbf{r}, s)$=0. This pair of equations may be combined to give vector diffusion equations, as was done in Chapter 3. The vector equations are 3×3 systems of partial differential equations (PDEs) where the independent variables are the components of either **E** or **B**. With the two dimensional earth conductivity $\sigma(x, z)$, however, it is possible to reduce the dimensions of the partial differential system to 2×2, in which case the independent variables become along–strike magnetic $\overline{b}_y(q, s)$ and electric $i\overline{e}_y(q, s)$ field components in the spatial wavenumber q domain (Stoyer and Greenfield 1976). The reduction by one in the number of PDEs that need to be solved affords a great reduction in both computer time and storage. Also, if the equations are to be solved by a finite element approximation, formulation of them in the wavenumber domain as described

above permits straightforward triangulation of a two dimensional mesh and avoids the numerical difficulties (Barton and Cendes 1987) and programming complexity associated with solving vector diffusion equations over tetrahedral or brick elements in a three dimensional mesh.

To begin, Ampere's Law (6.3) and Faraday's Law (6.2) must be transformed into the wavenumber domain and then resolved into their $\hat{x}$,$\hat{y}$,$\hat{z}$ components. The six component equations that result are then manipulated into just a pair of equations for the along–strike components $\overline{b}_y(q,s)$ and $\overline{e}_y(q,s)$. This is accomplished by eliminating the four $\hat{x}$ and $\hat{z}$ components of $\overline{\mathbf{b}}$ and $\overline{\mathbf{e}}$; the procedure is as follows. In the wavenumber domain, where the operator $\nabla=(\partial_x,\partial_y,\partial_z)$ becomes $\nabla_q=(\partial_x,-iq,\partial_z)$, the along–strike ($\hat{y}$) component of Ampere's Law (6.3) without the source term is

$$\frac{\partial \overline{b}_x}{\partial z} - \frac{\partial \overline{b}_z}{\partial x} = \mu_0 \sigma \overline{e}_y \tag{6.31}$$

and the orthogonal components (*i.e.* $\hat{x}$ and $\hat{z}$) of Faraday's Law (6.2) are

$$\left(s + \frac{q^2}{\mu_0 \sigma}\right) \overline{b}_z = \frac{iq}{\mu_0 \sigma} \frac{\partial \overline{b}_y}{\partial z} - \frac{\partial \overline{e}_y}{\partial x} \tag{6.32}$$

$$\left(s + \frac{q^2}{\mu_0 \sigma}\right) \overline{b}_x = \frac{iq}{\mu_0 \sigma} \frac{\partial \overline{b}_y}{\partial x} + \frac{\partial \overline{e}_y}{\partial z}. \tag{6.33}$$

Eliminating $\overline{b}_x$ and $\overline{b}_z$ from the above set of three equations leaves a single equation in $\overline{b}_y$ and $\overline{e}_y$, which is:

$$\frac{\partial}{\partial x}\left(\frac{\sigma}{u^2}\frac{\partial \overline{e}_y}{\partial x}\right) + \frac{\partial}{\partial z}\left(\frac{\sigma}{u^2}\frac{\partial \overline{e}_y}{\partial z}\right) - \sigma \overline{e}_y - \frac{iq}{\mu_0}\frac{\partial}{\partial x}\left(\frac{1}{u^2}\frac{\partial \overline{b}_y}{\partial z}\right) + \frac{iq}{\mu_0}\frac{\partial}{\partial z}\left(\frac{1}{u^2}\frac{\partial \overline{b}_y}{\partial x}\right) = 0 \tag{6.34}$$

where $u=\sqrt{q^2+\mu_0\sigma s}$. This is the first PDE of the 2×2 system. The second PDE is found by combining the along–strike component of Faraday's Law (6.2):

$$\frac{\partial \overline{e}_z}{\partial x} - \frac{\partial \overline{e}_x}{\partial z} = s\overline{b}_y \tag{6.35}$$

with the orthogonal components of Ampere's Law (6.3) without sources:

$$\left(\frac{q^2}{s} + \mu_0 \sigma\right) \overline{e}_z = \frac{iq}{s}\frac{\partial \overline{e}_y}{\partial z} + \frac{\partial \overline{b}_y}{\partial x} \tag{6.36}$$

$$\left(\frac{q^2}{s}+\mu_0\sigma\right)\bar{e}_x=\frac{iq}{s}\frac{\partial\bar{e}_y}{\partial x}-\frac{\partial\bar{b}_y}{\partial z}. \tag{6.37}$$

and eliminating the components $\bar{e}_x$ and $\bar{e}_z$. There results

$$\frac{\partial}{\partial x}\left(\frac{s}{u^2}\frac{\partial\bar{b}_y}{\partial x}\right)+\frac{\partial}{\partial z}\left(\frac{s}{u^2}\frac{\partial\bar{b}_y}{\partial z}\right)-s\bar{b}_y+iq\frac{\partial}{\partial x}\left(\frac{1}{u^2}\frac{\partial\bar{e}_y}{\partial z}\right)-iq\frac{\partial}{\partial z}\left(\frac{1}{u^2}\frac{\partial\bar{e}_y}{\partial x}\right)=0. \tag{6.38}$$

Following Stoyer and Greenfield (1976), multiplication of (6.34) by $i\mu_0$ and writing the resulting equation alongside (6.38) yields the desired 2×2 system:

$$\begin{pmatrix} \partial_x\left(\frac{s}{u^2}\partial_x\right)+\partial_z\left(\frac{s}{u^2}\partial_z\right)-s & q\partial_x\left(\frac{1}{u^2}\partial_z\right)-q\partial_z\left(\frac{1}{u^2}\partial_x\right) \\ q\partial_x\left(\frac{1}{u^2}\partial_z\right)-q\partial_z\left(\frac{1}{u^2}\partial_x\right) & \partial_x\left(\frac{\mu_0\sigma}{u^2}\partial_x\right)+\partial_z\left(\frac{\mu_0\sigma}{u^2}\partial_z\right)-\mu_0\sigma \end{pmatrix}\begin{pmatrix}\bar{b}_y\\ i\bar{e}_y\end{pmatrix}=0 \tag{6.39}$$

The 2×2 partial differential operator matrix in the above system of equations is both real and symmetric. The coupling of the two PDEs is evidenced by the appearance of non–zero off–diagonal terms in the operator matrix. Note, however, that for the zero wavenumber case, q=0, the above system de–couples into the two *independent* H–polarization and E–polarization modes:

$$\begin{pmatrix} \partial_x\left(\frac{1}{\sigma}\partial_x\right)+\partial_z\left(\frac{1}{\sigma}\partial_z\right)-\mu_0 s & 0 \\ 0 & \partial_x^2+\partial_z^2-\mu_0\sigma s \end{pmatrix}\begin{pmatrix}\bar{b}_y(q=0,s)\\ \bar{e}_y(q=0,s)\end{pmatrix}=0. \tag{6.40}$$

The separate 2–D polarized equations indicated in equation (6.40) have been solved already in Chapter 4, cf. equations (4.20) and (4.52). The mode separation occurring at zero wavenumber suggests that the effect of replacing an infinite source with a finite source (which need not be an HED) is simply to couple the equations for the along–strike electromagnetic field components, provided the earth has only a 2–D structure and Maxwell's equations have been transformed into the along–strike wavenumber domain.

6.4 2.5–D Finite Element Formulation

In this section of the thesis I shall describe the finite element solution of an electromagnetic boundary value problem (BVP) based on the system of PDEs (6.39). To

avoid singularities, the BVP must be solved over a domain which does not include source locations. The theory of finite element approximations on perturbed solution domains is reviewed in §4.1, and the notation in this section is kept consistent. For example, $\overline{b}_y^{\rm h}$ and $i\overline{e}_y^{\rm h}$ shall denote the exact solution to the system of PDEs over a perturbed domain $\Omega_{\rm h}$. The 2.5–D BVP may be phrased in terms of five equations, these include the 2×2 system of PDEs plus four other equations representing boundary conditions for the along–strike components $\overline{b}_y^{\rm h}$ and $i\overline{e}_y^{\rm h}$, and are given by:

$$\mathbf{\Lambda}\begin{pmatrix}\overline{b}_y^{\rm h}\\ i\overline{e}_y^{\rm h}\end{pmatrix}=0,\quad (x,z)\in\Omega_{\rm h}, q\geq 0, s>0 \tag{6.41a}$$

$$\overline{b}_y^{\rm h}(x_0,q,z_0,s)=0\quad (x_0,z_0)\in\partial\Omega_{\rm h0} \tag{6.41b}$$

$$i\overline{e}_y^{\rm h}(x_0,q,z_0,s)=0\quad (x_0,z_0)\in\partial\Omega_{\rm h0} \tag{6.41c}$$

$$\overline{b}_y^{\rm h}(x_1,q,z_1,s)=\begin{cases}\overline{b}_y^{\rm sea}(x,q,z,s) & z>0\\ \overline{b}_y^{\rm earth}(x,q,z,s) & z<0,\end{cases}\quad (x_1,z_1)\in\partial\Omega_{\rm h1} \tag{6.41d}$$

$$i\overline{e}_y^{\rm h}(x_1,q,z_1,s)=\begin{cases}i\overline{e}_y^{\rm sea}(x,q,z,s) & z>0\\ i\overline{e}_y^{\rm earth}(x,q,z,s) & z<0,\end{cases}\quad (x_1,z_1)\in\partial\Omega_{\rm h1}, \tag{6.41e}$$

with $\mathbf{\Lambda}$ the 2×2 partial differential operator matrix in equation (6.39). Note from the boundary conditions (6.41*b*,*c*) that the along–strike field components are assumed to vanish on the outer boundary of the mesh $\partial\Omega_{\rm h0}$ and from (6.41*d*,*e*) they are assumed to be equal to the double half–space analytic solutions (6.26–6.29) on the inner boundary $\partial\Omega_{\rm h1}$. Assumptions similar to these were also made during the numerical solution of the 2–D problems in Chapter 4. The finite element approximate solution to the above BVP is denoted by the two–vector $\tilde{\mathbf{u}}^{\rm h}$ and is written as a linear combination of the basis functions $\alpha_i(x,z), i=$ 1,2,...,N defined by equation (4.11), specifically:

$$\tilde{\mathbf{u}}^{\rm h}\equiv\begin{pmatrix}\tilde{\overline{b}}_y^{\rm h}\\ \\ i\tilde{\overline{e}}_y^{\rm h}\end{pmatrix}=\sum_{j=1}^{N-M}\begin{pmatrix}a_{1j}\\ \\ a_{2j}\end{pmatrix}\alpha_j(x,z)+\sum_{k=N-M_1+1}^{N}\begin{pmatrix}b_{1k}\\ \\ b_{2k}\end{pmatrix}\alpha_k(x,z). \tag{6.42}$$

The nodes have been numbered as they were for the 2–D problems, *i.e.* the mesh contains N nodes in total, of which M_0 are on the outer mesh boundary, M_1 are

on the inner mesh boundary and $M=M_0+M_1$. Since there are $N-M$ nodes in the interior of the mesh and two unknowns for every interior node, there are a total of $2(N-M)$ unknown co–efficients to be solved for, which are given by:

$$\begin{pmatrix} a_{1j} \\ \\ a_{2j} \end{pmatrix} = \begin{pmatrix} \tilde{\overline{b}}^{\mathrm{h}}_y(x_j, z_j) \\ \\ i\tilde{\overline{e}}^{\mathrm{h}}_y(x_j, z_j) \end{pmatrix} \quad j = 1, ..., N - M. \tag{6.43}$$

The co–efficients that are known *a priori* through the boundary conditions are those corresponding to nodes on the outer boundary of the mesh

$$b_{1k} = b_{2k} = 0 \quad k = N - M + 1, ..., N - M_1 \tag{6.44}$$

and those corresponding to nodes located on the inner boundary

$$\begin{pmatrix} b_{1k} \\ \\ b_{2k} \end{pmatrix} = \begin{pmatrix} \overline{b}^{\mathrm{h}}_y(x_k, z_k) \\ \\ i\overline{e}^{\mathrm{h}}_y(x_k, z_k) \end{pmatrix} \quad k = N - M_1 + 1, ..., N. \tag{6.45}$$

In equation (6.45), the right hand side is given by the double half–space analytic expressions (6.26–6.29) which were derived from the Hertz vector in §6.2.

A first order finite element method consists of solving for $\tilde{\mathbf{u}}^{\mathrm{h}}$ from the set of equations

$$\left(\mathbf{\Lambda} \tilde{\mathbf{u}}^{\mathrm{h}}, \begin{pmatrix} \alpha_l \\ \alpha_l \end{pmatrix} \right)_{\Omega \mathrm{h}} = 0, \quad l = 1, ..., N - M \tag{6.46}$$

where $(\cdot,\cdot)_{\Omega \mathrm{h}}$ is the Euclidean inner product defined in equation (4.8). The discretization of the BVP (6.41) by means of approximating the exact solution $\mathbf{u}^{\mathrm{h}}$ by $\tilde{\mathbf{u}}^{\mathrm{h}}$ leads to the 2×2–block matrix equation

$$\mathbf{\Gamma a} = \mathbf{g}. \tag{6.47}$$

A typical element $\mathbf{\Gamma}_{jl}$ of the block finite element matrix $\mathbf{\Gamma}$ is actually a 2×2 matrix of the form

$$\mathbf{\Gamma}_{jl} = \begin{pmatrix} \beta_{jl} - s\,(\alpha_j, \alpha_l)_{\Omega \mathrm{h}} & q\gamma_{jl} \\ \\ q\gamma_{jl} & \beta'_{jl} - \mu_0 \sigma\,(\alpha_j, \alpha_l)_{\Omega \mathrm{h}} \end{pmatrix}. \tag{6.48}$$

The elements of the matrix in equation (6.48) are expressible in terms of inner products over derivatives of the basis functions, as such:

$$\beta_{jl} = -\left(\frac{s}{u^2}\frac{\partial\alpha_j}{\partial x}\frac{\partial\alpha_l}{\partial x}\right)_{\Omega h} - \left(\frac{s}{u^2}\frac{\partial\alpha_j}{\partial z}\frac{\partial\alpha_l}{\partial z}\right)_{\Omega h} \tag{6.49}$$

$$\beta'_{jl} = -\left(\frac{\mu_0\sigma}{u^2}\frac{\partial\alpha_j}{\partial x}\frac{\partial\alpha_l}{\partial x}\right)_{\Omega h} - \left(\frac{\mu_0\sigma}{u^2}\frac{\partial\alpha_j}{\partial z}\frac{\partial\alpha_l}{\partial z}\right)_{\Omega h} \tag{6.50}$$

$$\gamma_{jl} = \left(\frac{1}{u^2}\frac{\partial\alpha_j}{\partial x}\frac{\partial\alpha_l}{\partial z}\right)_{\Omega h} - \left(\frac{1}{u^2}\frac{\partial\alpha_j}{\partial z}\frac{\partial\alpha_l}{\partial x}\right)_{\Omega h} \tag{6.51}$$

All of the inner products listed above are analytic, *i.e.* there is no numerical quadrature over triangular elements required. Finally, an element $\mathbf{g}_l$ of the RHS vector $\mathbf{g}$ in equation (6.47) is itself a 2–vector and is given by

$$\mathbf{g}_l = \begin{pmatrix} g_{1l} \\ \\ g_{2l} \end{pmatrix} = -\sum_{k=N-M_1+1}^{N} \Gamma_{kl} \begin{pmatrix} b_{1k} \\ \\ b_{2k} \end{pmatrix} \tag{6.52}$$

while an element $\mathbf{a}_j$ of the solution vector $\mathbf{a}$ is given by the 2–vector in equation (6.43). As was the case for the two dimensional H– and E–polarization discrete systems of equations solved in Chapter 4, the linear system (6.47) associated with the 2.5–D problem is solved by Gaussian elimination using subroutines from the NAG math library, and the mesh is once again that generated by the program TRIMESH.

Once the system $\mathbf{\Gamma a = g}$ has been solved, the transient solutions $B_y(y,t)$ and $E_y(y,t)$ may be approximated on the interior nodes by combining an inverse sine or cosine transform (equations 6.16 and 6.26) with the Gaver–Stehfest inverse Laplace transform (equations 3.45 and 3.46). The finite element approximation yields $\tilde{\bar{b}}_y^{\,h}$ and $\tilde{\imath\bar{e}}_y^{\,h}$, from which the transient solutions are approximated by

$$B_y(x_j,y,z_j,t) \approx \frac{\ln 2}{t}\int_0^\infty \sum_{l=1}^{n} V_l(n)\tilde{\bar{b}}_y^{\,h}\left(x_j,q,z_j,\frac{l\ln 2}{t}\right)\cos(qy)\,dq, \quad n,\text{even} \tag{6.54}$$

and

$$E_y(x_j,y,z_j,t) \approx \frac{-\ln 2}{t}\int_0^\infty \sum_{l=1}^{n} V_l(n)\tilde{\imath\bar{e}}_y^{\,h}\left(x_j,q,z_j,\frac{l\ln 2}{t}\right)\sin(qy)\,dq, \quad n,\text{even} \tag{6.55}$$

with j=1,...,N-M. The inverse transforms indicated above are performed using the methods described in Chapter 3. The finite element linear system must be solved for several values of the wavenumber q before the inverse sine and cosine transforms can be done. A rule of thumb has developed, through considerable trial and error, that wavenumbers are best chosen spaced logarithmically at about three per decade over the range of q in which the function to be inverted varies with wavenumber. To ensure that the function to be inverted has been sampled adequately, it is advisable to choose wavenumbers at four or even five per decade and solve equations (6.54) and (6.55) again, making sure the results do not change to within a required tolerance. Transient solutions as part of a model study will be presented in Chapter 7 of the thesis, the remainder of this chapter will be taken up with numerical analysis of the finite element approximation in the (q, s)–domain.

6.5 Errors and Convergence Properties

In §4.5, the relative error of the finite element approximation to the solution $\overline{B}_y(x, z, s)$ of the two dimensional H–polarization problem was found to converge according to $O(h)$, where h is the mesh triangle size. In this section, to study convergence of the approximate solution to the 2.5–D problem, the governing BVP (6.41) has been solved on two meshes; a coarse one of N=736 nodes containing triangles of size h and a finer one of $4N\approx$2880 nodes containing triangles of size $h/2$. The fine mesh is generated from the coarse mesh by dividing every triangle of the latter into four smaller triangles, as indicated in Figure 4.1*d*. Figures 6.7*a*,*b* show contours of the percent relative errors in both along–strike components $\overline{b}_y(q, s)$ and $i\overline{e}_y(q, s)$ on the mesh of size h as a function of position in the lower half–space of a double half–space conductivity model with a 3:1 conductivity contrast. The seafloor z=0 lies along the top of the figure, the HED occupies the upper left corner, and the boundary of the figure is a square whose sides are one Laplace domain skin depth, cf. Figure 4.2. The errors are evaluated based on comparing the output from the finite element program

with the analytic solutions to the double half–space problem derived in §6.2. For both components, as indicated in Figures 6.8*a* and 6.8*b*, the percent relative error on the mesh of size $h/2$ decreases everywhere within the plot boundary by a factor of two, the possible exceptions are near the corners of $\partial\Omega_h$, see §4.5. These results indicate that the convergence rate is $O(h)$, *i.e.* the finite element implementation of the 2.5–D problem is optimal.

In Figure 6.9*a* the finite element approximant $\tilde{\overline{b}}_y^h(x, q, z{=}0, s)$ appropriately normalized, is compared to the exact solution $\overline{b}_y(x, q, z{=}0, s)/\overline{b}_y^{max}$ plotted earlier in Figure 6.4. The dotted lines represent the numerical solution, which was performed on a mesh of size $h/2$. The misfit between the numerical and the analytic solution (solid lines) is indicative of the approximation error. Note that the misfit becomes greater as x, the distance along the seafloor from the HED, becomes smaller. In Figure 6.9*b*, similar results for the electric component are displayed. The misfit in the electric component is much less than that for the magnetic component. This is most likely due to the fact that there is a discontinuity in the vertical derivative of the magnetic component at the seafloor, but no discontinuity in any derivative of the electric component, and that linear finite element interpolating polynomials best resolve smooth functions.

6.6 An Extrapolation Formula

In this section of the thesis, I will describe an extrapolation technique which permits very low (<1–3%) relative errors to be achieved, using quite coarse ($N{\approx}3000$) meshes. The idea of using extrapolation of inaccurate numerical solutions to achieve greater accuracy is evident in Figure 6.10, where the analytic solution $\overline{b}_y(q, s)$ is plotted against corresponding approximate solutions on meshes of size h (squares) and $h/2$ (triangles). Let $\overline{b}_y^h$ be the numerical solution on the mesh of size h and $\overline{b}_y^{h/2}$ be the numerical solution on the mesh of size $h/2$. If the order of convergence of these

numerical solutions is *exactly* $O(h)$, then the following relationship holds:

$$\bar{b}_y = 2\bar{b}_y^{h/2} - \bar{b}_y^{h}. \tag{6.56}$$

Equation (6.56) expresses the fact that, if the finite element approximation is optimal, points on the curve representing the solution on mesh $h/2$ should lie half way between the analytic solution and the solution on mesh h. This appears to be the case in Figure 6.10. Figure 6.11 shows the extrapolated numerical solutions plotted, as a dotted line, against the analytical solutions. The extrapolation greatly reduces the misfit, and the relationship (6.56) is always satisfied to less than 3% relative accuracy.

Figure 6.12 shows that extrapolation can lead to accurate results even at nodes on the mesh where the individual numerical solutions $\bar{b}_y^{\,h}$ and $\bar{b}_y^{h/2}$ badly approximate the analytic solution. The plot corresponds to a node situated at z=0 and x=0.056δ_1^s, where δ_1^s is the skin depth in the lower conducting medium. This location on the seafloor is very close to the inner boundary of the mesh and is one where finite element solutions (triangles and squares) *most* poorly approximate the analytic solution (solid line). However, the extrapolated numerical solution (dotted line) still yields remarkable accuracy.

The results from this section suggest that the extrapolation procedure described by equation (6.56) can be used to model, to very high degrees of accuracy, the electromagnetic responses from complicated conductivity structures using relatively coarse meshes. However, the $O(h)$ convergence has been demonstrated explicitly only for the double half–space geometry. Observing how solutions change as a function of the number of nodes N, for more complex models, would test of the generality of the extrapolation procedure.

References

Adhidjaja, J.I. and G.W. Hohmann, 1989. A finite–difference algorithm for the transient electromagnetic response of a three–dimensional body, *Geophys. J. Int.*, **98**, 233–242.

Barton, M.L. and Z.J. Cendes, 1987. New vector finite elements for three–dimensional magnetic field computation, *J. Appl. Phys.*, **61**, 3919–3921.

Flossadottir, A.H. and C.S. Cox, 1989. Two–dimensional modelling of the electromagnetic controlled source response of mid–ocean ridge structures (abstract), *6th Scientific Assembly of I.A.G.A.*, July 25–August 4, 1989, Exeter U.K., I.A.G.A. Bulletin No. 53, p.167.

Hohmann, G.W., 1975. Three–dimensional induced polarization and electromagnetic modeling, *Geophysics*, **40**, 309–324.

Newman, G.A., G.W. Hohmann and W.L. Anderson, 1986. Transient electromagnetic response of a three–dimensional body in a layered earth, *Geophysics*, **51**, 1608–1627.

Pridmore, D.F., G.W. Hohmann, S.H. Ward and W.R. Sill, 1981. An investigation of finite–element modeling for electrical and electromagnetic data in three dimensions, *Geophysics*, **46**, 1009–1024.

San Filipo, W.A. and G.W. Hohmann, 1985. Integral equation solution for the transient electromagnetic response of a three–dimensional body in a conductive half–space, *Geophysics*, **50**, 798–809.

Smith, G.H., P.R. Williamson and K. Vozoff, 1990. The application of nested dissection to the solution of a 2.5D electromagnetic problem, Appl. Comput. Electromag., in press.

Sommerfeld, A., 1926. Über die Ausbreitung der Wellen in der drahtlosen Telegraphie (The propagation of waves in the wireless telegraphy), *Ann. Physik*, **81**, 1135–1153.

Stodt, J., 1978. Application of the finite element method to the finite source 2–D earth EM problem, *Workshop on modeling of electrical and electromagnetic methods, Proceedings*, May 17–19, 1978, Berkeley CA, 8–19.

Stoyer, C.H. and R.J. Greenfield, 1976. Numerical solutions of the response of a two–dimensional earth to an oscillating magnetic dipole source, *Geophysics*, **41**, 519–530.

Unsworth, M.J., A.D. Chave and B.J. Travis, 1990. The electric fields of a horizontal current source at the sea–floor (abstract), *10th Workshop on Electrical Induction in the Earth*, Aug. 22–29, 1990, Ensenada Mexico, I.A.G.A. Working Group I–2.

Wangsness, R.K., 1979. *Electromagnetic Fields*, John Wiley & Sons, New York, NY.

Wait, J.R., 1961. The electromagnetic fields of a horizontal dipole in the presence of a conducting half–space, *Can. J. Phys.*, **39**, 1017–1028.

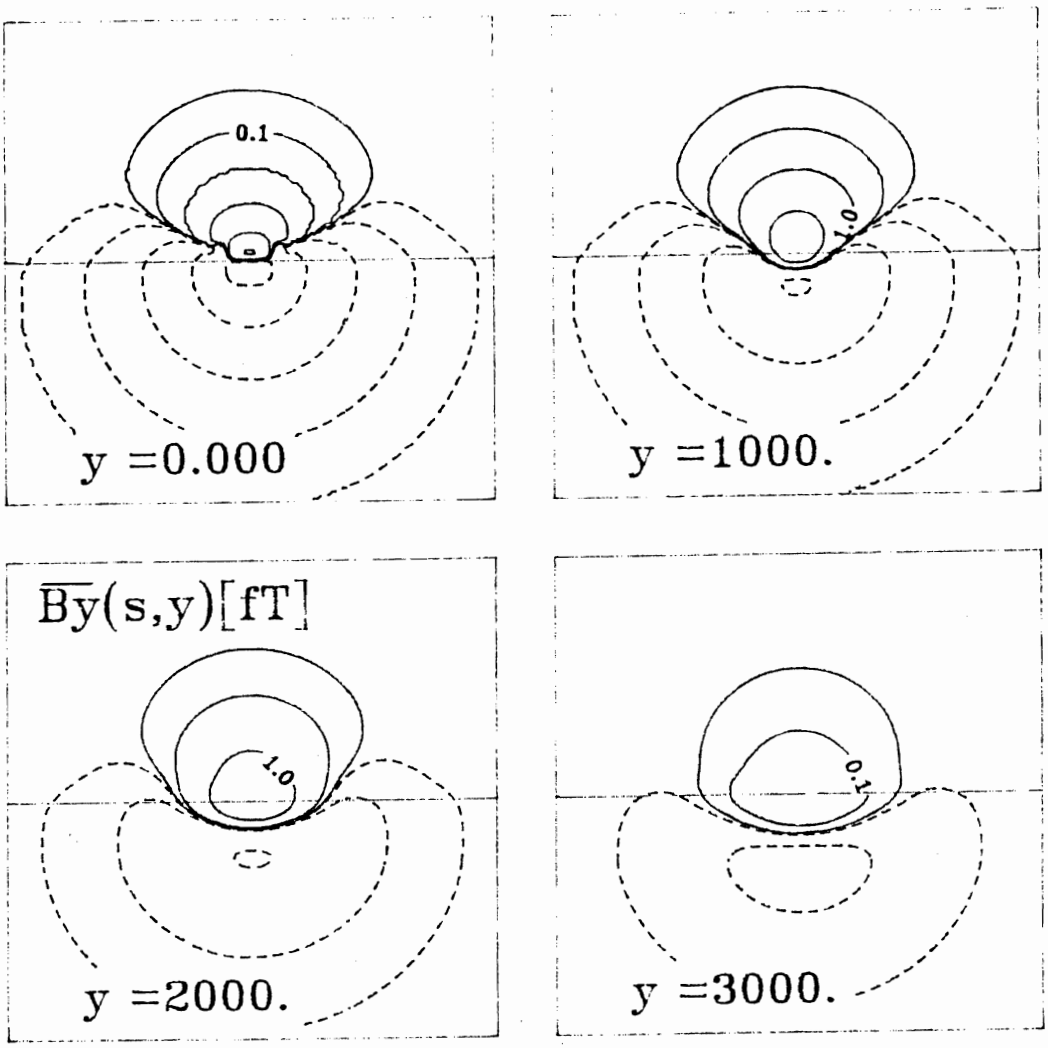

Fig.6.1 Laplace s–domain component $\overline{B}_y(x, y, z, s)$ of the solution to the vector diffusion equation satisfied by the magnetic field **B**, for double half–space electrical structure and a fixed value of s=1 Hz. Contours of $\overline{B}_y$ are shown for various distances y [m] along–strike. The field is produced by a unit moment, horizontal electric dipole (HED) situated at the origin of the Cartesian co–ordinates and is displayed to a depth of 6 km into the lower conductor. The conductivity contrast is 3:1. An "image" of the dipole becomes buried into the more resistive lower conductor as y increases.

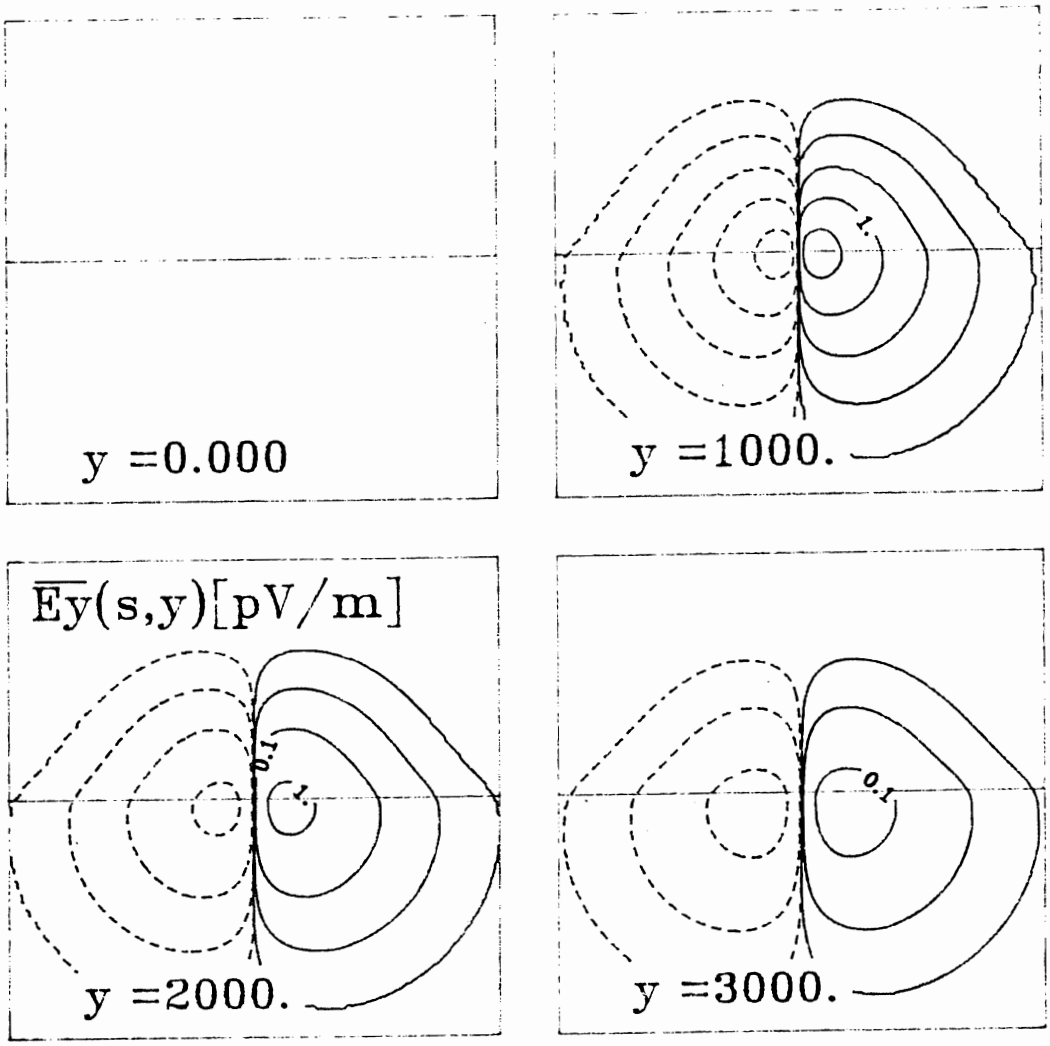

Fig.6.2 Laplace s–domain component $\overline{E}_y(x, y, z, s)$ of the solution to the vector diffusion equation satisfied by the magnetic field **E**, for double half–space electrical structure and a fixed value of s=1 Hz. Contours of $\overline{E}_y$ are shown for various distances y [m] along–strike. This field vanishes at y=0, *i.e.* in–line with the HED source.

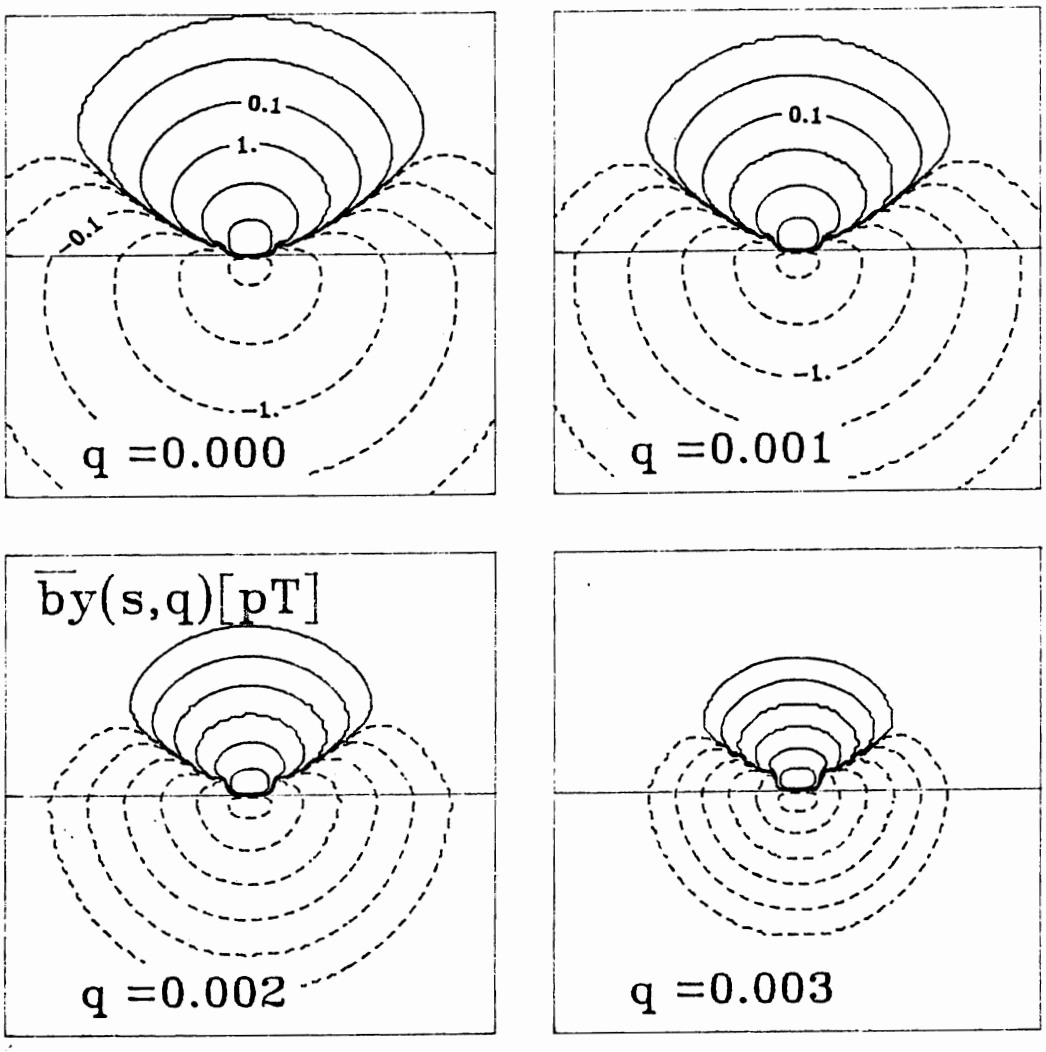

Fig.6.3 Cosine transform of the field $\overline{B}_y(x, y, z, s)$ shown in Fig.6.1 into the along–strike wavenumber q domain. The contours have a similar shape to those in the earlier figure. The magnitude of $\overline{b}_y(x, q, z, s)$ goes to zero as q increases. This field is of importance since it is computed directly by the 2.5–D finite element program.

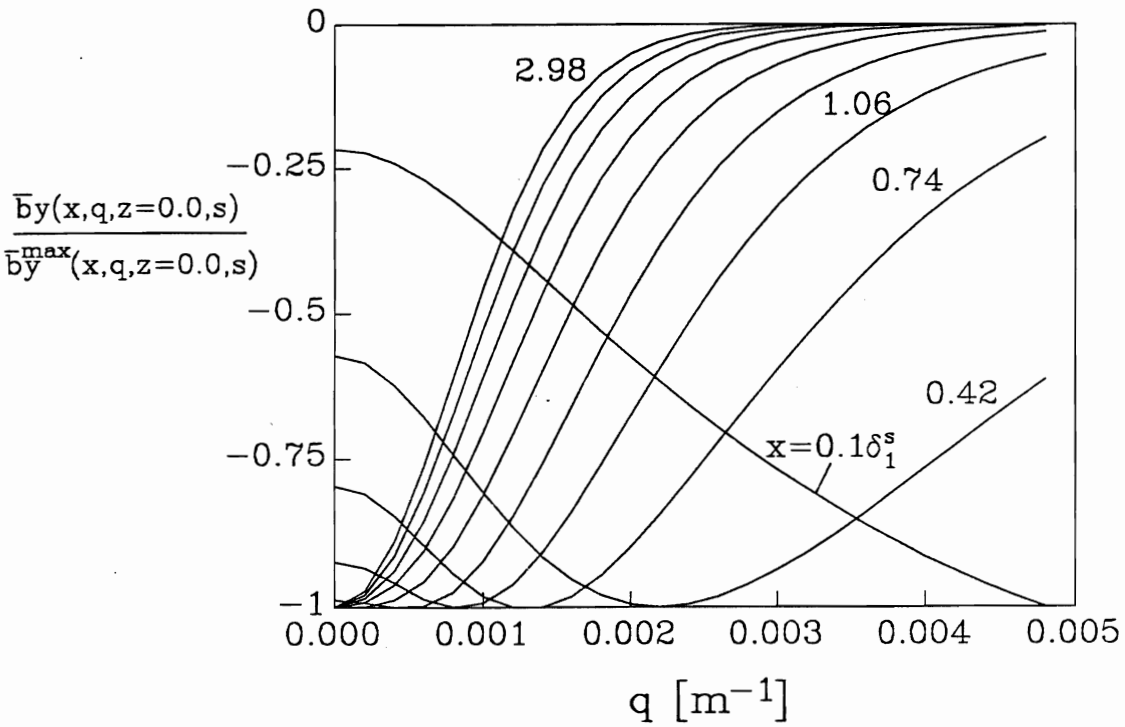

Fig.6.4 Along–strike magnetic component $\bar{b}_y(x, q, z, s)$ as in the previous figure, but normalized, evaluated at the seafloor z=0 for several distances x from the HED source, and plotted as a function of wavenumber q. The curves in this figure may be used as reference curves to check the 2.5–D finite element program and measure its convergence properties. The symbol δ_1^s refers to a skin depth in the lower conductor.

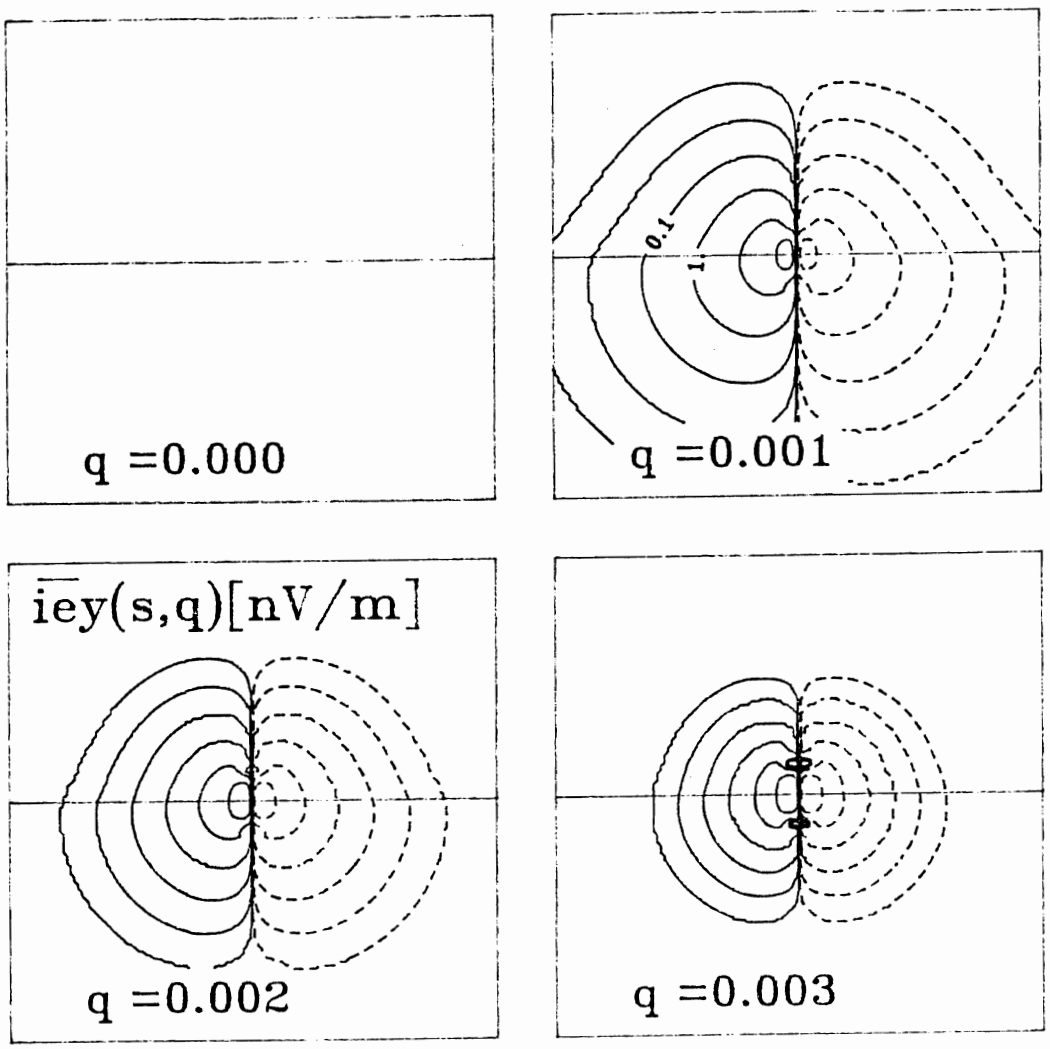

Fig.6.5 Sine transform of the field $\overline{E}_y(x, y, z, s)$ shown in Fig.6.2 into the along–strike wavenumber q domain. The quantity $i\overline{e}_y(x, q, z, s)$ vanishes at both q=0 and as $q \rightarrow \infty$. The field component $i\overline{e}_y$, along with $\overline{b}_y$, is computed directly by the 2.5–D finite element program.

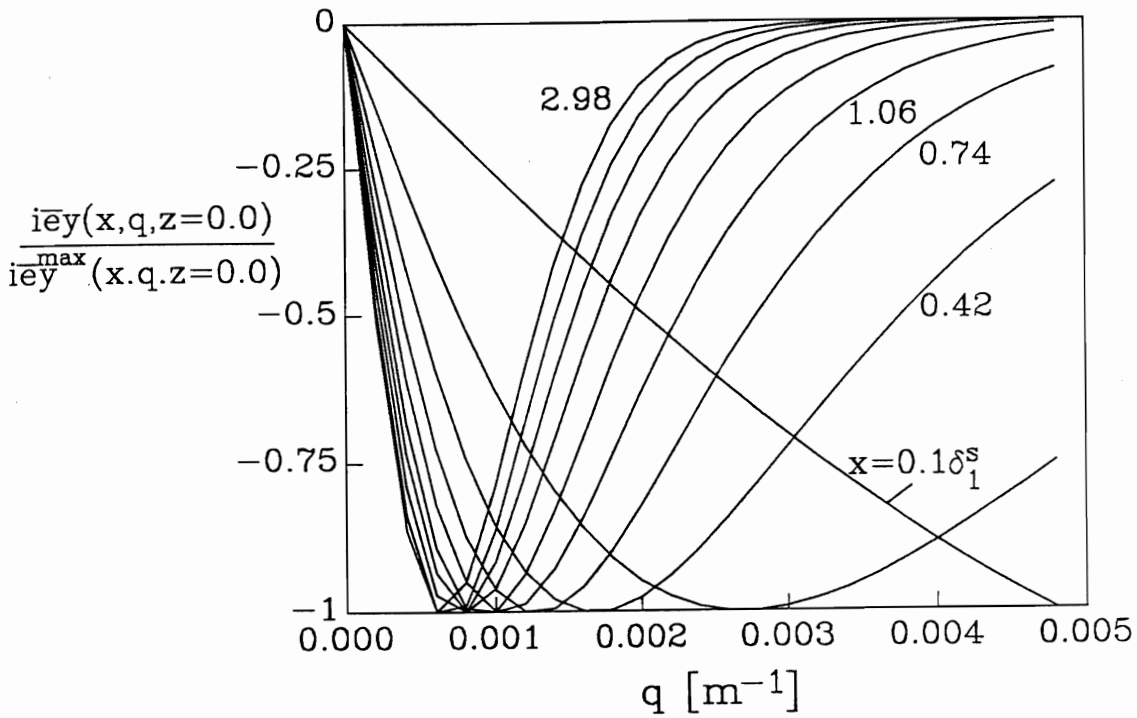

Fig.6.6 Along–strike electric component $i\bar{e}_y(x,q,z,s)$ as in the previous figure, but normalized, evaluated at the seafloor z=0 for several distances x from the HED source, and plotted as a function of wavenumber q. The curves in this figure may be used as reference curves to evaluate the 2.5–D finite element double half–space approximation errors.

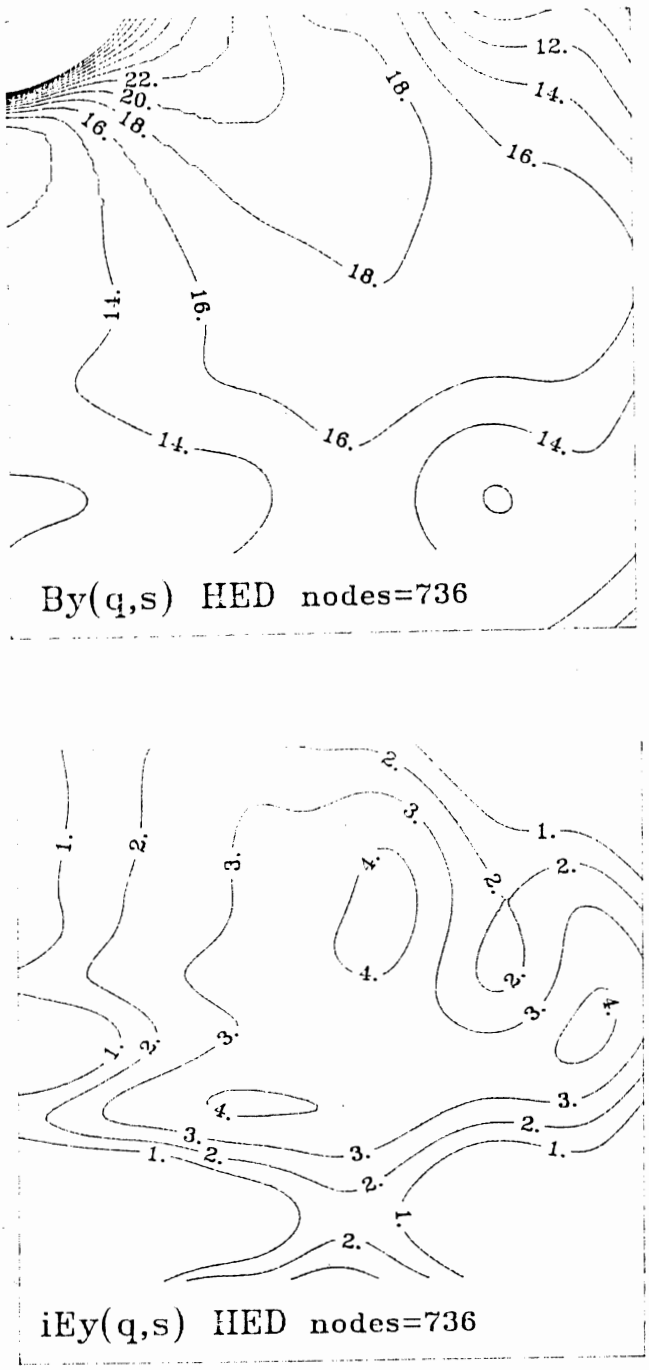

Fig.6.7 Contours of the percent relative error $\epsilon(x,z)$ in components $\overline{b}_y(q,s)$ (a, top) and $i\overline{e}_y(q,s)$ (b, bottom) on a mesh characterized by triangles of size h. The errors are computed by comparing the output from the 2.5–D forward code against an analytic solution to the HED double half–space problem.

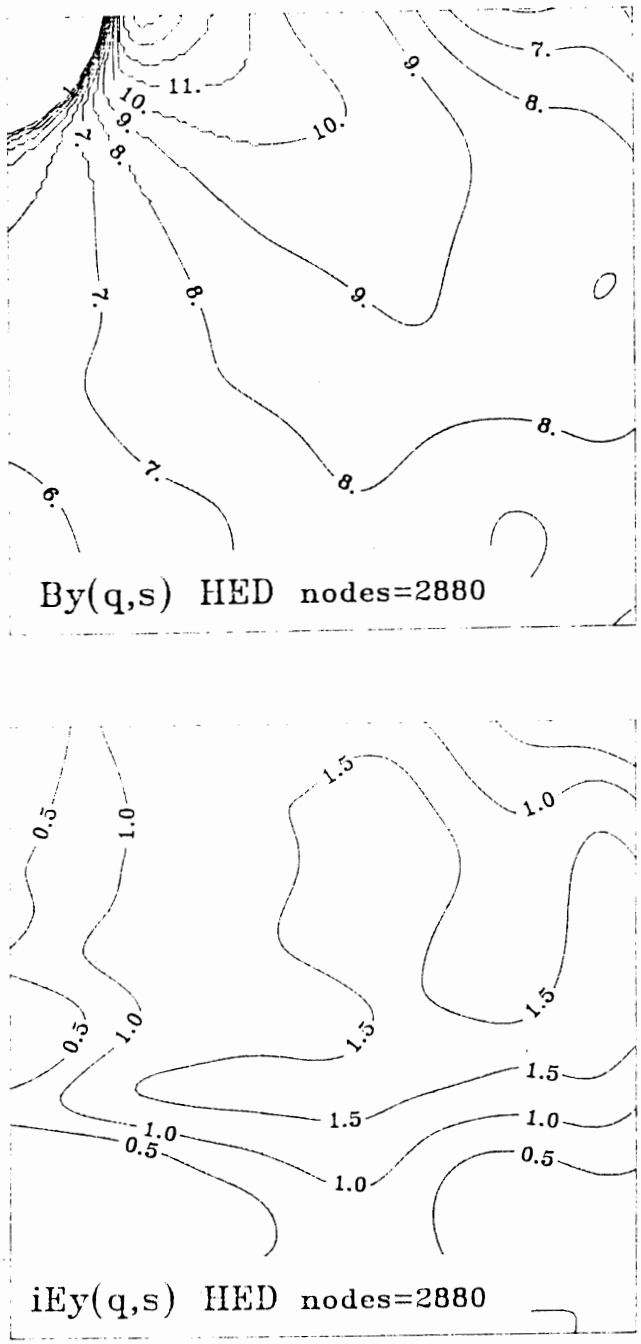

Fig.6.8 Contours of the percent relative error $\epsilon(x,z)$ in components $\overline{b}_y(q,s)$ (a, top) and $i\overline{e}_y(q,s)$ (b, bottom) on a mesh of size $h/2$. The errors in these plots are half those of Fig.6.7, which is consistent with an $O(h)$ convergence of the finite element approximation.

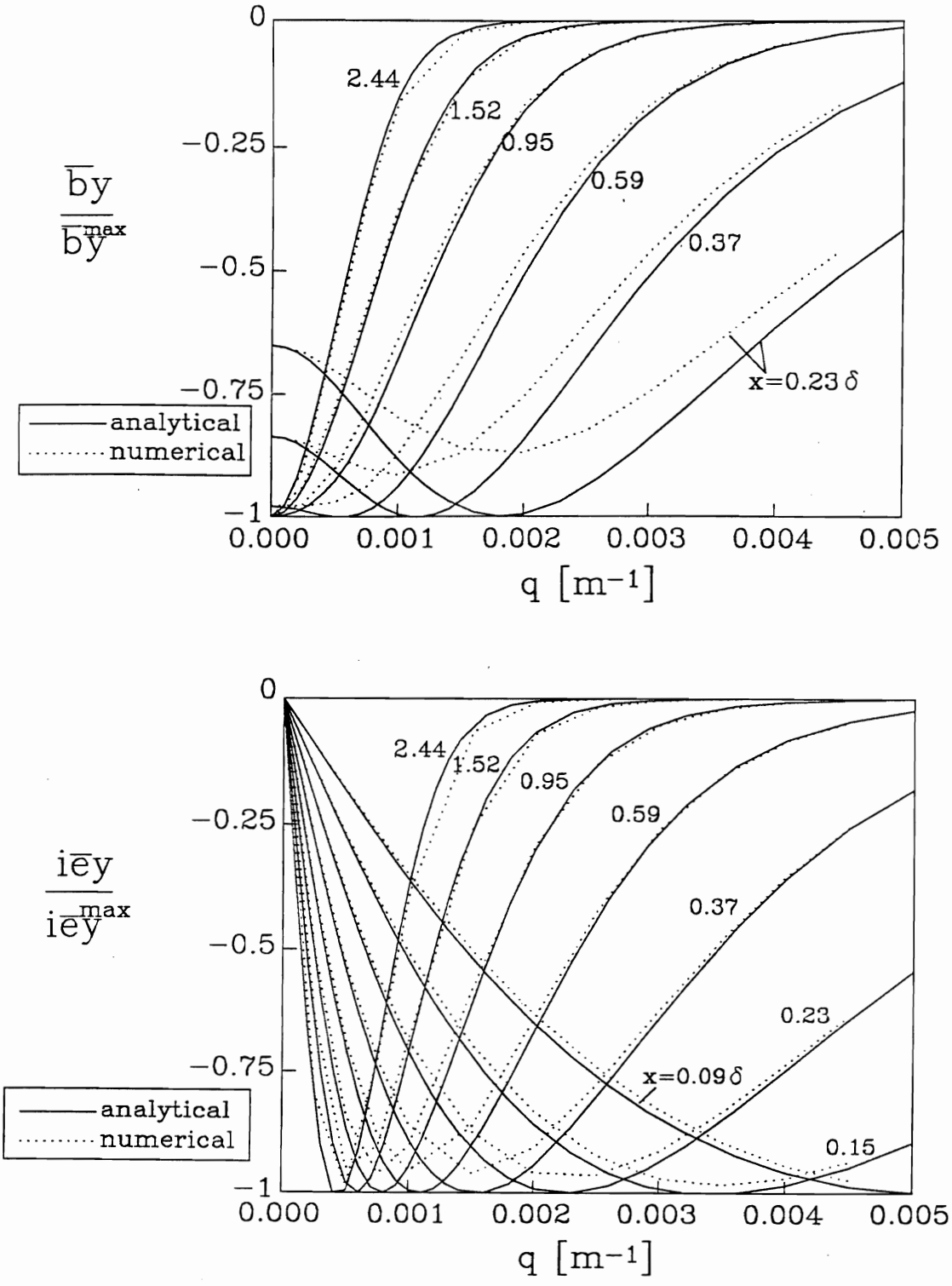

Fig.6.9 Comparison of normalized analytical (solid lines) and numerical (dotted lines) solutions to the 2.5–D HED double half–space problem, with σ_0=3.0 S/m, σ_1=1.0 S/m and s=1 Hz. The misfit between analytical and numerical curves is indicative of the finite element approximation error in $\overline{b}_y$ (a, top) and $i\overline{e}_y$ (b, bottom).

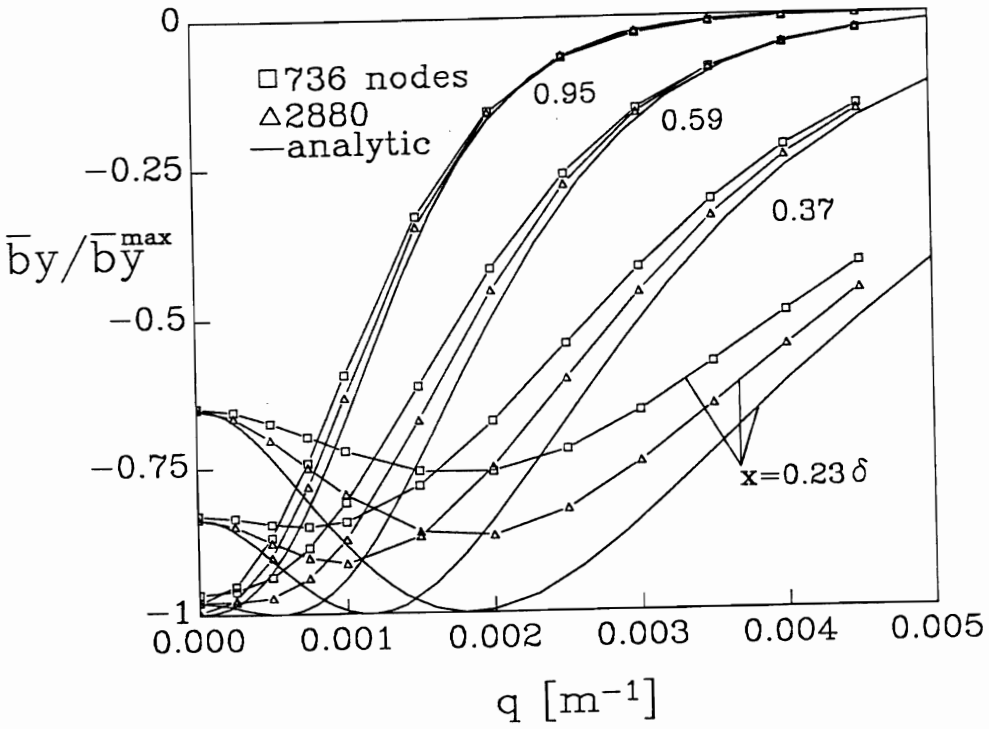

Fig.6.10 Normalized analytical (solid lines) and numerical (squares, mesh size h) $\overline{b}_y$ solutions. These curves are exactly the same as those in Fig.6.9*a*. For this figure, the numerical solution on a mesh of size $h/2$ (triangles) is also shown.

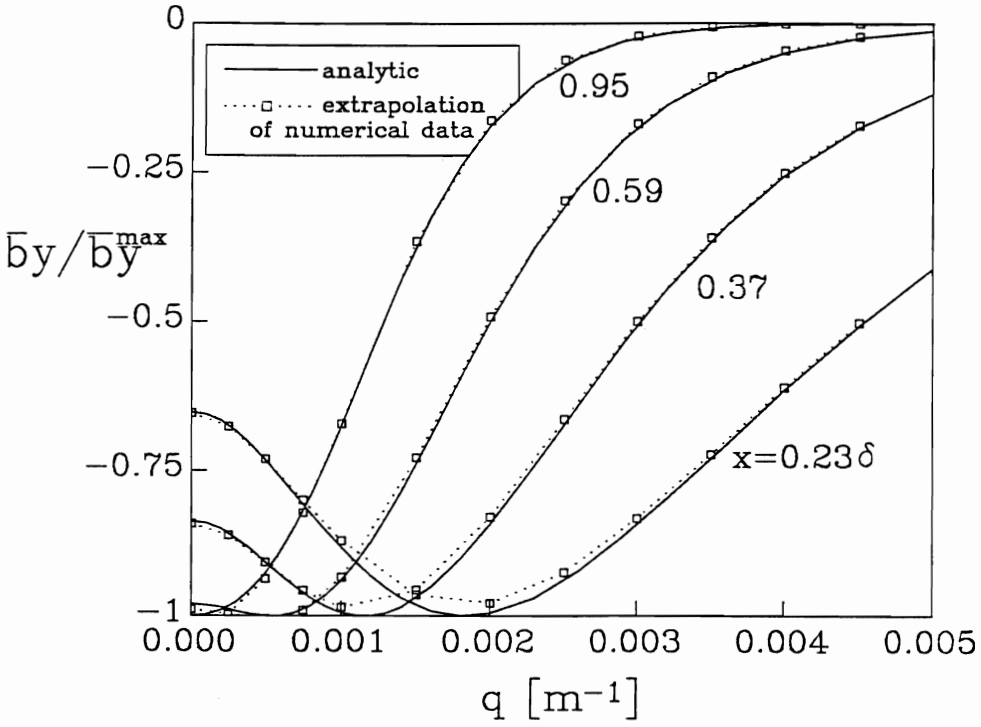

Fig.6.11 Comparison of a normalized analytical solution (solid lines) and a solution (squares) extrapolated from the finite element solutions on meshes of size h and $h/2$ by means of the formula $\overline{b}_y = 2\overline{b}_y^{h/2} - \overline{b}_y^{h}$. A close fit between the two curves is expected if the finite element approximation convergences according to $O(h)$. The appearance of a close fit in this figure suggests that the extrapolation formula given above can be used, in conjunction with the 2.5–D finite element program, to model electromagnetic fields accurately, even on relatively coarse meshes.

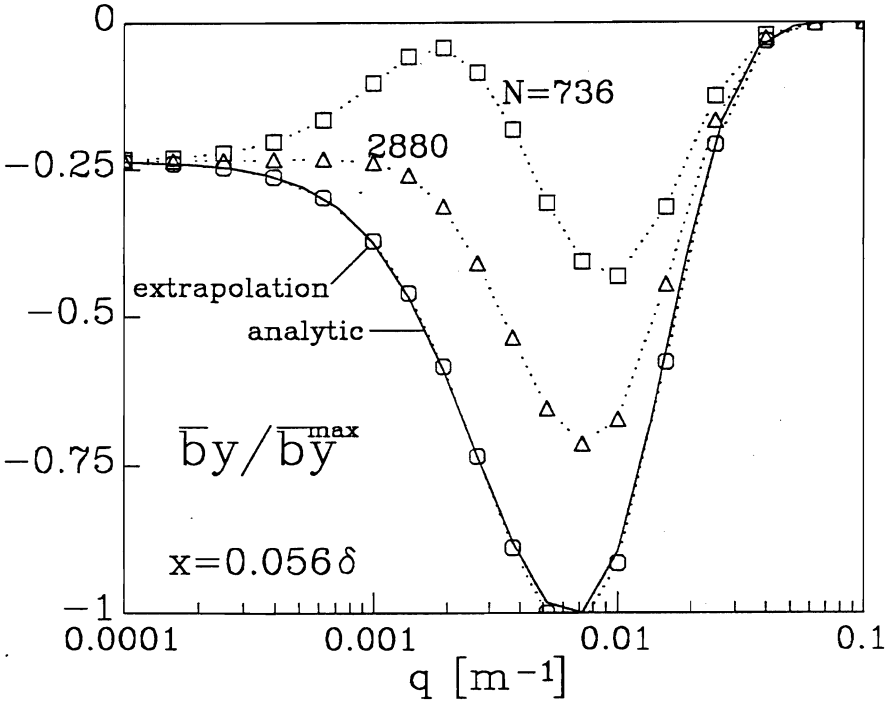

Fig.6.12 The extrapolation formula can be used successfully to obtain a close fit to the analytical solution (solid line) even when the individual numerical solutions (squares, triangles) *very* poorly approximate it. The extrapolated numerical solution is shown as circles in this plot.

Chapter 7

2.5–D Mid–Ocean Ridge Electromagnetics

7.0 Introduction

The purpose of this brief chapter is to present some transient solutions to the 2.5–D electromagnetic boundary value problem based on horizontal electric dipole excitation of a two dimensional mid–ocean ridge electrical model. This is done simply to demonstrate the utility of the 2.5–D code for modeling transient electromagnetic fields produced by point sources lying within two–dimensional conductors of arbitrary geometry, and to illustrate three dimensional, time–varying field patterns in a mid–ocean ridge environment. Variations in the field components $B_y(\mathbf{r},t)$ and $E_y(\mathbf{r},t)$ with time t and with distance y along–strike, at all points (x,z) in the electrical model, are examined qualitatively. It is worth noting here that while the code has been written specifically to assist interpretation of transient CSEM data from mid–ocean ridge–going experiments, it can be used to interpret data from many other places on the seafloor.

7.1 Formulation of a Mid–Ocean Ridge BVP

The electrical model chosen is shown in Figure 7.1, and represents a uniform magma chamber of conductivity σ=0.05 S/m (4.0 S/m), corresponding to 1–2% (60%) partial melt at 1200°C (Shankland and Waff 1977), embedded in an otherwise normal, layered model of young oceanic crust consisting of basalts, gabbros and peridotites (see Chapter 2 for a discussion on the layering of normal oceanic crust). The shape of the

magma chamber is consistent with the seismic reflection data of Detrick *et.al.* (1987) and the refraction data of Harding *et.al* (1989), both collected over the East Pacific Rise near 9°N. Hydrothermal fluid circulation in fractured basalt near the ridge axis is modeled as a continuous band of enhanced electrical conductivity σ=0.3 S/m above the lid of the magma chamber. Circulation extends througout the upper 1.5 km thick basalt layer. The layer of dry gabbros is 4.5 km thick and is assigned a conductivity of σ=0.001 S/m. At the bottom of the model, the upper mantle is assigned a conductivity of $\sigma=10^{-5}$ S/m, consistent with the controlled–source measurements of Cox *et.al.* (1986). The conductivity of the seawater is σ=3.2 S/m.

The finite element–Gaver–Stehfest method, outlined in Chapters 3 and 4, is used to compute the along–strike electromagnetic field components $b_y(x,q,z,t)$ and $e_y(x,q,z,t)$ that arise from excitation of the above model by a horizontal electric dipole. The mesh on which solutions to the governing 2×2 system of diffusion equations (6.39) are obtained is shown in Figure 7.2. The system of equations is solved for several N_q values of the along–strike wavenumber q, and then numerical cosine and sine transforms are used to transform the field components into the spatial domain y, *i.e.* to obtain $B_y(\mathbf{r},t)$ and $E_y(\mathbf{r},t)$. The transforms are performed numerically by a modified version of the software described in A.D. Chave (1983). Specifically, the kernels $b_y(q)$ and $e_y(q)$ of the cosine and sine transforms are computed by the FE—Gaver–Stehfest algorithm at each of N_q discrete values of the wavenumber q, the kernels are then *splined* to obtain a continuous representation of the kernels in the variable q, which is required by Chave's software.

Chave's algorithm automatically integrates the product of the kernel and the trigonometric function between zero crossings of the latter and sums the resulting series of partial integrations using a continued fraction (CF) expansion. Often, the terms in the series alternate in sign due to the oscillatory behaviour of sine and cosine functions, but the CF algorithm, which involves replacing the series by a rapidly converging expression, allows slowly convergent or even divergent integrals to be com-

puted easily and to an accuracy limited by machine precision. Chave uses the method of Häangi *et.al.* (1980) to cast the series of partial integrations into a continued fraction.

When solving the system of equations (6.39), an analytic solution in the along–strike wavenumber, Laplace frequency (q, s) domain is required to fix an exact condition on the inner boundary $\partial\Omega_{\mathrm{h1}}$ of the finite element mesh, see equations (6.41*d*) and (6.41*e*). In the present instance, the inner boundary $\partial\Omega_{\mathrm{h1}}$ is the rectangular cut–out near the center of the mesh shown in Figure 7.2, and it encloses the transmitting location. Analytic solutions for a HED source in air exciting a layered earth are given in Ward and Hohmann (1987). After slight modification to account for the fact that the HED is deployed in seawater, the solutions of Ward and Hohmann can be used to fix the inner boundary condition. The along–strike magnetic and electric field components, suitably modified and written in the (q, s) domain, are given by:

$$\overline{b}_y^{\mathrm{sea}}(q,s) = \frac{\mu_0 P}{2\pi s}\int_0^\infty \left[(1+\overline{r}_{\mathrm{TE}}) - \frac{p^2}{p^2+q^2}(\overline{r}_{\mathrm{TE}}+\overline{r}_{\mathrm{TM}})\right]\exp(-\overline{u}_0 z)\cos(px)\,dp \quad (7.1)$$

$$\overline{b}_y^{\mathrm{earth}}(q,s) = \frac{-\mu_0 P}{2\pi s}\int_0^\infty \left[(1-\overline{r}_{\mathrm{TE}}) + \frac{p^2}{p^2+q^2}(\overline{r}_{\mathrm{TE}}+\overline{r}_{\mathrm{TM}})\right]\exp(\overline{u}_1 z)\cos(px)\,dp \quad (7.2)$$

and

$$i\overline{e}_y^{\mathrm{sea}}(q,s) = \frac{-qP}{2\pi s}\int_0^\infty \frac{p}{p^2+q^2}\left[(1-\overline{r}_{\mathrm{TM}})\frac{\overline{u}_0}{\sigma_0} - (1+\overline{r}_{\mathrm{TE}})\frac{\mu_0 s}{\overline{u}_0}\right]\exp(-\overline{u}_0 z)\sin(px)\,dp \quad (7.3)$$

$$i\overline{e}_y^{\mathrm{earth}}(q,s) = \frac{-qP}{2\pi s}\int_0^\infty \frac{p}{p^2+q^2}\left[(1-\overline{r}_{\mathrm{TM}})\frac{\overline{u}_0}{\sigma_0} - (1+\overline{r}_{\mathrm{TE}})\frac{\mu_0 s}{\overline{u}_0}\right]\exp(\overline{u}_1 z)\sin(px)\,dp \quad (7.4)$$

where $\overline{r}_{\mathrm{TE}}$ and $\overline{r}_{\mathrm{TM}}$ are reflection co–efficients that depend on the conductivity and thickness of the layers and $\overline{u}_i = \sqrt{p^2+q^2+\mu_0\sigma_i s}$. The components $\overline{b}_y^{\mathrm{earth}}$ and $i\overline{e}_y^{\mathrm{earth}}$, as given by equations (7.2) and (7.4) respectively, are valid only in the uppermost layer. The leading P/s term is representative of a Heaviside step–on in the HED dipole moment at time t=0.

Assume that the seafloor has n layers, with the i–th layer of thickness h_i and electrical conductivity σ_i, and that the layering terminates in a half–space, *i.e.* $h_n \rightarrow \infty$. For such a layering, the reflection co–efficient $\overline{r}_{\rm TE}$ is given by

$$\overline{r}_{\rm TE} = \frac{\overline{u}_0 - Y_1}{\overline{u}_0 + Y_1} \tag{7.5}$$

with Y_i defined by a recursion relation

$$Y_i \equiv \overline{u}_i \left[\frac{Y_{i+1} + \overline{u}_i \tanh(\overline{u}_i h_i)}{\overline{u}_i + Y_{i+1} \tanh(\overline{u}_i h_i)} \right], \quad i = 1, ..., n-1 \tag{7.6}$$

and $Y_n = \overline{u}_n$. The other reflection co–efficient $\overline{r}_{\rm TM}$ is given by a similar expression

$$\overline{r}_{\rm TM} = \frac{\overline{u}_0 - \sigma_0 Z_1}{\overline{u}_0 + \sigma_0 Z_1} \tag{7.7}$$

with Z_i defined by the recursion

$$Z_i \equiv \frac{\overline{u}_i}{\sigma_i} \left[\frac{\sigma_i Z_{i+1} + \overline{u}_i \tanh(\overline{u}_i h_i)}{\overline{u}_i + \sigma_i Z_{i+1} \tanh(\overline{u}_i h_i)} \right], \quad i = 1, ..., n-1 \tag{7.7}$$

and $Z_n = \overline{u}_n / \sigma_n$. If the earth is comprised of n=2 layers, the reflection co–efficients are:

$$\overline{r}_{\rm TE} = \frac{\overline{u}_0 \left[\overline{u}_1 + \overline{u}_2 \tanh(\overline{u}_1 h_1) \right] - \overline{u}_1 \left[\overline{u}_2 + \overline{u}_1 \tanh(\overline{u}_1 h_1) \right]}{\overline{u}_0 \left[\overline{u}_1 + \overline{u}_2 \tanh(\overline{u}_1 h_1) \right] + \overline{u}_1 \left[\overline{u}_2 + \overline{u}_1 \tanh(\overline{u}_1 h_1) \right]} \tag{7.8}$$

$$\overline{r}_{\rm TM} = \frac{\overline{u}_0 \sigma_1 \left[\overline{u}_1 \sigma_2 + \overline{u}_2 \sigma_1 \tanh(\overline{u}_1 h_1) \right] - \overline{u}_1 \sigma_0 \left[\overline{u}_2 \sigma_1 + \overline{u}_1 \sigma_2 \tanh(\overline{u}_1 h_1) \right]}{\overline{u}_0 \sigma_1 \left[\overline{u}_1 \sigma_2 + \overline{u}_2 \sigma_1 \tanh(\overline{u}_1 h_1) \right] + \overline{u}_1 \sigma_0 \left[\overline{u}_2 \sigma_1 + \overline{u}_1 \sigma_2 \tanh(\overline{u}_1 h_1) \right]}. \tag{7.9}$$

The condition on the inner boundary $\partial\Omega_{\rm h1}$ of the finite element mesh is obtained simply by evaluating, at the co–ordinates nodes along $\partial\Omega_{\rm h1}$, the expressions for $\overline{b}_y$ and $i\overline{e}_y$ given by equations (7.1–7.4), with $\overline{r}_{\rm TE}$ and $\overline{r}_{\rm TM}$ given by equations (7.8) and (7.9) respectively. The inner boundary condition is an exact solution for a layered earth, so that, to preserve the well–posedness of the numerical BVP, any "secondary" electric and magnetic fields due to induced currents in 2–D conductivity structures such as the magma chamber and zone of hydrothermal circulation, when evaluated along the inner boundary of the mesh, must be very small fractions of the "primary"

layered earth fields. Parameters of the electrical model required for the calculation are σ_0=3.2 S/m, σ_1=0.1 S/m, σ_2=0.001 S/m and h_1=1.5 km.

For completeness, I include the along–strike electromagnetic field components in the spatial, Laplace frequency (y, s) domain which, for HED excitation of a layered earth, are also analytic. They appear in the form appropriate for a land–based HED in Ward and Hohmann, but may be easily derived from equations (7.1–7.4) by taking sine and cosine transforms. In either case, the results appropriate for a marine–based HED are

$$B_y^{\text{sea}}(\mathbf{r}, s) = \frac{\mu_0 P}{4\pi s} \int_0^\infty \left[(1 + r_{\text{TE}}) + \left(\frac{r_{\text{TM}} + r_{\text{TE}}}{\lambda^2} \right) \partial_{xx} \right] \exp(-u_0 z) J_0(\lambda\rho) \lambda \, d\lambda \tag{7.10}$$

$$B_y^{\text{earth}}(\mathbf{r}, s) = \frac{-\mu_0 P}{4\pi s} \int_0^\infty \left[(1 - r_{\text{TE}}) - \left(\frac{r_{\text{TM}} + r_{\text{TE}}}{\lambda^2} \right) \partial_{xx} \right] \exp(u_1 z) J_0(\lambda\rho) \lambda \, d\lambda \tag{7.11}$$

$$E_y^{\text{sea}}(\mathbf{r}, s) = \frac{P}{4\pi s} \int_0^\infty \left[\left(\frac{1 - r_{\text{TM}}}{\lambda^2} \right) \frac{u_0}{\sigma_0} - \left(\frac{1 + r_{\text{TE}}}{\lambda^2} \right) \frac{\mu_0 s}{u_0} \right] \exp(-u_0 z) \partial_{xy} J_0(\lambda\rho) \lambda \, d\lambda \tag{7.12}$$

$$E_y^{\text{earth}}(\mathbf{r}, s) = \frac{P}{4\pi s} \int_0^\infty \left[\left(\frac{1 - r_{\text{TM}}}{\lambda^2} \right) \frac{u_0}{\sigma_0} - \left(\frac{1 + r_{\text{TE}}}{\lambda^2} \right) \frac{\mu_0 s}{u_0} \right] \exp(u_1 z) \partial_{xy} J_0(\lambda\rho) \lambda \, d\lambda \tag{7.13}$$

The above equations (7.10–7.13) are the generalizations to an n–layered earth of the double half–space solutions derived in Appendix B.

7.2 Numerical Solutions

Numerical solutions to the mid–ocean ridge boundary value problem described in §7.1 are presented in this section of the thesis. Figures 7.3*a–c* show contours of the along–strike magnetic component $B_y(\mathbf{r}, t)$ for a range of times 0.3 s$\leq t \leq$5.0 s after step–on of the $\hat{x}$–directed HED and a range of distances 100 m$\leq y \leq$5 km in the strike direction. The HED is situated at the centers of the plots and at y=0. The plots indicate, in three dimensions and time, patterns of electromagnetic diffusion through a two dimensional mid–ocean conductivity structure. The conductivity of the magma

chamber is σ=0.05 S/m, and its presence does not noticeably affect the field patterns, judging by the fact that the contours are nearly symmetrical about the x=0 vertical axis. The component $B_y(\mathbf{r},t)$ is strongest at y=0, in–line with the transmitter, and decays with increasing distance y along–strike. Figures 7.4*a–c* show contours of the along–strike electric component $E_y(\mathbf{r},t)$ for the same times and distances along–strike. In contrast to the magnetic case, the presence of the magma chamber has a significant effect on the electric component, especially at distances along–strike greater than 100 m. At the earliest time shown, see Figure 7.4*a*, the electric component is enhanced in the magma chamber with respect to the surrounding dry gabbros. At later time, see the plot corresponding to y=1 km in Figure 7.4*c*, the electric component is excluded from the magma chamber.

Figures 7.5*a–c* show contours of $B_y(\mathbf{r},t)$ at 0.3 s$\leq t\leq$5 s after HED step–on, for a model which includes a magma chamber of electrical conductivity σ=4.0 S/m. This value corresponds to 60% partial melt. The effect of the high conductivity, as can be seen in the figures, is to slow the diffusion of B_y into the magma chamber, producing a distortion in the field patterns at the seafloor that might be measureable by seafloor magnetic sensors placed across the ridge axis. In order to confirm or refute this hypothesis, snapshots of B_y need to be computed at several more times, and response parameters extracted from the synthetic data. Figures 7.6*a–c* show the electric component $E_y(\mathbf{r},t)$ diffusing into the mid–ocean ridge model. At all times shown, the electric field intensity is greater in the resistive gabbros than in the conductive magma chamber. More modeling is required to confirm that the chamber can indeed be detected by seafloor electric field sensors.

The along–strike components $B_y(t)$ and $E_y(t)$ are computed directly by the 2.5–D finite element program. Of interest to the practical scientist is the transient ERER configuration which measures the *in–line* component $E_x(t)$ produced by a $\hat{x}$–directed horizontal electric dipole. The component $E_x(t)$ has been shown to respond strongly to variations in the sub–seafloor electrical conductivity (Edwards and Chave 1986)

and ERER equipment has been built and tested at sea (Everett *et.al.* 1989). Therefore, modeling by computer the response of the mid–ocean ridge to excitation by the transient ERER configuration is desirable. The $E_x(t)$ component may be obtained from the output of the 2.5–D finite element code as follows. In the (q, s) domain, $\overline{e}_x(q, s)$ is related to the along–strike components by:

$$\overline{e}_x(q,s) = \frac{q}{u^2}\frac{\partial(i\overline{e}_y)}{\partial x} - \frac{s}{u^2}\frac{\partial \overline{b}_y}{\partial z}. \tag{7.14}$$

The component $E_x(\mathbf{r}, t)$ is then obtained by taking a cosine and a Laplace transform. I plan to investigate ERER modeling in the near future.

References

Chave, A.D., 1983. Numerical integration of related Hankel transforms by quadrature and continued fraction expansion, *Geophysics*, **48**, 1671–1686.

Cox, C.S., S.C. Constable, A.D. Chave and S.C. Webb, 1986. Controlled–source electromagnetic sounding of the oceanic lithosphere, *Nature*, **320**, 52–54.

Detrick, R.S., P. Buhl, E. Vera, J. Mutter, J. Madsen and T. Brocher, 1987. Multi–channel seismic imaging of a crustal magma chamber along the East Pacific Rise, *Nature*, **326**, 35–41.

Edwards, R.N. and A.D. Chave, 1986. A transient electric dipole–dipole method for mapping the conductivity of the seafloor, *Geophysics*, **51**, 984–987.

Everett, M.E., R.N. Edwards, S.J. Cheesman, H. Utada and I.J. Ferguson, 1989. Interpretation of seafloor electromagnetic data in applied geophysics, in (ed. Miya, K.) *Applied electromagnetics in materials*, Pergamon Press, Oxford U.K., 143–153.

Häangi, P., F. Roesel and D. Trautmann, 1980. Evaluation of infinite series by use of continued fraction expansions: a numerical study, *J. Comp. Phys.*, **37**, 242–258.

Harding, A.J., J.A. Orcutt, M.E. Kappus, E.E. Vera, J.C. Mutter, P. Buhl, R.S. Detrick and T.M. Brocher, 1989. Structure of young oceanic crust at 13°N on the East Pacific Rise from expanding spread profiles, *J. Geophys. Res*, **94**, 12163–12196.

Shankland, T.J. and H.S. Waff, 1977. Partial melting and electrical conductivity in the upper mantle, *J. Geophys. Res*, **82**, 5409–5417.

Ward, S.H. and G.W. Hohmann, 1987. Electromagnetic theory for geophysical applications, in (ed. Nabighian, M.N.) *Electromagnetic Methods in Applied Geophysics*, Society of Exploration Geophysicists, Tulsa OK, 131–311.

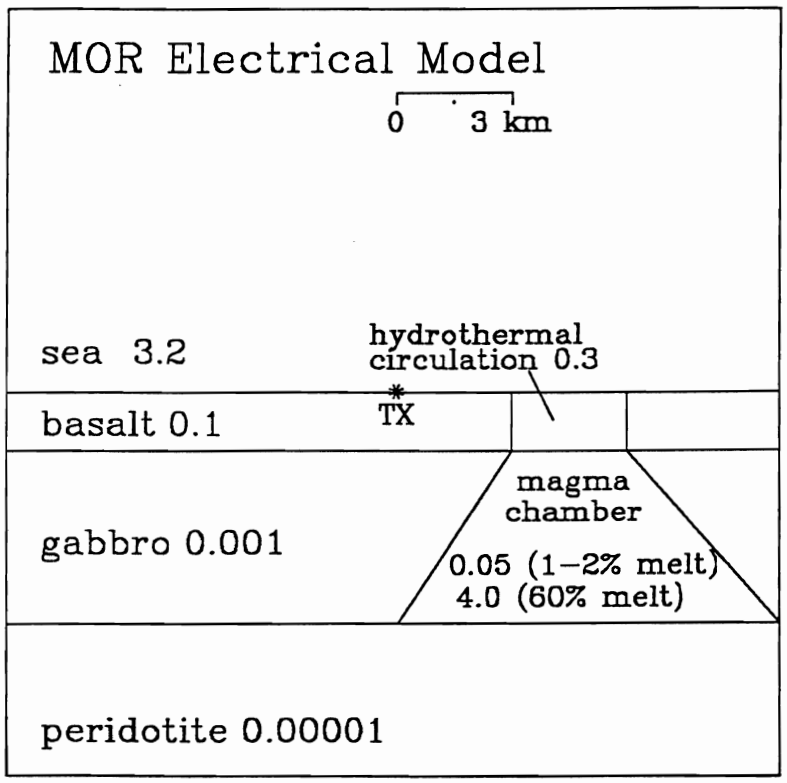

Fig.7.1 2–D electrical model of an active mid–ocean ridge used in a study designed to illustrate the utility of the 2.5–D finite element program. In the model, a uniform magma chamber is embedded in young oceanic crust consisting of basalt, gabbro and peridotite layers. The electrical conductivity of the magma chamber depends on its partial melt fraction, as shown. Hydrothermal fluid circulation in fractured basalt is modeled as a zone of enhanced electrical conductivity above the magma chamber. A suitable location for placement of a CSEM transmitter (Tx) is also shown.

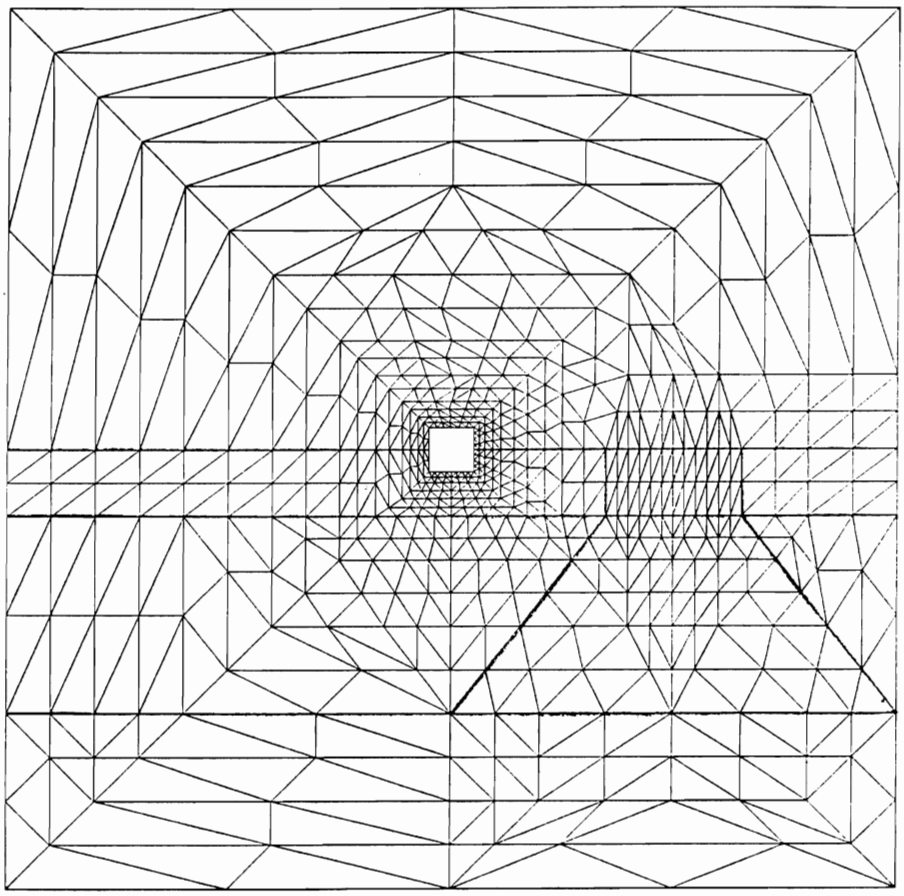

Fig.7.2 Mesh resulting from discretization of a domain based on the mid–ocean ridge electrical model of the previous figure. 2.5–D finite element solutions to the governing system of electromagnetic diffusion equations are computed on the nodes of this mesh.

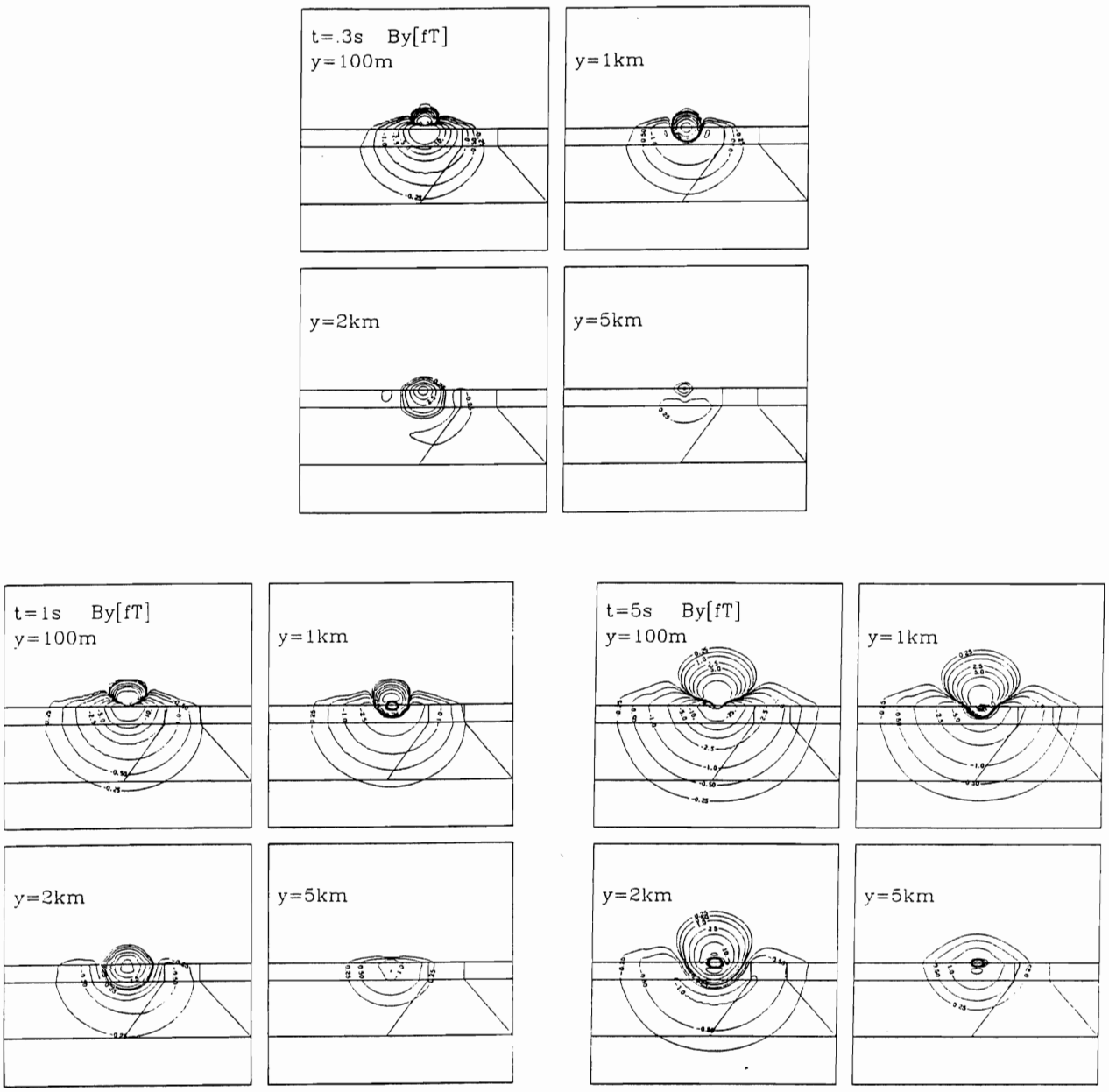

Fig.7.3 Contours of the magnetic component $B_y(x, y, z, t)$ show electromagnetic diffusion, in three spatial dimensions and time, from a HED transmitter located 5 km off–axis into the electrical model of the mid–ocean ridge shown in Fig.7.1 (*a–c*, counter–clockwise from top). The y co–ordinate measures the distance along the strike of the ridge from the $\hat{x}$–directed HED. The transmitter is switched on at time t=0 s. The electrical conductivity of the magma chamber is σ=0.05 S/m. Its presence does not greatly affect the field patterns.

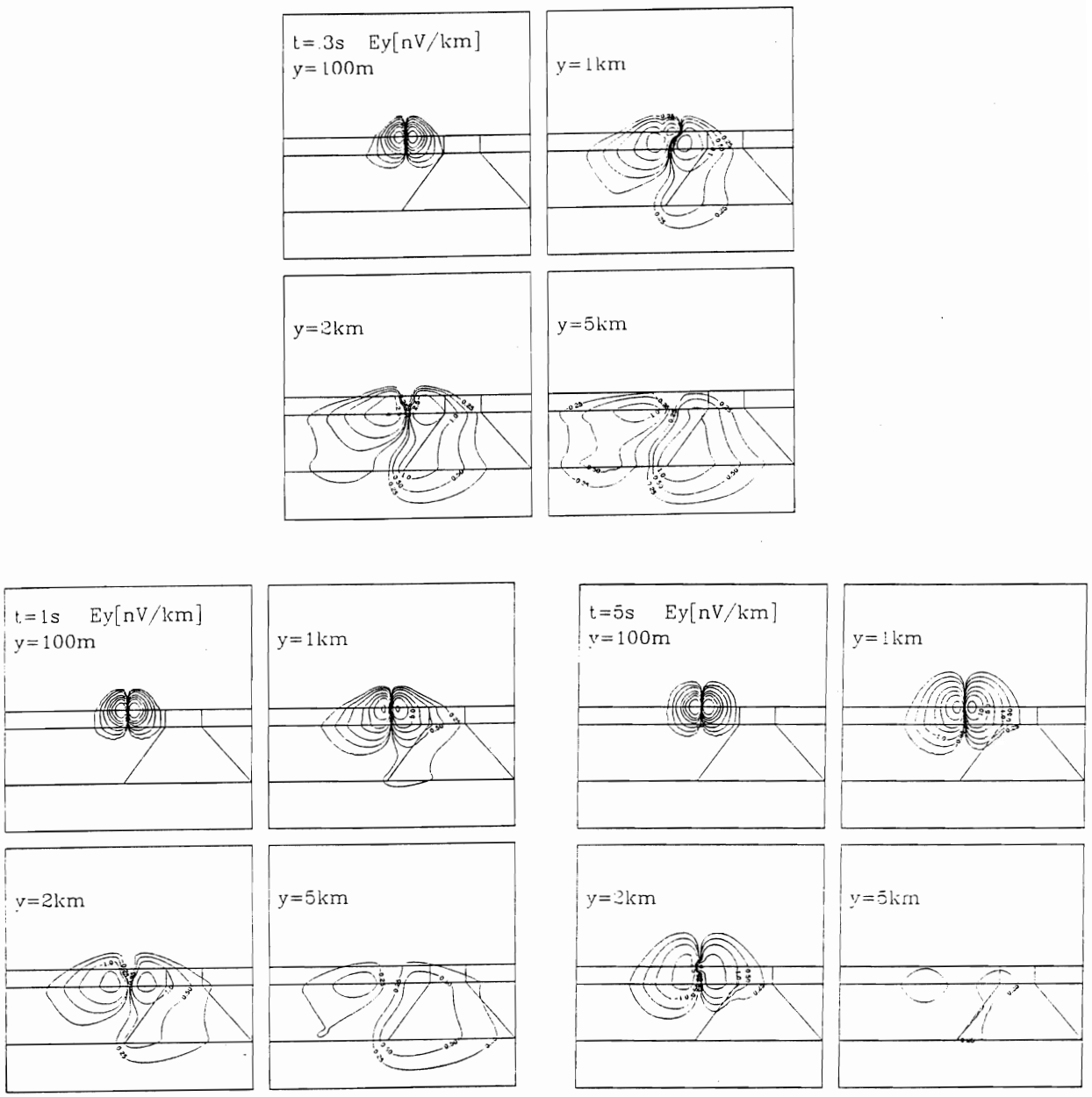

Fig.7.4 Contours of the electric component $E_y(x, y, z, t)$ showing diffusion into mid–ocean ridge electrical model (a–c, counter–clockwise from top). The presence of the magma chamber of electrical conductivity of σ=0.05 S/m, in contrast to the magnetic case (see Fig.7.4), has a significant effect on the field patterns. At t=0.3 s after transmitter switch–on, the field is enhanced in the magma chamber with respect to the surrounding gabbros. By t=5 s, this situation has reversed.

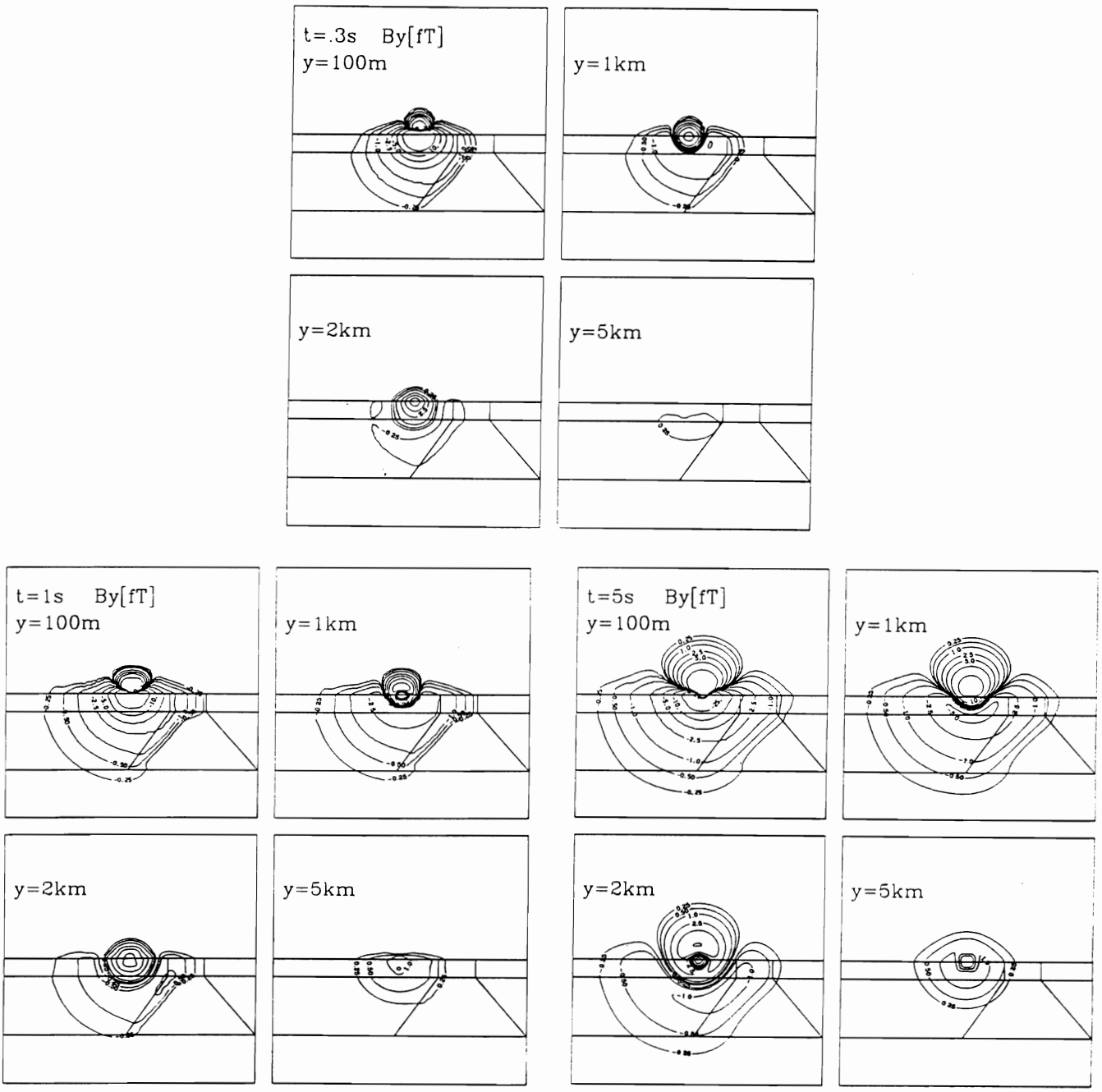

Fig.7.5 Contours of the magnetic component $B_y(x, y, z, t)$ showing diffusion into mid–ocean ridge electrical model (a–c, counter–clockwise from top). The magma chamber has electrical conductivity σ=4.0 S/m, corresponding to 60% partial melt. The presence of the highly conductive magma chamber slows the rate of electromagnetic diffusion across the ridge axis, producing a distortion in the field patterns that may be measureable at the seafloor.

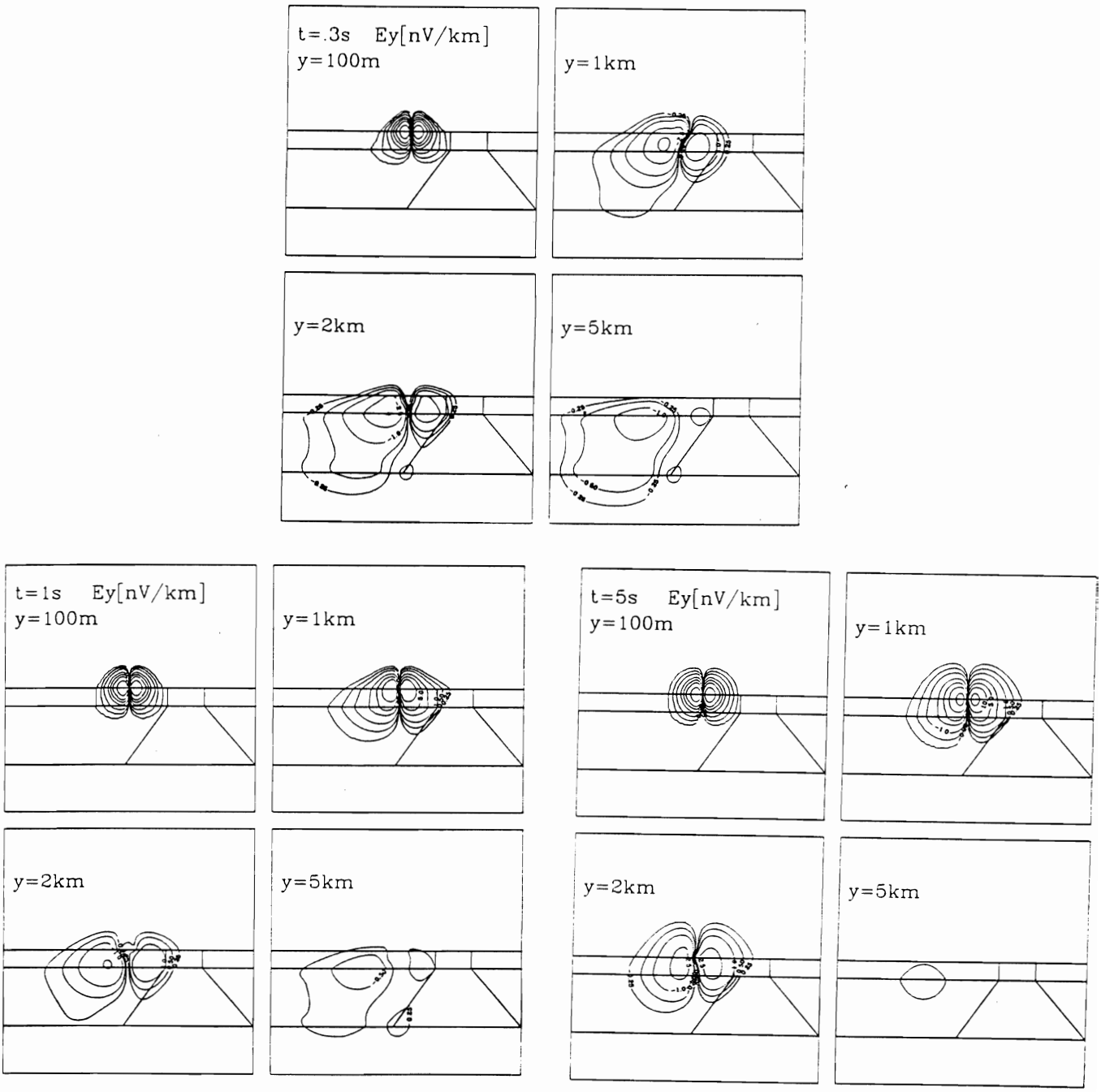

Fig.7.6 Contours of the electric component $E_y(x, y, z, t)$ showing diffusion into mid–ocean ridge electrical model (a–c, counter–clockwise from top). The electric field intensity, at all times shown, is greater in the resistive gabbros than in the conductive (σ=4.0 S/m) magma chamber.

Chapter 8

Conclusions

8.0 Conclusions

Constraining geodynamical models of ocean crust formation at active segments of the global mid–ocean ridge system requires a knowledge of the geological structure beneath the ridge. Hard constraints on the geology to depths of several kilometers can be obtained using controlled–source geophysical techniques. The most commonly used technique is seismic, which has provided clear images of the top of the partially molten, mid–crustal axial magma chamber at the East Pacific Rise near 9°N but only coarse estimates of the geometry and vigour of the associated hydrothermal circulation zones.

Electrical conductivity, unlike seismic velocities, is a very strong indicator of the amount, distribution, temperature and connectedness of partial melt and fluids within rocks. Therefore, if maps of the sub–surface electrical conductivity beneath active ridge segments could be obtained, they might be used to infer the presence of a magma chamber and the accompanying hydrothermal fluids. Controlled–source electromagnetic (CSEM) exploration techniques map electrical conductivity. CSEM experiments are, however, difficult and costly to perform.

In view of the above, there is a need to have design and interpretation tools, by which CSEM experiments can be planned and their results analyzed. This thesis has described 2–D and 2.5–D time domain forward modeling computer implementations which fulfill this need. The computer programs calculate the transient electromagnetic fields which would result if an arbitrary two dimensional system of conductors were to

be excited by a line source and a point source of electromagnetic energy, respectively. The codes have been validated through tests against known analytical solutions to the governing Maxwell's equations which assume the earth is uniformly conductive. The convergence of the finite element approximation to these solutions was found to be $O(h)$, where h measures the size of the triangles in the finite element mesh. A formula by which numerical solutions on progressively finer meshes are extrapolated permits great accuracy using only coarse meshes.

A numerical study of the performance of a certain, idealized transient CSEM system at the East Pacific Rise has been carried out using the 2–D code. The system consists of an infinite source located on the seafloor 5 km west of the ridge axis, and seafloor receivers placed at various distances across the ridge crest. The source is oriented with respect to the strike of the ridge so as to produce only the H–polarization mode of current flow. The results of the study indicate that this system can detect the axial magma chamber and the associated zones of hydrothermal melt by monitoring two electromagnetic response parameters, the diffusion time and the response amplitude, as a function of transmitter/receiver separation. The response parameters were chosen so as to be easily extracted from the measured data, which consists of seafloor recordings of magnetic and electric fields. The diffusion time measures the time taken for an electromagnetic signal to diffuse from the source through the earth to the receiver, while the response amplitude is a measure of the strength of the signal. The presence of the highly conductive magma chamber slows and attenuates signals diffusing beneath the ridge. The presence of hydrothermal fluid circulation in the highly fractured, extrusive basalt layer has the same effect on the data, but only if receivers are placed on the ridge crest itself. Inferences made from the numerical results suggest that a horizontal electric dipole of moment 10^4 A·m and receivers with sensitivity of 1 pT/s over a time window extending to 10 s are sufficient to detect crustal mid–ocean ridge targets.

Proper interpretation of transient CSEM data requires forward modeling using

a more realistic, finite source. The 2.5–D code is capable of doing this. Sample field patterns produced in the earth beneath the sea by a sudden switch–on of electric current in a horizontal electric dipole are computed. They illustrate diffusion, in three spatial dimensions and time, of various electromagnetic field components through typical mid–ocean ridge structures. Displaying the patterns demonstrates the utility of the 2.5–D code, *i.e.* its usefulness for interpreting data from a transient CSEM ridge–going experiment, as such results become available. While additional modeling might be required to determine the resolution of mid–ocean ridge structures to transient finite source excitation, all the necessary tools to do this may be found in the pages of this thesis.

Appendix A

Gaver–Stehfest Inverse Laplace Transform

I

In §I of this appendix, I derive a formula originally obtained by Gaver (1966) which may be used to compute an unknown function of time $P(t)$ given its inverse $\overline{P}(s)$ in the Laplace domain. For the sake of convenience, the derivation will closely follow the method and notation of Gaver's paper. The derivation of an acceleration formula due to Stehfest (1970a,b) appears in §II of the appendix. For fixed amounts of computer time and machine precision, Stehfest's procedure greatly improves the accuracy of the Gaver inversion formula.

First, it should be easily recognized that for an arbitrary function $P(t)$ the following is valid:

$$P(\tau) = \int_0^\infty \delta(t-\tau)P(t)\,dt \tag{1}$$

where $\delta(t-\tau)$ is the Dirac delta function. Gaver sought a discrete analog of the Dirac delta function, which he denoted by $\delta_{\mathrm{n,m}}(t,a)$, and required that the two functions be related in the following limit:

$$\lim_{n=m\to\infty} \delta_{\mathrm{n,m}}(t,a) = \delta(t-\tau). \tag{2}$$

Thus, as the indices n and m are made larger, the quantity

$$P_{\mathrm{n,m}} = \int_0^\infty \delta_{\mathrm{n,m}}(t,a)P(t)\,dt \tag{3}$$

converges to the desired result $P(\tau)$, *i.e.*:

$$P(\tau) = \lim_{n=m\to\infty} P_{\mathrm{n,m}}. \tag{4}$$

Consider the function:

$$\delta_{\mathrm{n,m}}(t,a) = \frac{(n+m)!}{n!(m-1)!}\left(1-\mathrm{e}^{-at}\right)^n a\mathrm{e}^{-mat}. \tag{5}$$

This function obeys equation (2) if the parameter a is suitably chosen and, as noted by Gaver, commonly occurs as a probability density function related to the exponential distribution in the statistical theory of single–server queues. In order to prove that $\delta_{\mathrm{n,m}}(t,a)$ has the required property in the limit of large n and m, it suffices to show that the large n,m limit of the expectation value $\mathrm{E}(X)$ and variance $\mathrm{VAR}(X)$ are given respectively by

$$\lim_{n,m\to\infty}\mathrm{E}(X) = \tau, \qquad \lim_{n,m\to\infty}\mathrm{VAR}(X) = 0 \tag{6}$$

where X is a random variable with probablity density given by equation (5). To determine $\mathrm{E}(X)$ and $\mathrm{VAR}(X)$ for all n,m, use is made of the *cumulant* function, defined by:

$$\ln\overline{\delta}_{\mathrm{n,m}}(s,a) \equiv \sum_{k=0}^{\infty} c_k\frac{(-s)^k}{k!}. \tag{7}$$

In equation (7), c_k is the k–th cumulant of the density function $\delta_{\mathrm{n,m}}(t,a)$; recall from probability theory that the first cumulant is c_1=E(X), the second is c_2=VAR(X), and so forth. The function $\overline{\delta}_{\mathrm{n,m}}(s,a)$ appearing in the above equation is the Laplace transform of the density function $\delta_{\mathrm{n,m}}(t,a)$.

To find all cumulants of the $\delta_{\mathrm{n,m}}(t,a)$, including the expectation value and the variance, we need to know the Laplace transform $\overline{\delta}_{\mathrm{n,m}}(s,a)$. The latter is defined as usual by:

$$\overline{\delta}_{\mathrm{n,m}}(s,a) = \int_0^{\infty}\mathrm{e}^{-st}\delta_{\mathrm{n,m}}(t,a)\,dt, \quad s>0. \tag{8}$$

Inserting equation (5) into equation (8) gives

$$\overline{\delta}_{\mathrm{n,m}}(s,a) = \frac{(n+m)!}{n!(m-1)!}\int_0^{\infty}\left(1-\mathrm{e}^{-at}\right)^n a\mathrm{e}^{-mat}\,dt. \tag{9}$$

It is expedient to evaluate the integral in the above equation by recognizing that there is a recursion relation satisfied by the functions $\overline{\delta}_{\mathrm{n,m}}(s,a), n{=}0,1,2,\ldots$ and m, fixed. With the first index set to $n-1$, for example, equation (9) becomes

$$\overline{\delta}_{\mathrm{n-1,m}}(s,a) = \frac{(n+m-1)!}{(n-1)!(m-1)!}\int_0^\infty \left(1-\mathrm{e}^{-at}\right)^{n-1} a\mathrm{e}^{-mat}\,dt \tag{10}$$

and, when evaluated at $s{=}s+a$, the function becomes

$$\overline{\delta}_{\mathrm{n-1,m}}(s+a,a) = \frac{(n+m-1)!}{(n-1)!(m-1)!}\int_0^\infty \left(1-\mathrm{e}^{-at}\right)^{n-1} \mathrm{e}^{-at} a\mathrm{e}^{-mat}\,dt. \tag{11}$$

Subtracting equation (11) from equation (10), and comparing the difference to equation (9) leads to the desired recursion relation:

$$\overline{\delta}_{\mathrm{n,m}}(s,a) = \frac{n+m}{n}\left[\overline{\delta}_{\mathrm{n-1,m}}(s,a) - \overline{\delta}_{\mathrm{n-1,m}}(s+a,a)\right]. \tag{12}$$

The end member $n{=}0$ of the recursion arises as a special case of equation (9), it is simply:

$$\overline{\delta}_{\mathrm{0,m}}(s,a) = \int_0^\infty \mathrm{e}^{-st} ma\mathrm{e}^{-mat}\,dt = \frac{ma}{ma+s}. \tag{13}$$

We can use formula (13) for $\overline{\delta}_{\mathrm{0,m}}(s,a)$ plus the recursion relation (12) and mathematical induction to generate the Laplace transforms of $\overline{\delta}_{\mathrm{n,m}}(s,a)$ for arbitrary n, for example:

$$\overline{\delta}_{\mathrm{1,m}}(s,a) = (m+1)\left[\overline{\delta}_{\mathrm{0,m}}(s,a) - \overline{\delta}_{\mathrm{0,m}}(s+a,a)\right] = \left[\frac{ma}{ma+s}\right]\left[\frac{(m+1)a}{(m+1)a+s}\right]. \tag{14}$$

For the general case, the Laplace transform of $\delta_{\mathrm{n,m}}(t,a)$ is a product of a finite number of terms each of which resemble the RHS of equation (13):

$$\overline{\delta}_{\mathrm{n,m}}(s,a) = \left[\frac{ma}{ma+s}\right]\left[\frac{(m+1)a}{(m+1)a+s}\right]\cdots\left[\frac{(m+n)a}{(m+n)a+s}\right] = \prod_{j=m}^{m+n}\frac{ja}{ja+s}. \tag{15}$$

From the Laplace transform of $\delta_{\mathrm{n,m}}(t,a)$, it is a simple matter to find an expression for the cumulant function, which is defined by equation (7). The derivation

proceeds by taking the natural logarithm of the finite product of terms in equation (15); this leads to the following finite sum of terms

$$\ln \prod_{j=m}^{m+n} \frac{ja}{ja+s} = \ln \left[\frac{ma}{ma+s}\right] + \ln \left[\frac{(m+1)a}{(m+1)a+s}\right] + ... + \ln \left[\frac{(m+n)a}{(m+n)a+s}\right]. \quad (16)$$

In order to write the terms in the above equation in forms which may be directly compared to corresponding terms in the defining series expansion for the cumulant function, equation (7), the following series representation of the logarithm function

$$\ln x = \left(\frac{x-1}{x}\right) + \frac{1}{2}\left(\frac{x-1}{x}\right)^2 + \frac{1}{3}\left(\frac{x-1}{x}\right)^3 + ... \quad (17)$$

is useful. For example, the first term of equation (16), after incorporating the series representation of $\ln x$, is:

$$\ln \left[\frac{ma}{ma+s}\right] = \frac{-s}{ma} + \frac{s^2}{2(ma)^2} - \frac{s^3}{3(ma)^3} + ... = \sum_{k=1}^{\infty} \frac{(-1)^k s^k}{k(ma)^k} \quad (18)$$

and each of the other terms in equation (16) has a similar form, the n–th term being

$$\ln \left[\frac{(m+n)a}{(m+n)a+s}\right] = \sum_{k=1}^{\infty} \frac{(-1)^k s^k}{k\left[(m+n)a\right]^k}. \quad (19)$$

Replacing all of the logarithmic terms by their series representations, as described above, gives the following expression for the cumulant function:

$$\ln \overline{\delta}_{\mathrm{n,m}}(s,a) = \sum_{l=0}^{n} \sum_{k=1}^{\infty} \frac{(-1)^k s^k}{k\left[(m+l)a\right]^k}. \quad (20)$$

All cumulants of $\delta_{\mathrm{n,m}}(t,a)$ may then be extracted by means of a term–by–term comparison of equation (20) to the definition of the cumulant function, equation (7), for example, the k–th cumulant c_k is a solution to the equation

$$\frac{c_k}{k!} - \sum_{l=0}^{\infty} \frac{1}{k\left[(m+l)a\right]^k} = 0. \quad (21)$$

The expectation value $\mathrm{E}(X)$ occurs when k=1, it is evidently

$$c_1 = \mathrm{E}(X) = \sum_{l=0}^{n} \frac{1}{(m+l)a} = \frac{1}{a}\left[\frac{1}{m} + \frac{1}{m+1} + ... + \frac{1}{m+n}\right] \tag{22}$$

and similarly when k=2 the variance of X is determined:

$$c_2 = \mathrm{VAR}(X) = \sum_{l=0}^{n} \frac{1}{(m+l)^2 a^2} = \frac{1}{a^2}\left[\frac{1}{m^2} + \frac{1}{(m+1)^2} + ... + \frac{1}{(m+n)^2}\right]. \tag{23}$$

The above expressions are valid for all values of the indices n, m, but for large values the expressions may be written in a convenient asymptotic form using the Euler–Maclaurin integral formula, which is:

$$\sum_{k=0}^{n} f(k) \approx \int_0^n f(x)\,dx + \frac{f(0)}{2} + \frac{f(n)}{2}. \tag{24}$$

Thus for $\mathrm{E}(X)$, we have that

$$a\mathrm{E}(X) = \sum_{k=0}^{n} \frac{1}{m+k} \approx \int_0^n \frac{dx}{m+x} + \frac{1}{2m} + \frac{1}{2(m+n)}, \tag{25}$$

and using the approximation

$$\frac{1}{x} \approx \ln\left(\frac{x+1}{x}\right) \tag{26}$$

which is valid for $x \gg 1$ it follows that $\mathrm{E}(X)$ can be written as a logarithm:

$$a\mathrm{E}(X) \approx \ln(m+n) + \ln\left(\frac{2m+1}{2m}\right) + \ln\left(\frac{2m+2n+1}{2m+2n}\right)$$

$$= \ln\left[\frac{(2m+2n+1)(2m+1)}{4m^2}\right]. \tag{27}$$

Similarly, the variance $\mathrm{VAR}(X)$ can be written in the form of an aymptotic expansion as follows:

$$\mathrm{VAR}(X) = \sum_{k=0}^{n} \frac{1}{(m+k)^2} \approx \int_0^n \frac{dx}{(m+x)^2} + O(\frac{1}{m^2}) \approx \frac{n}{m(n+m)}. \tag{28}$$

Examining the first two cumulants of $\delta_{\mathrm{n,m}}(t,a)$, it is clear that for large n and m this function reduces to the Dirac delta function, provided $a{=}\ln 2/\tau$. This may be seen explicitly by considering the limiting forms of equations (27) and (28), namely,

$$\lim_{n,m\to\infty} \mathrm{E}(X) = \frac{1}{a}\ln 2 \equiv \tau, \qquad \lim_{n,m\to\infty} \mathrm{VAR}(X) = 0. \tag{29}$$

Equation (28) therefore implies that

$$\lim_{n,m\to\infty} \delta_{\mathrm{n,m}}(t,a) = \lim_{n,m\to\infty} \left[\frac{\ln 2}{\tau}\right] \frac{(n+m)!}{n!(m-1)!} \left(1-\mathrm{e}^{-t\ln 2/\tau}\right)^n \mathrm{e}^{-mt\ln 2/\tau} = \delta(t-\tau). \tag{30}$$

The next task is use $\delta_{\mathrm{n,m}}(t,a)$ to obtain a Laplace inversion formula for $P(\tau)$. Starting from the binomial theorem

$$(1-x)^n = \sum_{k=0}^{n} \binom{n}{k} (-1)^k x^k \tag{31}$$

where the binomial coefficients $\binom{n}{k}$ are given by

$$\binom{n}{k} = \frac{n!}{k!(n-k)!}, \tag{32}$$

and combining with it equations (30) and (3) results in

$$P_{\mathrm{n,m}} = \left[\frac{\ln 2}{\tau}\right] \frac{(n+m)!}{n!(m-1)!} \sum_{k=0}^{n} \binom{n}{k} (-1)^k \int_0^\infty \mathrm{e}^{-kt\ln 2/\tau} \mathrm{e}^{-mt\ln 2/\tau} P(t)\, dt. \tag{33}$$

The integral in the RHS of the above equation is recognizable as a Laplace transform, with transform variable $s{=}(m+k)\frac{\ln 2}{\tau}$, *i.e.* it can be re–written as

$$P_{\mathrm{n,m}} = \left[\frac{\ln 2}{\tau}\right] \frac{(n+m)!}{n!(m-1)!} \sum_{k=0}^{n} \binom{n}{k} (-1)^k \overline{P}\left[(m+k)\frac{\ln 2}{\tau}\right]. \tag{34}$$

Setting $n{=}m$ I arrive finally at Gaver's formula for the inverse Laplace transform:

$$P_n(\tau) = \left[\frac{\ln 2}{\tau}\right] \frac{(2n)!}{n!(n-1)!} \sum_{k=0}^{n} \binom{n}{k} (-1)^k \overline{P}\left[(n+k)\frac{\ln 2}{\tau}\right]. \tag{35}$$

II

Gaver's formula (35) converges only very slowly to $P(\tau)$ as n increases. This section of the appendix contains the derivation of a technique originally used by Stehfest (1970) to accelerate the convergence. First, recognize that equations (35) and (4), taken together, imply the existence of the following asymptotic sequence:

$$P_n(\tau) = P(\tau) + \frac{\alpha_1}{n} + \frac{\alpha_2}{n^2} + \cdots. \tag{36}$$

The approximation $P_n(\tau)$ therefore has truncation error of order –1, *i.e.* the leading error term in equation (36) is of $O(1/n)$. Gaver found that linear combinations of the form

$$P_N(\tau) = \sum_{i=1}^{N} x_i(N) P_{2^{i-1}n}(\tau), \tag{37}$$

where $\{x_i, i=1,2,...,N\}$ is a set of coefficients to be determined, can increase significantly the order of the truncation error and hence lead to improved accuracy for estimates of $P(\tau)$. The computational cost associated with the improved accuracy is that the known inverse Laplace transform $\overline{P}(s)$ must be evaluated at $N(n+1)$ values of s instead of just the $n+1$ values as specified by equation (35). To see how the coefficient set $\{x_i, i=1,2,...,N\}$ is computed, consider at first the special cases of N=2,3. Using only equation (36) note that for N=2 the linear combination

$$2P_{2n}(\tau) - P_n(\tau) = P(\tau) + O\left(\frac{1}{n^2}\right) \tag{38}$$

cancels out the $O(1/n)$ error term thereby producing a truncation error of order –2. For N=3 the linear combination

$$\frac{1}{3}P_n(\tau) - 2P_{2n}(\tau) + \frac{8}{3}P_{4n}(\tau) = P(\tau) + O\left(\frac{1}{n^3}\right) \tag{38}$$

has truncation error of order –3. For a given N, therefore, the coefficients are chosen in order to cancel out error terms of order respectively $1/n, 1/n^2, ..., 1/n^{N-1}$. This

choice of $\{x_i\}$ makes the $P(\tau)$ truncation error of order $-N$. The term–by–term cancellation is achieved by selecting coefficients which obey the $N \times N$ linear system of equations

$$\sum_{i=1}^{N} \frac{x_i}{i^k} = \delta_{k0}, \quad k = 0, 1, ..., N. \tag{40}$$

The contribution of Stehfest to the inverse Laplace inversion problem lay in his recognition that a linear combination of the form

$$P_K(\tau) = \sum_{i=1}^{K} x_i(K) P_{n/2+1-i}(\tau) \tag{41}$$

can produce a much better approximation to $P(\tau)$ than the linear combination of the form (37) used by Gaver. Stehfest chose a new set of coefficients $\{x_i\}$ by requiring them to be the solution to the $K \times K$ linear system

$$\sum_{i=1}^{K} \frac{x_i}{(n/2+1-i)^k} = \delta_{k0}, \quad k = 0, 1, .., K-1. \tag{42}$$

In the next paragraph, I shall follow the approach of Stehfest (1970) to show that his coefficients, when inserted into the linear combination (41), gives a smaller truncation error for $P(\tau)$ than does the Gaver procedure which is based on equations (37) and (40).

The linear system of equations given in equation (42) can be written in matrix form as

$$\begin{pmatrix} 1 & 1 & \dots & 1 \\ (n/2)^{-1} & (n/2-1)^{-1} & \dots & (n/2+1-K)^{-1} \\ \vdots & \vdots & \ddots & \vdots \\ (n/2)^{1-K} & (n/2-1)^{1-K} & \dots & (1-K)^{-1} \end{pmatrix} \begin{pmatrix} x_1 \\ x_2 \\ \vdots \\ x_K \end{pmatrix} = \begin{pmatrix} 1 \\ 0 \\ \vdots \\ 0 \end{pmatrix}. \tag{43}$$

There is an analytic solution to the above matrix equation, which Stehfest gives as:

$$x_i(K) = \frac{(-1)^{i-1}}{K!} \binom{K}{i} i(n/2+1-i)^{K-1}, \quad i = 1, ..., K. \tag{44}$$

This solution can be verified by direct substitution and with the aid of the following formula for the Kronecker delta function:

$$\delta_{k0} = \frac{1}{K!}\sum_{i=0}^{K}(-1)^i \binom{K}{i}(a-i)^{K-k} \tag{45}$$

in which a and K are arbitrary constants. Combining equations (44) and equation (41), using the above formula for the Kronecker delta function and shifting the index of summation from $i \rightarrow i+1$ in equation (41) leads to a formula from which the truncation error of the Stehfest procedure may be evaluated:

$$\begin{aligned} P_K(\tau) &= P(\tau) + \alpha_1\delta_{10} + \alpha_2\delta_{20} + \ldots + \sum_{i=0}^{K-1}\frac{(-1)^i\alpha_K}{(n/2-i)i!(K-1-i)!} + \ldots \\ &= P(\tau) + \frac{\alpha_K}{\frac{n}{2}!}\left[\phi_1(K)(\frac{n}{2}-1)! + \ldots + (-1)^{K-1}\phi_K(K)(\frac{n}{2}-K)! + \ldots\right] \\ &= P(\tau) + \phi_K(K)\alpha_K(-1)^{K-1}\frac{(\frac{n}{2}-K)!}{\frac{n}{2}!} + \ldots \\ &= P(\tau) + (-1)^{K+1}\frac{(\frac{n}{2}-K)!}{\frac{n}{2}!}\alpha_K + O\left[\frac{(\frac{n}{2}-K)!}{(\frac{n}{2})!}\right]. \end{aligned} \tag{46}$$

The functions $\phi_i(K)$, i=1, 2, ..., K appearing in equation (46) have not been written explicitly in order to keep the formula simple but they do not depend on n. The Stehfest truncation error is

$$O\left[\frac{(n/2-K)!}{(n/2)!}\right]$$

instead of $O(n^{-K})$ as was the case with the Gaver procedure. Note that setting K=$n/2$ in equation (46) causes the leading term in the truncation error of the Stehfest formulation to vanish, which is why the Stehfest acceleration is so effective. With this choice of K, the Stehfest coefficients are

$$x_i(n/2) = \frac{(-1)^{i-1}(n/2+1-i)^{n/2-1}}{(i-1)!(n/2-i)!}. \tag{47}$$

The expression

$$P_K(\tau)|_{K=\frac{n}{2}} = \sum_{i=1}^{n/2} x_i P_{n/2+1-i}(\tau) \tag{48}$$

that the Stehfest procedure gives, when Gaver's formula for $P_n(\tau)$ given by equation (35) with the replacement $n \to n/2 + 1 - i$ is used, has come to be known as the Gaver–Stehfest formula. The explicit calculation is as follows (setting $b = \ln 2/\tau$):

$$\begin{aligned}
\frac{P_K(\tau)}{b} &= \sum_{i=1}^{\frac{n}{2}} \sum_{k=0}^{\frac{n}{2}+1-i} \frac{(-1)^{k+i-1}(\frac{n}{2}+1-i)^{\frac{n}{2}-1}(n+2-2i)!\overline{P}\left[(\frac{n}{2}+1-i+k)b\right]}{(\frac{n}{2}-i)!(\frac{n}{2}-i)!(i-1)!k!(\frac{n}{2}+1-i-k)!} \\
&= \frac{(\frac{n}{2})^{\frac{n}{2}-1}n!}{(\frac{n}{2}-1)!(\frac{n}{2}-1)!} \sum_{k=0}^{\frac{n}{2}} \frac{(-1)^k \overline{P}\left[(\frac{n}{2}+k)b\right]}{k!(\frac{n}{2}-k)!} \\
&\quad - \frac{(\frac{n}{2}-1)^{\frac{n}{2}-1}(n-2)!}{(\frac{n}{2}-2)!(\frac{n}{2}-2)!} \sum_{k=0}^{\frac{n}{2}-1} \frac{(-1)^k \overline{P}\left[(\frac{n}{2}+k-1)b\right]}{k!(\frac{n}{2}-1-k)!} \\
&\quad + \frac{(\frac{n}{2}-2)^{\frac{n}{2}-1}(n-4)!}{(\frac{n}{2}-3)!(\frac{n}{2}-3)!2!} \sum_{k=0}^{\frac{n}{2}-2} \frac{(-1)^k \overline{P}\left[(\frac{n}{2}+k-2)b\right]}{k!(\frac{n}{2}-2-k)!} \\
&\quad + \ldots + \\
&\quad + \frac{(-1)^{\frac{n}{2}-2}2^{\frac{n}{2}-1}3!}{(\frac{n}{2}-2)!} \sum_{k=0}^{2} \frac{(-1)^k \overline{P}\left[(k+2)b\right]}{k!(2-k)!} \\
&\quad + \frac{(-1)^{\frac{n}{2}-1}2!}{(\frac{n}{2}-1)!} \sum_{k=0}^{1} \frac{(-1)^k \overline{P}\left[(k+1)b\right]}{k!(1-k)!}.
\end{aligned} \tag{49}$$

Expanding the summation over the k indices in the above formula gives:

$$\begin{aligned}
\frac{P_K(\tau)}{b} &= \frac{(\frac{n}{2})^{\frac{n}{2}-1}n!}{(\frac{n}{2}-1)!(\frac{n}{2}-1)!} \left[\frac{\overline{P}\left[(\frac{n}{2})b\right]}{\frac{n}{2}!} - \frac{\overline{P}\left[(\frac{n}{2}+1)b\right]}{(\frac{n}{2}-1)!} + \ldots + \frac{(-1)^{\frac{n}{2}}\overline{P}\left[nb\right]}{\frac{n}{2}!} \right] \\
&\quad - \frac{(\frac{n}{2}-1)^{\frac{n}{2}-1}(n-2)!}{(\frac{n}{2}-2)!(\frac{n}{2}-2)!} \left[\frac{\overline{P}\left[(\frac{n}{2}-1)b\right]}{(\frac{n}{2}-1)!} + \ldots + \frac{(-1)^{(\frac{n}{2}-1)}\overline{P}\left[(n-2)b\right]}{(\frac{n}{2}-1)!} \right] \\
&\quad + \frac{(\frac{n}{2}-2)^{\frac{n}{2}-1}(n-4)!}{(\frac{n}{2}-3)!(\frac{n}{2}-3)!2!} \left[\frac{\overline{P}\left[(\frac{n}{2}-2)b\right]}{(\frac{n}{2}-2)!} + \ldots + \frac{(-1)^{(\frac{n}{2}-2)}\overline{P}\left[(n-4)b\right]}{(\frac{n}{2}-2)!} \right] \\
&\quad + \ldots + \\
&\quad + \frac{(-1)^{\frac{n}{2}-2}2^{\frac{n}{2}-1}3!}{(\frac{n}{2}-2)!} \left[\frac{\overline{P}[2b]}{2!} - \overline{P}[3b] + \frac{\overline{P}[4b]}{2!} \right] \\
&\quad + \frac{(-1)^{\frac{n}{2}-1}2!}{(\frac{n}{2}-1)!} \left[\overline{P}[b] - \overline{P}[2b] \right].
\end{aligned} \tag{50}$$

Re–arranging the above terms in order of increasing argument of the inverse Laplace function $\overline{P}[ib], i=1,2,...,n$ gives:

$$\frac{P_K(\tau)}{b} = (-1)^{\frac{n}{2}+1}\left[\frac{2\overline{P}[b]}{(\frac{n}{2}-1)!}\right] + (-1)^{\frac{n}{2}+2}\left[\frac{2^{\frac{n}{2}}3!\overline{P}[2b]}{(\frac{n}{2}-2)!}\right] + \ldots + \frac{(-1)^{\frac{n}{2}+n}\frac{n}{2}^{\frac{n}{2}}3!\overline{P}[nb]}{\frac{n}{2}!\frac{n}{2}!(\frac{n}{2}-1)!}, \tag{51}$$

and using the relationship for even values of n that $(-1)^{\frac{n}{2}+n}=(-1)^{\frac{n}{2}}$, equation (51) can in turn be re–written in the following form:

$$\begin{aligned}\frac{P_K(\tau)}{b} &= (-1)^{\frac{n}{2}+1}\sum_{k=1}^{\min[1,\frac{n}{2}]}\frac{k^{\frac{n}{2}}(2k)!\overline{P}[b]}{(\frac{n}{2}-k)!k!(k-1)!(i-k)!(2k-1)!} \\ &\quad + (-1)^{\frac{n}{2}+2}\sum_{k=2}^{\min[2,\frac{n}{2}]}\frac{k^{\frac{n}{2}}(2k)!\overline{P}[2b]}{(\frac{n}{2}-k)!k!(k-1)!(i-k)!(2k-1)!} \\ &\quad + \ldots + \\ &\quad + (-1)^{\frac{n}{2}+n}\sum_{k=\frac{n}{2}}^{\min[n,\frac{n}{2}]}\frac{k^{\frac{n}{2}}(2k)!\overline{P}[nb]}{(\frac{n}{2}-k)!k!(k-1)!(i-k)!(2k-1)!} \\ &= \sum_{i=1}^{n}(-1)^{\frac{n}{2}+i}\sum_{k=[\frac{i+1}{2}]}^{\min[i,\frac{n}{2}]}\frac{k^{\frac{n}{2}}(2k)!\overline{P}[ib]}{(\frac{n}{2}-k)!k!(k-1)!(i-k)!(2k-1)!}\end{aligned} \tag{52}$$

where $[(i+1)/2]$ is the integer part of $(i+1)/2$. Equation (52) is of the form

$$P_K(\tau)|_{K=\frac{n}{2}} = \frac{\ln 2}{\tau}\sum_{i=1}^{n}V_i(n)\overline{P}\left[i\frac{\ln 2}{\tau}\right], \quad n,\text{even} \tag{53}$$

where the set of coefficients $\{V_i(n), i=1,2,...,n\}$ are called the Gaver–Stehfest set and the i–th member is given by

$$V_i(n) = (-1)^{\frac{n}{2}+i}\sum_{k=[\frac{i+1}{2}]}^{\min[i,\frac{n}{2}]}\frac{k^{\frac{n}{2}}(2k)!}{(\frac{n}{2}-k)!k!(k-1)!(i-k)!(2k-i)!}. \tag{54}$$

Equations (53) and (54) together comprise the Gaver–Stehfest Laplace inversion algorithm. In theory, there is no reason why the approximant $P_{\frac{n}{2}}(\tau)$ should not become more accurate as n increases, but in practice rounding errors worsen the result if n becomes too large. This is because $|V_i|$ increases with n, reflecting the unbounded nature of the Laplace inverse operator (Stehfest, 1970). Therefore, at a fixed machine precision there is an optimal choice for n to return maximum accuracy.

Appendix B

Hertz Vector Representation of a Seafloor HED Lying Over a Uniform Earth

I

In §I of this appendix, I derive the Hertz vector potential $\mathbf{\Pi}(\mathbf{r}, s)$ due to excitation by a horizontal, $\hat{x}$–directed horizontal electric dipole (HED) lying in a uniformly conducting whole–space of conductivity σ. In §II, I shall consider a simple double half–space geometry.

The vector diffusion equation to be solved is

$$\nabla^2 \mathbf{\Pi}(\mathbf{r}, s) - \mu\sigma s \mathbf{\Pi}(\mathbf{r}, s) = \frac{\mathbf{J}_S}{\sigma} \tag{1}$$

with the HED source current density given by

$$\mathbf{J}_S = P\delta(\mathbf{r})\hat{x}. \tag{2}$$

In equation (2), P is the dipole moment, and $\hat{x}$ indicates the horizontal orientation of the dipole with $\hat{z}$ vertical and positive upwards. From (1) it follows that $\mathbf{\Pi}$ is parallel to $\mathbf{J}_S$, i.e.

$$\mathbf{\Pi} = \Pi_x \hat{x}. \tag{3}$$

From (1),(2) and (3) it follows that

$$\left(\nabla^2 - \mu\sigma s\right) \Pi_x = \frac{P\delta(\mathbf{r})}{\sigma} \tag{4}$$

is the equation to be solved. In cylindrical coordinates, there is from the symmetry of equation (4) $\partial_\phi \equiv 0$ so that the Laplacian operator reduces to

$$\nabla^2 = \nabla_\rho^2 + \frac{\partial^2}{\partial z^2} \tag{5}$$

and

$$\Pi_x(\mathbf{r}, s) = \Pi_x(\rho, z, s). \tag{6}$$

It is convenient to seek a solution to the differential equation (4) in the form of a Hankel transform

$$\Pi_x = \int_0^\infty f(\lambda, z) J_0(\lambda\rho)\lambda \mathrm{d}\lambda \tag{7}$$

where J_0 is the Bessel function of order zero. Using the relation

$$\nabla_\rho^2 J_0(\lambda\rho) = -\lambda^2 J_0(\lambda\rho) \tag{8}$$

and equation (7) the differential equation (4) can be re–written as

$$\int_0^\infty \left[-\lambda^2 + \frac{\partial^2}{\partial z^2} - \mu\sigma s\right] f(\lambda, z) J_0(\lambda\rho)\lambda \mathrm{d}\lambda = \frac{P\delta(\mathbf{r})}{\sigma}. \tag{9}$$

The Dirac delta function in cylindrical coordinates under the axial symmetry is, with arbitrary ϕ_0,

$$\delta(\mathbf{r}) = \frac{1}{\rho}\delta(\rho)\delta(\phi - \phi_0)\delta(z). \tag{10}$$

Inserting equation (10) into (9) and integrating both sides over all ϕ, there results

$$\int_0^\infty \left[\frac{\partial^2}{\partial z^2} - u^2\right] f(\lambda, z) J_0(\lambda\rho)\lambda \mathrm{d}\lambda = \frac{P\delta(z)}{2\pi\sigma} \int_0^\infty J_0(\lambda\rho)\lambda \mathrm{d}\lambda \tag{11}$$

where we use has been made of the identity

$$\delta(\rho) = \rho \int_0^\infty J_0(\lambda\rho)\lambda \mathrm{d}\lambda \tag{12}$$

and I have defined

$$u \equiv \sqrt{\lambda^2 + \mu\sigma s}. \tag{13}$$

Thus, from equation (12), the problem of solving the differential equation (4) reduces to the problem of solving

$$\left[\frac{\partial^2}{\partial z^2} - u^2\right] f(\lambda, z) = \frac{P\delta(z)}{2\pi\sigma} \equiv -g(z) \tag{14}$$

which is most easily attacked using the method of Green's functions. This method, solves all one–dimensional non–homogenous Sturm–Louiville problems of which equation (14) is one. The term in brackets in equation (14) is a modified Helmholtz, or diffusion, operator. Let the solution of equation (14) be of the form

$$f = \int_{-\infty}^{\infty} G(z,\tau)g(\tau)\mathrm{d}\tau \tag{15}$$

where $G(z,\tau)$ is a Green's function that can now be constructed.

Let f_1 be a solution to the homogenous equation associated with equation (14) that satisfies the boundary conditions at $f(z = +\infty) = 0$ and let f_2 be a solution that satisfies the boundary condtion $f(z = -\infty) = 0$. Appropriate choices are

$$f_1(\lambda, z) = \exp(-uz) \tag{16a}$$

and

$$f_2(\lambda, z) = \exp(uz). \tag{16b}$$

The Green's function is written generally, in two parts, as

$$G(z,\tau) = -\frac{1}{W} f_1(z) f_2(\tau), \qquad -\infty \leq z < \tau \tag{17a}$$

$$G(z,\tau) = -\frac{1}{W} f_1(\tau) f_2(z), \qquad \tau < z \leq +\infty. \tag{17b}$$

with W being the Wronskian

$$W = f_1(\tau) f_2'(\tau) - f_2(\tau) f_1'(\tau). \tag{18}$$

From equations (16a),(16b) and (28) the Wronskian for the diffusion operator reduces to

$$W = 2u \tag{19}$$

so that for the homogeneous problem associated with equation (14) the particular Green's function is

$$G(z,\tau) = -\frac{1}{2u}\exp(-uz)\exp(u\tau), \qquad -\infty \leq z < \tau \tag{20a}$$

$$G(z,\tau) = -\frac{1}{2u}\exp(-u\tau)\exp(uz), \qquad \tau < z \leq +\infty. \tag{20b}$$

Finally, inserting the Green's function just constructed into equation (15) and integrating yields the result

$$f(\lambda, z) = \frac{P}{4\pi\sigma u}\exp(\pm uz) \tag{21}$$

with the positive sign valid for $z < 0$ and the negative sign for $z > 0$.

Thus, the Hertz vector for an $\hat{x}$–directed HED in a wholespace of conductivity σ is found by combining equations (21) and (7). The result is

$$\mathbf{\Pi} = \frac{P\hat{x}}{4\pi\sigma}\int_0^\infty \frac{\exp(\pm uz)}{u} J_0(\lambda\rho)\lambda \mathrm{d}\lambda. \tag{22}$$

II

Assume the HED is resting on the seafloor, a horizontal interface at $z = 0$, with the ocean conductivity σ_0 above and the crust conductivity σ_1 below. By symmetry, there will be no electric field component in the $\hat{y}$ direction. The Hertz vector will have the form (Wait 1961)

$$\mathbf{\Pi}(\rho, z) = \Pi_x\hat{x} + \Pi_z\hat{z}. \tag{23}$$

The Hertz components in the ocean, denoted by superscript 1 can be writtem generally as

$$\Pi_x^1 = \frac{P}{2\pi\sigma_0}\int_0^\infty [1 + A(\lambda)]\frac{\exp(-u_0 z)}{u_0} J_0(\lambda\rho)\lambda \mathrm{d}\lambda \tag{24a}$$

$$\Pi_z^1 = \frac{P}{2\pi\sigma_0}\int_0^\infty C(\lambda)\exp(-u_0 z) J_0(\lambda\rho)\lambda \mathrm{d}\lambda \tag{24b}$$

where equation (24a) with its $[1 + A]$ term is written suggestively as a sum of primary and secondary Hertz components, that is

$$\Pi_x^{1,\mathrm{sec}} = \frac{P}{2\pi\sigma_0}\int_0^\infty A(\lambda)\frac{\exp(-u_0 z)}{u_0} J_0(\lambda\rho)\lambda \mathrm{d}\lambda. \tag{24c}$$

In the crust, region 2, there is

$$\Pi_x^2 = \frac{P}{2\pi\sigma_1}\int_0^\infty B(\lambda)\frac{\exp(u_1 z)}{u_1}J_0(\lambda\rho)\lambda \mathrm{d}\lambda \tag{25a}$$

$$\Pi_z^2 = \frac{P}{2\pi\sigma_1}\int_0^\infty D(\lambda)\exp(u_1 z)J_0(\lambda\rho)\lambda \mathrm{d}\lambda. \tag{25b}$$

In equations (24) and (25) I have set

$$u_i = \sqrt{\lambda^2 + \mu\sigma_i s}. \tag{26}$$

The coefficients A,B,C,D are found by ensuring that the tangential components of the electric and magnetic fields are continuous across the seafloor. These boundary conditions explicitly are now applied explicitly.

The first boundary condition to be considered is continuity of the secondary tangential magnetic field across–strike, i.e.,

$$B_y^{1,\mathrm{sec}}|_{z=0} = B_y^2|_{z=0}. \tag{27}$$

In terms of the Hertz vector components, see equation (6.4), this becomes

$$\sigma_0\left[\partial_z\Pi_x^{1,\mathrm{sec}} - \partial_x\Pi_z^1\right]_{z=0} = \sigma_1\left[\partial_z\Pi_x^2 - \partial_x\Pi_z^2\right]_{z=0} \tag{28}$$

and, after substitution of the equations (24) and (25) the condition

$$(D-C)\partial_x J_0(\lambda\rho) = (A+B)J_0(\lambda\rho) \tag{29}$$

is obtained. The second boundary condition is

$$B_x^1|_{z=0} = B_x^2|_{z=0} \tag{30}$$

which gives

$$\sigma_0\partial_y\Pi_z^1|_{z=0} = \sigma_1\partial_y\Pi_z^2|_{z=0}. \tag{31}$$

and leads to

$$C = D. \tag{32}$$

The remaining two constraints on the four unknown coefficients are obtained by ensuring continuity across the seafloor of the tangential components of the electric field.

The boundary condition

$$E_x^1|_{z=0} = E_x^2|_{z=0} \tag{33}$$

on the across–strike electric field implies, from equation (6.5),

$$\left[-\mu\sigma_0 s\Pi_x^1 + \partial_{xx}\Pi_x^1 + \partial_{xz}\Pi_z^1\right]_{z=0} = \left[-\mu\sigma_1 s\Pi_x^2 + \partial_{xx}\Pi_x^2 + \partial_{xz}\Pi_z^2\right]_{z=0} \tag{34}$$

which, upon substiution of equations (24) and (25), leads to the constraint

$$\left[\frac{-1-A}{u_0} + \frac{B}{u_1}\right] J_0(\lambda\rho) - \frac{1}{\mu s}\left[\frac{u_0 C}{\sigma_0} + \frac{u_1 D}{\sigma_1}\right] \partial_x J_0(\lambda\rho)$$

$$= \frac{1}{\mu s}\left[\frac{1+A}{u_0\sigma_0} - \frac{B}{u_1\sigma_1}\right] \partial_{xx} J_0(\lambda\rho). \tag{35}$$

The final boundary condition is

$$E_y^1|_{z=0} = E_y^2|_{z=0} \tag{36}$$

which gives

$$\left[\partial_{xy}\Pi_x^1 + \partial_{yz}\Pi_z^1\right]_{z=0} = \left[\partial_{xy}\Pi_x^2 + \partial_{yz}\Pi_z^2\right]_{z=0} \tag{37}$$

and leads to the final constraint equation

$$\left[\frac{1+A}{u_0\sigma_0} - \frac{B}{u_1\sigma_1}\right] \partial_{xy} J_0(\lambda\rho) = \left[\frac{u_0 C}{\sigma_0} + \frac{u_1 D}{\sigma_1}\right] \partial_y J_0(\lambda\rho). \tag{38}$$

The system of four equations (29),(32),(35) and (38) for the four unknown coefficients A–D has the solution

$$1 + A = \frac{u_0}{u_0 + u_1} \tag{39}$$

$$B = \frac{u_1}{u_0 + u_1} \tag{40}$$

$$C = D = \frac{-R\partial_x}{u_0 + u_1} \tag{41}$$

where we have defined

$$R \equiv \frac{\sigma_1 - \sigma_0}{\sigma_1 u_0 + \sigma_0 u_1}. \tag{42}$$

Inserting the above coefficients into equations (24) and (25) yields the final expressions for the Hertz vector components due to an HED source at the seafloor interface above a uniformly conducting earth. In the ocean, they are

$$\Pi_x^1 = \frac{P}{2\pi\sigma_0} \int_0^\infty \frac{\exp(-u_0 z)}{u_0 + u_1} J_0(\lambda\rho)\lambda \mathrm{d}\lambda \tag{43a}$$

$$\Pi_z^1 = \frac{P}{2\pi\sigma_0\mu_0 s} \int_0^\infty \frac{R\exp(-u_0 z)}{u_0 + u_1} \partial_x J_0(\lambda\rho)\lambda \mathrm{d}\lambda \tag{43b}$$

and in the earth

$$\Pi_x^2 = \frac{P}{2\pi\sigma_1} \int_0^\infty \frac{\exp(u_1 z)}{u_0 + u_1} J_0(\lambda\rho)\lambda \mathrm{d}\lambda \tag{44a}$$

$$\Pi_z^2 = \frac{P}{2\pi\sigma_1\mu_0 s} \int_0^\infty \frac{R\exp(u_1 z)}{u_0 + u_1} \partial_x J_0(\lambda\rho)\lambda \mathrm{d}\lambda. \tag{44b}$$